DESULFURIZED JET A FUEL PROCESSING TO PRODUCE HYDROGEN VIA AUTOTHERMAL REFORMING AND WATER-GAS SHIFT

by

Shuyang Zhang

A Dissertation Submitted to the Faculty of the

DEPARTMENT OF AEROSPACE AND MECHANICAL ENGINEERING

In Partial Fulfillment of the Requirements

For the Degree of

DOCTOR OF PHILOSOPHY

WITH A MAJOR IN MECHANICAL ENGINEERING

In the Graduate College

THE UNIVERSITY OF ARIZONA

2018

THE UNIVERSITY OF ARIZONA
GRADUATE COLLEGE

As members of the Dissertation Committee, we certify that we have read the dissertation prepared by *Shuyang Zhang*, titled *Desulfurized Jet A Fuel Processing to Produce Hydrogen via Autothermal Reforming and Water-Gas Shift* and recommend that it be accepted as fulfilling the dissertation requirement for the Degree of Doctor of Philosophy.

Peiwen Li Date: 7/26/2018

Cho Lik Chan Date: 4/30/2018

Yitshak Zohar Date: 4/19/2018

James Farrell Date: 4/19/2018

Final approval and acceptance of this dissertation is contingent upon the candidate's submission of the final copies of the dissertation to the Graduate College.

I hereby certify that I have read this dissertation prepared under my direction and recommend that it be accepted as fulfilling the dissertation requirement.

Dissertation Director: *Peiwen Li* Date: 7/26/2018

STATEMENT BY AUTHOR

This dissertation has been submitted in partial fulfillment of the requirements for an advanced degree at the University of Arizona and is deposited in the University Library to be made available to borrowers under rules of the Library.

Brief quotations from this dissertation are allowable without special permission, provided that an accurate acknowledgement of the source is made. Requests for permission for extended quotation from or reproduction of this manuscript in whole or in part may be granted by the head of the major department or the Dean of the Graduate College when in his or her judgment the proposed use of the material is in the interests of scholarship. In all other instances, however, permission must be obtained from the author.

SIGNED: Shuyang Zhang

ACKNOWLEDGEMENTS

I owe great gratitude to people who have supported me completing my work financially, physically, and mentally. I could never start a single word without anyone I mentioned here. First and foremost, my supreme gratitude is given to Prof. Li, who mentored and sponsored me during my Ph.D. career. Without his sagacious advice and patient instruction, my work would never exist. The knowledge of his rigorous attitude towards research, wisdom in time organization and patience in tedious work would benefit my entire life.

I also would like to acknowledge Prof. Chan, Prof. Zohar and Prof. Farrell for being the committee member of my comprehensive exam and final defense. Every single piece of their suggestions is making my research more reasonable and scientifical.

Grateful acknowledgement is given to the support from the Office of Naval Research of the USA (Grant # N00014-09-1-0695). I thank my colleges who are or were sharing the same office with me, Xiaoxin Wang, Ye Zhang and Edgar Molina, for making the after-school life more interesting and exciting. Special thanks are given to Xinhai Xu who made tremendous effort to preset-up the experimental testing system and obtain the preliminary results.

I continue to thank my wife Huijie Dai, mom Yujin Yang and dad Binbin Zhang for being endlessly supportive to my decision. I can’t even imagine any achievement in my research without them. Their love is the most important thing that keeps me warm and whole.

To my beloved wife Huijie and our daughter Maggie.

TABLE OF CONTENTS

LIST OF FIGURES

LIST OF TABLES

ABSTRACT

Hydrogen is an alternative fuel which is well recognized as one of the solutions to the fossil fuel depletion problem. As an energy carrier, hydrogen can be used to store and deliver energy or be converted into other types of energy, such as heat, electrical energy or mechanical work. Among all the applications, fuel cell is drawing increasing attention for its advantages such as higher theoretical energy conversion efficiency, no internal moving mechanical parts and environmentally friendly.

Almost all the common fuel cells require hydrogen gas as the fuel source oxidized to complete the half-reaction redox cycle, which makes hydrogen gas a crucial factor for the development of fuel cell technique. However, under some certain circumstances, hydrogen supply could be extremely constrained by the harsh environment. For example, fuel cells used onboard has critical requirement on the space and extremely limited energy source, which makes carrying extra hydrogen tanks not an option in most cases. Therefore, onboard hydrogen production via catalytic autothermal reforming (ATR) and water-gas shift (WGS) is considered beneficial to vehicles using fuel cells as auxiliary power unit because it eliminates the challenges of hydrogen storage and delivery.

The objective of this research is to develop a fuel processing system with reliable ATR and WGS catalysts to produce hydrogen feasibly from Jet A fuel, which is used as the primary fuel for both civilian and military transportation. Jet A fuel is expected to be converted into hydrogen gas, so that when considering onboard fuel cell applications, extra tanks of natural gas, ammonia or other hydrocarbons are not necessary.

However, before the process can be examined, the sulfur component containing in the Jet A fuel must be removed because sulfur can easily poison the catalysts participating in the conversion reactions and even the catalysts in the downstream fuel cells. An effective and reliable in-house-made adsorbent was developed through simple procedures and cheap raw materials. The adsorbent has a very large surface area of over 250 m^2/g with the optimal sulfur adsorption capacity of 2.95 mg-S/g-ads at the breakthrough point of 50 ppmw S in effluent fuel.

A kw_{th}-class fuel processing testing system was designed and fabricated afterwards in the lab to examine the system performance through experiments. The ATR of n-dodecane, working as the surrogate of Jet A fuel, was firstly studied with the initial simplified system under different operating conditions for better understanding each of the reactions. The compositions of system effluents in dry gas basis were detected by an on-site GC instrument and the gas temperature at distinct locations were monitored by a bunch of thermocouples connecting to a data acquisition (DAQ) system purchased from National Instruments company. Three indices, hydrogen yield, fuel conversion and energy efficiency were calculated based on the experimental results to evaluate the system performance.

In addition, a novel in-house-made honeycomb-type ATR catalyst was synthesized in the lab with exceptional catalytic activity. The hydrogen molar fraction in the reformate was stable at over 40% from 500 ^oC to 700 ^oC with the maximum hydrogen yield achieved at close to 2.1.

After that, the ATR of desulfurized Jet A fuel was investigated in a modified system and compared with the n-dodecane case. The results show that they had very different

behaviors and ATR of Jet fuel was significantly difficult than ATR of the pure hydrocarbon with the highest hydrogen molar fraction of 30% and yield of 1.4 obtained at 700 ^{o}C. Coke suppression was discovered regarding the higher fuel conversion under certain operating conditions.

To further decrease the carbon monoxide concentration and increase hydrogen yield, water-gas shift reaction was introduced after the ATR reformer so that the exhaust heat would not be wasted. Thus, it is required to perform the thermodynamic analysis and heat transfer modeling of the overall system consisted of an ATR reformer, a WGS reactor and two countercurrent flow heat exchangers (recuperators) to theoretically determine how large would the heat exchanging area be enough. By examining the required energy that is used to preheat the reactants and the reaction energy that could be possibly transferred to the reactants, the overall process has a potential to be self-sustainable, indicating the system does not require large amount energy input once the process is initiated.

Finally, WGS reaction performance was studied in the overall fuel processing system with the same evaluation indices as the ATR process. Results show that with the WGS reaction, hydrogen production is increased together with CO suppressed.

Chapter 1. Introduction

Hydrogen has been considered for use as an alternative fuel [1] due to its low-greenhouse gas emission [2], abundance in domestic sources [3], and crucial role in fuel cell systems [4]. Basically, fuel cell is a device which converts chemical energy stored in a fuel into electrical energy. A typical fuel cell unit is primarily composed of an anode, a cathode and an electrolyte separating between them. In operation, fuel (mainly hydrogen or carbon monoxide) and an oxidant are fed to the anode and cathode respectively with the electrochemical reaction occurring on either electrode depending on the type of the fuel cell. The electrons produced by the anode reaction get to the cathode through the external circuit, which generates electric current. [5] Since its first discovery in 19^{th} century, fuel cell has been developed competitively in many applications such as stationary power plant, transportation, and household portable power sources [6] [7]. Due to the advantages of fast start-up, high reliability, and compactness, solid oxide fuel cell (SOFC) and proton exchange membrane fuel cell (PEMFC) were investigated to serve as the auxiliary power units (APUs) on board of vessels and vehicles with hydrogen as the primary fuel [8] [9] [10] [11].

However, hydrogen does not exist naturally as a gas on the earth. It has to be produced from its sources which contains hydrogen as an element, such as water, hydrocarbon, ammonia and metal hydrides [12] [13]. The current dominant hydrogen production technique is natural gas steam reforming which produces 95% of hydrogen in the United States according to the Office of Energy Efficiency & Renewable Energy [14]. This technique requires natural gas and water reacting together with very high energy input so

that it is only promising in large central plants where continuous high-capacity energy source is available. Other state-of-the-art techniques include biomass steam reforming [15], electrolysis [16], gasification [17], thermochemical water splitting [18], photocatalytic [19], etc, which are still under research worldwide regarding either cost or reliability issues. Although in general the mature steam reforming and the other emerging techniques have the capability to satisfy the hydrogen demand for both industry and civilian, the option is limited when considering hydrogen production under some certain circumstances. For example, underwater exploration have critical requirement on the carry-on items and are exposed to extremely limited energy sources. Thus, to supply hydrogen to the onboard fuel cell system, it would be not practical to carry extra hydrogen or deploy any onsite hydrogen production techniques which require solar energy or very high energy input.

To solve this issue, researchers have focused their attention on another technique, namely autothermal reforming (ATR), to produce hydrogen from hydrocarbons (light or heavy) onboard so that there is no need to worry about hydrogen delivery and storage, which are still two primary challenges that a huge number of researchers are working on [20] [21] [22]. The Jet fuel would be simply selected as the hydrocarbon source, which is a hydrocarbon compound with complicated components, working as the logistic fuel for both civilian and military vessels [23]. Autothermal reforming is a combination of two processes, partial oxidation (POX) and steam reforming (SR). POX is an exothermic process with relatively high reaction rate and low hydrogen production, however, SR is endothermic with high hydrogen production and requires high energy input. Autothermal reforming process takes benefit from both processes, such as rapid thermal response,

relatively high hydrogen yields, and remarkable coke-suppression capability, making it the most feasible technique for onboard hydrogen production [24] [25].

$$C_aH_b + xO_2 + (a - 2x)H_2O \rightleftharpoons aCO + (a + b/2 - 2x)H_2 \quad (1)$$

Equation (1) shows the typical expression of a hydrocarbon autothermal reforming reaction. It can be manipulated by selecting different *x*s (oxygen to fuel ratio) to make the reaction either POX dominant or SR dominant, in other words, either endothermic, exothermic or even thermally neutral. Therefore, the combined process could be controlled to be slightly exothermic or thermally neutral so that if the reaction exhaust heat could be utilized efficiently, it potentially requires no need for any external heating or cooling source to maintain the reaction status once the process starts. That being said, the process has a potential to be self-sustainable.

Our target is to produce hydrogen through autothermal reforming of Jet A fuel, however, there still remains some issues. 1) The Jet fuel is a kerosene type compound with hundreds of complicated organic substances from C8 to C16 [26]. The primary groups of hydrocarbons in Jet fuel are paraffins, aromatics, naphthenes and olefins [27]. To enhance the fuel performance properties, additives such as antioxidant and metal deactivator are usually added into the Jet fuel as well, which further complicates the situation [28]. 2) The sulfur concentration containing in the Jet fuel is typically over 1000 ppmw. Sulfur is detrimental to most chemical catalysts including the ATR catalyst and the catalyst in the downstream fuel cells. It can deactivate the catalysts in a very short time and the deactivation process is usually irreversible [29]. 3) Autothermal reforming usually ends up with a mixture of H_2, CO, CO_2, H_2O in the reformate. It can be directly passed to an SOFC

since H_2 and CO are both eligible fuel. Nevertheless, it would bring troubles if a PEMFC is placed downstream, as CO could significantly poison the anode catalyst [30]. Although high temperature PEM (HT-PEM) fuel cells may have better CO-tolerance capability for as high as 4–5% [31] at 200 ^{o}C, effective CO removal techniques must be carried out before the reformate fueling to the fuel cell.

This study is aiming at seeking solutions to those issues involving in autothermal reforming of Jet fuel. Chapter 2 reviews some background knowledges about fuel cells, different hydrogen production techniques and some results on the desulfurization of a commercial Jet A fuel purchased from a local aviation service company. Although the experimental results are obtained with the collaboration of me and another graduate student, Xinhai Xu, who received his Ph.D. degree in 2014, I would not emphasize it as one of my contributions in this work.

Chapter 3 is particularly used to illustrate the study of autothermal reforming of n-dodecane and desulfurized Jet A fuel, both in literature survey and through experimental tests. The best operating condition is discovered by evaluating the system at variables such as reaction temperature, H_2O/C and O_2/C. In addition, the detailed set-up of the kW_{th}-class fuel processing system and some instruments that have been employed in the work will also be included.

To better understand the theoretical self-sustainability of the overall process, thermodynamic analysis and heat transfer modeling are demonstrated in Chapter 4. Based on the calculated heat exchanging area, two special shell-and-tube countercurrent flow heat exchangers are fabricated and integrated into the system. The WGS process is discussed in

Chapter 5 and the experimental results will be compared with the ATR process simultaneously to explicitly illustrate the overall system performance.

Finally, the overall conclusions will be shown in Chapter 6 together with some future expectations before the references and appendices.

Chapter 2. Literature Review and Preliminary Results

2.1. Fuel Cell

Fuel cell uses two electrochemical reactions to generate electric power. Compared with the conventional internal combustion engine, it eliminates the thermodynamic limitation – Carnot efficiency, which indicates that the efficiency of a fuel cell device will not be limited by the temperature. Because there are no flames and combustion process, fuel cell causes less pollution issues. Moreover, in fuel cell, the power is generated directly from electron circulation instead of the gas turbine connected with an electric generator in the power engine. It could be another advantage when quiet environment is crucial since there are no major moving parts in a fuel cell device. [5]

Unlike the battery which is considered as an energy storage device, fuel cell is used to convert the chemical energy into electrical energy. It cannot store any type of energy in any form, however, when a battery depletes its capacity it ceases to produce power, while a fuel cell can continuously work as long as the fuel and oxidant are fed to it. [32]

Figure 1 shows a typical Proton Exchange Membrane Fuel Cell consisted of an anode, a cathode and an electrolyte between them. Fuel (in most cases, hydrogen) is fed through the diffusion layer to the anode where it loses the electrons and gets oxidized, while the oxidant (oxygen or air) is fed to the cathode and receives the electrons through the outlet circuit. The redox reaction is separated at both electrodes and connected by the ions conducting through the electrolyte. Although depending on the fuel cell types, the materials of the electrodes and electrolytes could be selected differently, they all yield similar

properties as their functions are the same. Electrodes are usually porous materials with fantastic redox catalytic activity and high conductivity, so that the fuel/oxidant and the reaction product can be easily delivered to or removed from the surface sites and the electrons can suffer from low electrical resistance (internal ohmic loss, contact resistance, concentration polarization and activation polarization) [33]. Electrolytes generally have high ionic conductivity and negligible electronic conductivity, and are impermeable to gases and chemically stable [34].

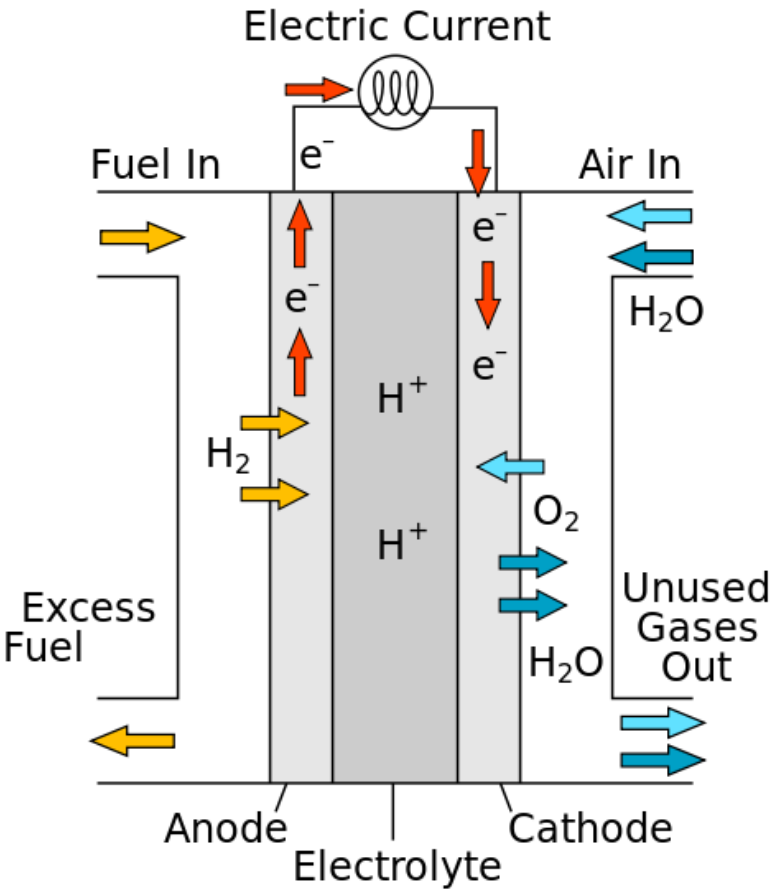

Figure 1. Schematic of typical PEMFC [41]. Anode reaction: $H_2 \rightarrow 2H^+ + e^-$; Cathode reaction: $½O_2 + e^- + 2H^+ \rightarrow H_2O$; Overall reaction: $H_2 + ½O_2 \rightarrow H_2O$.

To date, fuel cells are classified into five major groups regarding the significantly different electrolytes [35]:

i. Alkaline Fuel Cell (AFC)
ii. Proton Exchange Membrane Fuel Cell (PEMFC) and Direct Methanol Fuel Cell (DMFC)
iii. Phosphoric Acid Fuel Cell (PAFC)
iv. Molten Carbonate Fuel Cell (MCFC)
v. Solid Oxide Fuel Cell (SOFC)

Alkaline Fuel Cell is one of the most mature fuel cells that was used to supply power to space applications in the Apollo program [36]. It uses potassium hydroxide as the electrolyte with hydrogen and oxygen as the fuel and oxidant respectively. The OH^- is circulating in the electrolyte from the cathode to the anode in order to complete the redox reaction. The typical working temperature for an AFC is from 100 to 250 ^oC with a higher KOH solution concentration at higher temperature. After its early success in space activities, this type of fuel cell is rapidly replaced by the PEMFC in vehicle applications. [37]

Proton Exchange Membrane Fuel Cell and Direct Methanol Fuel Cell are classified in the same category because they are composed of the same type of electrolyte – perfluoro-sulphonic acid (PFSA) polymer membranes (e.g. Nafion), however, PEMFC requires hydrogen as the fuel and DMFC works on methanol. They are suitable in many applications such as transport, portable devices and power generation units and are currently the most popular type of fuel cell regard to unit shipment [35]. Because this membrane is limited to low operating temperature (60 – 100 ^oC), the fuel cell suffers from various issues, including

low conductivity, water management issue and low tolerance to impurities, e.g. CO and S. New types of polymer membranes could allow the fuel cell work at higher temperatures, improving the CO tolerance to as high as 4–5% [31] at 200 ^{o}C and significantly reducing the humidification issues. [38]

Phosphoric Acid Fuel Cell operates at 150 – 190 ^{o}C and is commercially available in stationary power unit applications. The acid electrolyte does not react with CO_2 and steam is usually not a problem, making this fuel cell expanding successfully in co-generation application. [39]

Molten Carbonate Fuel Cell is developing rapidly in recent years, favoring from the cost reduction and performance improvement. It uses a mixture of alkali carbonates as the electrolyte and typically operates at 600 – 700 ^{o}C. Due to its high operating temperature, MCFC avoids using the noble metal electrodes required by the low temperature fuel cells, and can work on flexible type of fuels including hydrogen, hydrocarbon and carbon monoxide. The application for this type of fuel cell is also stationary power plant.

Solid Oxide Fuel Cell can also work on various fuels and operates between 750 – 1100 ^{o}C. It is particularly employed to combined heat and power (CHP) applications and supply power to households and large industrial premises, which is compatible with the conventional power generation plant. The future research challenges involve the integration of the fuel processing to the fuel cell system and lowering operation temperature. [40]

2.2. Hydrogen Production Techniques

Gaseous hydrogen does not exist naturally on the earth and it can be produced from a variety of feedstocks, gas (methane), liquid (water) and solid (biomass). This section reviews some common hydrogen production techniques that are either dominating the market or still under laboratory development.

2.2.1. Hydrocarbon reforming

The hydrocarbons that can be reformed are those in gas phase or liquid phase. Although this technique is called hydrocarbon reforming in general, it also includes the transition of ethanol, ether and other organic compounds. Depending on the reactants, four basic reforming techniques are developed, steam reforming, partial oxidation, autothermal reforming [42] and dry reforming [43].

2.2.1.1. Steam reforming

Since the first introduction to industry in 1930 [44], steam reforming is becoming the most popular and reliable hydrogen production technique all over the world. In the United States, because the natural gas storage capacity is so big that 95% of hydrogen is produced via natural gas steam reforming [14]. Globally, natural gas steam reforming produces roughly 50% of the hydrogen and heavy oils reforming contributes another 30% [45] [46]. Steam reforming is a highly endothermic reaction with relatively low reaction rate [47] [48] [49]. It requires continuous external energy input to maintain the reaction status and the reactor size is usually larger compared to partial oxidation reactor [47]. However, the H_2 concentration in the product is higher and the operating temperature is usually lower than the other reforming techniques [46] [50].

$$CH_4 + H_2O \rightarrow CO + 3H_2, \qquad \Delta H^0_{298} = 206.1 \text{ kJ/mol} \tag{2}$$

The majority of research towards the hydrocarbon steam reforming since its industrialization are focusing on the catalysts deactivation mechanism investigation and the catalyst innovation for better coke suppression and sulfur tolerance capability. To study the catalysts deactivation caused by coke deposition and sulfur poisoning, Biswas and co-workers [51] related the surface structure and imperfection of several commercial Pt/Al_2O_3-based reforming catalysts to the corresponding deactivation process. Explanations on the atomic level were given to specify the role of poisons in catalytic reforming. Another group focused on the experimental test to predict the deactivation rates of the traditional tubular nickel catalysts [52]. An accelerated aging test was designed to simulate the different poisoning process for better understanding of the mechanisms. As a side product in biomass gasification, hydrogen sulfide could significantly affect the performance of methane steam reforming. Two commercial nickel-based catalysts from different companies were studied by Koningen under various sulfur concentrations [53]. Other research were either elucidating the poisoning mechanism through characterization techniques [54] or experimental testing results [55]. Depending on the reaction conditions, coking formation on the Pt/alumina catalyst can be different. Even if the operating conditions are the same, coke can be deposited on both metal and support surfaces, resulting in different behaviors towards being oxidized. With the help of a bunch of material characterization techniques, a more refractory coke was discovered to remain stable at even 600 ^oC, although the chemical composition was similar to the low-temperature coke [56]. The amorphous carbon formed by light olefins and aromatic compounds could deposit on Ni active sites, causing fast catalyst deactivation, while the

filamentous carbon produced by paraffin reforming only caused slow deactivation according to a research by Barbarias and co-workers [57]. The tetragonal structure in catalyst favored the formation of carbon in the presence of toluene in the feed. Severe coking was found over the catalysts during the steam reforming of hydrocarbon mixtures [58].

The conventional nickel-based reforming catalysts can be significantly affected by sulfur which is a common impurity in an industrial level feedstock, and coke formation which is almost evitable in all hydrocarbon participating high temperature process [59]. Because noble metals are usually less sensitive to sulfur and coke, quite a lot of research were focusing on the additive of noble metals to the current catalysts.

A patented methane steam reforming catalyst composed of iridium, palladium or platinum supported on lanthanum stabilized alumina or magnesium was developed and tested in the presence of 2300 parts per million of H_2S. The highest methane conversion achieved in the patent is of 65% at the temperature of 784 ^oC [60]. Another patented catalyst with the active components selected from platinum and ruthenium is tested for the steam reforming of various hydrocarbons with and without sulfur. No catalyst deactivation was detected after a 220-h continuous test using iso-octane with 100 ppm sulfur [50] [61]. Suzuki and the co-workers [62] worked on the steam reforming of kerosene over a highly dispersed Ru/Al_2O_3 catalyst. The sulfur resistance was improved dramatically using a ceria doped catalyst with the fuel conversion of 85.5% under 50–52 wt ppm of sulfur and maintained as high as 98–99% for over 8000 h under 0.1 ppm sulfur. Rhodium-based bimetallic or trimetallic catalysts have better performance towards steam reforming of toluene, kerosene and transportation fuels with sulfur [63] [64]. Some other researchers

[65] added Ni to the noble metal-based catalyst on purpose and recognized the Ni as a protective and sacrificial metal. The 2% Rh–10% Ni/CeO_2–Al_2O_3 catalyst is able to achieve >95% Jet fuel conversion with 22 ppm sulfur for 3 days. There were also a few reports [66] [67] that bimetallic catalysts exhibited promising sulfur tolerance for steam reforming of liquid fuel, even if noble metals were abandoned.

Coke formation is another tough issue and is usually found during the thermal cracking of hydrocarbons, such as ethylene or olefin [68] [69] [70]. The performance of ethanol steam reforming on Ni-based catalyst were decreasing gradually with time-on-stream at 600 ^oC due to the carbon formation. The one with La_2O_3 support showed enhanced stability and activity under higher H_2O:EtOH [71]. Other researchers found that the addition of small amounts of Rh and Pt on the commercial NiO-MgO catalyst was in favor of carbon inhibition. The formation of M-Ni alloy particles with high concentration of surface noble metals were the feasible reasons [72]. Two types of carbon – NiC_3 and extruded carbon, were observed on the Ru–Ni catalyst during the steam reforming of *n*-dodecane. However, they did not grow into the most refractory filamentous (whisker) carbon because the Ru–Ni clusters were with the ensemble size unsuitable for the growth of filaments [73]. Hua and co-workers [74] developed Ni-Cu-Fe alloy cermet as on-cell reforming catalyst which revealed pronounced capability towards coke suppression. Ceria was found to possess the capability of coke resistance by promoting coke removal and prevent catalytic deactivation through coking. Although as the support modifier, lanthana also enhanced the stability and prevent coke production, the hydrogen yield was not improved based on the experimental results [75]. Some other research affirmed the coke suppression capability of Ce by saying that the produced carbon could be gasified to CO by the oxygen released from ceria

reduction [76] [77]. Similar to sulfur tolerance, coking can be restrained by using bimetallic catalysts. Dagle and co-workers [78] developed bimetallic IrNi catalyst for steam reforming of hydrocarbons from biomass gasifier-derived syngas and found that small Ir clusters supported on large Ni particles exhibited superior stability and resistance to coking. Au and Ag together with the transition metals promoted Ni-based catalyst were also found to be beneficial to coke suppression. Bimetallic catalysts exhibited superior performance compared to monometallic Ni catalysts [79]. The formation of coke was favored at high reaction temperature, however, the addition of Sn to form a Sn-Pt interaction could effectively inhibit olefins (coke precursors) production during glycerol reforming, resulting in improved coke suppression [80]. Zn was also found to be helpful with coke resistance. Only 0.1 wt.% of coke deposition was detected on the used NiO-ZnO-Al_2O_3 catalyst with a Ni molar ratio of 35%. For a Ni-based Al_2O_3 catalyst, the amount of coke deposition was increasing with the increase of Ni content, nevertheless, with the addition of promoter Zn, the coke formation appeared to be restrained by the increase of Ni content [81]. The same result was obtained by Zhang and co-workers [82] on the steam reforming of acetic acid over Ni/γ-Al_2O_3 catalysts, with the increased catalytic stability and coking tolerance by promoting with the Ni loading.

Other research suggested the catalysts preparation method could affect the coke formation. For example, Jasso and the co-workers [83] used materials characterization techniques and found that the anchoring of the metal by calcination before the impregnation would be advantageous for coke resistance. Higher temperature and macro-mesoporous monolithic structure was also good at coke suppression and nickel sintering resistance. The Ni/Mg-Al catalyst exhibited stable ethanol steam reforming activity after 100 h on-stream

at 700 ^{o}C [84]. Coke deposition and metal oxidation could also be restricted through precipitation of sepiolite supported Ni catalyst by the steam reforming of glycerol at milder reaction conditions (350–400 ^{o}C) [85]. Besides, to revise the operating conditions by choosing a proper temperature and a higher steam-to-fuel ratio in order to maximize the reforming and WGS reactions, would also favor coke suppression. The regeneration of catalyst by coke combustion in another unit was a suitable way for the scaling up process [86]. Compared to the catalyst surface, coke formation is more intense to be found on the reactor wall above the catalyst bed. By spraying the liquid feedstock into the reactor could effectively result in minimization of carbon deposits. The carbonaceous deposits were found to be of the CH_x form after the observation over the TPO spectrum [87].

Numerous research focused on the catalyst design and synthesis method discussion by catalytic performance investigation without detecting any deactivation. Common elements that exhibited reforming catalysis ability are transition metals (Ni, Co, Fe, Cu), noble metals (Pt, Rh, Pd) and rare earth (Ce, La) [88] [89]. Dong and co-workers [90] found that the strong interaction between support (Ce-ZrO_2) and metal (Ni) played very important roles in the methane reforming. Ni doped lanthanum aluminate (LAO) was developed by Ohno [91] using chemical solution deposition method. Results show that the perovskite mono-phase was important factor with respect to the ethanol steam reforming. The nickel precursor also had effect on the reforming performance according to another research [92]. The experimental results and catalyst morphology indicated that the Ni supported on the gasification derived char from the nickel nitrate precursor showed preferred catalytic efficiency on the reforming of toluene and naphthalene than those from the nickel acetate. Yu and co-workers [93] studied the steam reforming of kerosene over Ni-La and Ni-La-

K/cordierite catalyst. The activity and selectivity are significantly improved by introducing K to the Ni-La catalyst. Although dramatic catalyst sintering was discovered at the reaction temperature of 973 K, the catalyst was able to maintain good stability at 873 K for the time-on-stream of 50 h. Other Ni-based reforming catalysts include NiO-MgO/cordierite [94] and Ni supported La, Ce and Zr oxides [95], etc [88]. Some researchers put attention on the Cu-based reforming catalysts. Matsumura [96] prepared the Cu-ZnO-ZrO_2-Y_2O_3-In_2O_3 coprecipitated on a zirconia support with the estimated lifetime as long as 53×10^2 h at 400 ^oC. However, at 400–550 ^oC the catalytic activity of methanol steam reforming gradually decreased due to the particle aggregation leading to the Cu sintering. The Cu sintering was also discovered by other researchers [97] on the Cu/γ-Al_2O_3/Al catalyst at 350 ^oC. Enhanced catalytic performance of dimethyl ether steam reforming could be obtained by doping proper amount of Ni into the Cu-based catalyst. The results of durability test showed the catalyst maintained 100% DME conversion during a 180-h test under critical conditions with 400 ^oC. Compared to Ni, Cu-based cascading metal foams exhibited preferable performance towards hydrogen production by the cylindrical laminated methanol steam reforming in a microreactor. This type of microreactor was promising for supplying hydrogen to PEMFCs and hydrogen power electronic devices [98]. Besides, Co-based [99] [100] and noble metal-based [101] [102] [103] catalysts were also popular choices in the research area of hydrocarbon steam reforming.

As kinetics are vital to chemical reaction process, quite a lot of researchers were focusing on the steam reforming kinetic model development. Although there is still disagreement because of experimental inaccuracies [104] and reaction pathways complexity [105], some accurate and reliable models are well investigated and recognized

by researchers. Only very brief reviews will be put in this work for reference. The most famous model was built by Xu and Froment in 1989 [106] for the methane steam reforming on a $Ni/MgAl_2O_4$ catalyst. Based on the consideration of no diffusional limitations in the catalysts bed, the obtained activation energy was 240.1 kJ/mol, which is very close to some other researchers' work. Other references include micro-kinetic model on Rh (111) and Ni (111) from James [107], kinetics of steam reforming of phenol on $Ni\text{-}Co/ArO_2$ from Nabgan [108] and steam methane reforming over NiO/Al_2O_3 from Abbas.

2.2.1.2. Partial oxidation

Instead of reacting with water, partial oxidation requires the hydrocarbons partially oxidized with oxygen to produce hydrogen. The process is exothermic with relatively high reaction rate. Therefore, the reactor is usually more compact compared to steam reforming process. However, the experimental results [109] show that in practical, the theoretical equilibrium constant can never be achieved at the temperature up to 1500 K, although the difference decreasing as the temperature raised. For a typical non-catalytic partial oxidation reaction, the mixture must be heated up to 700–900 ^oC in order for the reaction to proceed. Because of the high reaction temperature, coke formation is a serious issue for partial oxidation process [110] [111] [112] [113]. In addition, this reaction produces less hydrogen than steam reforming reaction based on the reaction expression shown below.

$$CH_4 + {}^1\!/_2\, O_2 \rightarrow CO + 2H_2, \qquad \Delta H^0_{298} = -35.5 \text{ kJ/mol} \tag{3}$$

Research on partial oxidation process concentrated in similar catalysts with steam reforming reaction. Compared to $Ni/\gamma\text{-}Al_2O_3$, $Ni/CaO/\gamma\text{-}Al_2O_3$, and Ni/CaO, Ni/La_2O_3 catalyst was found to be more stable under the same conditions of partial oxidation of

methane. The superior catalytic activity was detected at the temperature of 800 ^{o}C and ratio of $CH_4/O_2 = 2$. Kinetic analysis reveals that the reaction pathway is undergoing the indirect reaction scheme – methane is fully oxidized into H_2O and CO_2 first and reformed with H_2O and CO_2 to produce H_2, rather than direct partial oxidation to H_2 [114]. The mechanism of partial oxidation of methane over Ni/Al_2O_3 catalyst was studied by Jin and co-workers [115]. Contrary results were obtained that the observation of $Ni^{\delta+}$ and $O^{\delta-}$ produced from the activation of O_2 over Ni^0 sites was the evidence of direct oxidation route. Ni/Mg-Al oxide catalysts prepared by solid phase crystallization method from Mg-Al hydrotalcite-like precursors was able to display outstanding high activity and selectivity to partial oxidation of methane even at high space velocity [116]. Support effect in supported Ni catalysts was comprehensively investigated in Barbero's paper [117]. Among La_2O_3, MgO, and ZrO_2, La_2O_3 showed the strongest interaction with Ni, thus, resulted in high activity and selectivity. ZrO_2 catalyst formed a weak connection with Ni so that it could be easily deactivated by metal sintering. Other recent research on the Ni-based catalysts include subtler investigation of support basicity [118], support particle size [119] and surface reaction kinetics [110].

Considering Ni-based catalyst are prone to metal sintering and coke formation, other common catalytic metals as well as noble metals were extensively studied. In a review paper [120], Enger reported the carbon deposition relative rates were in the order: Ni > Pd > Rh > Ru > Pt, Ir. W, Mo, V, Ta and Fe were detrimental to both methane conversion and syngas selectivity when they were used to modify Co-based catalyst. Itome and Nelson [121] prepared *M*-8YSZ and *M*-CeO_2/8YSZ (*M* = Ni, Cu, Co, Ag) and found that at hight temperatures (over 973 K) the Co-CeO_2/8YSZ catalyst exhibited higher activity than Ni-

based catalyst, which might be promising to replace the anode cermets of a solid-oxide fuel cell. Alumina-supported noble metal catalysts were developed by Oh and the co-workers [122] to control the methane emission on a natural gas motor vehicle. Rh promoted catalyst had the highest tendency to form CO than Pd and Pt under reducing conditions. At atmospheric pressure and high reactant dilution conditions, Rh/hexaaluminate-based catalysts exhibited comparable activity and selectivity than the commercial Rh/α-Al_2O_3 catalyst. Under the operating conditions of $CH_4/O_2/N_2$ = 4/2/94 vol%, GHSV = 5000,000 $Ncm^3/(h\ g_{cat})$, *P* =1 atm, and temperature over 1050 K, the reaction approached to thermodynamic equilibrium with the methane conversion of 100% [123]. The ignition temperature could decrease with the increasing of the Rh loading based on the research by Eriksson and co-workers [124] of the Rh-based catalyst. Adding ceria to the support would result in the highest activity and formation of H_2 and CO. Akhlaghian and co-workers [125] supported Rh on TiO_2 and WO_3. Different Ti precursors resulted in different performance towards partial oxidation of methane. Rh-coated α-Al_2O_3 foam monolith was used to catalyze the partial oxidation of methane. The mechanism analysis was able to show that under technical relevant conditions, syngas was formed by a combination of direct partial oxidation and steam reforming [126]. In a later paper [127], their work on the effect of sulfur was performed over a Rh-Ce coated foam monolith. Results show that the deactivation saturates at a few ppm of sulfur and is due to the obstruction of steam reforming reaction. Another research [128] studied the support effect on the sulfur tolerance of Rh-based catalyst. The results also affirmed that the deactivation was caused by the inhibition of the reforming reaction. The presence of a sulphating support as La_2O_3-Al_2O_3 was much less affected in the test than the less sulphating SiO_2-Al_2O_3 support. More

detailed analysis could be found in their subsequent paper [129]. Rh-coated monolith catalyst was also found effective in partial oxidation of heavy hydrocarbons such as decane, hexadecane and diesel fuel with selectivity exceeding 80% nad >99% conversion of fuels and 100% conversion of oxygen [130]. A successive research [131] [132] [133] was carried out by the U.S. Department of Energy and Louisiana State University on the partial oxidation of n-tetradecane over the Rh-based catalysts. Results show that by substitution of Rh into the pyrochlore form, the catalyst was less susceptible to sulfur poisoning.

2.2.1.3. Autothermal reforming

Autothermal reforming is the combination of steam reforming and partial oxidation, i.e., fuel is reacting with both water and oxygen to produce syngas or hydrogen. The reaction can be manipulated by controlling the ratios of O_2/C and H_2O/C to become either endothermic, exothermic or thermally neutral. The pressure and temperature required are usually lower than partial oxidation [46] and the steam-to-carbon ratio is usually lower than steam reforming [134]. In general, all the operating conditions are optimized in autothermal reforming to make it beneficial to the other two reactions. The introduction of this reaction is stopped here as more detailed reviews will be summarized in Chapter 3.

$$CH_4 + (1 - 2x)H_2O + xO_2 \rightarrow CO + (3 - 2x)H_2 \quad (4)$$

2.2.1.4. Dry reforming

The beauty of dry reforming to produce hydrogen lies in the capability to remove two greenhouse gases (GHG) simultaneously. This reaction happens between the hydrocarbon and carbon dioxide, yielding the least ratio of H_2/CO in the product compared to the other reforming reactions. By looking at the reaction expression below, firstly, it requires

tremendous energy input to maintain the reaction status as the reaction is highly endothermic. Second, high carbon concentration would definitely create serious carbon deposition [135] [136]. Therefore, numerous research about dry reforming were focusing on the reaction operating conditions management and coke-resistance catalysts investigation.

$$CH_4 + CO_2 \rightarrow 2CO + 2H_2, \qquad \Delta H^0_{298} = 247.4 \text{ kJ/mol} \tag{5}$$

Hayakawa and co-workers [137] reported the Ni/perovskite catalyst prepared by solid phase crystallization method, exhibiting high activity as well as high sustainability due to the highly dispersed Ni evolved in the perovskite matrix. The effect of Ni contents was studied comprehensively by Akbari [138] and co-workers with the Ni-MgO-Al_2O_3 catalyst. The CH_4 and CO_2 conversions was improved with the increase of nickel content and reaction temperature. However, increasing Ni content also resulted in the increase of the carbon deposition, indicating that there should be an optimal point which led to the best activity as well as the best durability. Compared to the conventional Ni/SiO_2 catalyst, Ni@SiO_2 with core-shell structure and synthesized by water-in-oil micromulsion method had higher performance and stability. With a 30-h test under 850 ^oC in a mixture of CH_4 and CO_2 of 1:1, the catalyst showed very stable performance and low coke formation. The possible reason is due to the presence of alkaline earth metals and the mobile oxygen in the perovskite supports oxidizing the coke into carbon oxides. The reason is attributed to the stronger metal-support interaction and smaller Ni nanoparticles [139]. Another group [140] had researched on the yolk-shell structure catalyst based on the Ni@HSS (hollow silica spheres). Facile one-pot micro-emulsion method was used to synthesize the catalyst and

significantly enhanced CH_4 and CO_2 conversions performance was obtained without carbon deposition over 55 h. Other research about Ni-based catalysts include Ni-Co-MgO-Al_2O_3 catalyst [141], Ni-Ce/SBA-15 prepared with the ultrasonic-assisted impregnation method [142], $LaFe_{0.9}Ni_{0.1}O_3$ perovskite catalyst [143], mesocellular silica foam-based Ni catalyst [144] and Ni catalyst derived by active and stable hydrotalcite [145].

Bimetallic Ni-Rh catalysts was studied by Jóźwiak [146] towards the dry reforming of methane. SiO_2 supported monometallic Ni, Rh and bimetallic Ni-Rh catalysts all showed good activity, however, when considering the carbon formation resistance, Rh-rich catalyst was superior than the others. Ru was also found preferable to Ni-based catalyst since the one with Ru had remarkable activity and stability than the Ni/γ-Al_2O_3 catalyst at both activity test and steady state condition [147]. This was also confirmed by another research [148] on Ru (0 0 1) surfaces effect. Saad [149] performed dry reforming of waste plastics on a Ni-Co-Al_2O_3 catalyst. Results indicated the catalytic performance varied a lot with the preparation method. The one with rising-pH technique produced 17% higher of syngas than with the common impregnation method. To enhance the coke resistance capability, Mg/La promoted Co–Ni/MSU-S catalyst was prepared by sol-gel method. The best performance was achieved at 750 ^oC with the CH_4 and CO_2 conversion of 93% and 99%, respectively [150].

2.2.1.5. Other relevant techniques

A typical fuel processing system includes a reformer to produce syngas (mainly H_2, CO and CO_2) from fuels and followed by a series of high-temperature (583–723 K) and low-temperature (483–513 K) WGS reactors to convert carbon monoxide further into extra hydrogen [151], a preferential oxidation (PrOx) reactor to eliminate the trace amount of

CO [152] and a pressure swing adsorption (PSA) unit to separate H_2 from the other gases in order to obtain a high-purity (> 99.9 vol.%) stream of H_2 [153]. To be clear, if a SOFC is used downstream instead of a PEMFC, CO doesn't have to be removed from the syngas because it is also a fuel for the fuel cells.

WGS: $$CO + H_2O \rightarrow CO_2 + H_2, \qquad \Delta H^0_{298} = -41.2 \text{ kJ/mol} \tag{6}$$

PrOx: $$CO + {}^1/_2 O_2 \rightarrow CO_2, \qquad \Delta H^0_{298} = -280 \text{ kJ/mol} \tag{7}$$

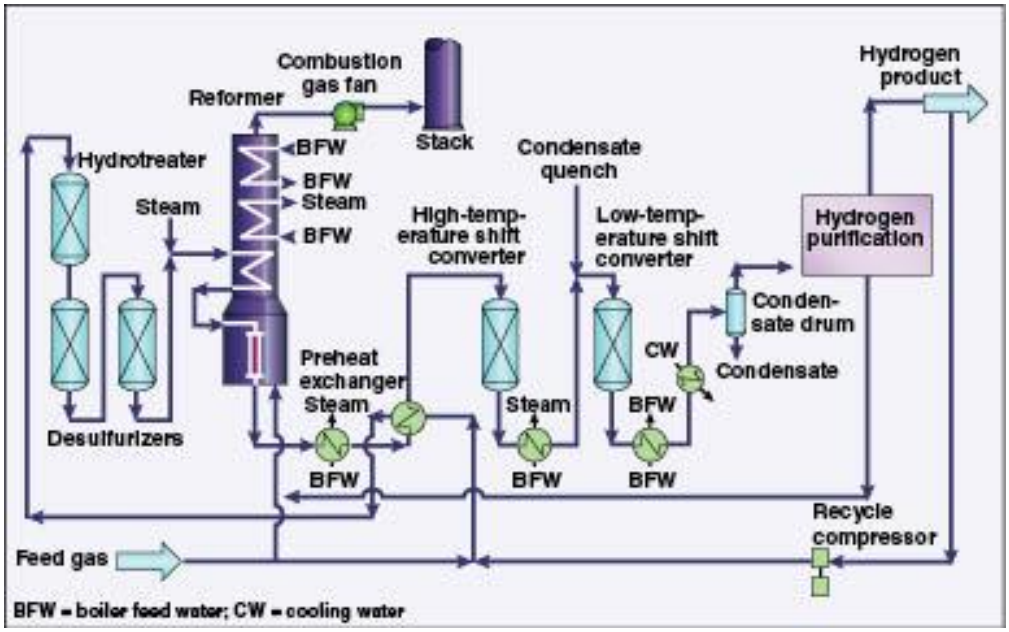

Figure 2. Schematic of a steam-methane reforming process [154].

To further improve the hydrogen production under different conditions, many other reforming related techniques were invented in the recent years. Sorption enhanced steam reforming (SESR) is aiming at increasing the energy efficiency and cost competitiveness of steam reforming process. This process integrates the reforming reaction together with the following CO elimination and CO_2 separation process into one single step, which can

directly produce the hydrogen with over 95% of purity. During SESR process, the reactor is usually packed with a mixture of steam reforming catalyst and a sorbent which is used to capture CO_2. Under a relatively lower temperature, the reforming reaction equilibrium is continuously pushed to the positive direction with the rate constant close to infinite large. Therefore, the reactor size could be much more compact compared with the conventional reformer, making the operating and investment cost decrease dramatically. The most common sorbents are CaO, since they are extremely cheap and can be repeatedly used through regeneration over high temperature. Nevertheless, some researchers spent their effort on the integration of the reforming catalysts and CO_2 sorbents to reduce the process complexity [155] and improve the conspicuous reduce of CO_2 absorption capacity [156]. The optimal system operating conditions for the sorption-enhanced steam reforming of different feedstocks were studied by other research [157] [153].

Another emerging technique is chemical-looping reforming (CLR), shown in Fig. 3, which originates from the chemical looping combustion (CLC). This technique is expected to be less energy consumptive than the endothermic steam reforming process. In general, CLR requires two parallel reactors with one called fuel reactor (or reducing reactor) and the other as the air reactor (or regeneration reactor). The process starts with the metal oxide (oxygen carrier) reduced by the fuel in the fuel reactor, followed by the circulation of the reduced metal oxide to the air reactor. The cycle is then completed by the oxygen carrier re-oxidized and circulated back to the fuel reactor [158]. In CLR, the heat required by the endothermic reforming reaction can be partially provided by the exothermic oxidation of the metal oxide [159]. Moreover, the temperature for the metal oxide reduced by the fuel is often lower than the reforming reaction. Therefore, the low energy demand makes it a

promising way towards the future hydrogen production. The current recognized oxygen carrier is NiO, however, quite a few researches are focusing on new oxygen carriers search in order to improve the redox properties [160]. In addition, due to the flexibility of CLR, alternative processes are allowed to follow the same pathway and even with the same type of oxygen carrier. Thus, a number of studies are proposed to utilize it for other applications development, e.g., producing nitric oxide and hydrogen using ammonia and metal oxides [161].

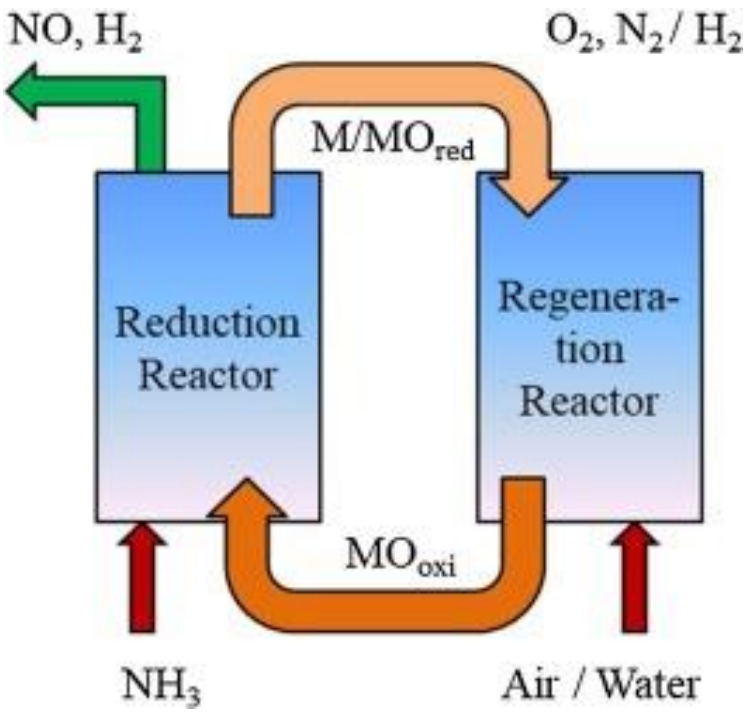

Figure 3. Chemical-looping reforming to produce H_2 and NO [161].

Other less common reforming techniques include electric field assisted low temperature dry reforming [162], non-thermal plasma autothermal reforming [163], solar-

driven steam reforming [164] [165], aqueous phase reforming [166], combined CO_2 and H_2O reforming [167] or tri-reforming [168], and on-cell reforming [169] [141].

2.2.2. Gasification

Similar to reforming process converting liquid or gas feedstocks to syngas, gasification was first used to deal with solid carbonaceous materials, such as coal and biomass. Nevertheless, the definitions are getting more and more ambiguous. Generally gasification uses steam and/or limited oxygen (than combustion) for syngas production in large plants for better economy and efficiency. The typical gasification operating conditions are above 500 ^oC and high pressure with the products of H_2, CO, CO_2, CH_4, char (solid residue) and tar (liquid residue) [170] [171]. Therefore, the syngas must be separated from the solid and liquid products in a cooling device and fed through a series of purification system listed above to yield high purity hydrogen. Depending on the reactants, gasification techniques are classified as air gasification, steam gasification, air-steam, oxygen-steam and enriched air-steam gasification. The gas from air gasification has lower heat value, however, due to the low investment cost, simple operation and stable running, it is the most common technique applied in industry [172].

The power derived from hydrogen or syngas is considered as renewable energy if they are produced from renewable source such as biomass. Therefore, most research on the gasification technique are focusing on the different types of biomass gasification [173] [174]. To extend the technique to high water content biomass or waste water slurries, some other researchers studied the gasification of renewable glucose with supercritical water as the reactant [175] [176]. Although compared to reforming technique, gasification process

consumes more energy and is more complex, since coal is abundant in many parts of the world, it is still worthwhile to explore under certain circumstances [177].

2.2.3. Catalytic cracking

A common drawback of reforming and gasification is the formation of carbon monoxide and carbon dioxide, which have to be removed from a sequence of costly processes. Moreover, during the gasification, the biomass tar needs to be taken care of in order to maintain the stability of the system [178]. Catalytic cracking is a promising technique to eliminate those issues and produce hydrogen from a variety of hydrocarbons. During this process, hydrocarbon fuels are directly converted into hydrogen and carbon at high temperature and atmospheric pressure. Compared with reforming and gasification, the hydrogen concentration in the gaseous product is already high. Even if there are unconverted fuels or some short-chain gaseous hydrocarbons (e.g. ethylene), the separation of hydrogen from them is much simpler than from CO and CO_2. In addition, the carbon produced from cracking are usually filamentous carbon nanotubes, which are valuable materials in many applications [179].

$$CH_4 \rightarrow C + 2H_2, \qquad \Delta H^0_{298} = 74.8 \text{ kJ/mol} \tag{8}$$

Similar to reforming process, Ni-based catalysts also exhibit outstanding activity in catalytic cracking [180] [181]. The catalysts with high catalytic performance in reforming reaction could have a chance to be a good candidate in cracking process. However, because the filamentous carbon is also a valuable product, the catalyst used here must be able to promote carbon formation and have high efficiency (hydrocarbon conversion) under accumulation of carbon [182].

2.2.4. Electrolysis

As the most well-known and oldest hydrogen production technique, electrolysis has many exceptional advantages than the other techniques. It does not require sophisticated control process to produce ultra-pure (> 99.999%) hydrogen with no need to concern about emission problems. The process is flexible to be applied in either large-scale industrial hydrogen plants or small household fuel cell devices. However, the key barriers of electrolysis are the cost of electricity and electrolyzers. To produce 1 kilogram of hydrogen at 25 ^{o}C and 1 atmosphere pressure, 39 kWh of electricity and 8.9 L of water are required (at an efficiency of 100%) [12]. The most common electrolyzers are alkaline and polymer electrolyte membrane (used as the inverse process of PEMFC) which still use high-cost materials such as platinum. Numerous studies are proposed on the research of low-cost electrodes with high performance and efficiency [183] [184]. Some researchers proposed by taking advantage of the surface activity of some certain metal oxide, electrolysis of water can be catalyzed to occur on the oxide surface [185]. Others attempted to add catalysts and additives to the current electrode, expecting to minimize the internal loss and omega loss and improve the electrode activity [186].

The efficiency of electrolysis is increasing with the temperature, therefore, a high temperature electrolysis might be preferable when high temperature heat is available. It is usually carried out in a solid oxide electrolyzer under a temperature at 700 to 1000 ^{o}C [46]. At this condition, the energy barrier of the electrolyzer reaction is smaller so that the required energy would be much lower than at lower temperature. Another research approach is to electrolyze water with renewable energy, especially wind energy and solar

energy. Then of course, the hydrogen production would be potentially considered as an energy storage technique to supply power in the absence of the primary energy source.

2.2.5. Thermochemical water splitting

Instead of using electricity, thermochemical water splitting technique requires a large amount of heat to decompose water into oxygen and hydrogen. Since water is so stable, it usually cannot be taken apart with the temperature of a heat source less than 2500 K [46] [12]. Thus, the most reasonable energy would be concentrated solar energy collected by solar tower, parabolic trough or dish collector. Because this technique directly uses the solar heat without transferring it into electricity (electrolysis) or light (photoelectrochemistry), it has a potential to be the most efficient way to produce hydrogen from solar. Two basic cycles are considered promising in thermochemical water splitting:

Two-step cycle [187]:

$$M_xO_y \rightarrow M_xO_{y-z} + {}^{z}/_{2}\,O_2, \quad (9)$$

$$M_xO_{y-z} + zH_2O \rightarrow M_xO_y + zH_2 \quad (10)$$

S-I cycle [46]:

$$H_2SO_4(aq) \rightarrow H_2O\,(g) + SO_3\,(g) \quad (11)$$

$$SO_3\,(g) \rightarrow {}^{1}/_{2}\,O_2\,(g) + SO_2\,(g) \quad (12)$$

$$SO_2\,(g) + I_2\,(g) + 2H_2O\,(l) \rightarrow 2HI\,(g) + H_2SO_4(aq) \quad (13)$$

$$2HI\,(g) \rightarrow H_2\,(g) + I_2\,(g) \quad (14)$$

The redox oxides in the two-step cycle are generally chosen from manganese oxides [188] [189], ferrite [190] [191], zinc oxides, cerium oxides [187], lithium redox couple [192], etc under the temperature from 700–2000 ^{o}C. S-I cycle usually works at much lower temperature of 100–850 ^{o}C as most reactions occur in the aqueous phase. The current

research are coupled with the concentrated solar system, e.g. concentrators, solar receivers, construction materials and technical problems.

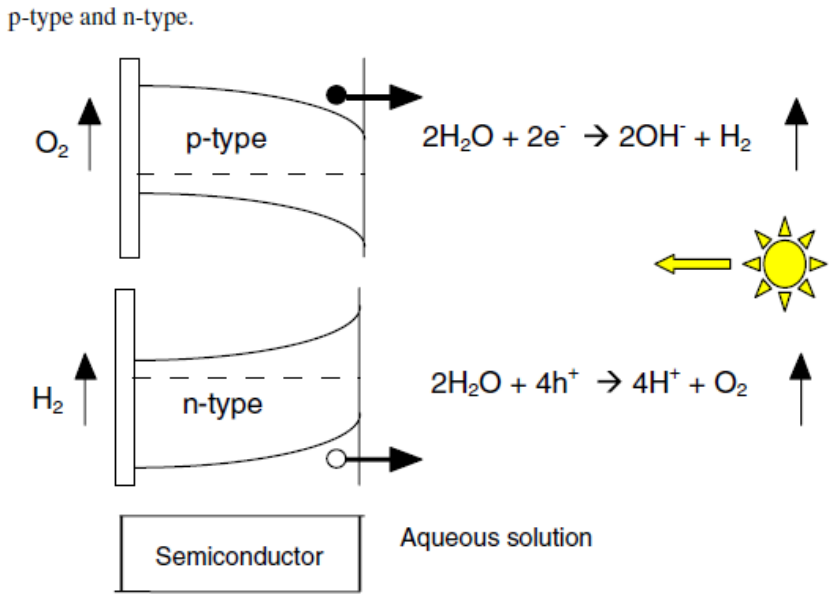

Figure 4. Schematic of a PEC water splitting device with the electrode reactions [12].

2.2.6. Photoelectrochemistry

Direct photoelectrochemistry (PEC) basically converts water upon illumination, shown in Fig. 4. It combines a PV cell and an electrolyzer into one single compact device and uses the photons with higher energy than the band gap to generate electron-hole pairs in the semiconductor to split water. To make this process feasible, the key criteria are 1) the semiconductor must generate sufficient voltage; 2) the band edge positions must straddle the hydrogen and oxygen redox potential; 3) the system must be stable in aqueous environment [193]. Many kinds of photosensitive semiconductors were investigated in the literature. To date, the most successful options are n-type TiO_2 [194], WO_3 [195] [196], α-Fe_2O_3 [197] and amorphous silicon [198].

2.2.7. Fermentation

Hydrogen can also be produced from biological process so that literally no any external energy source is needed. During the dark fermentation process, many types of anaerobic microorganisms produce sugars by hydrolyzing the organic wastes, and then convert the sugars to hydrogen [199]. Although there are bacteria which are able to produce hydrogen under light irradiation, compared to photofermentation, dark fermentation is advantageous at that it has a simple system and operation and the anaerobic microbial ecosystem can deal with very complex substrates in the organic wastes [200] [201]. Further research needs to be carried out on the discover of bacteria with high efficiency and yielding high hydrogen production, as well as the operational parameters such as pH, pressure and temperature effect on the fermentation process.

2.3. Jet A Fuel Desulfurization

2.3.1. Jet A fuel

Turbine fuels are extensively used for both aircrafts and vessels in the United States. Depending on the application, they are separated for commercial and military use. Commercial turbine fuels include a kerosene-type fuel – Jet A (with Jet A-1 used outside of the United States) and a wide-cut fuel – Jet B. Jet B is a fuel mixture of gasoline and kerosene still used in some cold areas such as Canada and Alaska. For military turbine fuels, the army primarily relies on the kerosene-type JP-8 and wide-cut type JP-4 was only used by U.S. Air Force in a very short period because of the higher volatility during

operation [26] [202]. However, Jet A fuel is becoming more and more attractive in military applications due to the availability and performance.

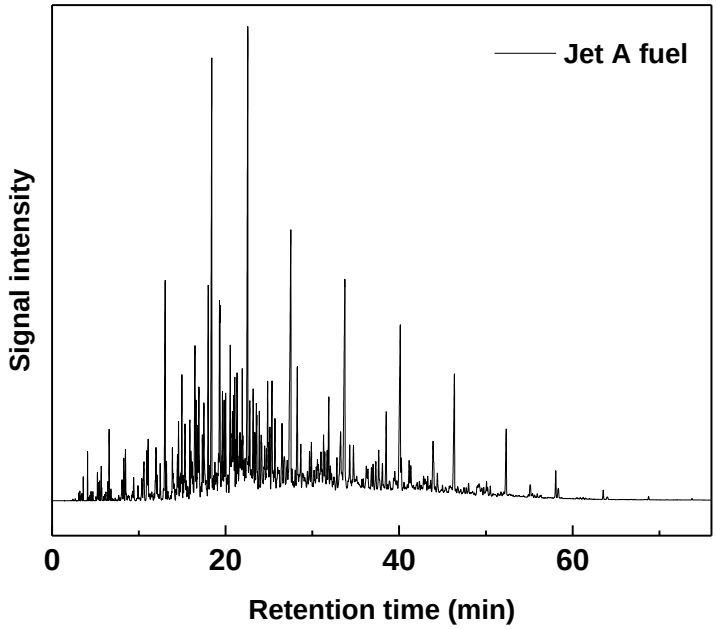

Figure 5. Gas chromatography spectrum of the original Jet A fuel used in this research.

Jet A fuel is a mixture of hundreds of hydrocarbons with the most groups of paraffin (including isoparaffins), cycloparaffins or naphthenes, aromatics and olefins. The carbon number distribution in a kerosene-type jet fuel is between about 8 and 16 carbon numbers. Some research [28] showed the average chemical formula for Jet A fuel is $C_{11.6}H_{22.3}$, which will be extensively employed in my entire research. Fig. 5 depicts the gas chromatography spectrum of the original commercial Jet A fuel purchased from a local aviation company. According to the specification properties by ASTM D1655, Jet A fuel has a boiling point in the range from 205 ^{o}C to 300 ^{o}C, density of 775–840 at 15 ^{o}C, freezing point of -40 ^{o}C and net heat of combustion of 42.8 MJ/kg.

Table 1. Selected specification properties of Jet A fuel.

	Jet A fuel
Average chemical formula	$C_{11.6}H_{22.3}$
Molecular weight (g/mol)	161.5
Liquid density (g/ml)	0.81
Lower heating value (LHV, MJ/kg)	42.8
Original sulfur concentration (ppm)	1140

As a distillation product of crude oil, sulfur compounds are inevitably contained in jet fuel. The Environmental Protection Agency (EPA) allows a maximum sulfur concentration of 3000 ppm and based on the test result of the Jet A fuel, the sulfur concentration is at the level of 1000 ppm. The specification properties of the Jet A fuel employed in our research are listed in Table 1 for reference.

2.3.2. Previous desulfurization results

Sulfur is the primary "killer" for most catalysts. Research [129] [203] show that sulfur facilitates reforming catalysts poisoning and deactivation, which dramatically inhibits syngas production. Simson and co-workers [55] studied the sulfur impact on the catalyst performance, the reversibility of sulfur poisoning and the used catalyst morphology comprehensively. Results show that 5 ppm of sulfur increased the deactivation rate by a factor of 30 and the deactivation was caused by the increase rate of coke formation. Although removing sulfur could reduce coke deposition, the permanent impacts on the catalyst surface was considered irreversible. Moreover, even if some catalysts are specially designed to have outstanding sulfur-tolerance, the PEMFC electrodes can experience significantly irreversible deactivation under the exposure of sulfur [204]. To reform a jet

fuel with 1000 ppm of sulfur would be definitely a disaster for both reforming catalyst and fuel cell electrodes. Thus, it is required to reduce the sulfur concentration to a relatively low threshold before the jet fuel is ready to be reformed.

The most versatile desulfurization techniques are classified into two groups regarding whether hydrogen is used. Hydrodesulfurization (HDS) needs hydrogen to decompose and eliminate the sulfur compounds usually under high temperature and high pressure. However, this technique is limited by that it cannot reduce sulfur content to zero level without altering the composition and thus, the property of the fuel. Non-hydrodesulfurization (non-HDS) techniques mainly include extraction, precipitation, selective oxidative desulfurization and adsorption [205] and are usually called "deep desulfurization" techniques. These techniques do not need hydrogen and are very effective for removing thiophenic compounds which are the common sulfur source in the jet fuel. In our research, the selective adsorption desulfurization was chosen to bring the sulfur content down because of its marvelous efficiency and system simplicity. Very brief work and results are shown below with detailed work summarized in Xinhai's papers [206] [207] [208] and dissertation [209].

In-home-made NiO-CeO_2/Al_2O_3-SiO_2 adsorbents were synthesized by blending-extrusion method from low-cost precursors, i.e. nickel acetate, cerium acetate, Pseudo-boehmite power (68–72% Al_2O_3) and diatomite power (> 95% SiO_2). After the adsorbents were calcined in reducing atmosphere (N_2 or Ar gas) at 650 ^oC for 2 h, they were ground into granules or powders with different sizes depending on the experimental requirements. Because the surface area of the adsorbents is around 250 m^2/g, making them highly

moisture absorptive, thermal activation in reducing atmosphere needs to be carried out before each test.

Figure 6. Adsorptive desulfurization test rig.

Fixed bed tests were conducted for evaluation of the dynamic sulfur adsorption performance in a lab-scale test rig located in a fume hood, which is shown in Fig. 6. The test rig consisted of a fuel tank, an HPLC pump, a fixed-bed column, tubes and connectors as well as an off-site total sulfur analyzer (Thermo TS3000) to measure sulfur concentration. During each test, jet fuel (contained sulfur) was continuously fed by the HPLC pump at a constant flow rate to the stainless-steel column fully packed with the adsorbents through the tubes and connectors in between. A beaker was placed under the vertical column to collect the effluent. The effluent fuel was then intermittently collected by sample vials and analyzed in the instrument.

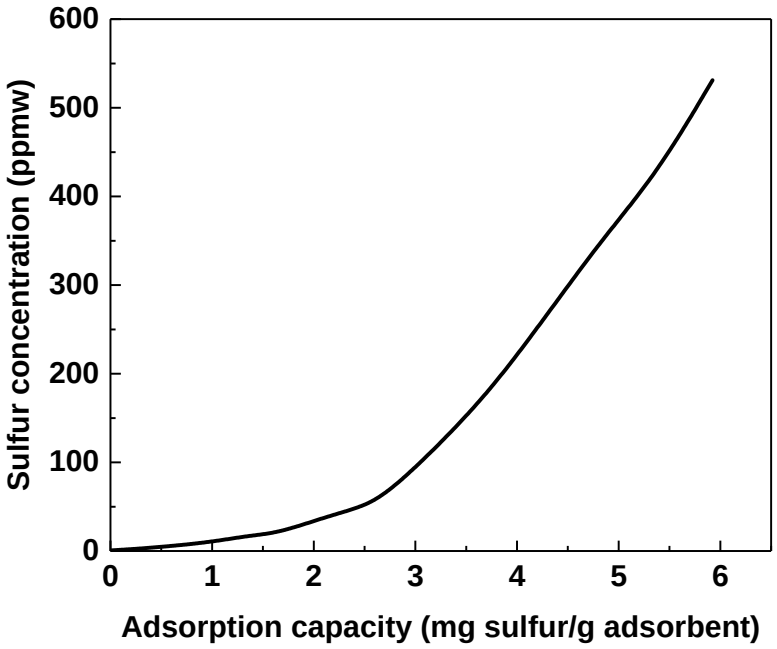

Figure 7. Adsorption performance of the NiO-CeO_2/Al_2O_3-SiO_2 adsorbents.

To evaluate the performance of adsorbents, the effect of LHSV (liquid hourly space velocity), particle size, column dimension, flow direction and regeneration capability were comprehensively investigated. The adsorption curve of the sulfur concentration in the effluent with respect to the accumulated adsorption capacity is shown in Fig. 7. The testing conditions are: column dimension at L = 203.2 mm, D = 7.747 mm; fuel flow rate = 0.1 ml/min; LHSV = 0.63; adsorbent particle size = 0–0.125 mm; fuel initial sulfur concentration = 1037 ppmw; mass of adsorbent = 4.88 g. A very high sulfur adsorption capacity of 0.633 mg S/g ads was obtained at a breakthrough point of 10 ppmw sulfur remaining in the effluent fuel. At the breakthrough point of 30 ppmw, the accumulated adsorption capacity was achieved at1.98 mg S/g ads.

Chapter 3. Autothermal Reforming of n-Dodecane and Jet A Fuel

3.1. ATR Catalyst

Onsite catalytic Jet A fuel reforming is the preferable way to produce hydrogen for an onboard fuel cell system for the reasons that 1) no need to worry about hydrogen storage and delivery; 2) no need to carry extra tanks of feedstocks; 3) the process can be initiated really fast with relatively small initial energy input; 4) the system can be extremely compact and operation is simple. By taking benefits from both steam reforming and partial oxidation, autothermal reforming can produce decent amount of hydrogen with high reaction rate.

Table 2. Comparison of different reforming techniques.

Technique	H_2 production amount	Enthalpy of reaction, ΔH	Reaction rate	Reaction temperature	Coke suppression
Steam reforming	2m + ½n	>0	low	700-1000 °C	high
Partial oxidation	½n	<0	high	900 °C	low
Autothermal reforming	2m – 2x + ½n	≤0	high	700-900 °C	moderate

SR: $$C_mH_n + 2mH_2O \rightarrow mCO_2 + (2m + {}^1/_2\, n)H_2 \quad (15)$$

POX: $$C_mH_n + mO_2 \rightarrow mCO_2 + {}^1/_2\, nH_2 \quad (16)$$

ATR: $C_mH_n + 2(m - x)H_2O + xO_2 \rightarrow mCO_2 + (2m - 2x + {}^1/_2\, n)H_2$ (17)

Comparisons of the three reforming reactions can be found in Table 2. The reaction temperature is generally in the range of 700–1000 ^oC and the process can be manipulated by controlling the operating conditions such as the steam-to-carbon ratio (H_2O/C) and oxygen-to-carbon ratio (O_2/C), making it either endothermic, exothermic or thermally neutral. It would be always reasonable to hold the process to be thermally neutral or slightly exothermic so that if the exhaust heat can be fully exploited, once the reaction starts, there is no need to have any external heating or cooling source to maintain the reaction status. That being said, the overall process has a potential to be self-sustainable.

Autothermal reforming of heavy hydrocarbons to produce hydrogen has been introduced since late 20th century. Based on the literature survey, the majority of the work were focusing on the catalyst-facilitated autothermal reforming of pure chemicals. Therefore, a large amount of different types of catalysts were synthesized in order to achieve higher hydrogen yield and better system performance. Villegas and his co-workers [210] performed the activity tests to study the performance of Ni, Ru and Ni–Ru/Al_2O_3 monolith catalyst on the ATR of isooctane. The results showed that bimetallic catalysts had better performance than the monometallic catalysts. The rate of production of the reformate exhibited stable behavior after 140 h of tests at 700 ^oC. Qi et al. [211] evaluated the performance of n-octane ATR on Ru/K_2O-CeO_2/γ-Al_2O_3 catalysts based on the thermodynamic analysis. The optimal operating conditions were obtained through experiments with the operating temperature around 750–800 ^oC, O_2/C and H_2O/C ratios of 0.35–0.45 and 1.5–2.2, respectively. Under these conditions, the maximum hydrogen (H_2 + CO) yield is measured at ca. 2.0–2.1 mol/(mol C) with a H_2 concentration around 40–

42.5 mol%. Autothermal reforming of dimethyl ether (DME) was investigated by Nilsson et al. [212] over Pd-based catalysts. CO_2 selectivity, DME conversion, and H_2 concentration were analyzed with consideration of various parameters such as the catalysts composition, inlet temperature, ratios of O_2/DME and H_2O/DME. Other studies have been focused on the ATR of acetic acid [213], hexadecane ($C_{16}H_{34}$, surrogate of diesel) [214] as well as dodecane ($C_{12}H_{24}$, surrogate of jet fuel) [2] [215] [216] [217]. Although n-dodecane is well acknowledged to be used as the surrogate of jet fuel, concerns may arise when it comes to the compound fuel which could have a sulfur content as high as 1000 ppmw. Research [218] [219] show that sulfur facilitates catalyst poisoning and deactivation, which dramatically inhibits the production of syngas. Therefore, results obtained from ATR of dodecane may not be fully applicable to jet fuel.

In order to implement the commercial fuel processing, both sulfur removal techniques and sulfur-tolerant catalysts must be developed simultaneously. The commonly used desulfurization techniques are hydrodesulfurization (HDS) and selective adsorption desulfurization (SADS). HDS is effective for removing large sulfur levels in refineries which requires high pressure [220]. For deep sulfur removal with small sulfur levels, SADS is usually the preferable way [221]. Our research group have developed a novel adsorbent with remarkable desulfurization performance at room temperature, which is able to decrease the sulfur content in the jet fuel from 1000 ppmw to ca. 10–20 ppmw [207]. However, the conventional Ni-based catalyst tends to be easily poisoned by trace sulfur. Thus, novel ATR catalyst with exceptional performance and sulfur-tolerant capability has been focused on in recent years. Precious-metal-coated metallic oxide catalysts were extensively studied because of the unique sulfur-resistance capability of the precious

metals (Pt, Pd, Rh, Ru, etc.). Strohm et al. [222] prepared bimetallic Rh–Ni/CeO_2–Al_2O_3 catalyst by wet-impregnated method and sieved the catalyst to 0.5–1 mm before experiment. The catalyst was able to tolerant 22 ppm sulfur in JP-8 for 72 h with fuel conversion >95%. Sulfur-tolerance was also discovered over Pt-based catalysts [223]. Xue and his co-workers prepared Pt/Gd_2O_3–CeO_2–Al_2O_3 catalysts by stepwise incipient wetness impregnation (IWI) method and performed activity tests on the ATR of retail gasoline with 158–500 ppm sulfur. The optimal conditions were found at 800 ^oC with gasoline WHSV (weight hourly space velocity) of 0.9 h^{-1}, and a H_2O/O_2/C molar ratio of 5/0.35/1. Microlith™ technology developed by PCI [224] had been used for reforming of E85 fuel to improve the catalyst sulfur tolerance. The catalyst substrates were built on catalytically coated metal meshes with very small channel diameters. With this technology, the catalysts were able to achieve >95% fuel conversion and over 70% reforming efficiency (LHV based) in the presence of 20 ppm sulfur, and also reached >95% fuel conversion and >66% reforming efficiency in the presence of 100 ppm sulfur. Commercial catalysts with precious metals were adopted by other researchers [219] [225] [226] [28] [227] [228]. At low sulfur concentration, all catalysts exhibited considerable sulfur-tolerance capability. However, when the sulfur content increased to 200 ppm [9], the fuel efficiency dropped dramatically from 100% to 75% with H_2 concentration decreasing from 28% to 19%.

The recorded ATR catalysts were listed in Table 3 for reference. To synthesize an in-house-made catalyst with inexpensive materials and high activity towards autothermal reforming as well as high sulfur and coke resistance, efforts have been spent in the preparation method. A honeycomb-type monolith made of cordierite was selected as the support of the catalyst and purchased from a Chinese company. It came with 100 or 400

cpsi (cells per square inch) on the cross-section, length of 60 mm and diameter of 40 mm. Fig. 8 shows a picture of the support (white) with 400 cpsi. This type of material can withstand very high temperature and thermal shock, because of the cells it can dramatically decrease the pressure drop and increase system stability. The cordierite support was firstly impregnated in a bubbled 10% nitric acid solution to remove any impurities and increase the water absorbability. After flushed with distilled water, the acid-treated support was put into an oven and dried for overnight. Then it was covered with a thin layer of Al_2O_3 and cerium acetate (precursor of CeO_2) suspension mixture for the purpose of surface area increase. The support was dried, calcined in a kiln at 800 ^oC for 2 h and weighted on a balance to measure the loading. The process would be repeated several times until the desired loading was achieved. Finally, a solution of active component precursors – Rh, nickel acetate, lanthanum acetate and potassium nitrate was prepared based on desired stoichiometry and washcoated onto the support by impregnation method. Dried, calcined and repeating the procedure several times before the catalyst was ready for experimental test.

The surface area of the ATR catalyst is obtained of 6.273 m^2/g by the liquid nitrogen physisorption method carried out in a Micromeritics TriStar II 3020 instrument. An X-ray diffraction instrument (Rigaku MiniFlex 600) is used to analyze the crystal structure of the active component. As is shown in Fig. 9, nickel is split into nickel oxide and perovskite lanthanum nickel oxide whose structure is proven to be beneficial to hydrocarbon reforming by other researchers [11] [229] [230]. Cerium has fantastic oxygen storage capacity and is widely used in catalysts. K and the 0.3% of Rh are used to suppress sulfur and coke. An interesting observation is that the potassium does not explicitly exhibit in the

XRD pattern. The possible reason could be that the potassium ions enter the crystal lattice of the perovskite La(NiO_3) and slightly distort the structure.

Table 3. ATR catalysts recorded in literatures.

Catalyst	Fuel	Research Institite
Ni, Rh and Ni–Rh/Al_2O_3	isooctane	Université Lyon
Ru/K_2O-CeO_2/γ-Al_2O_3	n-octane	Royal Military College of Canada & Dalian Institute of Chemical Physics
Pd-Zn/γ-Al_2O_3	dimethyl ether	KTH - Royal Institute of Technology
$MgNi_{0.2}Ca_{0.8}$−x$Fe_xO_{2\pm\delta}$ (x = 0–0.8)	acetic acid	Chengdu University of Technology
Gd-doped CeO_2 with 0.5 wt.% Pt (CGO-Pt)	isooctane, hexadecane	Korea Advanced Institute of Science and Technology (KAIST)
Ni/monolith, Ni supported on cerium–zirconium oxide (CZO)	dodecane	University of Michigan
Ru/12SrO–7Al_2O_3 (S12A7)	dodecane and toluene	Kogakuin University
noble metal catalyst (supplied by BASF®)	dodecane	University of Salerno
Pt/Gd_2O_3–CeO_2–Al_2O_3	gasoline	East China Normal University
Microlith™	E85 Fuel	Precision Combustion Inc.
commercial RhPt/Al_2O_3–CeO_2	diesel and kerosene, Jet A-1	Forschungszentrum Jülich GmbH
Pt, Rh, and Pd based commercial catalyst	JP8	Henry Krumb School of Mines
noble metal catalysts (BASF ATR-7B)	JP8	US Army Research
commercial precious metals, proprietary of UMICORE and Suedchemie	jet fuel	Fraunhofer ISE, Heidenhofstr
Commercial noble metal-based catalysts supported on monolithic cordierite	diesel and jet fuel	KTH–Royal Institute of Technology
Ru−Ni−Ce−Al_2O_3	n‑dodecane	Hampton University
Rh/Gd-CeO_2	gasoline	Illinois Institute of Technology & Argonne National Laboratory
Rh-ceria on a ceramic foam	ethanol	University of Minnesota

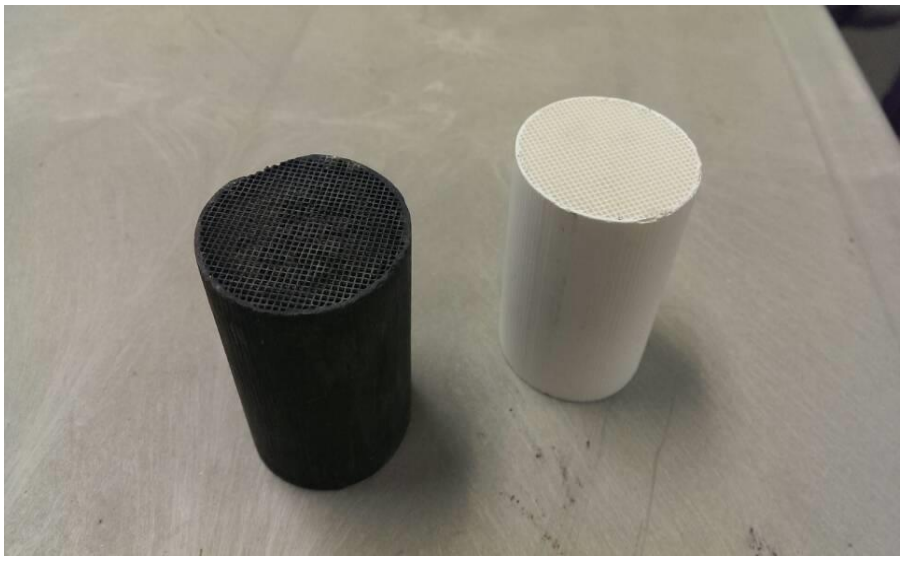

Figure 8. Picture of the Rh-NiO/La-K-Ce-Al-Ox/cordierite ATR catalyst (black) and support (white).

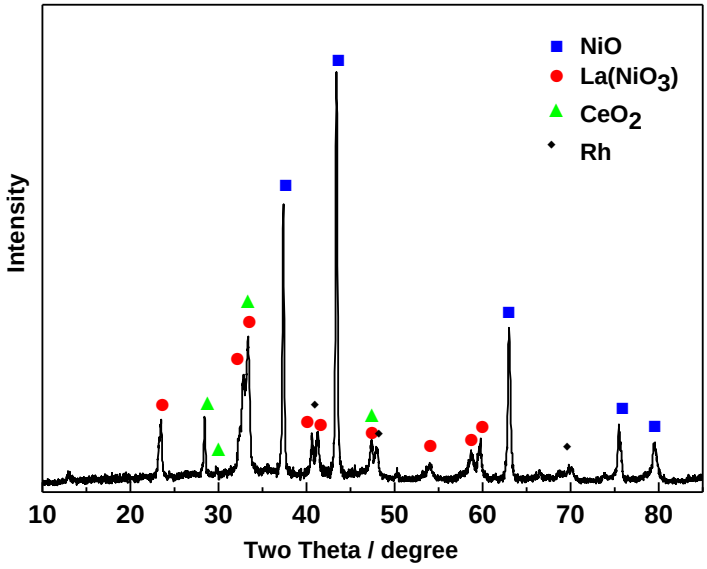

Figure 9. X-ray diffraction pattern of the ATR catalyst active component.

3.2. ATR System Set-up

To better understand each process, the autothermal reforming system was set up without considering the downstream water-gas shift reactor and heat exchangers. The overall system was introduced in Chapter 5. Two versions of ATR performance evaluation system were designed and fabricated with the picture of the previous version and schematic of the two shown in Fig. 10 and Fig. 11, respectively. The reactor was fabricated in stainless steel to withstand the high reaction temperature and overcome the hot spot generated on catalyst by superior heat transfer. Flanges and graphite gaskets were used to seal between different parts because of the relatively low pressure in the pipe. The size of the ATR reformer was determined based on the catalyst support diameter and the GHSV test results shown in our previous work [231]. For WGS reactor, because the reaction is relatively simple compared with the ATR reaction, the size of the reactor is determined based on the reaction equilibrium analysis and is shown in Chapter 5. Air and steam were injected into the reactor through the two flow distributors located in the front part which are shown as the left part in Fig. 10. Each of them had 4 portals and was connected with stainless steel tubes. Details of the distributer design are available from our previous work [231]. Fuel was firstly preheated by a heating hose (Hillsheim) and passed to a high-temperature misting nozzle spraying into the reactor. A tubular furnace (MTI Corporation, OTX-1200) was used to maintain the temperature of the reaction zone.

Several modifications including heating cables, rear-inserted thermocouples, and post-cooling device have been made based on the previous ATR system [8]. In order to compensate for the heat loss due to imperfect insulation, a piece of heating cable with temperature controller (BriskHeat) was wired on the outside surface at the mixing zone

before the furnace. A length of 3 inches was left between the head of the fuel nozzle and the mixing zone to prevent nozzle congestion caused by the fuel carbonation if it is too close to the high temperature region. Two K-type thermocouples (Omega, T0, T1 with uncertainty of 0.2 ^{o}C) were plugged into the reactor through the welded fittings to measure the actual temperature of the reactants at mixing zone (T0) and before the catalyst (T1), respectively. T1 is called "feeding temperature" and is the most important temperature in our test, because it is the temperature of the reactant mixture right before the catalyst. It basically represents the temperature of the three reactants that should be heated up to before they can react with each other. At the rear side of the reactor, four K-type thermocouples (T2–T5) at different depth were inserted through the flange cap to measure the temperature at distinct locations (i.e. front, middle, and end) of the catalytic reaction zone. With these modifications, the actual temperatures in the reaction zone were able to be directly measured. The temperatures at distinct locations on the catalyst are expected to disclose the reaction mechanism to some extent. The diameter of the rear thermocouple probes was 0.062 inches (1.57 mm) which could fit into the honeycomb monolith cells with 100 cpsi. To accurately measure the reformate gas flow rate, a condenser tank filled with water adsorbents was included into the post-cooling system for the purpose of preventing liquid water from flowing into the flowmeter.

All parts exposed to high temperature were made of stainless steel and designed by AutoCAD and SOLIDWORKS. After the system was assembled, tubes between the preheating device and tubular furnace were wrapped with a thick layer of glass fiber for better insulation.

Figure 10. Previous version of ATR reactor without insulation.

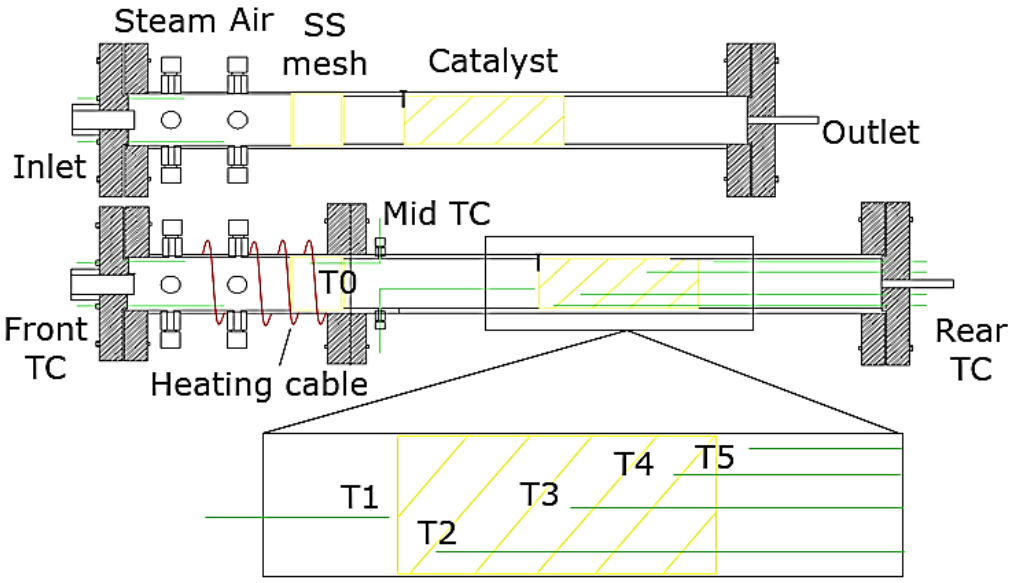

Figure 11. Schematic of previous ATR reactor (upper) and modified version (lower) with magnified view of thermocouple locations.

3.3. System Performance Test

The ATR performance tests were carried out in the system described above. n-Dodecane or desulfurized Jet-A fuel was pumped into the reactor through an HPLC (high-performance liquid chromatography) pump at constant flow rate of 3 ml/min. To ensure better evaporation, a heating hose (Hillsheim) was used to preheat the fuel before it was sprayed by the misting nozzle. Another HPLC pump was used to deliver water to the reactor at the specific flow rate based on the desired H_2O/C ratio. Superheated steam was generated by passing water through tube coils in a heated kiln (Paragon). Compressed air was connected to a contaminant trap device and regulated by a flowmeter (Dwyer) based on the calculated O_2/C ratio. After preheating, air was injected into the reactor from the distributer located a few centimeters behind steam. The heating cable wired outside of the reactor was set at 500 ^oC in order to evaporate the fuel and assure better mixing. The catalyst monolith with a length of 60 mm and diameter of 40 mm was placed at the middle of the reaction zone. Outside of the reactor a tubular furnace was used to provide accurate temperature control for the reaction to proceed. A cooling system was placed at the outlet of the ATR reactor, including a set of copper coil, a liquid collector, and a condenser tank which collects any liquid from the reactor. The volumetric flow rate and the composition of reformate under dry basis were measured by a flowmeter (uncertainty of 2% of reading) and a gas chromatograph instrument (GC, Agilent 6890, accurate to 1%), respectively, before evacuated to a fume hood.

The dry reformate after ATR reaction contains mainly H_2, CO, CO_2, O_2, N_2, CH_4. The GC equipped with a TCD (thermal conductivity detector) was used to qualitatively and quantitatively analyze the reformate composition. A Hayesep Q column (Agilent 80/100

mesh, 10 FT × 1/8 IN) followed by a molecular sieve 5A column (Supelco, 60/80 mesh, 6 FT × 1/8 IN) was connected in sequence to separate all the reformate except CO_2. Because molecular sieve column would completely absorb CO_2, as a result, CO_2 was detected by switching a valve off between the two columns so that only the first column was used. Calibrated gas mixtures purchased from Air Liquide USA were applied to calibrate the potential reformate gas mixtures for the purpose of quantitative analysis based on the multiple point external standard method.

The following indices were used to evaluate the performance of Jet-A fuel autothermal reforming:

$$\mathrm{H_2Yield} = \frac{n_{\mathrm{H_2}} + n_{\mathrm{CO}}}{11.6 \times n_{\mathrm{C_{11.6}H_{22.3}}}} \tag{18}$$

$$\text{Fuel Conversion} = \frac{n_{\mathrm{CH_4}} + n_{\mathrm{CO}} + n_{\mathrm{CO_2}}}{11.6 \times n_{\mathrm{C_{11.6}H_{22.3}}}} \tag{19}$$

$$\text{Energy efficiency} = \frac{n_{\mathrm{H_2}} \times \mathrm{LHV_{H_2}} + n_{\mathrm{CO}} \times \mathrm{LHV_{CO}}}{n_{\mathrm{C_{11.6}H_{22.3}}} \times \mathrm{LHV_{C_{11.6}H_{22.3}}}} \tag{20}$$

where *n*i and LHVi denote the molar flow rate and lower heating value of the ith species. H_2 yield was defined as the molar flow rates of hydrogen and carbon monoxide (which had the potential to be converted into hydrogen after water-gas shift reaction) divided by the molar flow rate of carbon containing inside the fuel. Obviously H_2 yield will not be limited to 1.0 by this definition because of the contribution of water. Fuel conversion was evaluated via carbon atom balances between reactant and gaseous phase product with the assumption that hydrocarbons other than CH_4 was neglected in the reformate. Lower heating values of H_2 and CO generated by ATR reaction were calculated to compare with the fuel to

determine the thermal energy efficiency which was considered to be a key factor for the energy system.

3.4. Thermodynamic Analysis

3.4.1. Ratios of O_2/C and H_2O/C determined theoretically

Accompanying with ATR of hydrocarbons, various reactions are occurring inside the reformer, including water-gas shift, methanation, hydrocarbon oxidation, and coke formation, etc. [4] It is well recognized that WGS reaction often occurs on the same type of reforming catalyst [232]. The equations of autothermal reforming of jet fuel and the overall reaction with stoichiometric coefficients undetermined are written as follows:

$$C_{11.6}H_{22.3} + x(O_2 + 3.76N_2) + (11.6 - 2x)H_2O \rightleftharpoons 11.6CO + (22.75 - 2x)H_2 + 3.76xN_2 \quad (21)$$

$$C_{11.6}H_{22.3} + x(O_2 + 3.76N_2) + (23.2 - 2x)H_2O \rightleftharpoons 11.6CO_2 + (34.35 - 2x)H_2 + 3.76xN_2 \quad (22)$$

where x is the oxygen-to-fuel molar ratio usually depending on the reaction temperature. It can be clearly seen that x is particularly important in controlling the ratios of O_2/C, H_2O/C as well as the reaction thermodynamic properties [233] and further the theoretical maximum H_2 yield.

Equation (23) and (24) are used to calculate the heat of reaction ΔH and systematic Gibbs free energy change ΔG with λ_i, H_i and G_i denoting the reaction stoichiometric coefficient, absolute enthalpy and Gibbs free energy of the ith species. P and R represent product and reactant, respectively. The heat of reaction at 298 K – 1073 K as a function of

oxygen-to-fuel molar ratio is plotted in Fig. 12, in which the heat of reaction decreases linearly with the increase of *x* value at all temperatures. The maximum oxygen-to-fuel ratio required to maintain thermal neutral is noticed to be achieved at 298 K with the value of x_0 = 4.23. O_2/C and H_2O/C are calculated from Eq. (25) and Eq. (26). At x_0 = 4.23, O_2/C and H_2O/C are calculated to be 0.36 and 1.27, respectively. It is understandable that with the decrease of O_2/C, H_2O/C rises and the endothermic SR reaction tends to dominate the overall reaction. The more SR reaction occurs inside the reactor, the more heat is consumed, causing the heat of reaction being positive, and vice versa.

$$\Delta H = \sum_{\mathrm{P}}^{i} \lambda_i H_i - \sum_{\mathrm{R}}^{i} \lambda_i H_i \tag{23}$$

$$\Delta G = \sum_{\mathrm{P}}^{i} \lambda_i G_i - \sum_{\mathrm{R}}^{i} \lambda_i G_i \tag{24}$$

$$\mathrm{O_2/C} = \frac{x}{11.6} \tag{25}$$

$$\mathrm{H_2O/C} = \frac{23.2 - 2x}{11.6} \tag{26}$$

As an indicator reflecting the spontaneity of the reaction, Gibbs free energy change as a function of the oxygen-to-fuel ratio and temperature is shown in Fig. 13. At $x_0 \geq 4.23$, the Gibbs free energy change of the reaction under all calculated temperatures are smaller than 0 indicating the ATR reaction is exergonic in all cases. Therefore, to remain the overall reaction exothermic and exergonic, O_2/C must be larger than 0.36. In this practical work, O_2/C was regulated in the range of 0.5–1.0. Meanwhile H_2O/C was set in the range of 1.1–2.5, instead of the calculated value for the purpose of coke suppression.

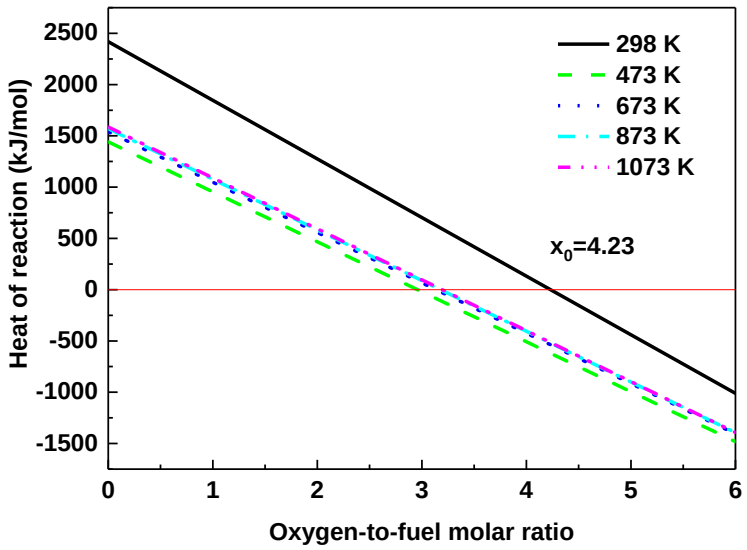

Figure 12. Heat of reaction as a function of the oxygen-to-fuel molar ratio at 298 K – 1073 K.

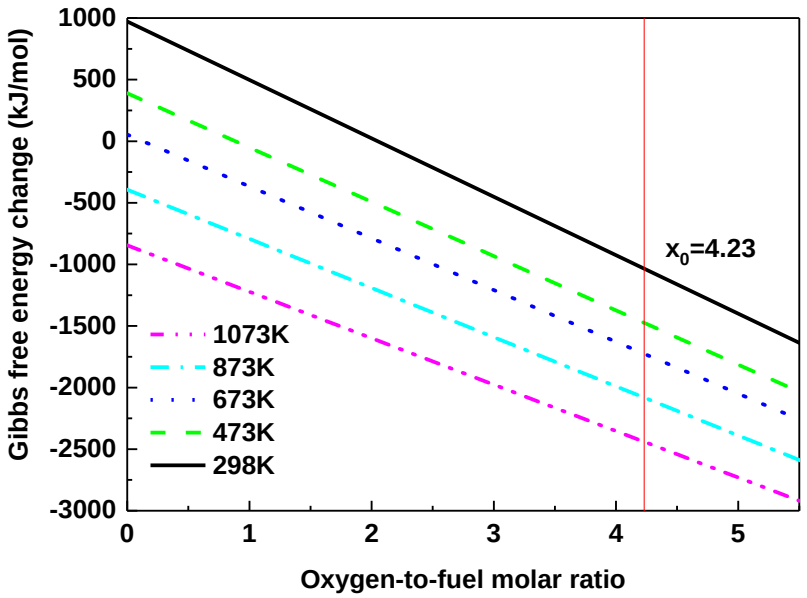

Figure 13. Gibbs free energy change as a function of the oxygen-to-fuel molar ratio at 298 K – 1073 K.

3.4.2. Pressure effect on reaction equilibrium

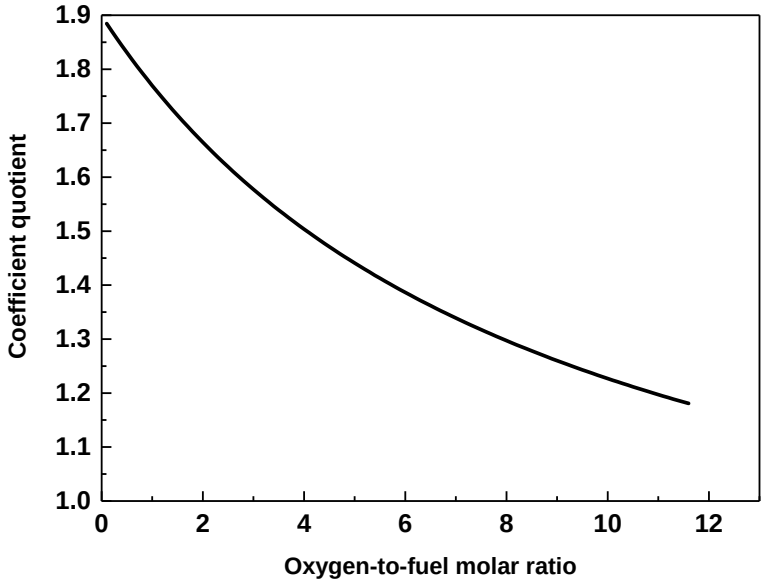

Figure 14. Coefficient quotient variation as a function of the oxygen-to-fuel molar ratio.

The pressure effect on the reaction equilibrium was demonstrated in terms of the coefficient quotient variation of Equation (22) with respect to the oxygen-to-fuel ratio. The coefficient quotient is defined as the sum of gaseous product coefficients over the sum of gaseous reactant coefficients, as is shown in Eq. (27). Fig. 14 depicts the results of coefficient quotient profile vs. *x*. Although it is apparent the quotient is decreasing with *x* increasing, within reasonable range of oxygen-to-fuel ratio, it is always larger than 1, which indicates that the amount of gas particles produced through the reaction is always greater than them in the reactants. In other words, a decrease in pressure would favor the forward reaction. This result can also be proved by the Gibbs free energy change of the chemical reaction as is shown in Eq. (28). The exponent over pressure *P* is always positive within

the reasonable range of x, which indicates that the decreasing pressure would result in a lower ΔG.

$$\text{Coefficient quotient} = \frac{\sum_{\mathrm{P}}^{\mathrm{i}} \lambda_{\mathrm{i}}}{\sum_{\mathrm{R}}^{\mathrm{i}} \lambda_{\mathrm{i}}} \tag{27}$$

$$\Delta G = \Delta G^0 + RT\, ln \frac{[\mathrm{CO_2}]^{11.6}[\mathrm{H_2}]^{(34.35-2x)}}{[\mathrm{C_{11.6}H_{22.3}}][\mathrm{O_2}]^{x}[\mathrm{H_2O}]^{(23.2-2x)}} \left(\frac{P}{P^0}\right)^{(21.75-x)} \tag{28}$$

3.5. Experimental Results

3.5.1. System performance on ATR of n-dodecane

n-dodecane is used for preliminary study of the autothermal reforming process. By controlling the operating temperature with a furnace, each measurement was made after the temperature stabilized for 40 min or longer. The operating conditions are: flow rate of n-dodecane = 3 ml/min, O_2/C = 0.5, H_2O/C = 1.8, GHSV = 38,890 h^{-1}. Fig. 15 and Fig. 16 show the effect of the operating temperature on the reformate molar fraction, H_2 yield, fuel conversion and energy efficiency, respectively. It can be observed from Fig. 15 that the H_2 molar fraction was at a relative stable level between 41% and 43.5% at different operation temperatures, whereas CO fraction increased from 7.9% to 14.6%, and CO_2 decreased from 13.9% to 10.2% as the operating temperature increased from 500 ^oC to 750 ^oC. CH_4 had a relatively high concentration of 1.7% at the operating temperature of 500 ^oC, and its fraction decreased gradually as the temperature increased. When the operating temperature was above 650 ^oC, the CH_4 concentration reduced to below 0.1%. Although the internal reforming of methane is possible in SOFC, the concentration of methane is expected to be

as low as possible in the dry reformate. Fuel conversion and energy efficiency were relatively stable at above 85% during the measurement, whereas H_2 yield was at low levels at 500 ^oC as shown in Fig. 16. All parameters increase significantly as the operating temperature increases. At 700 ^oC the H_2 yield and energy efficiency were slightly higher than those at 750 ^oC, which could be because of the measurement uncertainty associated with the flowmeter. But still, Fig. 16 indicates that an operating temperature of 700 ^oC is the highest point to the reforming process, at which satisfactory system performance was obtained.

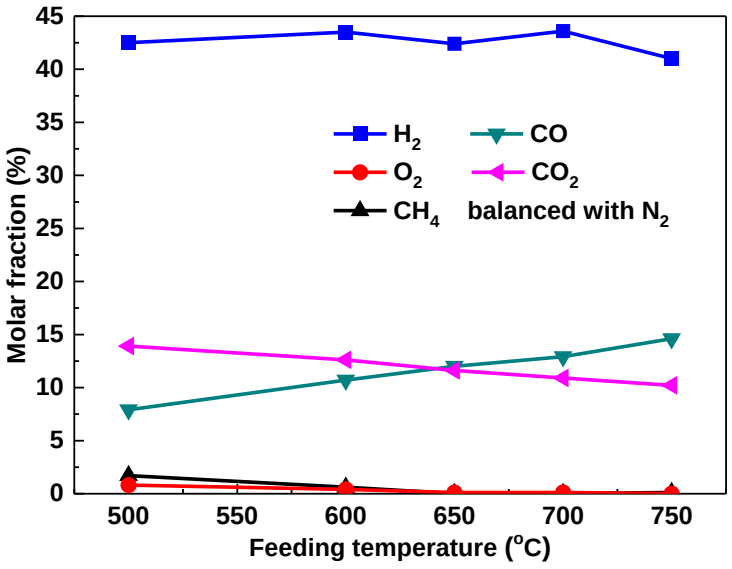

Figure 15. Effect of feeding temperature on reformate molar fraction. Fuel: n-dodecane, O_2/C = 0.5, H_2O/C = 1.8.

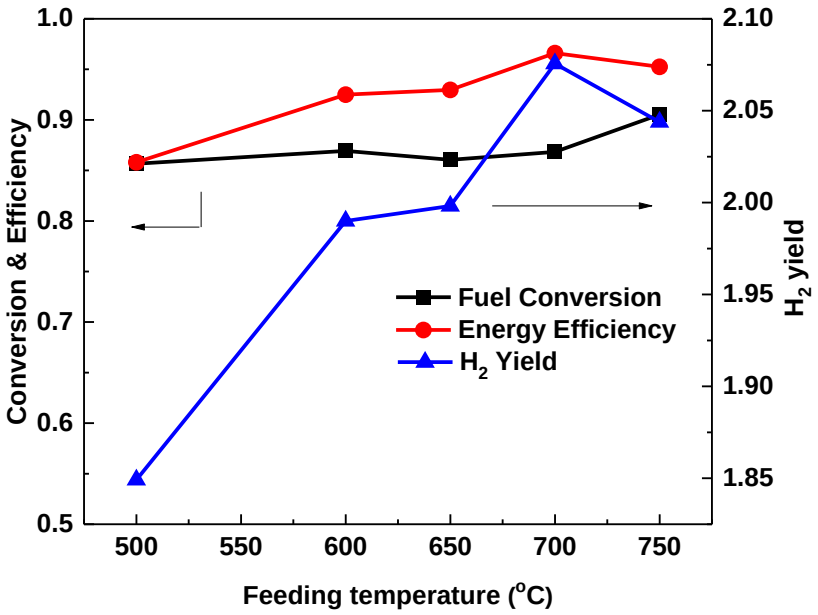

Figure 16. Effect of feeding temperature on fuel conversion, energy efficiency and H_2 yield. Fuel: n-dodecane, $O_2/C = 0.5$, $H_2O/C = 1.8$.

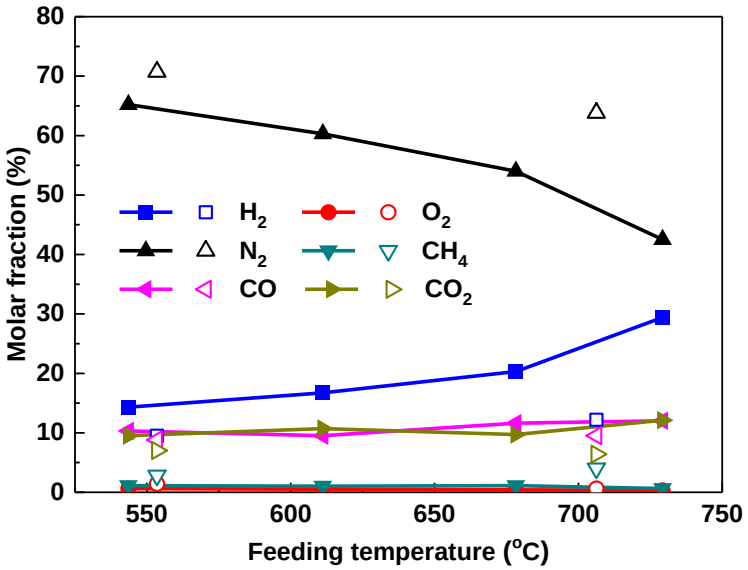

Figure 17. Effect of feed temperature on reformate molar fraction with catalyst (solid symbols with lines), and blank test (open symbols). Fuel: desulfurized Jet A fuel, $O_2/C = 0.5$, $H_2O/C = 1.8$.

3.5.2. System performance on ATR of desulfurized Jet A fuel

3.5.2.1. Results of reformate compositions with and without catalyst

Reformate composition is a crucial factor for the ATR reaction as it directly determines the successive strategy for fuel processing, such as WGS catalyst selection and recuperator design. Fig. 17 shows the reformate molar fraction variation under different feeding temperatures, with and without catalyst. The feeding temperature is the temperature measured at T1 location (see Fig.11), representing the temperature of the reactant mixture right before contacting with the catalyst. It could be clearly seen that under catalytic reaction, the molar fraction of H_2 was rising with the increasing of feeding temperature with the highest concentration of 29.4% at 729 ^oC. The reason is that higher temperature is in favor of endothermic SR reaction, which leads to the reaction equilibrium shifting to the H_2 production direction. Moreover, feeding the same amount of fuel, the amount of hydrogen produced through SR reaction is higher than that through exothermic POX reaction, resulting in the H_2 molar fraction rise even though the POX reaction is suppressed by the high temperature. The molar fractions of O_2 were below 1% in all cases indicating that O_2 was approximately completely consumed via ATR reaction. CH_4 could also be neglected in the reformate when considering the downstream procedure, as the molar fractions of CH_4 were around 1%. The fractions of CO and CO_2 showed opposite trends towards the feeding temperature with slight fluctuations at 10%. This is the explicit evidence that reactions between CO and CO_2 such as oxidation, WGS and RWGS (reverse water gas shift) were occurring on the ATR catalyst.

Non-catalytic ATR reaction was also observed occurring in the reactor at high temperature, with molar fractions of H_2, CO and CO_2 being 12.2%, 9.5%, and 6.4%,

respectively at 706 ^{o}C. Compared to the catalytic reaction, the H_2 molar fraction in non-catalytic case was less than half of the catalytic case, suggesting that the catalyst played an important role in the process.

3.5.2.2. Effect of feeding temperature, ratios of H_2O/C, and O_2/C on the performance of ATR

In this section, reformate composition, fuel conversion, H_2 yield as well as the energy efficiency as a function of feeding temperature, ratios of H_2O/C and O_2/C will be discussed. The ATR performance versus H_2O/C and O_2/C were illustrated in Fig. 18 – Fig. 20, respectively.

The variation of reformate molar fractions with feeding temperature was similar to the trends in Fig. 17 at all H_2O/C ratios. Comparison between different ratios of H_2O/C (Fig. 18 (a) to (e)) showed that H_2 molar fraction has a positive correlation with H_2O/C, which could be explained that at high H_2O/C, SR reaction dominates the overall reaction with more H_2 generated. With the decrease of H_2O/C, SR reaction was suppressed by POX reaction, resulting in the drop of H_2 molar fraction. In addition, the slope of H_2 molar fraction profile was steeper at higher H_2O/C than that of the lower case, indicating that the temperature dependence was greater at higher H_2O/C. With the above observation, the maximum H_2 molar fraction should be obtained at both high temperature and high H_2O/C, which was corroborated in our work with the achieved highest H_2 molar fraction of 29.4% at 729 ^{o}C and H_2O/C = 1.8.

The molar fraction of O_2 was lower than 1% in the first four cases and rose up to 2.8% at 561 ^{o}C and H_2O/C = 1.1, indicating that the ATR reaction was retarded by both low

temperature and low H_2O/C. Another interesting observation is that at higher H_2O/C the fraction of CO was lower than that of CO_2 (Fig. 18 (a), (b)). With the decrease of H_2O/C, the two fractions were getting closer (12.0% of CO and 12.1% of CO_2) with slight fluctuation (Fig. 18 (c)). At low H_2O/C (Fig. 18 (d), (e)) the fraction of CO was higher than CO_2, achieving 14.9% vs. 8.4% at 767.8 ^oC and H_2O/C = 1.1. This was also the evidence that WGS reaction occurred possibly on the catalyst accompanying with the ATR reaction, as increasing H_2O/C caused decreasing of CO and simultaneous increasing of CO_2.

Due to the fact that the required amount of desulfurized fuel for a single test is tremendous compared to the retarded and time-consuming desulfurization process, the test repeatability is shown by repeating the product composition measurement obtained at feeding temperature of 690 ^oC, H_2O/C = 2.0 and O_2/C = 0.5 once, listed in Table 4. The results show that the two measurements gave relatively close product compositions.

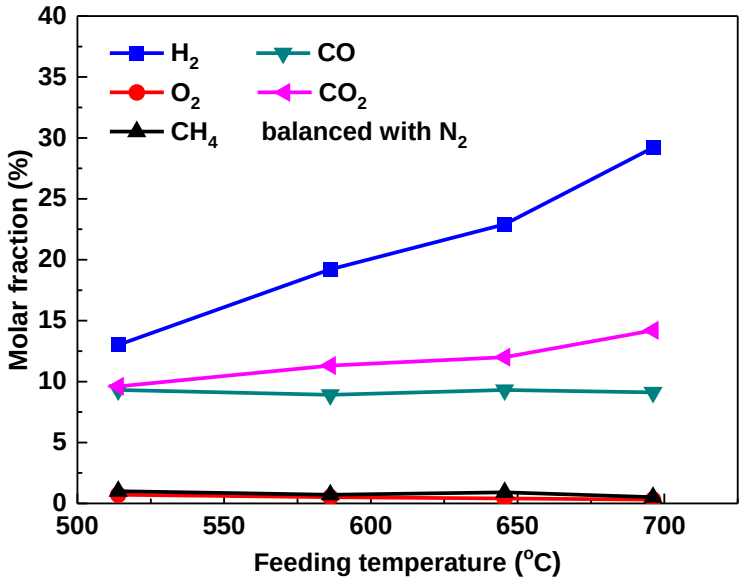

(a) H_2O/C = 2.5

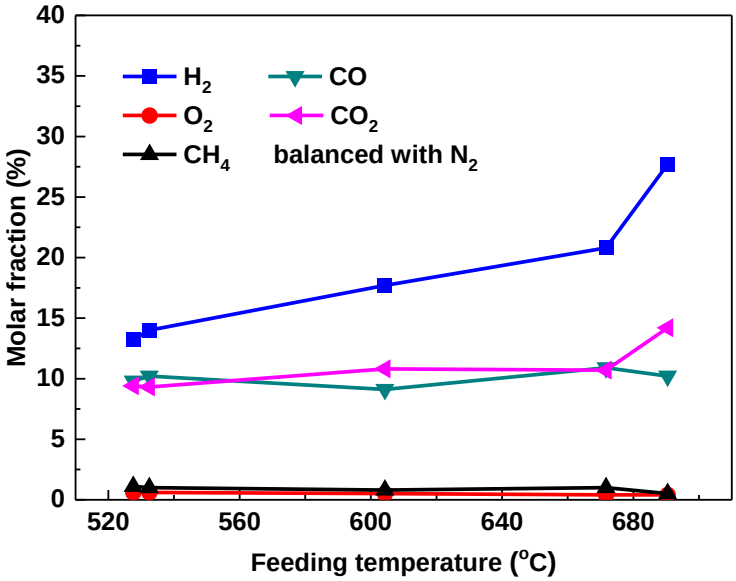

(b) $H_2O/C = 2.0$

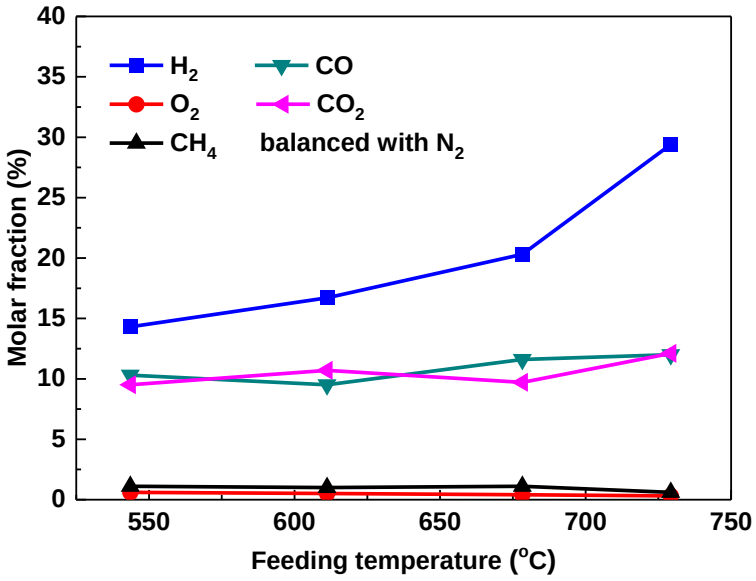

(c) $H_2O/C = 1.8$

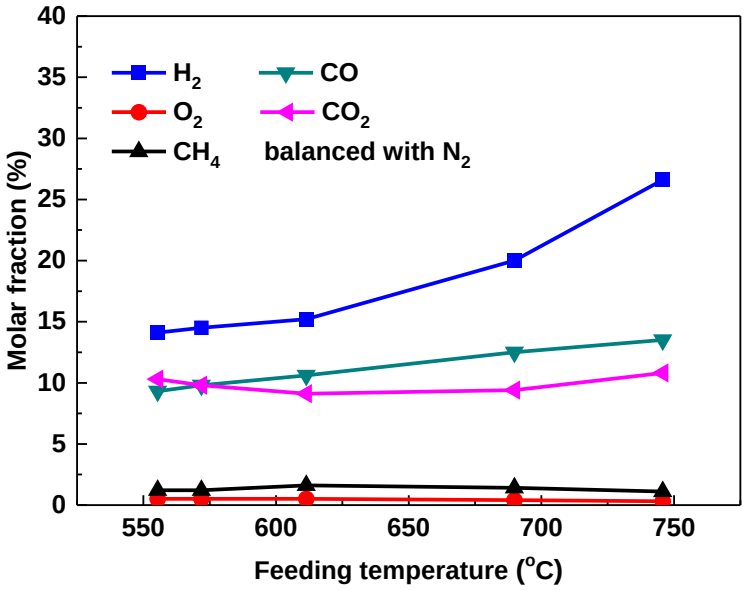

(d) $H_2O/C = 1.5$

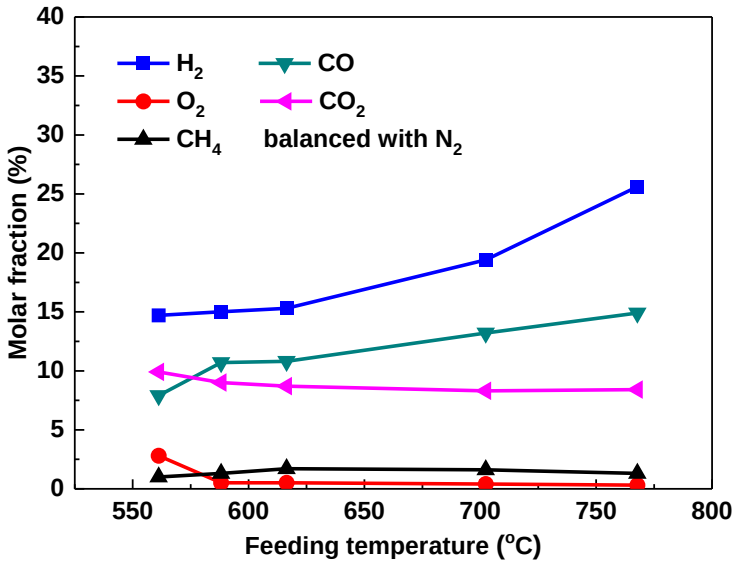

(e) $H_2O/C = 1.1$

Figure 18. Effect of feed temperature on reformate molar fraction. Fuel: desulfurized Jet A fuel, $O_2/C = 0.5$ at different H_2O/C.

Table 4. Test repeatability by comparing two GC test results at the same operating condition.

Test No.	Product gas mixture composition (%)					
	H_2	O_2	N_2	CH_4	CO	CO_2
1	26.1	0.5	48.1	0.3	9.8	14.0
2	27.7	0.4	46.9	0.5	10.2	14.2

Figure 19 ((a) to (e)) shows the effect of feeding temperature and H_2O/C on the fuel conversion, H_2 yield, and energy efficiency. Similar trends were found for the H_2 yield and energy efficiency that with the increase of feeding temperature, both were increasing correspondingly. The highest H_2 yield and energy efficiency were both obtained at 696.2 ^oC and H_2O/C = 2.5 with the values being 1.44 and 0.65, respectively. At lower H_2O/C, the increase of the two indices vs. temperatures slowed down at higher feeding temperatures, which was associated to the same reason discussed above. Different from H_2 yield and energy efficiency, at low H_2O/C, the fuel conversion showed an inflection point at around 700 ^oC, decreasing with the increasing of feeding temperature, which could be attributed to the formation of a type of refractory coke based on the investigation of Shamsi and co-workers [33]. The explanation that the inflection point did not show up at high H_2O/C could be that coke formation was inhibited by the high H_2O flow rate in the reactant. The maximum fuel conversion was obtained at 690.5 ^oC and H_2O/C = 2.0 with a value of 0.93. However, when H_2 yield and energy efficiency were taken into consideration, the best operating condition was chosen at feeding temperature of 696.2 ^oC and H_2O/C = 2.5 with fuel conversion, H_2 yield, and energy efficiency of 0.89, 1.44, and 0.65, respectively. Under that condition, the reformate molar fractions were measured with H_2 of 29.2%, O_2 of 0.3%, N_2 of 43.9%, CH_4 of 0.5%, CO of 9.1% and CO_2 of 14.2%.

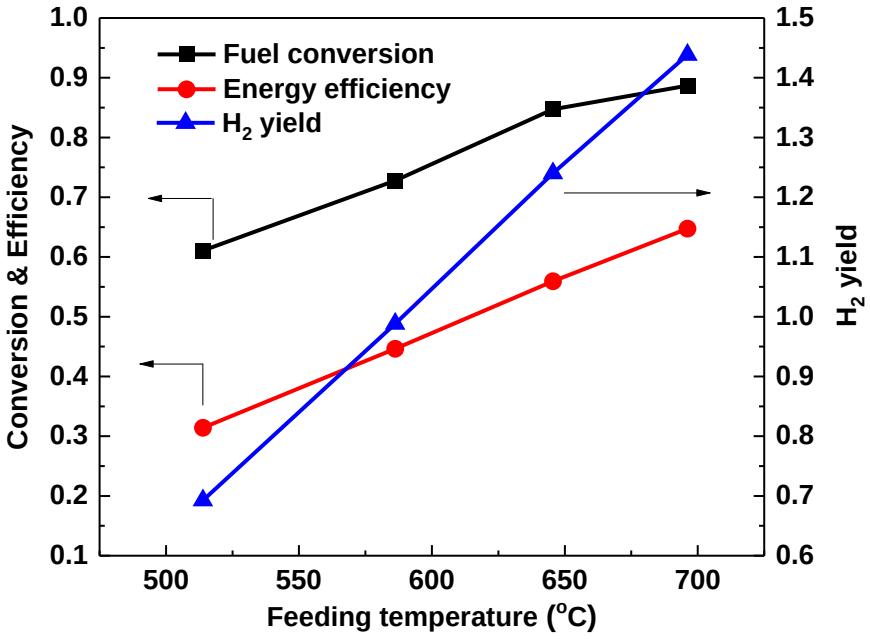

(a) $H_2O/C = 2.5$

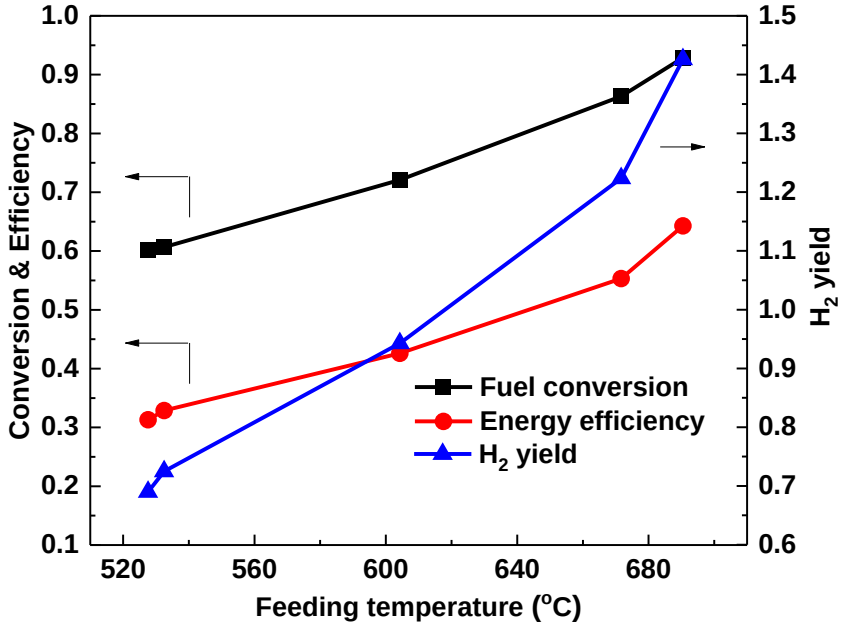

(b) $H_2O/C = 2.0$

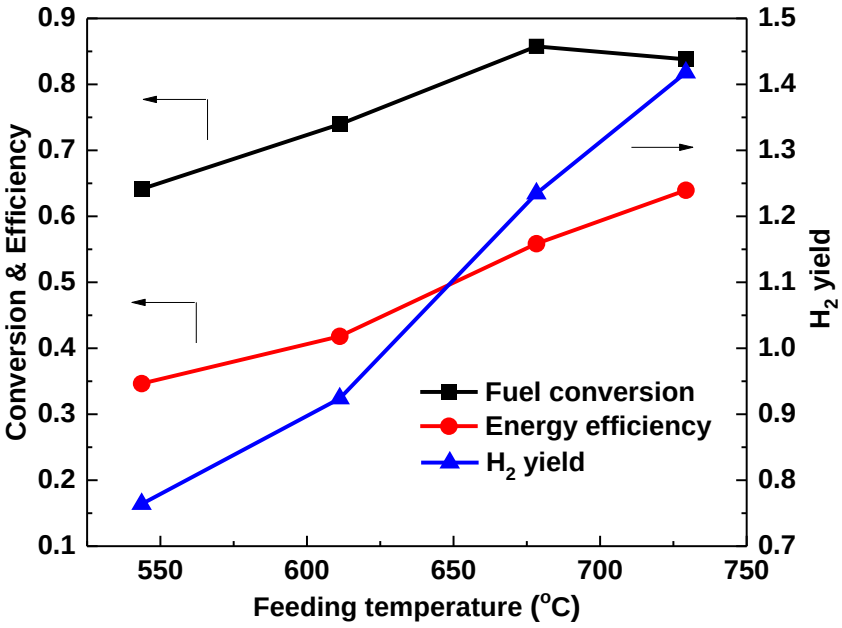

(c) $H_2O/C = 1.8$

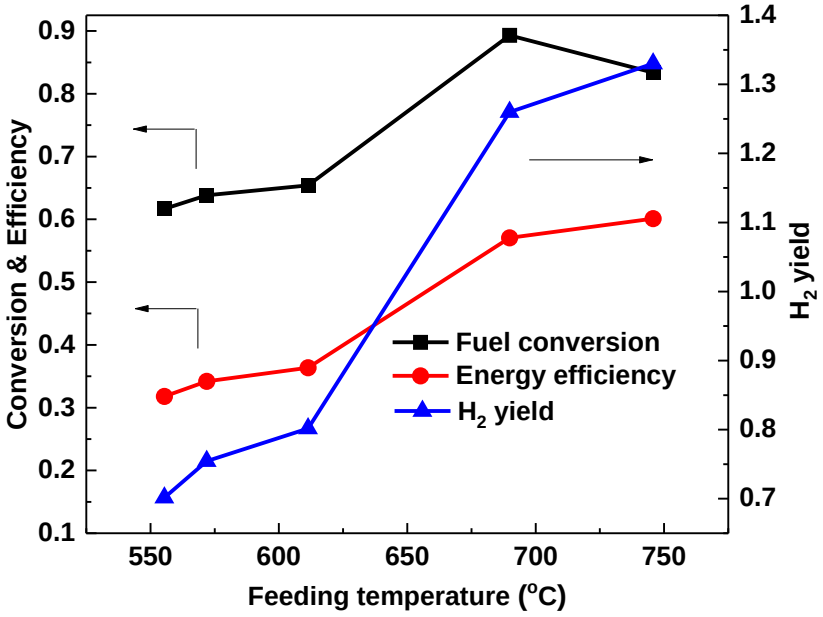

(d) $H_2O/C = 1.5$

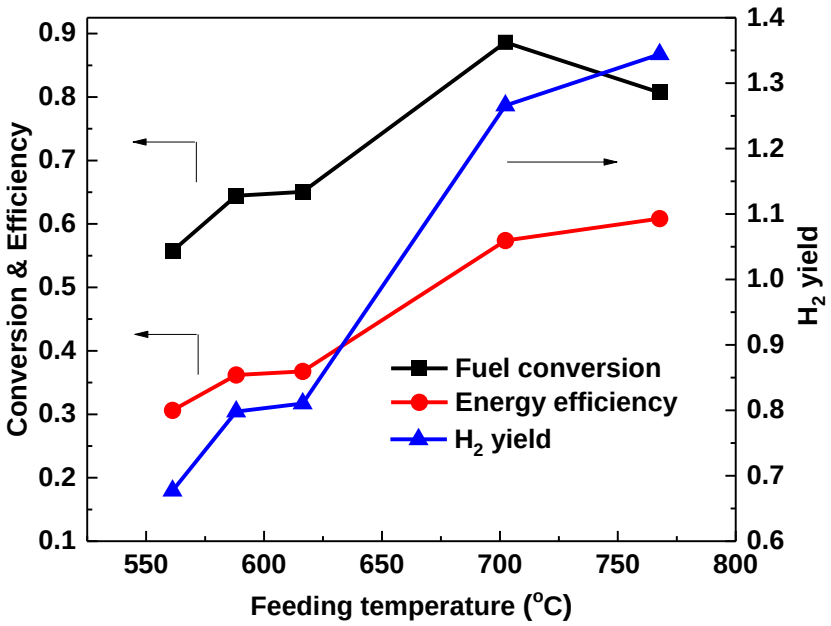

(e) $H_2O/C = 1.1$

Figure 19. Effect of feed temperature on fuel conversion, energy efficiency and H_2 yield. Fuel: desulfurized Jet A fuel, $O_2/C = 0.5$ at different H_2O/C.

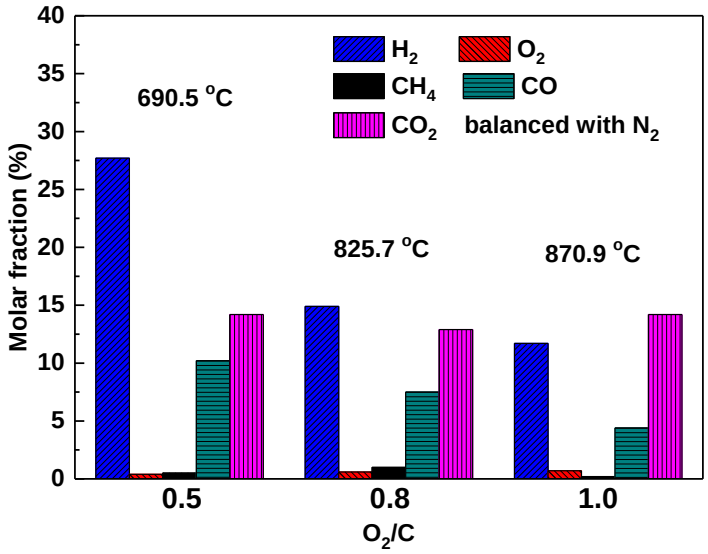

(a) molar fractions

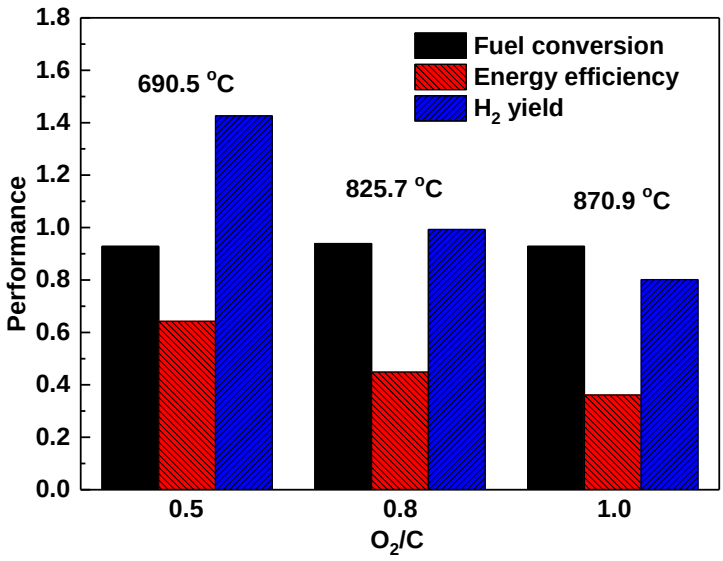

(b) fuel conversion, energy efficiency, and H_2 yield.

Figure 20. Effect of O_2/C at H_2O/C = 2 on ATR of desulfurized Jet A fuel.

Effect of O_2/C on reformate composition, fuel conversion, energy efficiency, and H_2 yield were shown in Figure 20. H_2 molar fraction and corresponding H_2 yield as well as energy efficiency were found dramatically decreasing from 27.7%, 1.43 and 0.64 to 11.7%, 0.80 and 0.36, respectively with the increase of O_2/C from 0.5 to 1.0. The explanation could be that with the increase of O_2/C, the overall reaction was tends to be dominated by POX reaction, which further led to the decline of H_2 production. On the other hand, the feeding temperature rose up from 690.5 °C to 870.9 °C due to the exothermic oxidation of jet fuel before the reactants reached the catalyst, where the high temperature should be in favor of the H_2 production based on the discussion in the last section. The competition of these two effects showed that the ratio of O_2/C is a more crucial factor than the feeding temperature as it directly determines the reaction thermodynamics. Fuel conversion achieved stable at

over 0.9 in all three cases regardless of the particularly high feeding temperature that conducive to coke formation. The reason could be that the existence of excess O_2 due to high O_2/C made it difficult to form coke even if under high temperatures. Therefore, besides high H_2O/C, high O_2/C is another effective way to suppress coke formation.

3.5.2.3. Temperature variation in the reactor

Temperatures at different locations in the reactor were measured at different ratios of H_2O/C and O_2/C, as shown in Figures 21 (a) to (e) and Figure 22, respectively. T1 to T5 represent temperatures at five different locations, sequentially named feeding temperature, catalyst front temperature, catalyst mid temperature, catalyst back temperature, and reformate temperature, as were labeled in Fig. 11. The temperatures at T2, T3 and T4 locations were varying quite ambiguously because they were located on the catalyst where complicated reactions occurred. A tiny variation of feeding temperature or H_2O/C and O_2/C could possibly cause large diversity of the reaction pathway, leading to those locations being the most susceptible to temperature variation. However, the temperatures detected at T2 and T4 locations were higher than that at T3 location in most of the cases (especially at lower H_2O/C), which could be explained by the observation found by many other researchers [234] [235] [236] – exothermic POX reaction with a high reaction rate usually occurred at the most front part of the catalyst, followed by the endothermic SR reaction occurring in the mid with the heat absorbed. At the back part of the catalyst there occurred WGS reaction or CO oxidation reaction, bringing the temperature up again. This assumption could be verified by the low H_2O/C case that the instant temperature detected at the T2 location was always higher than that at T3 location as POX reaction was enhanced

in these cases. The maximum temperature gradient detected was around 300 ^{o}C under low feeding temperature situation and minimized to within 100 ^{o}C at high level of feeding temperature, which was beneficial to both catalyst durability and coke suppression. The influence of POX reaction on the reaction temperature was more clearly depicted in Fig. 22 that with the increase of O_2/C, all the temperatures including the feeding temperature increased correspondingly. The high temperature at T3 location at high O_2/C might be because POX reaction took up most of the portions of the catalyst so that only a small portion in the back was used for SR reaction, leading to poor H_2 production performance, as elaborated in the previous section.

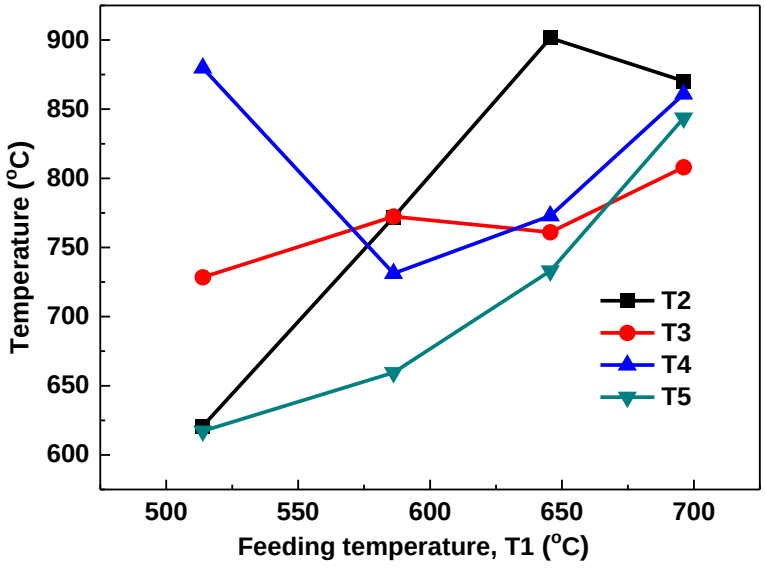

(a) H_2O/C = 2.5

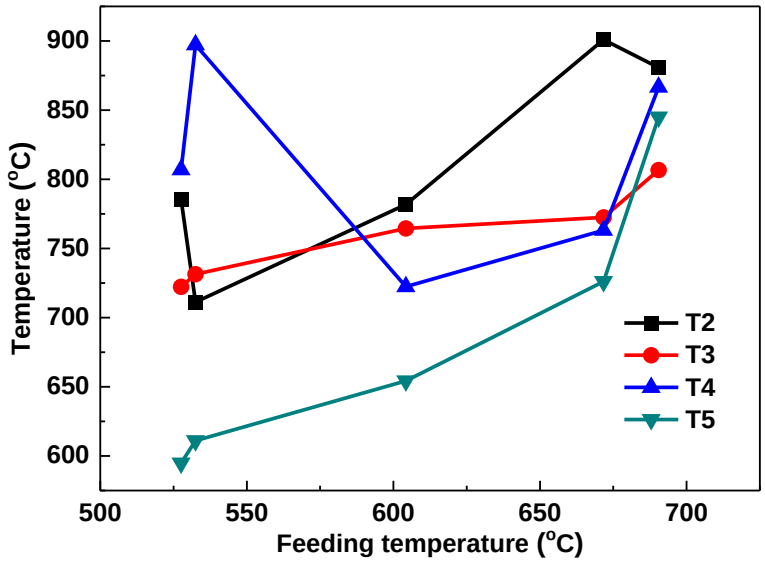

(b) $H_2O/C = 2.0$

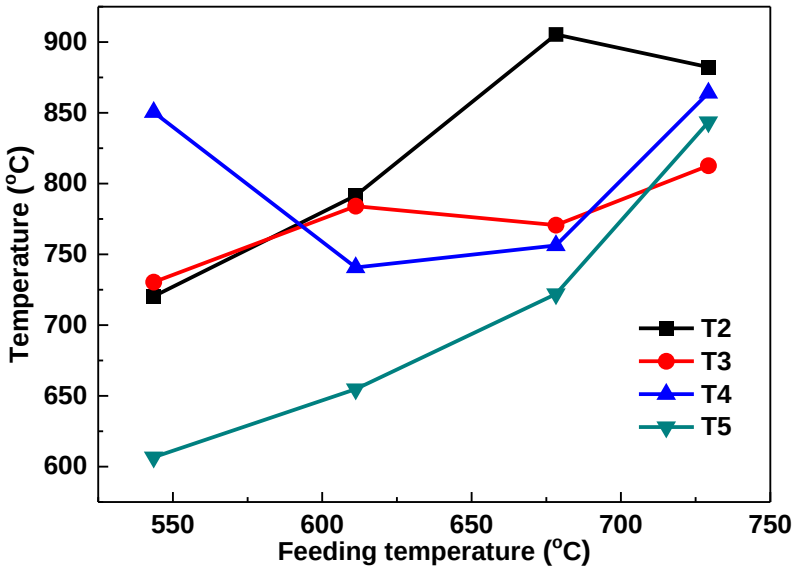

(c) $H_2O/C = 1.8$

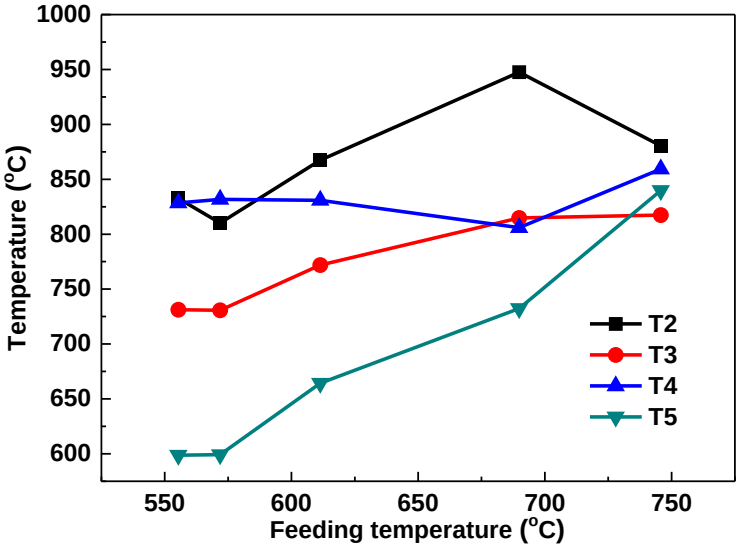

(d) $H_2O/C = 1.5$

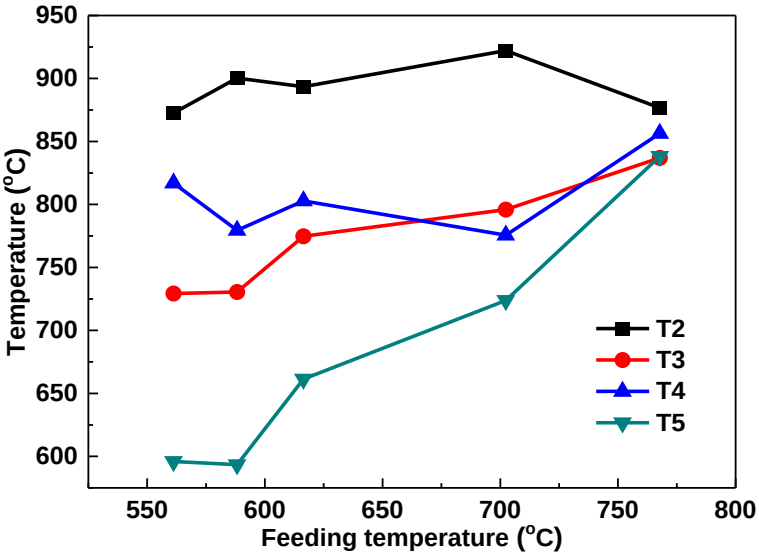

(e) $H_2O/C = 1.1$

Figure 21. Temperature variation profile at different locations with different H_2O/C.

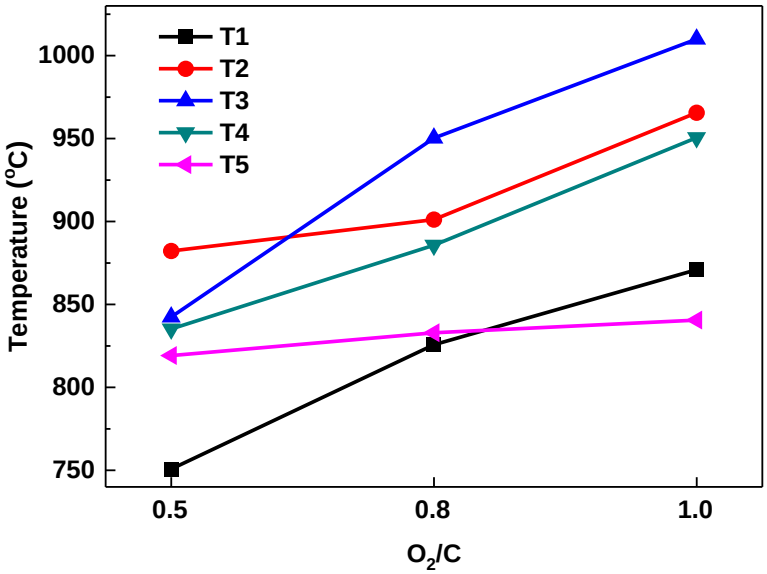

Figure 22. Temperature variation profile at different locations with different O_2/C.

Chapter 4. Self-Sustainability Validation

4.1. Methodology

A typical reformate obtained from the ATR performance test consists of 29.2% H_2, 9.1% CO, 14.2% CO_2, 43.9% N_2, unreacted steam and fuel, as well as traces amount of O_2 and CH_4. It can be directly passed to an SOFC since H_2 and CO are both eligible fuel. Nevertheless, it would bring troubles if a PEMFC is placed downstream, as CO could significantly poison the anode catalyst [30]. Although high temperature PEM (HT-PEM) fuel cells may have better CO-tolerance capability for as high as 4–5% [31] at 200 ^oC, effective CO removal techniques must be carried out before the reformate fueling to the fuel cell. Water-gas shift reaction shown in Eq. 6 is an attractive way to consume CO and further increase the H_2 yield.

Our target is to build a kW_{th}-class fuel processor which is capable to produce maximum amount of hydrogen and minimize the carbon monoxide concentration from Jet-A fuel so that it can be directly connected to the anode of a PEMFC. To achieve this, autothermal reforming is used to convert the jet fuel into syngas, followed by the water-gas shift reaction eliminating carbon monoxide and further increasing the hydrogen yield. Because the overall reaction tends to be exothermic, there is a potential to make the entire process self-sustainable by taking full benefit of the waste heat. Two countercurrent-flow heat exchangers (recuperators) are incorporated in the system with the first one sandwiched between ATR reformer and WGS reactor and the secondary recuperator placed in the back. However, the process depends on the operating conditions significantly that a tiny change

in the ratios of H_2O/C and O_2/C would have tremendous effect on the reaction equilibrium and thus, thermodynamics and reformate composition. For example, according to Fig. 12, if the oxygen-to-fuel molar ratio is smaller than 4.23 under the reaction temperature of 298 K, the reaction would transform to endothermic, indicating the overall process can never be self-sustainable. The self-sustainability can be achieved if and only if the overall process release heat and the heat is enough to preheat the reactants from room temperature to the desired feeding temperature to proceed the process. Therefore, thermodynamic analysis towards the overall process is required to be embedded before any experimental test can be conducted.

To perform the thermodynamic analysis, the overall reaction expression must be determined with stoichiometric fully defined. However, since the reactions involved in fuel processing are extremely complicated, it is impossible to list all the reactions and sum them up together to find an overall reaction expression. To solve this problem, reasonable assumptions and some previous experimental results are incorporated with a detailed example illustrated below.

Under the operating condition of $H_2O/C = 2.5$, $O_2/C = 0.5$ and feeding temperature of 696 ^oC, the overall reaction expression with undetermined coefficients can be written as follows:

$$\begin{aligned} &C_{11.6}H_{22.3} + 29H_2O + 5.8O_2 + 21.8N_2 \rightleftharpoons xCO + yCO_2 + zH_2 + \\ &(40.15 - 11.15w - z)H_2O + 21.8N_2 + wC_{11.6}H_{22.3} \end{aligned} \tag{29}$$

Here assumptions are made that CH_4 and O_2 are neglected in the reformate because their molar fractions are both small compared with other species, and no hydrocarbons except unconverted fuel exist in the reformate. From the previous results shown in the Chapter 3,

the H_2/CO molar ratio in the reformate is 3.2 under this particular operating condition. The calculated conversion of Jet A fuel equals 0.89, which gives $w = 0.11$ as the unconverted fuel remaining in the product. With the help of element balance, it is easy to find the ATR reaction equation as

$$\begin{aligned} &C_{11.6}H_{22.3} + 29H_2O + 5.8O_2 + 21.8N_2 \rightleftharpoons 4.52CO + 5.81CO_2 + \\ &14.45H_2 + 24.47H_2O + 21.8N_2 + 0.11C_{11.6}H_{22.3} \end{aligned} \tag{30}$$

Then if further assuming there is only 4% CO remaining in the final product, the fully-determined overall reaction expression can be demonstrated as Eq. 31.

$$\begin{aligned} &C_{11.6}H_{22.3} + 29H_2O + 5.8O_2 + 21.8N_2 \rightleftharpoons 1.96CO + 8.37CO_2 + \\ &17.01H_2 + 21.91H_2O + 21.8N_2 + 0.11C_{11.6}H_{22.3} \end{aligned} \tag{31}$$

The ATR and WGS reaction temperature are determined under the assumption that both reactions are adiabatic and no work is done to or extracted by the system. Therefore, during the reactions the enthalpy of reactants is equal to the enthalpy of products. The ATR reaction temperature can be determined by the following equations:

$$\Delta H = \sum_{\text{prod}} n_i h_i^{T_{\text{ATR}}} - \sum_{\text{reac}} n_i h_i^{T_{\text{feed}}} = 0 \tag{32}$$

$$h_i^T = h_{f,i}^0 + A_i t + \frac{B_i t^2}{2} + \frac{C_i t^3}{3} + \frac{D_i t^4}{4} + \frac{E_i}{t} + F_i - H_i \tag{33}$$

where the enthalpy of each species is in the unit of *kJ/mol* according to Shomate equation. The CO concentration in the WGS reaction product is assumed to be 4% when working with a HT-PEM fuel cell and the amount of unconverted fuel remains constant during the WGS reaction. In addition, the WGS reaction feeding temperature and fuel cell operating temperature are empirically set as 623 K [237] and 473 K [31] respectively.

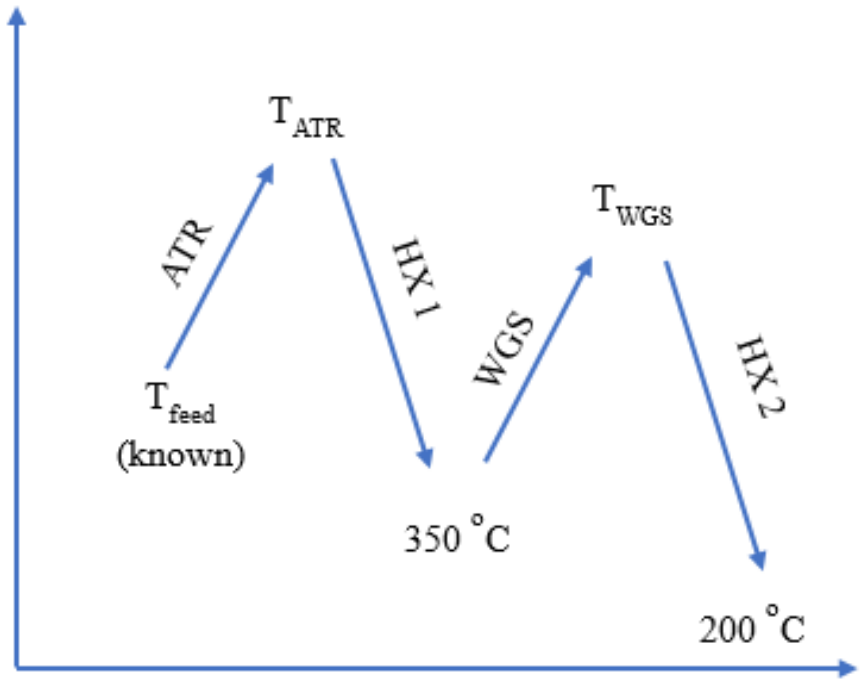

Figure 23. Fuel processing system temperature evolution.

Self-sustainability analysis is performed based on the simplified model including, an ATR reformer, a WGS reactor and two recuperators. Three principal energy aspects are considered at steady state, 1) the preheating energy (Q_{preheat}) to preheat the three reactants from room temperature to the desired feeding temperature, 2) the maximum exchanging energy ($Q_{\text{exchange1}}$) that can be provided by the reformate to cool down from the ATR reaction temperature to the WGS reaction feeding temperature in the first recuperator, and 3) the maximum exchanging energy ($Q_{\text{exchange2}}$) than can be provided by the overall product to cool down from the WGS reaction temperature to the final temperature which is also the operating temperature for the fuel cell in the secondary recuperator. The excess heat was then defined by the following equation:

$$Q_{\text{excess}} = Q_{\text{exchange1}} + Q_{\text{exchange2}} - Q_{\text{preheat}} \quad (34)$$

In order for the simple model to be valid, assumptions of no heat loss at any locations of the system have been made. For a self-sustainable system which requires no external heating source, it is required that Q_{excess} is greater than 0. That is to say, the exchanging energy that can be provided by the heat transfer from the products to the reactants must be enough to preheat the reactants to the desired feeding temperature. The preheating energy depends on the desired feeding temperature as well as the thermal properties of the reactants. During the preheating process, air is assumed to exhibit ideal gas behavior. Phase change has occurred for both fuel and water, thus, enthalpy change between different temperatures are used for the calculation.

$$Q_{\text{preheat}} = \sum_{i=1}^{2} \left(\int_{0.298}^{t_{\text{feed}}} 1000 n_i Cp_i dt \right) + n_{\text{H}_2\text{O}} \left(h_{g,\,\text{H}_2\text{O}}^{T_{\text{feed}}} - h_{f,\,\text{H}_2\text{O}}^{298} \right) + n_{\text{fuel}} \left(h_{g,\,\text{fuel}}^{T_{\text{feed}}} - h_{f,\,\text{fuel}}^{298} \right) \quad (35)$$

where i denotes the ith species, in this case, either O_2 or N_2. $t = T/1000$ which is used to keep the units coincide. The heat capacities of all gaseous species and liquid water used in this work were calculated based on the Shomate equation with the parameters provided by National Institute of Standards and Technology (NIST) database.

$$Cp_i = A_i + B_i t + C_i t^2 + D_i t^3 + E_i / t^2 \quad (36)$$

Table 5. Shomate equation parameters by NIST database.

Gases	Temperature (K)	A	B	C	D	E	F	G	H
O_2	100 – 700	31.32	-20.24	57.87	-36.51	-0.01	-8.90	246.79	0.00
	700 – 2000	30.03	8.77	-3.99	0.79	-0.74	-11.32	236.17	0.00
N_2	100 – 500	28.99	1.85	-9.65	16.64	0.00	-8.67	226.42	0.00
	500 – 2000	19.51	19.89	-8.60	1.37	0.53	-4.94	212.39	0.00
H_2	298 – 1000	33.07	-11.36	11.43	-2.77	-0.16	-9.98	172.71	0.00
	1000 – 2500	18.56	12.26	-2.86	0.27	1.98	-1.15	156.29	0.00
CO	298 – 1300	25.57	6.10	4.05	-2.67	0.13	-118.01	227.37	-110.53
	1300 – 6000	35.15	1.30	-0.21	0.01	-3.28	-127.84	231.71	-110.53
CO_2	298 – 1200	25.00	55.19	-33.69	7.95	-0.14	-403.61	228.24	-393.52
	1200 – 6000	58.17	2.72	-0.49	0.04	-6.45	-425.92	263.61	-393.52
H_2O	298 – 500	-203.61	1523.29	-3196.41	2474.46	3.86	-256.55	-488.72	-285.83
	500 – 1700	30.09	6.83	6.79	-2.53	0.08	-250.88	223.40	-241.83

The specific heat capacity and absolute enthalpy of n-dodecane were approximated to n-heptylcyclopentane ($C_{12}H_{24}$) based on Wang [238] due to the closeness of the two hydrocarbon family. The thermodynamic coefficients are listed in Table 6.

$$\frac{Cp_{\text{fuel}}}{R} = a_1 + a_2T + a_3T^2 + a_4T^3 + a_5T^4 \tag{37}$$

$$\frac{h_{\text{fuel}}^T}{RT} = a_1 + \frac{a_2}{2}T + \frac{a_3}{3}T^2 + \frac{a_4}{4}T^3 + \frac{a_5}{5}T^4 + \frac{a_6}{T} \tag{38}$$

$Q_{\text{exchange1}}$ and $Q_{\text{exchange2}}$ are related to the thermal properties of the products and the temperature of ATR and WGS reaction respectively. Therefore, similar expressions are employed as is shown in Eq. 39.

$$Q_{\text{exchange1}} = \sum_i n_i\left(h_i^{T_{\text{ATR}}} - h_i^{623}\right) \tag{39}$$

Table 6. Thermodynamic coefficients of n-dodecane. [238]

	300 – 1000 K	**1000 – 5000 K**
$\boldsymbol{a_1}$	3.9508691	36.440206
$\boldsymbol{a_2}$	0.10207987	0.054614801
$\boldsymbol{a_3}$	0.13124466×10^{-4}	-0.16091151×10^{-4}
$\boldsymbol{a_4}$	-0.76649284×10^{-7}	0.21478497×10^{-8}
$\boldsymbol{a_5}$	0.34503763×10^{-10}	$-0.10131180\times10^{-12}$
$\boldsymbol{a_6}$	-52093.574	-63890.109
$\boldsymbol{a_7}$	21.980951	-157.98973

4.2. Thermodynamic Analysis Results

4.2.1. Feeding temperature and H_2O/C ratio effect on reaction temperature

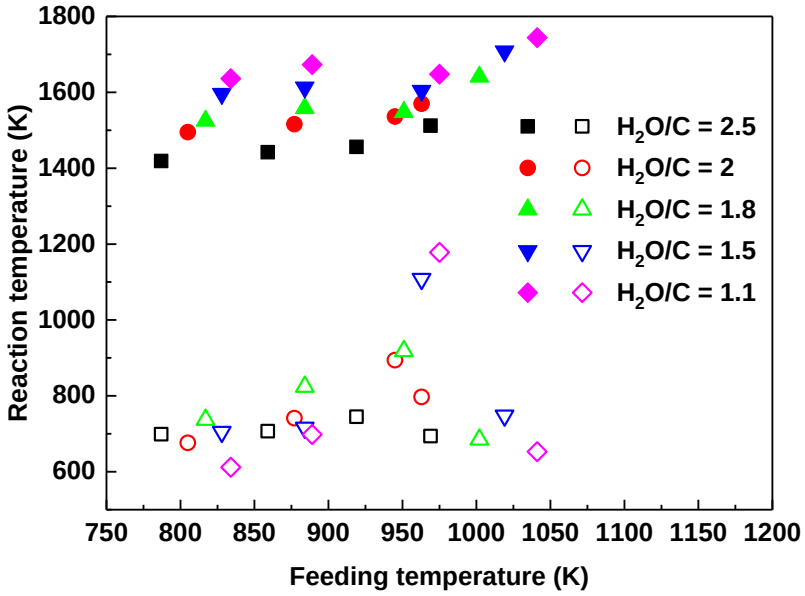

Figure 24. Effect of feeding temperature on reaction temperature at H_2O/C ratio from 2.5 to 1.1, O_2/C = 0.5. Solid symbols: ATR reaction, open symbols: WGS reaction.

Feeding temperature is the desired temperature that the three reactants must be heated up to before they can react on the ATR catalysts. Based on the previous experimental results, it is a key factor affecting the ATR reaction temperature and the reformate compositions which directly determine the reaction thermodynamics. In order to theoretically investigate the self-sustainability behavior of the fuel processor, the results illustrated in this section were based on the methodology described in section 4.1 with the help of reformate flow rates obtained from the experiments. Fig. 24 shows the effect of feeding temperature on the ATR and WGS reaction temperatures. Both reaction

temperatures were calculated assuming adiabaticity. For ATR reaction, the reaction temperature showed positive response with respect to the feeding temperature under higher H_2O/C ratios, indicating the product temperature depends on the enthalpy, because rising feeding temperature would result in rising enthalpy. However, when the H_2O/C ratio decreased to 1.5, a slight drop at high temperature was observed in the plot. Those weird behavior could be explained by that the product temperature does not solely depend on the enthalpy. Because the flow rate under each operating condition varied a lot, according to Eq. 31, the temperature could go down with increasing enthalpy as long as the flow rate had a big jump. To confirm that, the corresponding volumetric flow rate plot measured by a flowmeter is depicted in Fig. 25. At $H_2O/C = 1.5$ or 1.1, there was certainly a sudden increase of the flow rate from 13.0 L/min to 16.5 L/min. Under the same H_2/C ratio, a maximum WGS reaction temperature was discovered at the corresponding feeding temperature where the ATR reaction temperature drop appeared. For water-gas shift, the reaction feeding temperature was fixed at 623 K, therefore, the ATR feeding temperature can only impact the process by the reformate composition and flow rate. This could be the possible reason that the variation for WGS reaction temperature had similar trends with the volumetric flow rate.

Comparisons were made among different H_2O/C ratios to investigate the H_2O/C ratio effect to the reaction temperature. The graph shows that the ATR reaction temperature was inversely proportional to H_2O/C ratio especially at lower feeding temperatures, which could be explained by the balance between lowered enthalpy and lowered flow rate both influenced by the lower H_2O/C ratio. Furthermore, the WGS reaction temperature had

random deviations against H_2O/C at different feeding temperatures, indicating indirect effects from ratio of H_2O/C.

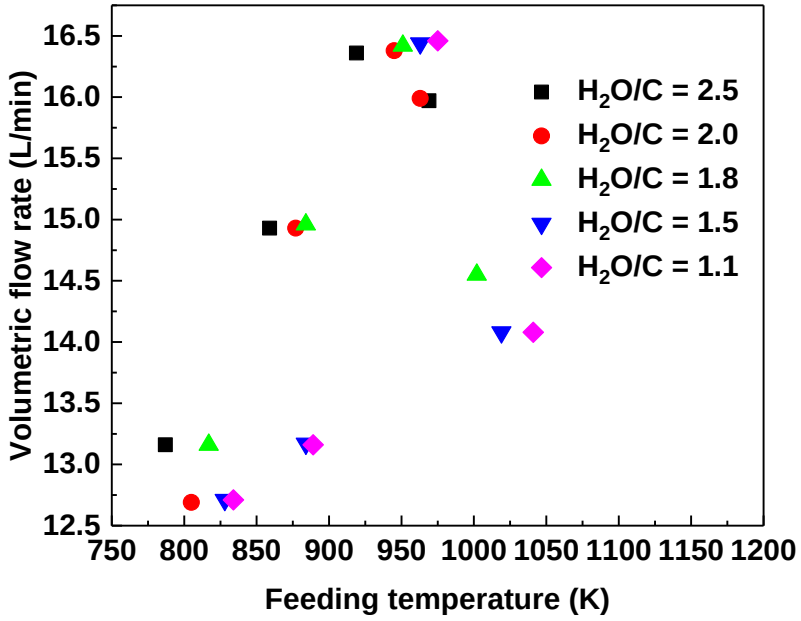

Figure 25. Corresponding volumetric flow rates at different operating conditions.

4.2.2. Feeding temperature and H_2O/C ratio effect on system energy

With the reaction temperatures obtained in the last section, system energy variations based on the feeding temperature and H_2O/C ratios were calculated and plotted in Figure 26. Although the exchanging energies in the two recuperators usually have positive relationship with the preceding corresponding reaction temperatures, they cannot be simply represented by the temperature variations as the flow rate of the mixture is also a crucial factor.

Figure 26 (a) to (e) shows the effect of feeding temperature on the system energy at H_2O/C ratio varying from 2.5 to 1.1, respectively. All the investigated energy at different H_2O/C ratios exhibited similar behaviors. The preheating energy was predictably

increasing with the increase of the feeding temperature. An optimal point appears in the exchanging energy in the second recuperator due to the maximum flow rate measured under those operating conditions. Not much influence of feeding temperature on the exchanging energy in the first recuperator was observed based on the calculation in all cases. $Q_{\text{exchange1}}$ had lower sensibility towards the feeding temperature compared with the ATR reaction temperature, which could be explained by the balance of the increase of product enthalpy and the decrease of maximum energy that can be potentially transferred due to the reformate composition. The excess energy remained positive at low feeding temperatures since the required preheating energy is quite low. It hit a maximum (in all cases except at $H_2O/C = 2.5$) at the corresponding optimal point in the $Q_{\text{exchange2}}$ profile and then dropped drastically.

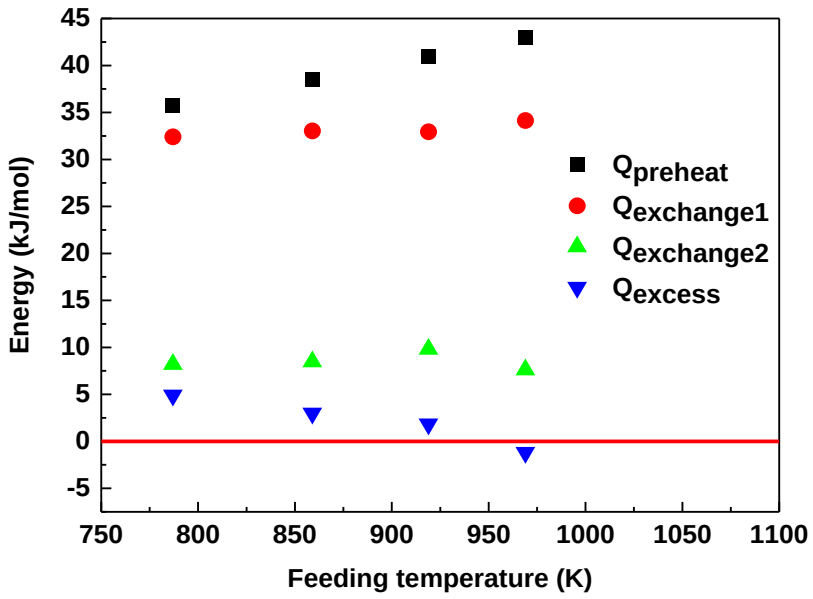

(a) $H_2O/C = 2.5$

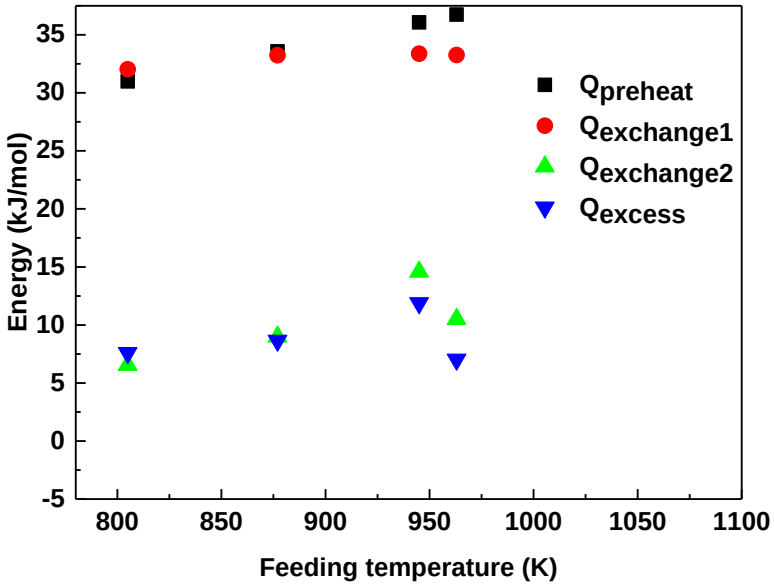

(b) $H_2O/C = 2.0$

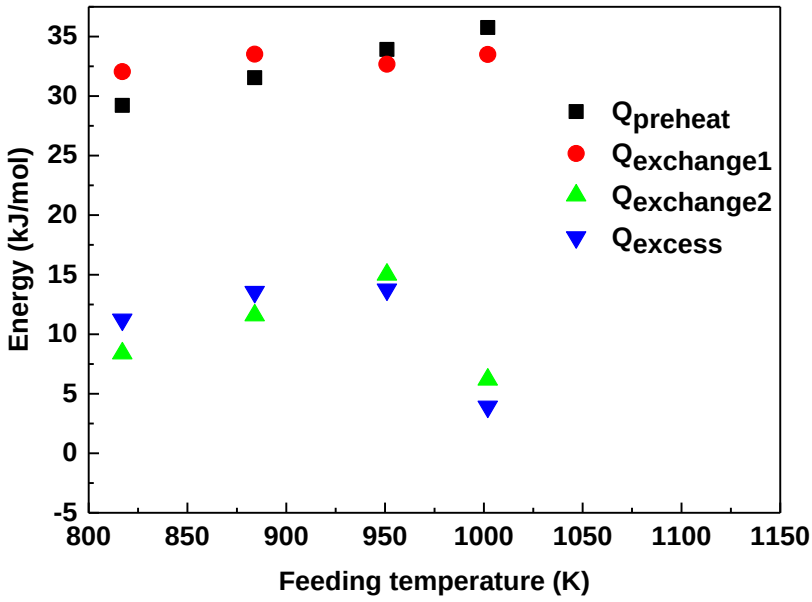

(c) $H_2O/C = 1.8$

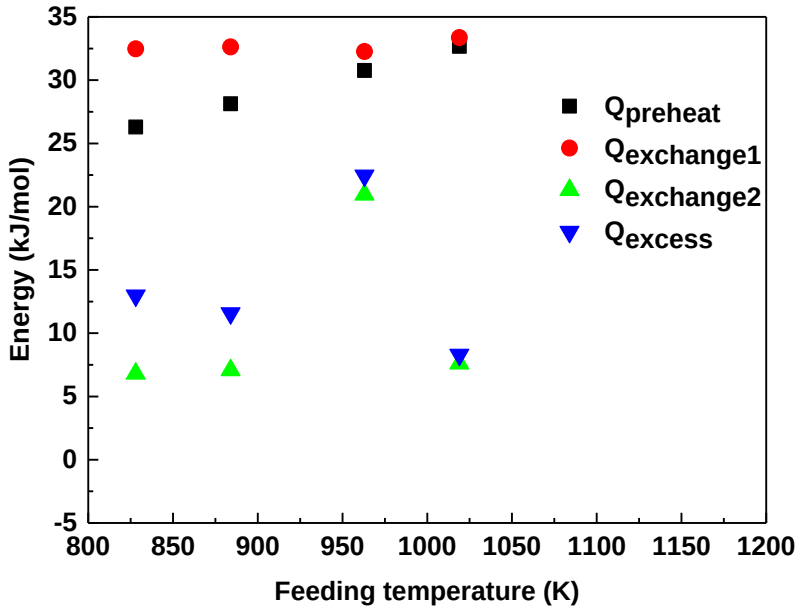

(d) $H_2O/C = 1.5$

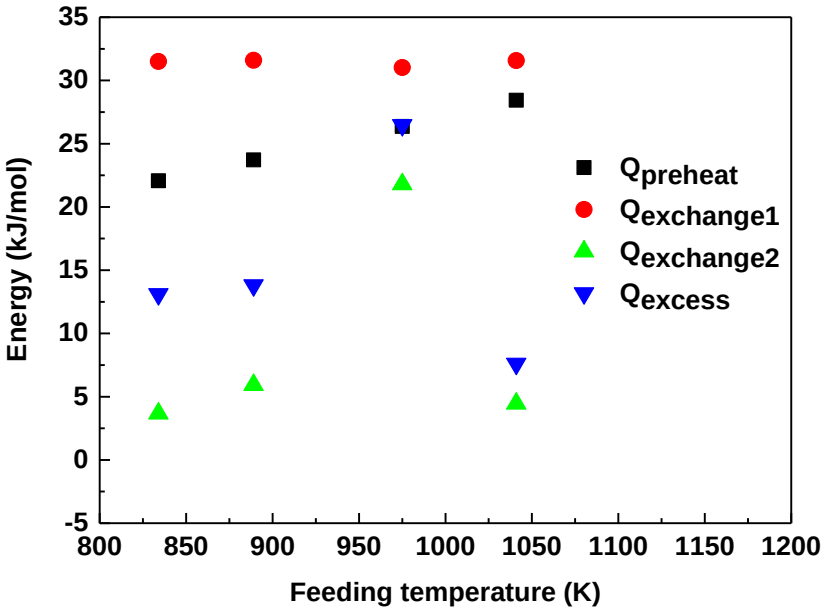

(e) $H_2O/C = 1.1$

Figure 26. Effect of feeding temperature on system energy at H_2O/C ratio from 2.5 to 1.1, O_2/C = 0.5.

H_2O/C ratios effect on the system energies were shown by comparing Fig. 26 through (a) to (e). Lower H_2O/C ratios corresponded to lower preheating energy due to the reduced need for water preheating and therefore higher excess energy. The exchanging energy in the first recuperator did not vary too much in different cases because the reformate flow rate decreasing caused by the H_2O/C ratio decreasing was offset by the increasing reaction temperature discussed in the las section. The excess energy was positive in almost all the cases except at both high temperature and H_2O/C ratio, i.e. at 969 K and H_2O/C = 2.5, which is happened to be the best operating condition obtained from the previous ATR experimental test. Unfortunately, this observation indicates that if the system is working under this operating condition, it is impossible to be self-sustainable. Therefore, the old best operating condition is not applicable to the overall system regardless that it provides the highest hydrogen production. Nevertheless, under most of the previous experimental conditions especially at lower H_2O/C ratios, the exchanging energy is adequate to preheat the reactants without inputting any additional heating source.

Chapter 5. Water-Gas Shift and Overall System Performance

5.1. Heat Transfer Modeling

5.1.1. Methodology

To collect the exhaust heat from the reactions and utilize them to preheat reactants, two countercurrent flow heat exchangers (recuperators) are incorporated after ATR reformer and WGS reactor respectively. In industry recuperators are commonly plugged into thermal systems because they can economically and effectively save a large amount of energy. In our current work, they are the most vital part since they directly determine the sustainability of the processor. Therefore, heat transfer modeling regarding recuperators was performed for each operating condition based on the thermodynamic analysis and previous experimental data.

The primary design specifications of the recuperators are shown in Table 7. It is convenient to start the analysis from the 2nd recuperator because the temperature there is much lower than the first recuperator, making them pass through the second recuperator prior to the first one. In order to obtain relative accurate prediction, the heat convection between the fluid and heat exchanging coils requires the acknowledgement of the convective heat transfer coefficient calculated from the Nusselt number which further depends on the Reynolds number and Prandtl number as well as the appropriate heat transfer configuration. Thereafter, the thermal and kinetic properties (thermal conductivity,

viscosity, heat capacity) of the individual reactants and bulk flow (reaction product mixture) need to be carefully determined. Finding the properties for individual species is not difficult, however, it is nontrivial when the properties of gas mixtures are needed since there are not existing values. Appropriate models are usually required to accurately predict the behavior of gas mixtures. Thus, in this work, some exclusive models for the gas mixture property determination are picked up based on the composition and recuperator configuration.

Table 7. Design specifications of the recuperators.

Reactor diameter (m)	0.043
Coil exterior diameter (m)	0.0032
Coil wall thickness (m)	0.000508
Coil wall heat conductivity (W m^{-1} K^{-1})	19
Fuel molar flow rate (mol min^{-1})	0.015
Air molar flow rate (mol min^{-1})	0.4154
WGS reaction starting temperature (K)	623
Fuel cell operating temperature (K)	473
2nd recuperator inlet water temperature (K)	373
2nd recuperator inlet fuel temperature (K)	433
2nd recuperator inlet max. air temperature (K)	473

Three parts contribute to the overall heat transfer coefficient, heat convection of the bulk flow in the reactor against the exterior wall of the heat exchanging coil h_{ex}, heat conduction through the coil wall k_{coil}, and the heat convection of the individual reactant in the coil against the interior wall h_{in}.

$$U_{\text{overall}} = \frac{1}{\frac{1}{h_{\text{ex}}} + \frac{\tau_{\text{wall}}}{k_{\text{coil}}} + \frac{1}{h_{\text{in}}}} \tag{40}$$

Nusselt number is related to the property and configuration of the heat transfer process. Reynolds number and Prandtl number characterize the ratio of inertial force to viscous force and the ratio of momentum diffusivity to thermal diffusivity, respectively. Therefore, the primary mission is to find the properties of gas mixture.

According to Davidson [239], the gas mixture dynamic viscosity can be calculated by:

$$\mu = \frac{1}{\varphi} \tag{41}$$

$$\varphi = \sum_{i,j} \left[\frac{y_i \cdot y_j}{\sqrt{\mu_i} \cdot \sqrt{\mu_j}} \cdot E_{i,j}^{A} \right] \tag{42}$$

$$y_i = \frac{x_i \cdot \sqrt{M_i}}{\sum_i \left(x_i \cdot \sqrt{M_i} \right)} \tag{43}$$

$$E_{i,j} = \frac{2 \cdot \sqrt{m_i} \cdot \sqrt{m_j}}{\left(m_i + m_j \right)} \tag{44}$$

Here A is equal to 1/3 based on the experimental results from Davidson. This particular model is adopted for the reason that it considers the molecule interaction when they are colliding with each other and can acquire more accurate results where hydrogen is inevitable in the mixture. Thereafter, Reynolds number is calculated from

$$\mathrm{Re}_D = \frac{\rho \cdot v \cdot D_{coil}}{\mu} = \frac{m \cdot D_{coil}}{A_{coil} \cdot \mu} \tag{45}$$

Partial molar capacity is used to determine the specific heat capacity of the mixture under the assumption of ideal gas behavior.

$$Cp = \sum_i x_i Cp_i \tag{46}$$

Thermal conductivity of the gas mixture is predicted by Milke/Blottner/Eucken model [240] since it is adequate for multicomponent gas mixture with relatively slow speeds. Prandlt number is therefore calculated by Eq. 49.

$$k = \sum_i \frac{x_i \cdot k_i}{\sum_j (x_j \cdot \phi_{ij})} \tag{47}$$

$$\phi_{ij} = \frac{\left[1 + \left(\frac{\mu_i}{\mu_j}\right)^{0.5} \left(\frac{M_j}{M_i}\right)^{0.25}\right]^2}{\sqrt{8}\left[1 + \left(\frac{M_i}{M_j}\right)\right]^{0.5}} \tag{48}$$

$$\mathrm{Pr} = \frac{Cp \cdot \mu}{k} \tag{49}$$

Different configurations result in significantly different heat transfer behavior. To obtain relatively accurate prediction, the convective heat transfer models must be compared and carefully selected (Table 8) before the heat transfer coefficient is calculated. Fully developed laminar pipe flow under constant wall temperature is adopted at low Reynolds number with the Nusselt number of 3.66. Gilinsky correlation has better prediction on the turbulent pipe flow with a large range of Reynolds number from 2300 to 5×10^6 with the help of the friction factor which also depends on the properties of the flow. The heat transfer behavior between the bulk flow and the heat exchanging coils is modelled with flow across the tube bundles by Zukauskas correlation. It is capable to predict based on very large ranges of Re and Pr for both gases and liquids. In our case, the correlation expression corresponding to gases across the aligned tube rows with low Reynolds number is used for better accuracy.

After Nusselt numbers are obtained, the heat transfer coefficient h can be calculated from Eq. 50 and the effective heat transfer coefficient U_{overall} can be determined by Eq. 40. Finally, the heat exchanging area A_{wall} is calculated by Eq. 52

$$h = \frac{\text{Nu}_D \cdot k}{d_{coil}} \tag{50}$$

$$\text{LMTD} = \frac{\Delta T_a - \Delta T_b}{\ln \frac{\Delta T_a}{\Delta T_b}} \tag{51}$$

$$A_{\text{wall}} = \frac{Q_{\text{exchange}}}{\text{LMTD} \cdot U_{\text{overall}}} \tag{52}$$

Table 8. Heat transfer correlations for different configurations involved in our system. [241]

	Configuration	**Criterion**	**Heat transfer correlation**
	Laminar pipe flow	$\text{Re}_D < 2000$	$\text{Nu}_D = 3.66$
Gnielinski's correlation	Turbulent pipe low	$2300 \leq \text{Re}_D \leq 5\times10^6$, $0.5 < \text{Pr} < 200$	$f = \frac{1}{(1.82 \log_{10} \text{Re}_D - 1.64)^2}$, $\text{Nu}_D = \frac{(f/8)(\text{Re}_D - 1000)\text{Pr}}{1 + 12.7\sqrt{f/8}\,(\text{Pr}^{2/3} - 1)}$
Zukauskas's correlation	Flow across tube bundles	$10 \leq \text{Re}_D \leq 100$	$\text{fn}\,(\text{Re}_D) = 0.8\text{Re}_D^{0.4}$, [a] $Nu_D = \text{Pr}^{0.36}\text{fn}\,(\text{Re}_D)$

[a] a function of Reynolds number

5.1.2. Heat Transfer Modeling Results

Heat exchanging areas for fuel, water and air in the first and second recuperators were calculated following the procedures demonstrated above. Fuel bypassed the first recuperator and directly was pumped into the inlet after passed through the second to avoid

carbonization due to the high temperature. Thus, the ideal temperature of the fuel before mixing with the other two reactants was set at 433 K. The rest of the heat required to preheat the fuel up to the feeding temperature was supplied by the water instead. The temperature of water after heat exchanging in the second recuperator was proposed at 373 K for calculation convenient. The contribution of water boiling convection had been neglected when calculating the heat convection between the water and the heating coil since it was too small to the overall heat transfer coefficient compared with the heat convection between the bulk flow and the coil. In addition, the maximum air temperature at the second recuperator inlet cannot exceed 473 K in order to obtain reasonable temperature difference for the heat exchanging in the first recuperator. With the status of the three reactants fully defined in the second recuperator, the exchanging heat and process heat should be recalculated. The results under different operating conditions were presented in Table 9. At H_2O/C = 2.5, O_2/C = 0.5 and the feeding temperature of 969 K, the excess heat was smaller than zero making the overall process endothermic. Although this option yielded the best operating condition based on the experimental result of the product composition, H_2 yield and fuel conversion, it would not be considered in the practical operation mode. Comparisons among case 2 to 5 were carried out regarding the minimum required heat exchanging areas of each species. Both the water and air in the first recuperator had increasing heat exchanging areas with the decreasing bulk flow heat transfer coefficient (dominating the overall process) in the first recuperator, since the exchanging heat did not vary too much at different H_2O/C ratios. In the second recuperator, the fuel and air exhibited similar trends with the WGS reaction temperature, however, water had irregular variations due to the change of the temperature and H_2O/C ratio. For case 6 and 7, due to

pretty low H_2 molar fraction and H_2 yield in the reformate, they were not taken into account either when practical experiments were performed. The excess heat of the other six cases were all positive, however, comprehensively considering the heat exchanging area, product composition, H_2 yield and fuel conversion of the ATR reaction, case 2 was selected as the primary operation mode in the following experiments.

Table 9. Heat exchanging areas for different operation conditions.

No.			**1**	**2**	**3**	**4**	**5**	**6**	**7**
$T_{\mathbf{feed}}$ **(K)**			969	963	1002	1019	1041	965	1099
$T_{\mathbf{ATR}}$ **(K)**			1512	1571	1641	1708	1744	1838	2060
$T_{\mathbf{WGS}}$ **(K)**			694	797	685	748	653	635	680
H_2O/C			2.5	2	1.8	1.5	1.1	2.5	2
O_2/C			0.5	0.5	0.5	0.5	0.5	0.8	0.8
$h_{ex,\,1st}$ $(Wm^{-2}K^{-1})$			N/A	132.8	132.6	125.3	121.5	131.8	122.8
Heat exchanging area (cm^2)	First recuperator	Water	N/A	20	24	30	72	13	22
		Air	N/A	36	38	39	41	41	53
	Secondary recuperator	Fuel	N/A	11	14	12	15	17	16
		Water	N/A	13	14	11	9.2	24	19
		Air	N/A	21	34	23	29	46	57

5.2. Overall System Set-up

A typical simplified fuel processor includes an ATR reformer, a series of high-temperature (583 – 723 K) and low-temperature (483 – 513 K) WGS reactors [151], heat

exchangers and preferential oxidation (PrOx) reactors [242]. For a HT-PEM fuel cell, the low-temperature WGS and PrOx reactors are not necessary since the high-temperature WGS reaction is usually sufficient to enable the CO content lower than 4%. However, heat exchangers are implemented for the purpose of efficiency improvement and considered as the crucial component particularly in a self-sustainable process.

Unlike the small-scale test rig for catalyst exploration or reaction mechanism study, various issues need to be considered on a kW_{th}-class fuel processor, such as system size and layout, reactor material, reactants inlet configuration, heat exchanger design, mass and heat transfer, thermal stability, measurement accuracy, start-up, safety, etc. According to the literature survey, there are not much study on a fuel processing system at this scale. One of the system was developed by Ahmed and his co-workers [242] with an on-board gasoline processor for automotive fuel cell systems. Start-up strategy, process train and operating parameters have been investigated by simulation of computer models. Another group from Germany [243] [244] also focused on the gasoline processor with their emphasis on the dynamics analysis and performance experimental test of a compact prototype. The system is capable to output 3-9 kW thermal power with the start-up time within 1800 s, the maximum H_2 content of 43% in dry basis, and CO content of 160 ppm. Krumpelt et al. [245] developed a 10-kW integrated gasoline fuel processor for a PEMFC and studied the issues including startup time minimization and reduction of heat loss. The processor is capable of producing 40 mol% H_2 at steady state and 25% H_2 at 25% of full power during startup. Nuvera Fuel Cells, Inc and Renault [246] [247] collaborated on a fuel processor compatible with gasoline, ethanol and methanol, and later they were able to extend it to the processing of diesel-type fuels [248]. Yoon [249] and Pasel [250] both

designed and fabricated their own kW-class fuel processor for diesel fuel and performed experimental tests in terms of start-up strategy and temperature effect.

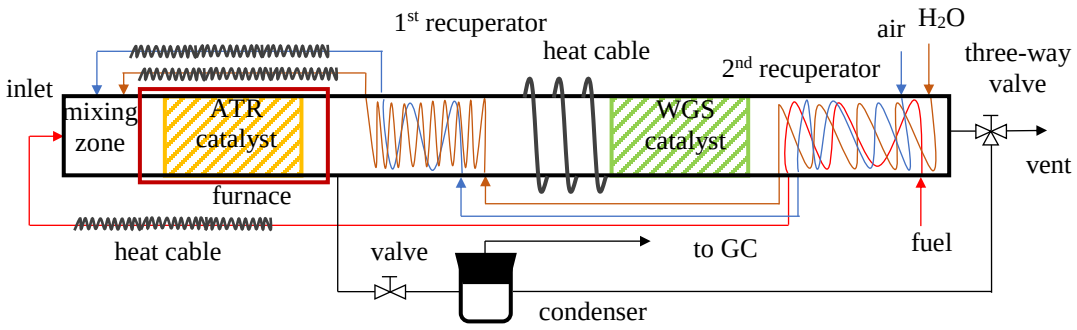

(a) Schematic of integrated fuel processor.

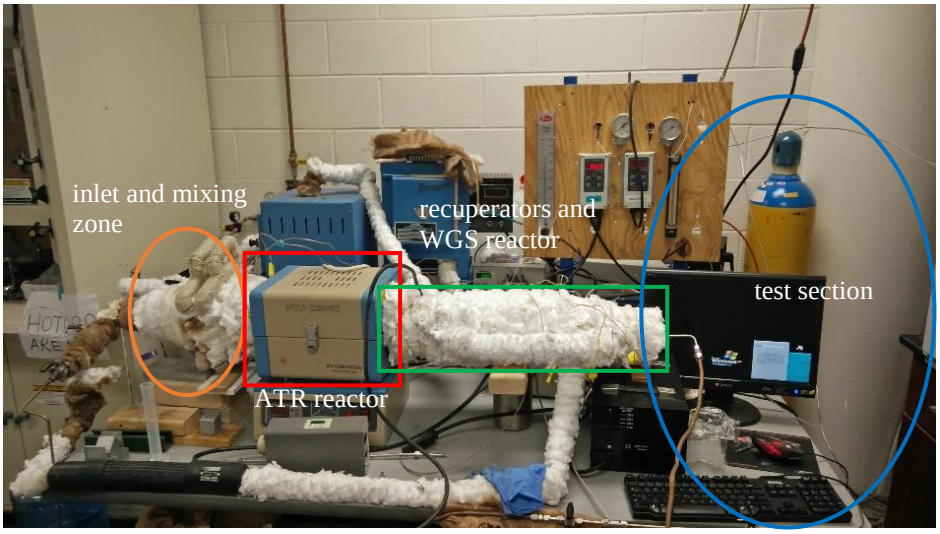

(b) Fuel processing system layout.

Figure 27. Fuel processing testing system

The proposed fuel processing system consists of the injection section, an ATR reactor, a WGS reactor, two countercurrent flow heat exchangers and the test section, as is shown in Fig. 27. Three reactants, fuel, water and air are firstly passed through the two heat exchangers at the back part of the processor and get preheated by the exhaust heat of the

products. Fuel is injected through a nozzle mounted in the middle of the front cap, which is particularly used to generate a uniform mist to enhance the mixing. After mixing with water and air in the mixing zone, the reactants are directly conducted to the ATR reactor. The ATR reactor is placed in a tubular furnace which is used to provide the required ATR reaction temperature. After the reaction, the reformate is passed through the first heat exchanger and then to the WGS reactor. Two specially designed recuperators were placed after the ATR reactor and WGS reactor respectively. Inside the recuperators, 1/8 in. stainless steel coils were used to separate the bulk flow and the reactants. The surface areas of the coils were predicted based on the heat transfer empirical equations which were discussed in the next section. This special shell-and-tube recuperator is designed for easy assembly and better heat exchanging between liquid reactants (water and jet fuel) and gaseous bulk flow. In order to monitor the temperature gradient, thermocouples (K type) were inserted before and after each of the coils (shown in Figure 28). To investigate water content effect to the WGS reaction without affecting the upstream reaction, an extra feed of water can be injected right before the WGS reactor as needed. A heating cable is wired outside of the WGS reactor to compensate for the heat loss and provide the required reaction temperature. A three-way valve and a regular valve were used to regulate the flow direction so that either the ATR reformate or the effluent (overall system product) was able to be analyzed solely through GC system. Any water, unreacted fuel or other liquids were removed by the absorbents filled in the condenser. Temperatures at different locations were monitored to display the longitudinal temperature gradient distribution in the system. All the reactors, passages, connectors before the test section are made of stainless steel for

better heat transfer and higher temperature/pressure resistance. Insulation is performed by enclosure of thick glass fibers to the outside of the exposed parts.

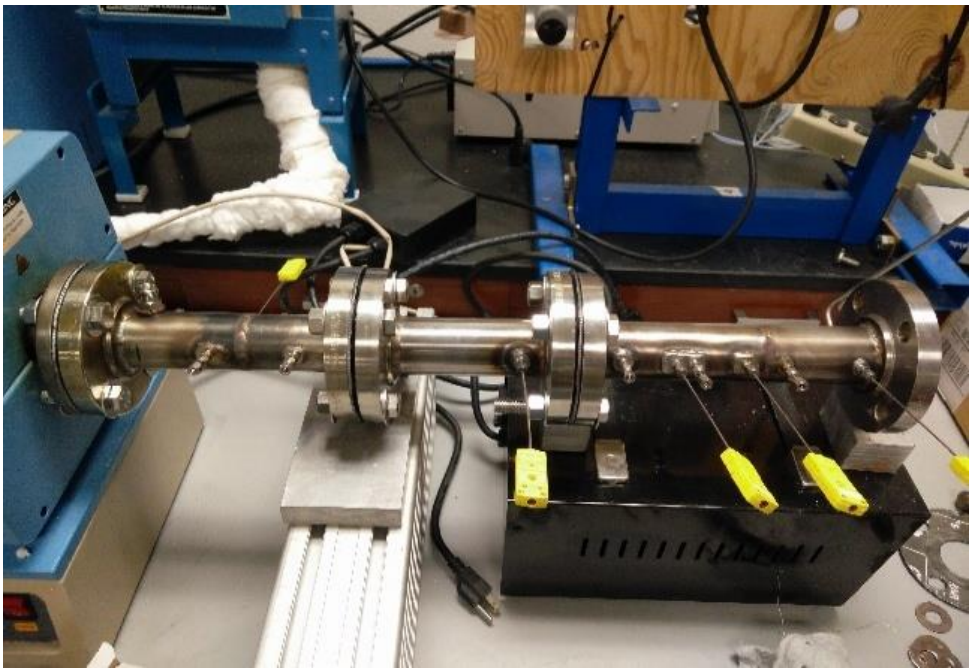

Figure 28. Main part of fuel processor without insulation. From left to right, first recuperator, WGS reactor and secondary recuperator.

5.3. Water-Gas Shift Catalysts

Water-gas shift (WGS) reaction is an attractive way to consume CO and further increase the H_2 yield. This is a reversible exothermic reaction with the backward reaction known as reverse water-gas shift (RWGS) reaction. The direction of the reaction highly depends on the reaction temperature. Lower temperature will lead to higher H_2 yield, however extremely low temperature is not favored by the reaction kinetics, as catalysts

usually require higher temperature to be activated. Moreover, reformate composition is another crucial factor since it directly determines the reaction equilibria. All the above four species are existing in the reformate. Based on our test results [24], the typical temperature of the reformate is around 850 ^{o}C with the composition of 29.2% H_2, 9.1% CO, 14.2% CO_2, 43.9% N_2 in dry basis, and small amount of unreacted fuel and steam. Different operating conditions of ATR process will lead to different reformate temperature and compositions which will further affect the WGS reaction.

The in-house-made ATR catalyst have been prepared and studied based on different operating conditions. Although results show that it exhibits some WGS activity, the catalyst specifically for WGS reaction needs to be designed and investigated. In general, the WGS catalyst is classified into three categories: iron-based catalysts, copper-based catalysts and cobalt-molybdenum oxides catalysts [251]. The iron-based catalysts are usually composed of Fe_2O_3, Cr_2O_3 and MgO, operating for high-temperature WGS reaction which occurs at about 350–450 ^{o}C [252]. At lower temperature (200–250 ^{o}C) the copper-based Cu/Zn catalysts are the typical choice [253]. Cobalt-molybdenum oxide on alumina which has decent activity at both high and low temperature is developed later for the purpose that it is completely insensitive to sulfur. With the concerns on the toxicity of chromium oxide, many researchers have been focusing on new types of WGS catalysts recently. Less toxic metallic oxides such as CeO_2 promoted iron on ceramic foams were developed by Lang and his co-workers for high-temperature WGS reaction [254]. The maximum CO conversion (close to 50%) was obtained at gas hourly space velocity (GHSV) of 1800 h^{-1} at 450 ^{o}C with steam-to-carbon (S/C) ratio of 2 on 45 ppi catalysts. Carbon deposition was detected during the test and temperature programmed oxidation

(TPO) results show that higher S/C ratio is beneficial to coke suppression. Noble metal catalysts were also effective for WGS reaction. Nanostructured Au or Pt on cerium oxide catalysts were investigated by Fu and his co-workers [255]. This nanosized catalyst was able to achieve remarkable WGS reaction rate at low temperature. Miao [256] characterized platinum supported on strontium hydroxy and fluoroapatite catalysts and studied the performance on WGS reaction. Over 90% CO conversion was observed above 350 ^{o}C with the reactant mixture of 5% CO and 20% H_2O in He at GHSV = 150,000 mL $gcat^{-1}$ h^{-1}.

Table 10. WGS catalysts recorded in recent literatures.

Catalysts	**Research Institite**
commercial Fe_2O_3, Cr_2O_3 and MgO for high-temperature WGS	
commercial 32.7% CuO, 47% ZnO, and 11% Al_2O_3 catalysts for low-temperature WGS	
commercial Co-Mo oxide on alumina	
CeO_2 promoted iron on ceramic foams	ICPEES
Nanostructured Au or Pt on cerium oxide	Tufts University
platinum supported on strontium hydroxy and fluoroapatite	Dalian Institute of Chemical Physics
commercial Fe-Cr-Cu	CSIRO Energy Technology
Cu-Ce(La)Ox	Tufts University
Ni/SiO_2 and Ni/Al_2O_3	Institut de Recherches sur la Catalyse
Au/Fe_2O_3 and Au/TiO_2	Università degli Studi di Torino
$Pt\text{-}CeO_2/Al_2O_3$	French National Centre for Scientific Research
Ru/La_2O_3	Adam Mickiewicz University
Ir/TiO_2	Institute of Solid State and Radiochemistry & Reaction Kinetics Research Group of the Hungarian Academy of Science

Several WGS catalysts were synthesized for the experimental performance test in our research. For a preliminary study, the Rh-NiO/La-K-Ce-Al-Ox/cordierite catalyst with great autothermal reforming activity was placed in the WGS reactor. Monometallic oxide (NiO, Fe_2O_3, CuO, ZnO) catalysts were also loaded onto the La-K-Ce-Al-Ox/cordierite support via wet-impregnation method for performance screening. Besides, two types of pellet catalysts (Fe_3O_4/Al_2O_3-SiO_2 and CuO-ZnO-Al_2O_3) were synthesized by the blending-extrusion method illustrated in Section 2.3.2. Fe_3O_4 was obtained by Fe_2O_3 reduction under 10% H_2/N_2 gas mixture at 500 ^oC for 2 h. For the test with pellet catalysts, fine wire meshes were placed at both sides of the WGS reactor to prevent the dispersion of the catalyst.

5.4. Water-Gas Shift Reaction Kinetics

Four models developed by other researchers particularly for iron-based catalyst are implemented to describe the high-temperature water-gas shift kinetics. The rate equations are used to determine the requisite catalyst loading and reactor size. Eq. 53 is used to relate the reactor size to the reaction rate.

$$V = F_{\mathrm{A0}} \int_0^x \frac{dx_{\mathrm{A}}}{-r_{\mathrm{A}}} \tag{53}$$

where V is the reactor volume, F_{A0} denotes the molar flow rate of species A at initial, r_A and x_A denote the reaction rate and conversion of species A, respectively. In order to determine the reactor volume, the rate equations must be known explicitly. The first-rate equation [257] was developed based on the Langmuir-Hinshelwood model which is shown

as Eq. 54. This kinetic rate equation is determined by listing all the elementary reactions associated with the mechanism of the Langmuir-Hinshelwood process. Therefore, it is related to the concentrations of all the species involved in WGS reaction. Another two rate equations based on the power-law model were derived by Hla [258] through experiments over two commercial catalysts in a differential reactor at constant temperature of 450 ^{o}C. Eq. 55 and 56 are used to calculate the reaction rate as a function of the partial pressures of each species and equilibrium constant. Finally, a more practical rate expression [259] for commercial reactors is adopted shown as Eq. 57. This model is a first-order equation with respect to the conversion of CO only, nevertheless it requires to calculate a lightly complicated effectiveness factor by considering the diffusional resistance. Other issues regarding age of catalyst, pressure and H_2S poisoning were also taken into account in this model, making it relatively accurate for large scale commercial reactors.

$$r = \frac{kK_{\mathrm{CO}}K_{\mathrm{H_2O}}([\mathrm{CO}][\mathrm{H_2O}] - [\mathrm{CO_2}][\mathrm{H_2}]/K)}{\left(1 + K_{\mathrm{CO}}[\mathrm{CO}] + K_{\mathrm{CO_2}}[\mathrm{CO_2}] + K_{\mathrm{H_2O}}[\mathrm{H_2O}] + K_{\mathrm{H_2}}[\mathrm{H_2}]\right)^2} \tag{54}$$

$$r = 10^{2.845}\exp\left(\frac{-111}{RT}\right)P_{\mathrm{CO}}^{1.0}P_{\mathrm{CO_2}}^{-0.36}P_{\mathrm{H_2}}^{-0.09}\left(1 - \frac{1}{K}\frac{P_{\mathrm{CO_2}}P_{\mathrm{H_2}}}{P_{\mathrm{CO}}P_{\mathrm{H_2O}}}\right) \tag{55}$$

$$r = 10^{0.659}\exp\left(\frac{-88}{RT}\right)P_{\mathrm{CO}}^{0.9}P_{\mathrm{H_2O}}^{0.31}P_{\mathrm{CO_2}}^{-0.156}P_{\mathrm{H_2}}^{-0.05}\left(1 - \frac{1}{K}\frac{P_{\mathrm{CO_2}}P_{\mathrm{H_2}}}{P_{\mathrm{CO}}P_{\mathrm{H_2O}}}\right) \tag{56}$$

$$r = \mathrm{Eff} \times 2.32 \times 10^{13}\exp\left(\frac{-27760}{R_gT}\right)\left(x_{\mathrm{CO}} - \frac{x_{\mathrm{H_2}}x_{\mathrm{CO_2}}}{x_{\mathrm{H_2O}}K}\right) \tag{57}$$

To consider the diffusional resistances in the rate equation, Eq. 57 incorporates an effectiveness factor Eff in terms of Thiele Modulus *h*. Thiele Modulus reveals the relationship between diffusion and reaction rate in porous catalyst pellets with no mass transfer limitations and is defined as shown in Eq. 59. *k* is the reaction rate constant which

equals to 4230.67 cm^3/h g in this equation. r_0 = pore radius, D_e = effective diffusivity, V_p = volume of the pellet, S_x = external surface area of pellet, D_k = Knudsen diffusivity, D_B = bulk diffusivity. T is the reaction temperature and M_A denotes the average molecular weight. For a shift catalyst at low pressure, Knudsen diffusivity is the controlling mode so that the bulk diffusivity can be neglected.

$$\text{Eff} = \frac{\tanh h}{h} \tag{58}$$

$$h = L\sqrt{\frac{2k}{r_0 D_e}} \tag{59}$$

$$L = \sqrt{2}\frac{V_p}{S_x} \tag{60}$$

$$D_e = \frac{1}{1/D_k + 1/D_B} \tag{61}$$

$$D_k = 9700 r_0 \sqrt{\frac{T}{M_A}} \tag{62}$$

Table 11. Minimum amount of catalysts required based on different reaction rate models.

	Required catalyst amount (g)
Langmuir-Hinshelwood model	124
Power-law model 1	1372
Power-law model 2	520
Practical model	2436

The calculated results based on the four rate expressions are listed in table 11. Under the same operating condition, the amounts of catalyst required are deviating from different models significantly. The fundamental model without considering any types of diffusion yields a result of close to 20 times smaller than the practical model. By examining the

computational result, if the diffusional resistances are ignored by eliminating the effectiveness factor in the practical model, the result would be a lot closer to the fundamental model, giving a mass of 310 g.

5.5. Overall System Experimental Results

5.5.1. Preliminary test

The best operating condition for the system obtained from the consideration of both experiment and model analysis was at feeding temperature of 963 K, $H_2O/C = 2$, $O_2/C = 0.5$, which was adopted for the overall fuel processor performance test. Preliminary test was conducted with another ATR catalyst monolith placed in the WGS reactor. By controlling the WGS reaction temperature, the effluents composition and system performance were shown in Figure 29 (a) and (b), respectively. The results of autothermal reforming from previous experiments were also depicted in the figures to compare with the overall process. The H_2 molar fraction and H_2 yield in the final effluent were always larger than them in the reformate, suggesting that H_2 was produced in the WGS reactor. The increase of fuel conversion compared with it through the ATR reaction indicated the reforming reaction was taken place in the WGS reactor to some extent. The energy efficiency which was closely related to the H_2 yield increased from 0.65 to over 0.8 at lower temperature and 0.75 at higher temperature. The molar fractions of CO and CO_2 showed opposite trends towards the ATR reaction with the minimum CO content of 8.4% in the final effluent.

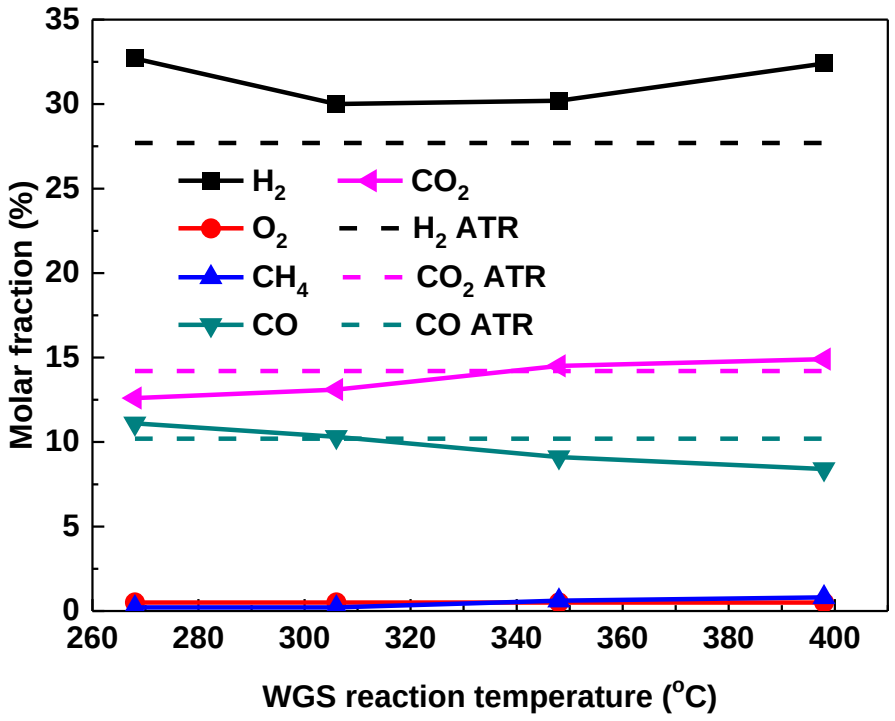

(a)

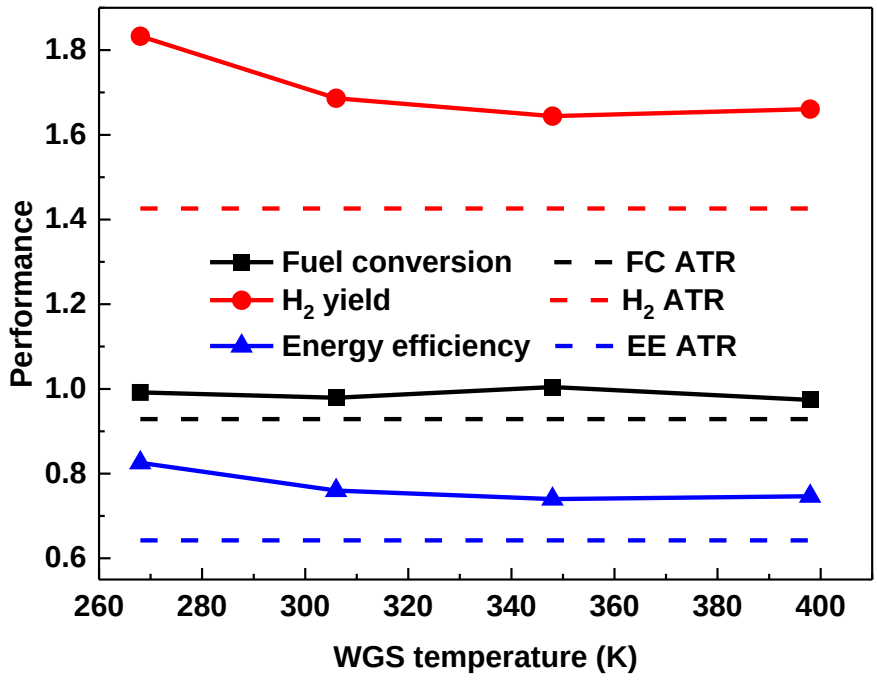

(b)

Figure 29. Effluents composition and system performance variations with the WGS reaction temperature.

The WGS reaction temperature effect was shown with each measurement in Figure 29 (a) and (b). The H_2 molar fraction and yield were decreasing at lower temperature and increasing again at higher temperature. It was discussed in our previous paper that in the ATR reaction the increasing feeding temperature would increase the H_2 molar fraction and yield. However, the decreasing with the temperature in this case could be only explained by the exothermic nature of the WGS reaction. Increasing the reaction temperature would cause the reaction equilibrium shifting to the reverse WGS reaction which further decreased the H_2 production. The behavior of CO and CO_2 molar fraction were similar to the ATR reaction thus it corresponds to the reforming process.

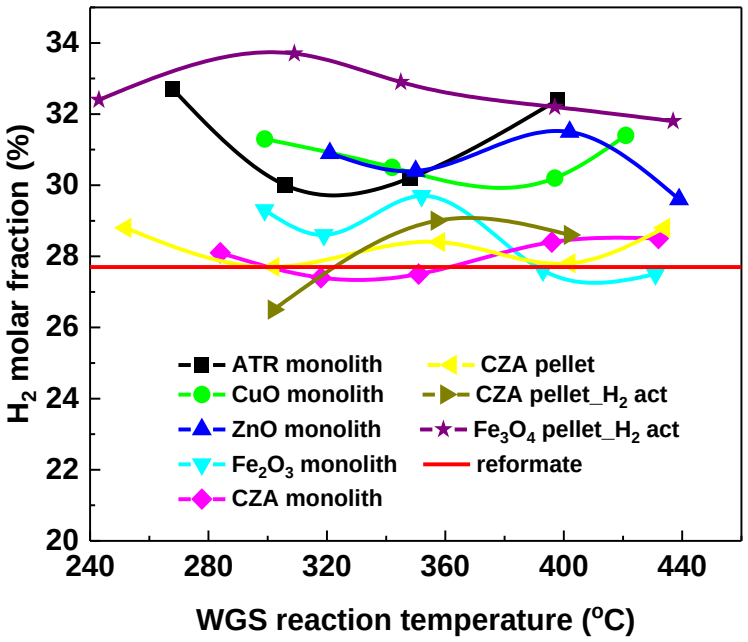

(a)

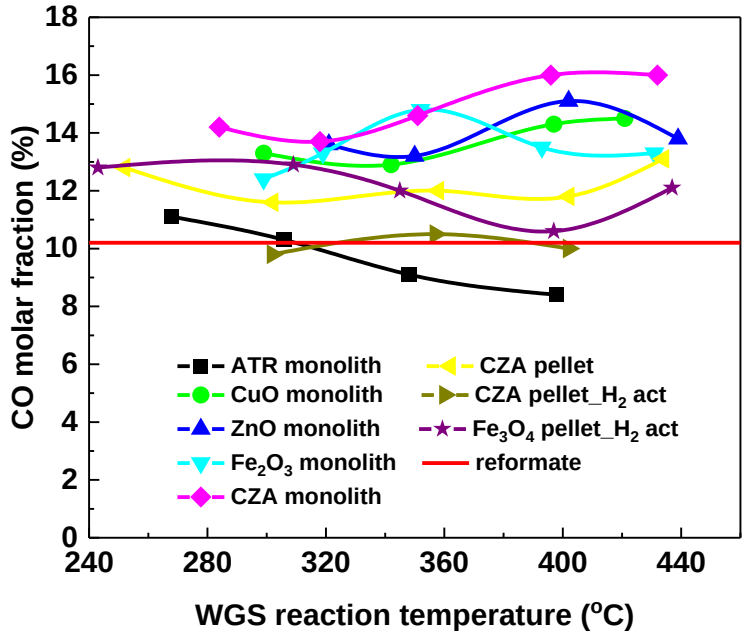

(b)

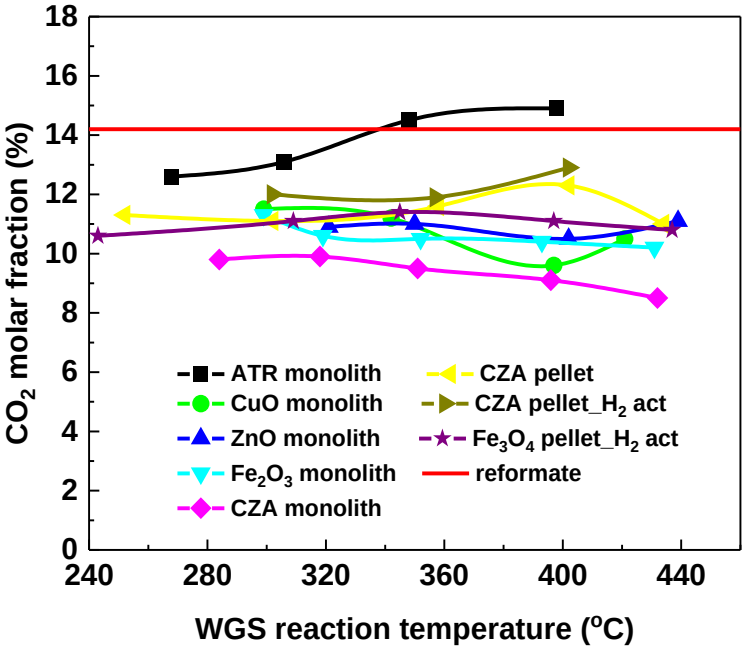

(c)

Figure 30. WGS temperature effect on overall product composition with different catalysts.

5.5.2. WGS temperature effect on overall system performance

Several types of WGS catalysts were synthesized to evaluate the overall system performance based on the literature review. Monometallic oxide (CuO, ZnO, Fe_2O_3) and CuO-ZnO-Al_2O_3 (denoted as CZA) supported on the cordierite monolith with 400 cpsi were prepared via wet-impregnation method and calcined in the air at 500 ^oC for 2 h. Blending-extrusion method was used to prepare CuO-ZnO-Al_2O_3 pellet catalyst. One of the test was conducted with the catalyst activated with diluted H_2/N_2 gas prior of time, which denotes as CZA pellet_H_2 act in Fig. 30 and Fig. 31. Fe_3O_4 pellet catalyst, with Fe_3O_4 pellet_H_2 act representing the test after the catalyst was reduced and activated in H_2 gas, was made through the precipitation of Fe^{3+} by excess NaOH solution and calcination in the air. To evaluate the WGS catalyst performance, H_2, CO and CO_2 molar fractions in the final product, H_2 yield, fuel conversion and energy efficiency of the overall system with respect to the WGS reaction temperature were recorded and plotted in Fig. 30 and Fig. 31, respectively. The corresponding results obtained from the previous ATR experimental test were also included in these figure for comparison. Different catalysts were acting diversely towards the WGS performance. H_2 molar fractions in most cases, and H_2 yields as well as energy efficiencies in all results are higher than them in the reformate, indicating that the investment of WGS process could indeed improve the H_2 production. Under some specific conditions, the H_2 molar fraction, H_2 yield and energy efficiency were dramatically improved from 28%, 1.42, 0.65 to 33%, 1.85, 0.83, respectively. However, the CO or CO_2 molar fractions in the final product are surprisingly higher or lower than the ATR reformate in most cases from Fig. 30 (b) or (c). This observation contradicts the water-gas shift reaction and thus indicates that the prevailing process in the WGS reactor in most cases is

not as expected. One possible explanation could be revealed from Fig. 31 (a) that the fuel conversions of the overall system were improved over the WGS catalyst, which is attributed to the CO_2 reforming (probably also steam reforming) reaction dominating the process in WGS reactor. CO_2 and steam reforming are both endothermic reactions, therefore, to suppress the undesired processes requires lower WGS reaction temperature or/and CO_2 sorption techniques. Moreover, adding extra water right before WGS reactor is also a feasible way to enhance water-gas shift reaction by shifting the equilibrium towards the positive direction.

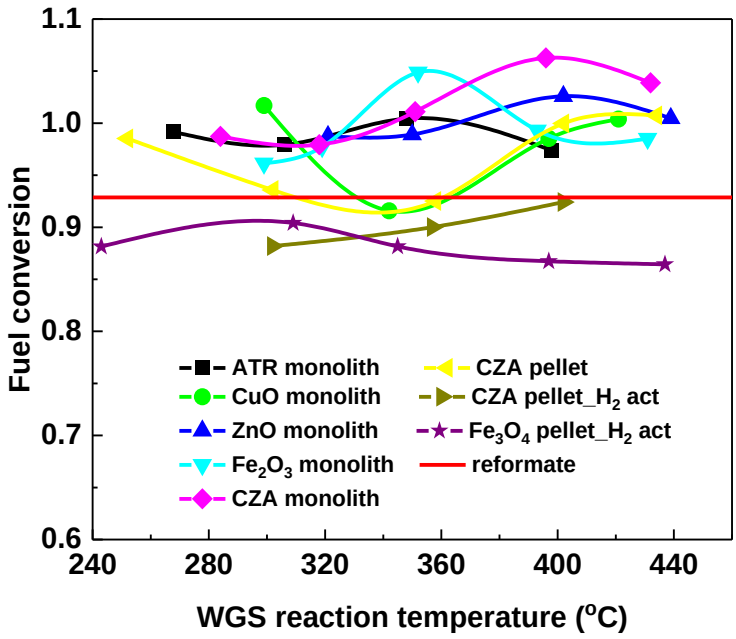

(a)

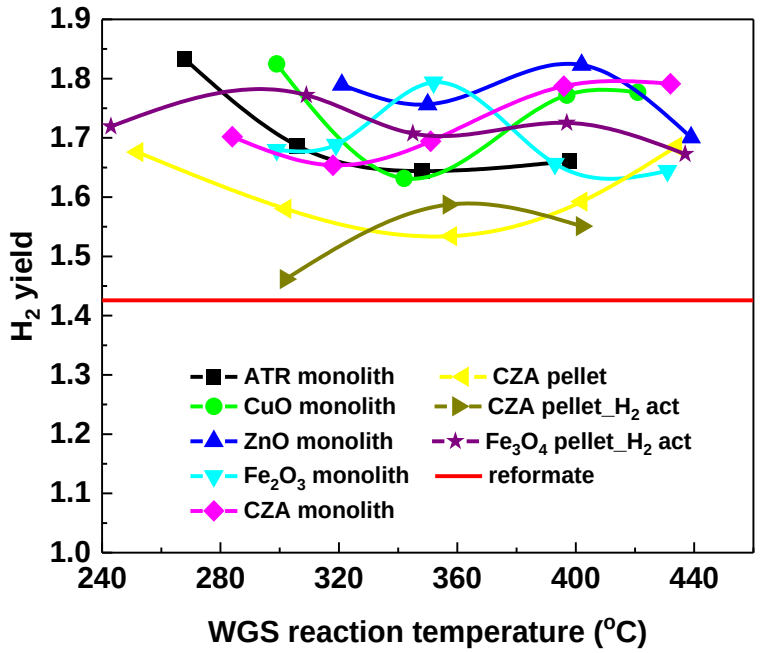

(b)

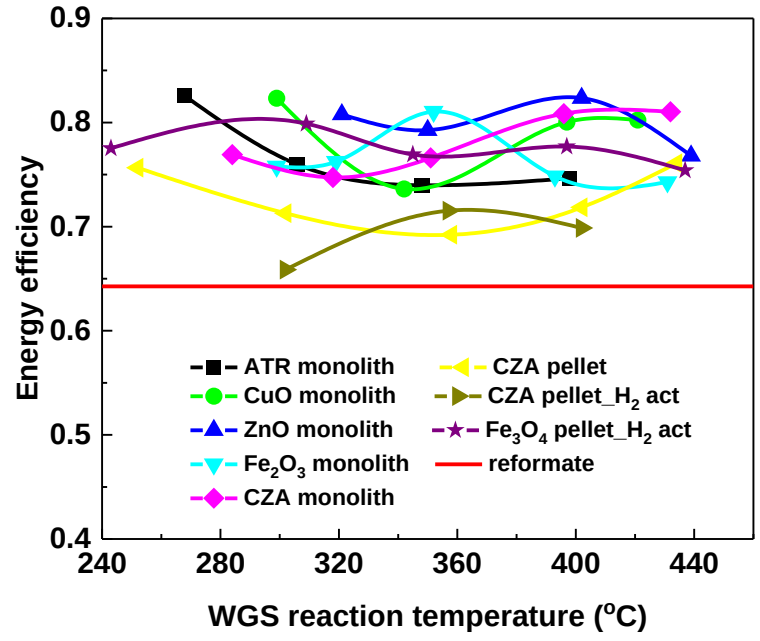

(c)

Figure 31. WGS temperature effect on overall system performance with different catalysts.

5.5.3. Extra water effect on overall system performance

To suppress the reforming reaction in the WGS reactor, extra water was injected right before the catalyst and the flow rate was regulated by another HPLC pump. The effect of water flow rate on the overall product composition, H_2 yield, fuel conversion and energy efficiency was studied and depicted in Fig. 32. Fe_3O_4 pellet catalyst was used for the investigation because it yields the highest H_2 molar fraction based on the previous results. Before the reactants were introduced, dilute H_2/N_2 gas was passed through the reactor chamber to activate the catalyst. The WGS temperature was maintained at 440 ^oC since Fe-based catalyst usually had the highest activity at 400–500 ^oC, according to other research. Fig. 32 (a) clearly shows the expected water-gas shift reaction equilibrium variation with respect to the extra water flow rate, which is with the water flow rate increasing, the molar fractions of H_2 and CO increasing while CO_2 decreasing. The maximum H_2 molar fraction can be achieved is over 35%, however, the minimum CO is still at the same level as the ATR reformate. Considering the fuel conversion in Fig. 32 (b) is also increasing with the extra water flow rate, it can be concluded that although water-gas shift reaction is enhanced with the extra water feed, reforming reaction is still dominating the process.

Other attempts were made to mix the WGS catalyst with hydrated lime, $Ca(OH)_2$, to adsorb CO_2 gas in order to suppress reforming reaction, as well as further shift the WGS reaction equilibrium to the positive direction. The results were not shown here as no improvement was detected up to date.

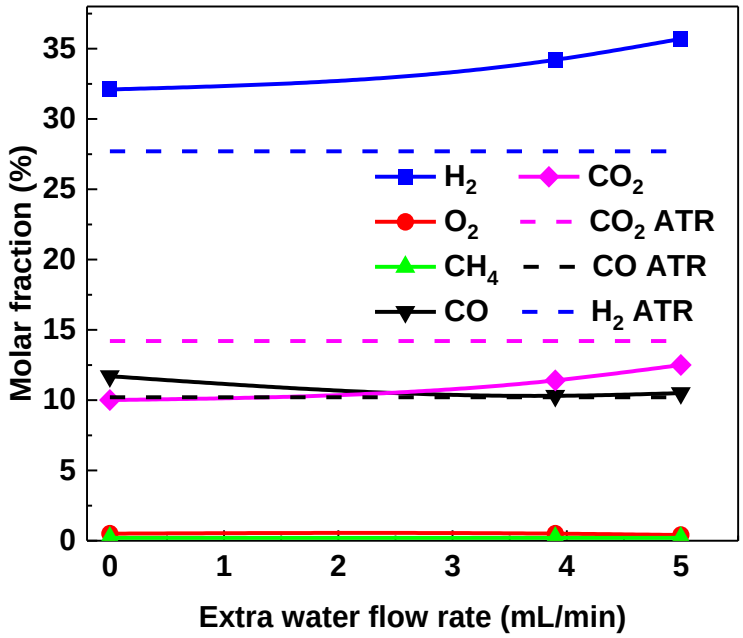

(a)

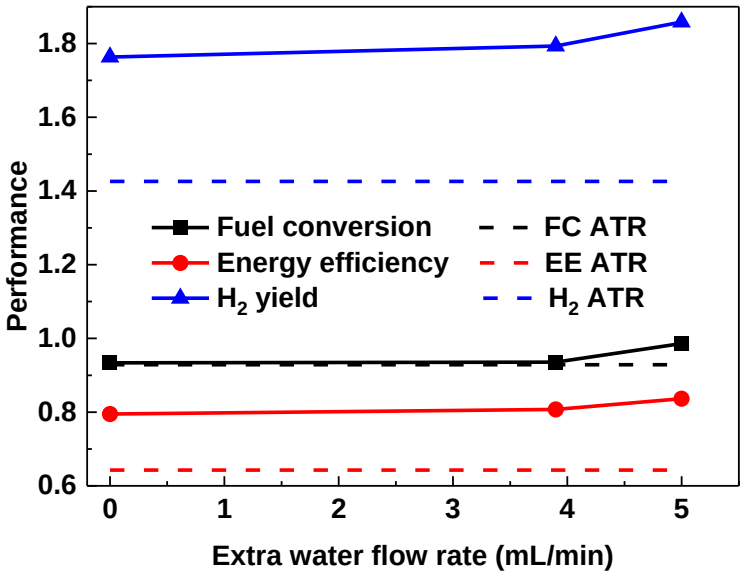

(b)

Figure 32. Extra water effect on overall system performance.

Chapter 6. Conclusions and Future Work

Autothermal reforming of Jet A fuel followed by water-gas shift are proven to be the most feasible and effective way to produce hydrogen onboard for a fuel cell system. To study the process in the lab, a kW_{th}-class fuel processing system consisted of the injection section, ATR reformer, WGS reactor, two countercurrent flow heat exchangers and test section was designed and fabricated based on carefully addressing the issues such as injection and mixing strategy, heat loss compensation, assembly accessibility, etc. An in-house-made ATR catalyst supported on industrial-level cordierite honeycomb monolith was prepared with inexpensive precursors by impregnation method.

After the simplified system was assembled and protected with thick-layer insulation, experimental test was conducted to evaluate the performance of ATR process. Preliminary study was carried out on the autothermal reforming of n-dodecane which is working as the surrogate of Jet A fuel. Over 40% H_2 molar fraction and over 85% fuel conversion as well as energy efficiency were achieved within the wide temperature range of 500–750 ^oC at the ratios of $H_2O/C = 1.8$ and $O_2/C = 0.5$. However, with similar operating conditions, the autothermal reforming of Jet A fuel was proved to be more difficult than the pure hydrocarbon. The best ATR performance was obtained at the feeding temperature of 696 ^oC, $H_2O/C = 2.5$ and $O_2/C = 0.5$, with the reformate composition yielding, H_2 29.2%, O_2 0.3%, N_2 43.9%, CH_4 0.5%, CO 9.1% and CO_2 14.2%. The three indices fuel conversion, H_2 yield and energy efficiency were then computed based on definition as 0.89, 1.44 and 0.65, respectively. Experimental results also show that coke formation can be suppressed dramatically at low temperature, high H_2O/C and high O_2/C.

Autothermal reforming is advantageous at the perspective of self-sustainability during operation. For this reason, excess energy analysis was performed based on the consideration of three energy aspects in the entire process, preheating energy and two exchanging energies in the first and secondary recuperator. Results indicate the system has a potential to be self-sustainable under all operating conditions that are considered in the research except the previous best operating condition obtained through ATR performance test. To determine new condition and design heat exchangers, relatively accurate heat transfer models were built based on the careful selection of gas mixture models when calculating their thermodynamic properties. Heat exchanging area of each species of the reactants were obtained as the results and case 2 with relatively small heat exchanging area as well as the second highest H_2 production was selected as the new operating condition.

To evaluate the overall system performance after the WGS reactor and recuperators were incorporated, catalyst type and WGS operating condition studies were carried out through experiments. Instead of water-gas shift reaction, all catalysts exhibited CO_2 and steam reforming activity under tested operating conditions. Although extra water and CO_2 adsorbents were adopted to suppress reforming process while enhance water-gas shift reaction, with all observed results, steam reforming is still dominating in the WGS reactor.

Future work includes experimental tests on the combination of lower temperature and extra water effect on different WGS catalysts to seek the best operating condition which can reduce the CO molar fraction to 4% level. Because the desulfurization of Jet A fuel is extremely tedious and time-consuming, n-dodecane is expected to substitute for the jet fuel. Furthermore, an individual small-scale WGS reactor is probably a good way to investigate catalytic behavior than the current evaluation system due to the fact that it requires less

feedstock and catalyst. Besides, the risk of uncontrollable variables would be less and testing bench would be much simpler.

The ultimate version of the fuel processor is expected to be actuated by a simple ignition system regardless of whether a warm start is available. The ignition system can be a heating coil, a spark plug, or even a piezoelectric device, which is able to generate sparks or high temperature with limited inputs. In this case, the mixing zone has to be modified to accommodate for the gadget. By comparing a cold start and a warm start, the start-up strategy can be generally optimized with respect to different reactants injection orders.

Fuel processor using 3D printing is also a perspective in the future. The schematic and 3D graphs created in solidworks are shown in Fig. 33 and Fig. 34, respectively. By printing the heat exchanger with 55 tubes with the I.D. of 3 mm in a cross section, the reactor would be more compact, the heat transfer would be more efficient and temperature distribution would be more uniform.

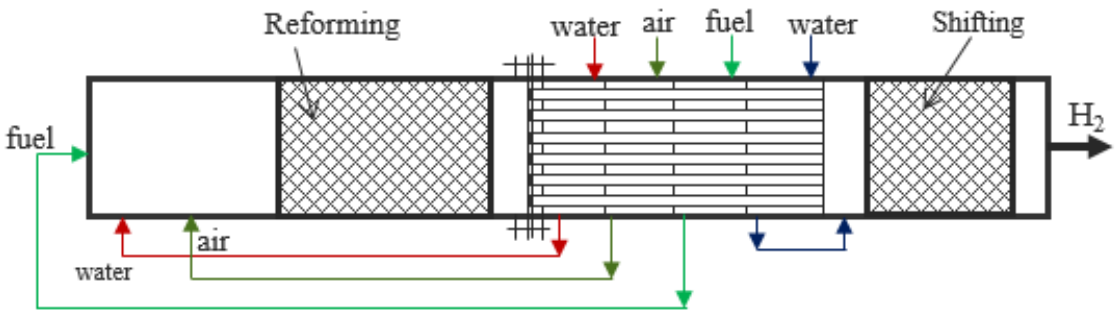

Figure 33. Schematic of fuel processor using 3D printing technique.

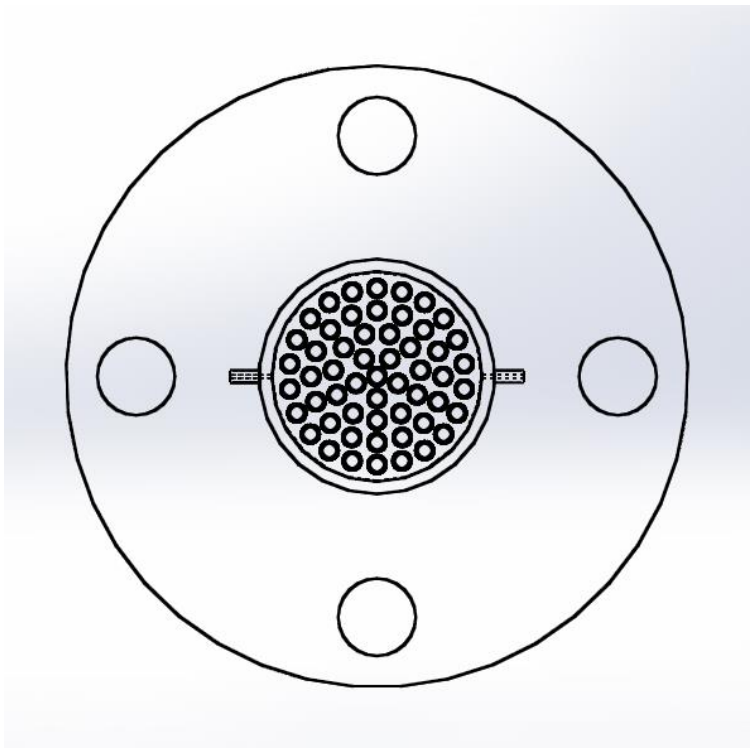

(a)

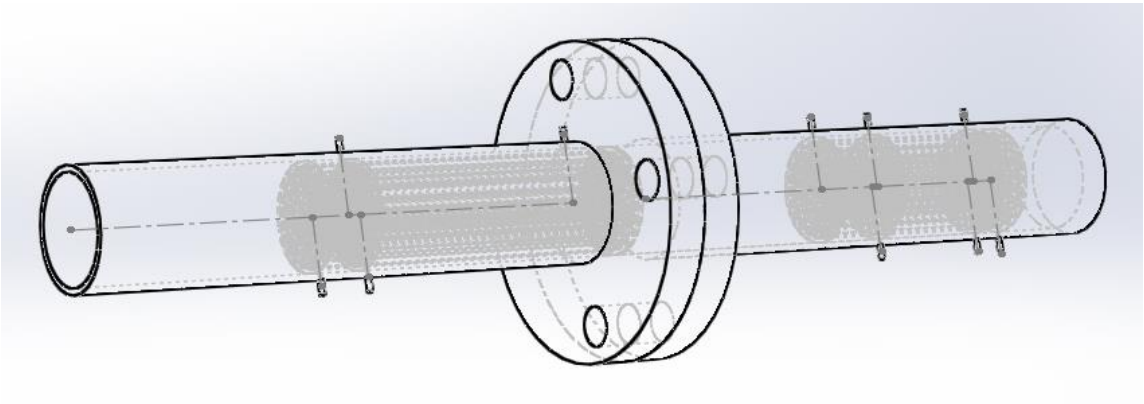

(b)

Figure 34. SOLIDWORKS graph of fuel processor using 3D printing technique. (a) Cross-seciton view; (b) Overall system perspective view.

REFERENCE

[1] T. L. LeValley, A. R. Richard and M. Fan, "The progress in water gas shift and steam reforming hydrogen production technologies – a review," *International Journal of Hydrogen Energy*, vol. 39, no. 30, pp. 16983-17000, 2014.

[2] H. Iida, N. Onuki, T. Numa and A. Igarashi, "Steam reforming of dodecane and toluene over Ru/12SrO–7Al_2O_3 (S12A7) catalysts," *Fuel Processing Technology*, vol. 142, pp. 397-402, 2016.

[3] J. Yoo, Y. Bang, S. J. Han, S. Park, J. H. Song and I. K. Song, "Hydrogen production by tri-reforming of methane over nickele–alumina aerogel catalyst," *Journal of Molecular Catalysis A: Chemical*, vol. 410, pp. 74-80, 2015.

[4] H. Wang, X. Wang, M. Li, S. Li, S. Wang and X. Ma, "Thermodynamic analysis of hydrogen production from glycerol autothermal reforming," *International Journal of Hydrogen Energy*, vol. 34, no. 14, pp. 5683-5690, 2009.

[5] EG&G Technical Services, Inc., "Fuel Cell Handbook (Seventh Edition)," National Technical Information Service, U.S. Department of Commerce, Springfield, 2004.

[6] A. Sgobbi, W. Nijs, R. DeMiglio, A. Chiodi, M. Gargiulo and C. Thiel, "How far away is hydrogen? Its role in the medium and long-term decarbonisation of the European energy system," *International Journal of Hydrogen Energy*, vol. 41, no. 1, pp. 19-35, 2016.

[7] C. Azenha, C. Mateos-Pedrero, S. Queirós, P. Concepción and A. Mendes, "Innovative ZrO2-supported CuPd catalysts for the selective production of hydrogen from methanol steam reforming," *Appllied Catalysis B: Environmental*, vol. 203, pp. 400-407, 2017.

[8] X. Xu, S. Zhang, X. Wang and P. Li, "Fuel adaptability study of a lab-scale 2.5 kWth autothermal reformer," *International Journal of Hydrogen Energy*, vol. 40, no. 21, pp. 6798-6808, 2015.

[9] X. Karatzas, M. Nilsson, J. Dawody, B. Lindström and L. J. Pettersson, "Characterization and optimization of an autothermal diesel and jet fuel reformer for 5 kWe mobile fuel cell applications," *Chemical Engineering Journal*, vol. 156, no. 2, pp. 366-379, 2010.

[10] L. Shi and D. J. Bayless, "Analysis of jet fuel reforming for solid oxide fuel cell applications in auxiliary power units," *International Journal of Hydrogen Energy*, vol. 33, no. 3, pp. 1067-1075, 2008.

[11] P. Dinka and A. S. Mukasyan, "Perovskite catalysts for the auto-reforming of sulfur containing fuels," *Journal of Power Sources,* vol. 167, no. 2, pp. 472-481, 2007.

[12] J. Turner, G. Sverdrup, M. K. Mann, P.-C. Maness, B. Kroposki, M. Ghirardi, R. J. Evans and D. Blake, "Renewable hydrogen production," *International Journal of Energy Research,* vol. 32, pp. 379-407, 2008.

[13] M. S. Ìzgi, Ö. Sahin and C. Saka, "Hydrogen production from NaBH4 using Co—Cu—B catalysts prepared in methanol: Effect of plasma treatment," *International Journal of Hydrogen Energy*, vol. 41, no. 3, pp. 1600-1608, 2016.

[14] U.S. Office of Energy Efficiency & Renewable Energy, [Online]. Available: https://www.energy.gov/eere/fuelcells/hydrogen-production-natural-gas-reforming. [Accessed 8 3 2018].

[15] A. Arregi, G. Lopez, M. Amutio, M. Artetxe, I. Barbarias, J. Bilbao and M. Olazar, "Role of operating conditions in the catalyst deactivation in the in-line steam reforming of volatiles from biomass fast pyrolysis," *Fuel,* vol. 216, pp. 233-244, 2018.

[16] C. Dixon, S. Reynolds and D. Rodley, "Micro/small wind turbine power control for electrolysis applications," *Renewable Energy*, vol. 87, pp. 182-192, 2016.

[17] M. B. Chowdhury, M. Z. Hossain, J. Mazumder and A. K. Jhawar, "La-based catalysts to enhance hydrogen production during supercritical water gasification of glucose," *Fuel*, vol. 217, pp. 166-174, 2018.

[18] S. Kubo, H. Nakajima, S. Kasahara, S. Higashi, T. Masaki, H. Abe and K. Onuki, "A demonstration study on a closed-cycle hydrogen production by the thermochemical water-splitting iodine–sulfur process," *Nuclear Engineering and Design,* vol. 233, no. 1-3, pp. 347-354, 2004.

[19] A. Madhumitha, V. Preethi and S. Kanmani, "Photocatalytic hydrogen production using TiO2 coated iron-oxide core shell particles," *International Journal of Hydrogen Energy*, vol. 43, no. 8, pp. 3946-3956, 2018.

[20] H. T. Hwang and A. Varma, "Hydrogen storage for fuel cell vehicles," *Current Opinion in Chemical Engineering*, vol. 5, pp. 42-48, 2014.

[21] C. Yang and J. Ogden, "Determining the lowest-cost hydrogen delivery mode," *International Journal of Hydrogen Energy,* vol. 32, no. 2, pp. 268-286, 2007.

[22] A. Shukla, S. Karmakar and R. B. Biniwale, "Hydrogen delivery through liquid organic hydrides: Considerations for a potential technology," *International Journal of Hydrogen Energy,* vol. 37, no. 4, pp. 3719-3726, 2012.

[23] K. Liu, C. Song and V. Subramani, Hydrogen and Syngas Production and Purification Technologies, Hoboken: John Wiley & Sons, Inc., 2009.

[24] S. Zhang, X. Xu, X. Wang and P. Li, "Hydrogen production via catalytic autothermal reforming of desulfurized Jet-A fuel," *International Journal of Hydrogen Energy,* vol. 42, no. 4, pp. 1932-1941, 2017.

[25] G. Han, S. Lee and J. Bae, "Diesel autothermal reforming with hydrogen peroxide for low-oxygen environments," *Applied Energy,* vol. 156, pp. 99-106, 2015.

[26] Chevron Corporation, "Aviation Fuels Technical Review," 2006.

[27] D. Lawicki, "Jet Fuel Characteristics," 2002.

[28] B. Lenz and T. Aicher, "Catalytic autothermal reforming of Jet fuel," *Journal of Power Sources,* vol. 149, pp. 44-52, 2005.

[29] J. K. Dunleavy, "Sulfur as a Catalyst Poison," *Platinum Metals Review,* vol. 50, no. 2, p. 110, 2006.

[30] J. Divisek, H. F. Oetjen, V. Peinecke, V. M. Schmidt and U. Stimming, "Components for PEM fuel cell systems using hydrogen and CO containing fuels," *Electrochimica Acta,* vol. 43, no. 24, pp. 3811-3815, 1998.

[31] R. Scenna and A. K. Gupta, "Partial oxidation of JP8 in a well-insulated distributed reactor," *Fuel Processing Technology,* vol. 142, pp. 174-181, 2016.

[32] N. H. Behling, Fuel Cells, Elsevier, 2013.

[33] W. Zhu and S. Deevi, "A review on the status of anode materials for solid oxide fuel cells," *Materials Science and Engineering: A,* vol. 362, no. 1-2, pp. 228-239, 2003.

[34] S. M. Haile, "Materials for fuel cells," *Materials Today,* vol. 6, no. 3, pp. 24-29, 2003.

[35] D. K. Niakolas, M. Daletou, S. G. Neophytides and C. G. Vayenas, "Fuel cells are a commercially viable alternative for the production of “clean” energy," *Ambio*, Vols. 45, Supplement 1, pp. 32-37, 2016.

[36] K. R. Williams, "Francis Thomas Bacon, 21 December 1904 - 24 May 1992," *Biographical Memoirs of Fellows of The Royal Society*, pp. 1-18, 1994.

[37] G. F. McLean, T. Niet, S. Prince-Richard and N. Djilali, "An assessment of alkaline fuel cell technology," *International Journal of Hydrogen Energy*, vol. 27, no. 5, pp. 507-526, 2002.

[38] K. Scott and A. K. Shukla, "Polymer electrolyte membrane fuel cells: Principles and advances," *Reviews in Environmental Science and Bio/Technology*, vol. 3, no. 3, pp. 273-280, 2004.

[39] S. Basu, Recent Trends in Fuel Cell Science and Technology, New Delhi, India: Anamaya, 2007.

[40] R. M. Ormerod, "Solid oxide fuel cells," *The Royal Society of Chemistry*, vol. 32, pp. 17-28, 2003.

[41] R. Dervisoglu, "WIKIPEDIA_Fuel cell," [Online]. Available: https://en.wikipedia.org/wiki/Fuel_cell. [Accessed 11 3 2018].

[42] J. D. Holladay, Y. Wang and E. Jones, "Review of Developments in Portable Hydrogen Production Using Microreactor Technology," *Chemical Reviews*, vol. 104, pp. 4767-4790, 2004.

[43] M. Usman, W. W. Daud and H. F. Abbas, "Dry reforming of methane: Influence of process parameters—A review," *Renewable and Sustainable Energy Reviews*, vol. 45, pp. 710-744, 2015.

[44] J. R. Nielsen, "Steam reforming of hydrocarbons. A historical perspective," *Studies in Surface Science and Catalysis*, vol. 147, pp. 121-126, 2004.

[45] P. Nikolaidis and A. Poullikkas, "A comparativeoverviewofhydrogenproductionprocesses," *RenewableandSustainableEnergyReviews*, vol. 67, pp. 597-611, 2017.

[46] I. Dincer and C. Acar, "Review and evaluation of hydrogen production methods for better sustainability," *International Journal of Hydrogen Energy*, vol. 40, no. 34, pp. 11094-11111, 2015.

[47] d. S. C.R.H, Partial oxidation of methane to synthesis gas : reaction kinetics and reactor modelling, Eindhoven: Technische Universiteit Eindhoven, 2000.

[48] K. Supat, S. Chavadej, L. L. Lobban and R. G. Mallinson, "Combined Steam Reforming and Partial Oxidation of Methane to Synthesis Gas under Electrical Discharge," *Industrial & Engineering Chemistry Research,* vol. 42, no. 8, pp. 1654-1661, 2..3.

[49] S. Pruksawan, B. Kitiyanan and R. M. Ziff, "Partial oxidation of methane on a nickel catalyst: Kinetic Monte-Carlo simulation study," *Chemical Engineering Science,* vol. 147, pp. 128-136, 2.16.

[50] Q. Ming, T. Healey, L. Allen and P. Irving, "Steam reforming of hydrocarbon fuels," *Catalysis Today,* vol. 77, pp. 51-64, 2002.

[51] J. Biswas, G. M. Bickle, P. G. Gray, D. D. Do and J. Barbier, "The Role of Deposited Poisons and Crystallite Surface Structure in the Activity and Selectivity of Reforming Catalysts," *Catalysis Reviews: Science and Engineering,* vol. 30, no. 2, pp. 161-247, 1988.

[52] A. L. Wagner, R. S. Osborne and J. P. Wagner, "Prediction of Deactivation Rates and Mechanisms of Reforming Catalysts," *Preprints of Papers - American Chemical Society Division of Fuel Chemistry,* vol. 48, no. 2, pp. 748-749, 2003.

[53] J. Koningen and K. Sjöström, "Sulfur-Deactivated Steam Reforming of Gasified Biomass," *Industrial & Engineering Chemistry Research,* vol. 37, no. 2, pp. 341-346, 1998.

[54] Y. Chen, C. Xie, Y. Li, C. Song and T. B. Bolin, "Sulfur poisoning mechanism of steam reforming catalysts: an X-ray absorption near edge structure (XANES) spectroscopic study," *Physical Chemistry Chemical Physics,* vol. 12, pp. 5707-5711, 2010.

[55] A. Simson, S. Crowley and M. J. Castaldi, "The Impact of Sulfur on Ethanol Steam Reforming," *Catalysis Letters,* vol. 146, no. 8, pp. 1361-1372, 2016.

[56] A. Shamsi, J. P. Baltrus and J. J. Spivey, "Characterization of coke deposited on Pt/alumina catalyst during reforming of liquid hydrocarbons," *Applied Catalysis A: General,* vol. 293, pp. 145-152, 2005.

[57] I. Barbarias, G. Lopez, M. Amutio, M. Artetxe, J. Alvarez, A. Arregi, J. Bilbao and M. Olazar, "Steam reforming of plastic pyrolysis model hydrocarbons and catalyst deactivation," *Applied Catalysis A: General,* vol. 527, pp. 152-160, 2016.

[58] E. Silveira, R. Rabelo-Neto and F. Noronha, "Steam reforming of toluene, methane and mixtures over Ni/ZrO2 catalysts," *Catalysis Today,* vol. 289, pp. 289-301, 2017.

[59] J. Sehested, "Four challenges for nickel steam-reforming catalysts," *Catalysis Today,* vol. 111, pp. 103-110, 2006.

[60] H. J. Setzer, S. Karavolis and J. A. Bett, "Steam Reforming Catalyst". US Patent 4,755,498, 5 Jul. 1988.

[61] Q. Ming, T. Healey and P. M. Irving, "Hydrocarbon fuel reforming catalyst and use thereof". US Patent 7067453, 15 Jul. 2002.

[62] T. Suzuki, H.-i. Iwanami and T. Yoshinari, "Steam reforming of kerosene on Ru/Al2O3 catalyst to yield hydrogen," *International Journal of Hydrogen Energy,* vol. 25, pp. 119-126, 2000.

[63] A. C. McCoy, M. J. Duran, A.-M. Azad, S. Chattopadhyay and M. A. Abraham, "Performance of Sulfur Tolerant Reforming Catalysts for Production of Hydrogen from Jet Fuel Simulants," *Energy & Fuels,* vol. 21, pp. 3513-3519, 2007.

[64] S. L. Lakhapatri, "Analysis of Deactivation Mechanism on a Multi-Component Sulfur-Tolerant Steam Reforming Catalyst," The University of Toledo, 2010.

[65] J. J. Strohm, J. Zheng and C. Song, "Low-temperature steam reforming of jet fuel in the absence and presence of sulfur over Rh and Rh–Ni catalysts for fuel cells," *Journal of Catalysis,* vol. 238, pp. 309-320, 2006.

[66] L. Wang, K. Murata and M. Inaba, "Development of novel highly active and sulphur-tolerant catalysts for steam reforming of liquid hydrocarbons to produce hydrogen," *Applied Catalysis A: General,* vol. 257, pp. 43-47, 2004.

[67] K. Sato and K. Fujimoto, "Development of new nickel based catalyst for tar reforming with superior resistance to sulfur poisoning and coking in biomass gasification," *Catalysis Communications,* vol. 8, no. 11, pp. 1697-1701, 2007.

[68] L.-Y. Hou, X.-X. Zhang and Z.-Y. Ren, "Coke suppression of kerosene by wall catalytic steam reforming," *Fuel Processing Technology,* vol. 154, pp. 117-122, 2016.

[69] L. F. Albright and J. C. Marek, "Coke Formation during Pyrolysis: Roles of Residence Time, Reactor Geometry, and Time of Operation," *Industrial & Engineering Chemistry Research*, vol. 27, no. 5, pp. 743-751, 1988.

[70] J. A. Liu, "Kinetics, catalysis and mechanism of methane steam reforming," WORCESTER POLYTECHNIC INSTITUTE, 2006.

[71] A. N. Fatsikostas, D. Kondarides and X. E. Verykios, "Production of hydrogen for fuel cells by reformation of biomass-derived ethanol," *Catalysis Today*, vol. 75, pp. 145-155, 2002.

[72] M. Nurunnabi, Y. Mukainakano, S. Kado, B. Li, K. Kunimori, K. Suzuki, K.-i. Fujimoto and K. Tomishige, "Additive effect of noble metals on NiO-MgO solid solution in oxidative steam reforming of methane under atmospheric and pressurized conditions," *Applied Catalysis A: General*, vol. 299, pp. 145-156, 2006.

[73] V. S. Guggilla, J. Akyurtlu, A. Akyurtlu and I. Blankson, "Steam Reforming of n-Dodecane over Ru-Ni-Based Catalysts," *Industrial & Engineering Chemistry Research*, vol. 49, pp. 8164-8173, 2010.

[74] B. Hua, M. Li, J.-l. Luo, J. Pu, B. Chi and J. Li, "Carbon-resistant Ni-Zr0.92Y0.08O2-d supported solid oxide fuel cells using Ni-Cu-Fe alloy cermet as on-cell reforming catalyst and mixed methane-steam as fuel," *Journal of Power Sources*, vol. 303, pp. 340-346, 2016.

[75] I. García-García, E. Acha, K. Bizkarra, J. Martínez de Ilarduya, J. Requies and J. Cambra, "Hydrogen production by steam reforming of m-cresol, a bio-oil model compound, using catalysts supported on conventional and unconventional supports," *International Journal of Hydrogen Energy*, vol. 40, no. 42, pp. 14445-14455, 2015.

[76] E. M. A. J. M. A. Ananda Vallezi Paladino Lino, "Hydrotalcites derived catalysts for syngas production from biogas reforming: Effect of nickel and cerium load," *Catalysis Today*, vol. 289, pp. 78-88, 2017.

[77] M. Muñoz, S. Moreno and R. Molina, "Promoter effect of Ce and Pr on the catalytic stability of the Ni-Cosystem for the oxidative steam reforming of ethanol," *Applied Catalysis A: General*, vol. 526, pp. 84-94, 2016.

[78] V. L. Dagle, R. Dagle, L. Kovarik, A. Genc, Y.-G. Wang, M. Bowden, H. Wan, M. Flake, V.-A. Hlezakou, D. L. King and R. Rousseau, "Steam reforming of hydrocarbons from biomass-derived syngas over MgAl2O4-supported transition

metals and bimetallic IrNi catalysts," *Applied Catalysis B: Environmental,* vol. 184, pp. 142-152, 2016.

[79] H. Wu, V. La Parola, G. Pantaleo, F. Puleo, A. M. Venezia and L. F. Liotta, "Ni-Based Catalysts for Low Temperature Methane Steam Reforming: Recent Results on Ni-Au and Comparison with Other Bi-Metallic Systems," *catalysts,* vol. 3, pp. 563-583, 2013.

[80] L. Pastor-Pérez and A. Sepúlveda-Escribano, "Low temperature glycerol steam reforming on bimetallic PtSn/C catalysts: On the effect of the Sn content," *Fuel,* vol. 194, pp. 222-228, 2017.

[81] L. Dong, C. Wu, H. Ling, J. Shi, P. T. Williams and J. Huang, "Promoting hydrogen production and minimizing catalyst deactivation from the pyrolysis-catalytic steam reforming of biomass on nanosized NiZnAlOx catalysts," *Fuel,* vol. 188, pp. 610-620, 2017.

[82] Z. Zhang, X. Hu, J. Li, G. Gao, D. Dong, R. Westerhof, S. Hu, J. Xiang and Y. Wang, "Steam reforming of acetic acid over Ni/Al2O3 catalysts: Correlation of nickel loading with properties and catalytic behaviors of the catalysts," *Fuel,* vol. 217, pp. 389-403, 2018.

[83] P. Jasso, M. Torres, F. Tzompanzi and M. Asomoza, "Nanostructured Carbon on Steam Reforming Catalysts," *Journal of New Materials for Electrochemical Systems,* vol. 11, pp. 95-98, 2008.

[84] R. GU, G. ZENG, J. SHAO, Y. LIU, J. W. Schwank and Y. LI, "Sustainable H2 production from ethanol steam reforming over a macro-mesoporous Ni/Mg-Al-O catalytic monolith," *Frontiers of Chemical Science and Engineering,* vol. 7, no. 3, pp. 270-278, 2013.

[85] M. Menor, S. Sayas and A. Chica, "Natural sepiolite promoted with Ni as new and efficient catalyst for the sustainable production of hydrogen by steam reforming of the biodiesel by-products glycerol," *Fuel,* vol. 193, pp. 351-358, 2017.

[86] A. Arregi, G. Lopez, M. Amutio, M. Artetxe, I. Barbarias, J. Bilbao and M. Olazar, "Role of operating conditions in the catalyst deactivation in the in-line steam reforming of volatiles from biomass fast pyrolysis," *Fuel,* vol. 216, pp. 233-244, 2018.

[87] A. C. Basagiannis and X. E. Verykios, "Steam reforming of the aqueous fraction of bio-oil over structured Ru/MgO/Al2O3 catalysts," *Catalysis Today,* vol. 127, pp. 256-264, 2007.

[88] A. Haryanto, S. Fernando, N. Murali and S. Adhikari, "Current Status of Hydrogen Production Techniques by Steam Reforming of Ethanol: A Review," *Energy & Fuels,* vol. 19, pp. 2098-2106, 2005.

[89] M. Lazar, M. Mihet, M. Dan, V. Almasan and P. Marginean, "Preparation and characterization of nickel based multicomponent catalysts," *Journal of Physics: Conference Series,* vol. 182, 2009.

[90] W.-S. Dong, H.-S. Roh, K.-W. Jun, S.-E. Park and Y.-S. Oh, "Methane reforming over Ni/Ce-ZrO2 catalysts: effect of nickel content," *Applied Catalysis A: General,* vol. 226, pp. 63-72, 2002.

[91] T. Ohno, T. Masuda, S. Ochibe, S. Hirai, H. Suzuki, T. Arai, N. Sakamoto, N. Wakiya and T. Matsuda, "Effect of the reduction condition on the catalytic activity for steam reforming process using Ni doped LaAlO3 nano-particles," *Advanced Powder Technology,* vol. 27, no. 1, pp. 179-183, 2016.

[92] K. Qian and A. Kumar, "Catalytic reforming of toluene and naphthalene (model tar) by char supported nickel catalyst," *Fuel,* vol. 187, pp. 128-136, 2017.

[93] X. Yu, S. Zhang, L. Wang, Q. Jiang, S. Li and Z. Tao, "Hydrogen production from steam reforming of kerosene over Ni–La and Ni–La–K/cordierite catalysts," *Fuel,* vol. 85, pp. 1708-1713, 2006.

[94] J. Peng, Y. Wang, Q. Zhao, S. Ye and W. G. Wabg, "Steam Reforming of Methane using Ni-based Monolith Catalyst in Solid Oxide Fuel Cell System," in *10th European SOFC Forum*, Lucerne, Switzeland, 2012.

[95] J. Zhao, Y. Yu, X. Han and H. He, "Fuel reforming over Ni ' based catalysts coupled with selective catalytic reduction of NOx," *Chinese Journal of Catalysis,* vol. 34, pp. 1407-1417, 2013.

[96] Y. Matsumura, "Durable Cu composite catalyst for hydrogen production by high temperature methanol steam reforming," *Journal of Power Sources,* vol. 272, pp. 961-969, 2014.

[97] F. Fan, Q. Zhang, X. Wang, Y. Ni, Y. Wu and Z. Zhu, "A structured Cu-based/c-Al_2O_3/Al plate-type catalyst for steam reforming of dimethyl ether: Self-activation behavior investigation and stability improvement," *Fuel*, vol. 186, pp. 11-19, 2016.

[98] W. Zhou, Y. Ke, Q. Wang, S. Wan, J. Lin, J. Zhang and K. Hui, "Development of cylindrical laminated methanol steam reforming microreactor with cascading metal foams as catalyst support," *Fuel*, vol. 191, pp. 46-53, 2017.

[99] F. L. Carvalho, Y. J. Asencios, J. D. Bellido and E. M. Assaf, "Bio-ethanol steam reforming for hydrogen production over Co3O4/CeO2 catalysts synthesized by one-step polymerization method," *Fuel Processing Technology*, vol. 142, pp. 182-191, 2016.

[100] N. Yu, H. Zhang, S. D. Davidson, J. Sun and Y. Wang, "Effect of ZnO facet on ethanol steam reforming over Co/ZnO," *Catalysis Communications*, vol. 73, pp. 93-97, 2016.

[101] D. K. Liguras, D. I. Kondarides and X. E. Verykios, "Production of hydrogen for fuel cells by steam reforming of ethanol over supported noble metal catalysts," *Applied Catalysis B: Environmental*, vol. 43, pp. 345-354, 2003.

[102] M. Wichert, R. Zapf, A. Ziogas, G. Kolb and E. Klemm, "Kinetic Investigations of the Steam Reforming of Methanol over a Pt/In2O3/Al2O3 Catalyst in Microchannels," *Chemical Engineering Science*, vol. 155, pp. 201-209, 2016.

[103] Y. Li, X. Wang and C. Song, "Spectroscopic characterization and catalytic activity of Rh supported on CeO2-modified Al2O3 for low-temperature steam reforming of propane," *Catalysis Today*, vol. 263, pp. 22-34, 2016.

[104] P. v. Beurden, "ON THE CATALYTIC ASPECTS OF STEAM-METHANE REFORMING," 2004.

[105] M. Andersson, H. Paradis, J. Yuan and B. Sundén, "Review of catalyst materials and catalytic steam reforming reactions in SOFC anodes," *International Journal of Energy Research*, vol. 35, pp. 1340-1350, 2011.

[106] J. Xu and G. F. Froment, "Methane Steam Reforming, Methanation and Water-Gas Shift: 1. Intrinsic Kinetics," *AIChE Journal*, vol. 35, no. 1, pp. 88-96, 1989.

[107] J. A. Liu, "Kinetics, catalysis and mechanism of methane steam reforming," 2006.

[108] W. Nabgan, R. Mat, T. A. T. Abdullah, B. Nabgan, Y. Gambo and Z. Y. Zakaria, "Development of a kinetic model for hydrogen production from phenol over Ni-

Co/ZrO2 catalyst," *Journal of Environmental Chemical Engineering,* vol. 4, pp. 4444-4452, 2016.

[109] M. PRETT, C. EICHNE and M. PERRIN, "THE CATALYTIC OXIDATION OF METHANE TO CARBON MONOXIDE AND HYDROGEN," *Transactions of the Faraday Society,* vol. 42, pp. 335b-339, 1946.

[110] K. H. Delgado, L. Maier, S. Tischer, A. Zellner, H. Stotz and O. Deutschmann, "Surface Reaction Kinetics of Steam- and CO2-Reforming as Well as Oxidation of Methane over Nickel-Based Catalysts," *Catalysts,* vol. 5, pp. 871-904, 2015.

[111] N. Burke and D. Trimm, "Coke formation during high pressure catalytic partial oxidation of methane to syngas," *Reaction Kinetics and Catalysis Letters,* vol. 84, no. 1, pp. 137-142, 2005.

[112] A. M. De Groote and G. F. Froment, "The role of coke formation in catalytic partial oxidation for synthesis gas production," *Catalysis Today,* vol. 37, no. 3, pp. 309-329, 1997.

[113] S. Sengodan, R. Lan, J. Humphreys, D. Du, W. Xu, H. Wang and S. Tao, "Advances in reforming and partial oxidation of hydrocarbons for hydrogen production and fuel cell applications," *Renewable and Sustainable Energy Reviews,* vol. 82, pp. 761-780, 2018.

[114] V. A. Tsipouriari, Z. Zhang and X. Verykios, "Catalytic Partial Oxidation of Methane to Synthesis Gas over Ni-Based Catalysts. I. Catalyst Performance Characteristics," *Journal of Catalysis,* vol. 179, pp. 283-291, 1998.

[115] R. Jin, Y. Chen, W. Li, W. Cui, Y. Ji, C. Yu and Y. Jiang, "Mechanism for catalytic partial oxidation of methane to syngas over a Ni/Al2O3 catalyst," *Applied Catalysis A: General,* vol. 201, pp. 71-80, 2000.

[116] T. Shishido, M. Sukenobu, H. Morioka, M. Kondo, Y. Wang, K. Takaki and K. Takehira, "Partial oxidation of methane over Ni/Mg-Al oxide catalysts prepared by solid phase crystallization method from Mg-Al hydrotalcite-like precursors," *Applied Catalysis A: General,* vol. 223, pp. 35-42, 2002.

[117] J. Barbero, M. Peña, J. Campos-Martin, J. Fierro and P. Arias, "Support effect in supported Ni catalysts on their performance for methane partial oxidation," *Catalysis Letters,* vol. 87, pp. 211-218, 2003.

[118] H. Özdemir, M. F. Öksüzömer and M. A. Gürkaynak, "Preparation and characterization of Ni based catalysts for the catalytic partial oxidation of methane:

Effect of support basicity on H2/CO ratio and carbon deposition," *International Journal of Hydrogen Energy*, vol. 35, pp. 12147-12160, 2010.

[119] R. K. Singha, A. Shukla, A. Yadav, L. S. Konathala and R. Bal, "Effect of metal-support interaction on activity and stability of Ni-CeO2 catalyst for partial oxidation of methane," *Applied Catalysis B: Environmental,* vol. 202, pp. 473-488, 2017.

[120] B. C. Enger, R. Lødeng and A. Holmen, "A review of catalytic partial oxidation of methane to synthesis gas with emphasis on reaction mechanisms over transition metal catalysts," *Applied Catalysis A: General,* vol. 346, pp. 1-27, 2008.

[121] M. Itome and A. E. Nelson, "Methane oxidation over M–8YSZ and M–CeO2/8YSZ (M=Ni, Cu, Co, Ag) catalysts," *Catalysis Letters,* vol. 106, pp. 21-27, 2006.

[122] S. H. Oh, P. J. Mitchell and R. M. Siewert, "Methane Oxidation over Alumina-Supported Noble Metal Catalysts with and without Cerium Additives," *Journal of Catalysis,* vol. 132, pp. 287-301, 1991.

[123] L. Majocchi, G. Groppi, C. Cristiani, P. Forzatti, L. Basini and A. Guarinoni, "Partial oxidation of methane to synthesis gas over Rh-hexaaluminate-based catalysts," *Catalysis Letters,* vol. 65, pp. 49-56, 2000.

[124] S. Eriksson, M. Nilsson, M. Boutonnet and S. Järås, "Partial oxidation of methane over rhodium catalysts for power generation applications," *Catalysis Today,* vol. 100, pp. 447-451, 2005.

[125] F. Akhlaghian, J. Towfighi and A. Mohajeri, "Partial oxidation of methane on Rh/TiO2 catalysts: Effects of the titania precursor and the presence of tungsten oxide," *Scientia Iranica,* vol. 19, no. 6, pp. 1608-1615, 2012.

[126] R. Horn, K. Williams, N. Degenstein and L. Schmidt, "Syngas by catalytic partial oxidation of methane on rhodium: Mechanistic conclusions from spatially resolved measurements and numerical simulations," *Journal of Catalysis,* vol. 242, pp. 92-102, 2006.

[127] A. Bitsch-Larsen, N. Degenstein and L. Schmidt, "Effect of sulfur in catalytic partial oxidation of methane over Rh–Ce coated foam monoliths," *Applied Catalysis B: Environmental,* vol. 78, pp. 364-370, 2008.

[128] R. Torbati, S. Cimino, L. Lisi and G. Russo, "The Effect of Support on Sulphur Tolerance of Rh Based Catalysts for Methane Partial Oxidation," *Catalysis Letters,* vol. 127, pp. 260-269, 2009.

[129] S. Cimino and L. Lisi, "Impact of Sulfur Poisoning on the Catalytic Partial Oxidation of Methane on Rhodium-Based Catalysts," *Industrial & Engineering Chemistry Research,* vol. 51, pp. 7459-7466, 2012.

[130] J. J. Krummenacher, K. N. West and L. D. Schmidt, "Catalytic partial oxidation of higher hydrocarbons at millisecond contact times: decane, hexadecane, and diesel fuel," *Journal of Catalysis,* vol. 215, pp. 332-343, 2003.

[131] D. Shekhawat, T. H. Gardner, D. A. Berry, M. Salazar, D. J. Haynes and J. J. Spivey, "Catalytic partial oxidation of n-tetradecane in the presence of sulfur or polynuclear aromatics: Effects of support and metal," *Applied Catalysis A: General,* vol. 311, pp. 8-16, 2006.

[132] D. J. Haynes, D. A. Berry, D. Shekhawat and J. J. Spivey, "Catalytic partial oxidation of n-tetradecane using pyrochlores: Effect of Rh and Sr substitution," *Catalysis Today,* vol. 136, pp. 206-213, 2008.

[133] D. J. Haynes, D. A. Berry, D. Shekhawat and J. J. Spivey, "Catalytic partial oxidation of n-tetradecane using Rh and Sr substituted pyrochlores: Effects of sulfur," *Catalysis Today,* vol. 145, pp. 121-126, 2009.

[134] A. F. Ibarreta and C.-J. Sung, "Optimization of Jet-A fuel reforming for aerospace applications," *International Journal of Hydrogen Energy,* vol. 31, pp. 1066-1078, 2006.

[135] M. Usman, W. W. Daud and H. F. Abbas, "Dry reforming of methane: Influence of process parameters—A review," *Renewable and Sustainable Energy Reviews,* vol. 45, pp. 710-744, 2015.

[136] F. Polo-Garzon, M. He and D. A. Bruce, "Ab initio derived reaction mechanism for the dry reforming of methane on Rh doped pyrochlore catalysts," *Journal of Catalysis,* vol. 333, pp. 59-70, 2016.

[137] T. Hayakawa, S. Suzuki, J. Nakamura, T. Uchijima, S. Hamakawa, K. Suzuki, T. Shishido and K. Takehira, "CO2 reforming of CH4 over Ni/perovskite catalysts prepared by solid phase crystallization method," *Applied Catalysis A: General,* vol. 183, pp. 273-285, 1999.

[138] E. Akbari, S. M. Alavi and M. Rezaei, "Synthesis gas production over highly active and stable nanostructured NiAMgOAAl2O3 catalysts in dry reforming of methane: Effects of Ni contents," *Fuel,* vol. 194, pp. 171-179, 2017.

[139] F. Wang, L. Xu and W. Shi, "Syngas production from CO2 reforming with methane over core-shell Ni@SiO2 catalysts," *Journal of CO2 Utilization,* vol. 16, pp. 318-327, 2016.

[140] Y. Lu, D. Guo, Y. Ruan, Y. Zhao, S. Wang and X. Ma, "Facile one-pot synthesis of Ni@HSS as a novel yolk-shell structure catalyst for dry reforming of methane," *Journal of CO2 Utilization,* vol. 24, pp. 190-199, 2018.

[141] L. Barelli, G. Bidini, G. Cinti, F. Gallorini and M. Pöniz, "SOFC stack coupled with dry reforming," *Applied Energy,* vol. 192, pp. 498-507, 2017.

[142] H. Setiabudi, C. Chong, S. Abed, L. Teh and S. Chin, "Comparative study of Ni-Ce loading method: Beneficial effect of ultrasonic-assisted impregnation method in CO2 reforming of CH4 over Ni-Ce/SBA-15," *Journal of Environmental Chemical Engineering,* vol. 6, pp. 745-753, 2018.

[143] B. Zhao, B. Yan, S. Yao, Z. Xie, Q. Wu, R. Ran, D. Weng, C. Zhang and J. G. Chen, "LaFe0.9Ni0.1O3 perovskite catalyst with enhanced activity and coke-resistance for dry reforming of ethane," *Journal of Catalysis,* vol. 358, pp. 168-178, 2018.

[144] O. Daoura, M.-N. Kaydouh, N. El-Hassan, P. Massiani, F. Launay and M. Boutros, "Mesocellular silica foam-based Ni catalysts for dry reforming of CH4 (by CO2)," *Journal of CO2 Utilization,* vol. 24, pp. 112-119, 2018.

[145] D. Y. Kalai, K. Stangeland, Y. Jin and Z. Yu, "Active and stable hydrotalcite derived Ni catalysts for CO2 reforming of methane: Comparison with catalysts by incipient wetness," *Journal of CO2 Utilization,* 2018.

[146] W. Jóźwiak, M. Nowosielska and J. Rynkowski, "Reforming of methane with carbon dioxide over supported bimetallic catalysts containing Ni and noble metal I. Characterization and activity of SiO2 supported Ni–Rh catalysts," *Applied Catalysis A: General,* vol. 280, pp. 233-244, 2005.

[147] I. Luisetto, C. Sarno, D. De Felicis, F. Basoli, C. Battocchio, S. Tuti, S. Licoccia and E. Di Bartolomeo, "Ni supported on γ-Al2O3 promoted by Ru for the dry reforming of methane in packed and monolithic reactors," *Fuel Processing Technology,* vol. 158, pp. 130-140, 2017.

[148] C. Egawa, "Methane dry reforming reaction on Ru(0 0 1) surfaces," *Journal of Catalysis,* vol. 358, pp. 35-42, 2018.

[149] J. M. Saad and P. T. Williams, "Pyrolysis-catalytic dry (CO2) reforming of waste plastics for syngas production: Influence of process parameters," *Fuel,* vol. 193, pp. 7-14, 2017.

[150] R. Amin, B. Liu, Z. B. Huang and Y. C. Zhao, "Hydrogen and syn gas production via CO2 dry reforming of methane over Mg/La promoted CoeNi/ MSU-S catalyst," *International Journal of Hydrogen Energy,* vol. 41, no. 2, pp. 807-819, 2016.

[151] C. Rhodes, G. Hutchings and A. Ward, "Water-gas shift reaction: finding the mechanistic boundary," *Catalysis Today,* vol. 23, no. 1, pp. 43-58, 1995.

[152] S. Ahmed, R. Ahluwalia, S. Lee and S. Lottes, "A gasoline fuel processor designed to study quick-start performance," *Journal of Power Sources,* vol. 154, no. 1, pp. 214-222, 2006.

[153] M. V. Gil, J. Fermoso, C. Pevida, D. Chen and F. Rubiera, "Production of fuel-cell grade H2 by sorption enhanced steam reforming of acetic acid as a model compound of biomass-derived bio-oil," *Applied Catalysis B: Environmental,* vol. 184, pp. 64-76, 2016.

[154] R. Elshout, "HYDROGEN PRODUCTION BY STEAM REFORMING," 1 May 2010. [Online]. Available: http://www.chemengonline.com/hydrogen-production-by-steam-reforming/?printmode=1. [Accessed 23 March 2018].

[155] C. Dang, H. Wang, H. Yu and F. Peng, "Co-Cu-CaO catalysts for high-purity hydrogen from sorption-enhanced steam reforming of glycerol," *Applied Catalysis A: General,* vol. 533, pp. 9-16, 2017.

[156] B. Jiang, B. Dou, K. Wang, C. Zhang, M. Li, H. Chen and Y. Xu, "Sorption enhanced steam reforming of biodiesel by-product glycerol on Ni-CaO-MMT multifunctional catalysts," *Chemical Engineering Journal,* vol. 313, pp. 207-216, 2017.

[157] A. Lysikov, V. Derevschikov and A. Okunev, "Sorption-enhanced reforming of bioethanol in dual fixed bed reactor for continuous hydrogen production," *International Journal of Hydrogen Energy,* vol. 40, pp. 14436-14444, 2015.

[158] F. Cheng, V. Dupont and M. V. Twigg, "Temperature-programmed reduction of nickel steam reforming catalyst with glucose," *Applied Catalysis A: General,* vol. 527, pp. 1-8, 2016.

[159] G. Diglio, P. Bareschino, E. Mancusi and F. Pepe, "Simulation of hydrogen production through chemical looping reforming process in a packed-bed reactor," *Chemical Engineering Research and Design,* vol. 105, pp. 137-151, 2016.

[160] Y. Shen, K. Zhao, F. He and H.-b. Li, "Synthesis of three-dimensionally ordered macroporous LaFe0.7Co0.3O3 perovskites and their performance for chemical-looping steam reforming of methane," *Journal of Fuel Chemistry and Technology,* vol. 44, no. 10, pp. 1168-1176, 2016.

[161] S. K. Thengane, A. Hoadley, S. Bhattacharya, S. Mitra and S. Bandyopadhyay, "Thermodynamic evaluation of chemical looping based nitric oxide and hydrogen production," *Chemical Engineering Research and Design,* vol. 132, pp. 252-275, 2018.

[162] T. Yabe, K. Mitarai, K. Oshima, S. Ogo and Y. Sekine, "Low-temperature dry reforming of methane to produce syngas in an electric field over La-doped Ni/ZrO2 catalysts," *Fuel Processing Technology,* vol. 158, pp. 96-103, 2017.

[163] T. Paulmier and L. Fulcheri, "Use of non-thermal plasma for hydrocarbon reforming," *Chemical Engineering Journal,* vol. 106, pp. 59-71, 2005.

[164] F. Wang, Z. Guan, J. Tan, Z. Yan and Y. Leng, "Unsteady state thermochemical performance analyses of solar driven steam methane reforming in porous medium reactor," *Solar Energy,* vol. 122, pp. 1180-1192, 2015.

[165] H. v. Storch, M. Roeb, H. Stadler, C. Sattler and B. Hoffschmidt, "Available online Efficiency potential of indirectly heated solar reforming with different types of solar air receivers," *Applied Thermal Engineering,* vol. 92, pp. 202-209, 2016.

[166] A. Seretis and P. Tsiakaras, "Hydrogenolysis of glycerol to propylene glycol by in situ produced hydrogen from aqueous phase reforming of glycerol over SiO2–Al2O3 supported nickel catalyst," *Fuel Processing Technology,* vol. 142, pp. 135-146, 2016.

[167] L. Li, H. Wang, X. Jiang, Z. Song, X. Zhao and C. Ma, "Microwave-enhanced methane combined reforming by CO2 and H2O into syngas production on biomass-derived char," *Fuel,* vol. 185, pp. 692-700, 2016.

[168] J. Yoo, Y. Bang, S. J. Han, S. Park, J. H. Song and I. K. Song, "Hydrogen production by tri-reforming of methane over nickel–alumina aerogel catalyst," *Journal of Molecular Catalysis A: Chemical,* vol. 410, pp. 74-80, 2015.

[169] B. Hua, M. Li, J.-l. Luo, J. Pu, B. Chi and J. Li, "Carbon-resistant Ni-Zr0.92Y0.08O2-d supported solid oxide fuel cells using Ni-Cu-Fe alloy cermet as on-cell reforming catalyst and mixed methane-steam as fuel," *Journal of Power Sources,* vol. 303, pp. 340-346, 2016.

[170] V. Kirubakaran, V. Sivaramakrishnan, R. Nalini, T. Sekar, M. Premalatha and P. Subramanian, "A review on gasification of biomass," *Renewable and Sustainable Energy Reviews,* vol. 13, no. 1, pp. 179-186, 2009.

[171] X. Fan, Z. Liu, J. M. Norbeck and C. S. Park, "A simple kinetic analysis of syngas during steam hydrogasification of biomass using a novel inverted batch reactor with instant high pressure feeding," *Bioresource Technology,* vol. 200, pp. 731-737, 2016.

[172] Q. Fu, Y. Huang, M. Niu, G. Yang and Z. Shao, "Experimental and predicted approaches for biomass gasification with enriched air–steam in a fluidised bed," *Waste Management & Research,* vol. 32, no. 10, pp. 988-996, 2014.

[173] Z. A. El-Rub, E. A. Bramer and G. Brem, "Review of Catalysts for Tar Elimination in Biomass Gasification Processes," *Industrial & Engineering Chemistry Research,* vol. 43, no. 22, pp. 6911-6919, 2004.

[174] S. Heidenreich and P. U. Foscolo, "New concepts in biomass gasification," *Progress in Energy and Combustion Science,* vol. 46, pp. 72-95, 2015.

[175] M. B. Chowdhury, M. Z. Hossain, J. Mazumder, A. K. Jhawar and P. A. Charpentier, "La-based catalysts to enhance hydrogen production during supercritical water gasification of glucose," *Fuel,* vol. 217, pp. 166-174, 2018.

[176] I. Behnia, Z. Yuan, P. Charpentier and C. Xu, "Production of methane and hydrogen via supercritical water gasification of renewable glucose at a relatively low temperature: Effects of metal catalysts and supports," *Fuel Processing Technology,* vol. 143, pp. 27-34, 2016.

[177] T. Riis, E. F. Hagen, P. J. S. Vie and Ø. Ulleberg, "HYDROGEN PRODUCTION R&D: PRIORITIES AND GAPS," INTERNATIONAL ENERGY AGENCY, Paris, 2006.

[178] X. Zou, Z. Ma, H. Liu, D. Chen, C. Wang, P. Zhang and T. Chen, "Green synthesis of Ni supported hematite catalysts for syngas production from catalytic cracking of toluene as a model compound of biomass tar," *Fuel,* vol. 217, pp. 343-351, 2018.

[179] A. M. Amin, E. Croiset and W. Epling, "Review of methane catalytic cracking for hydrogen production," *International Journal of Hydrogen Energy*, vol. 36, no. 4, pp. 2904-2935, 2011.

[180] B. Monnerat, L. Kiwi-Minsker and A. Renken, "Hydrogen production by catalytic cracking of methane over nickel gauze under periodic reactor operation," *Chemical Engineering Science,* vol. 56, pp. 633-639, 2001.

[181] T. Zhang and M. D. Amiridis, "Hydrogen production via the direct cracking of methane over silica-supported nickel catalysts," *Applied Catalysis A: General,* vol. 167, pp. 161-172, 1998.

[182] M. Ermakova, D. Ermakov and G. Kuvshinov, "Effective catalysts for direct cracking of methane to produce hydrogen and filamentous carbon Part I. Nickel catalysts," *Applied Catalysis A: General,* vol. 201, pp. 61-70, 2000.

[183] M. Carmo, D. L. Fritz, J. Mergel and D. Stolten, "A comprehensive review on PEM water electrolysis," *International Journal of Hydrogen Energy,* vol. 38, pp. 4901-4934, 2013.

[184] S. Grigoriev, V. Porembsky and V. Fateev, "Pure hydrogen production by PEM electrolysis for hydrogen energy," *International Journal of Hydrogen Energy,* vol. 31, pp. 171-175, 2006.

[185] J. Rossmeisl, Z.-W. Qu, H. Zhu, G.-J. Kroes and J. Nørskov, "Electrolysis of water on oxide surfaces," *Journal of Electroanalytical Chemistry,* vol. 607, no. 1-2, pp. 83-89, 2007.

[186] K. Zeng and D. Zhang, "Recent progress in alkaline water electrolysis for hydrogen production and applications," *Progress in Energy and Combustion Science,* vol. 36, no. 3, pp. 307-326, 2010.

[187] S. Abanades, A. Legal, A. Cordier, G. Peraudeau, G. Flamant and A. Julbe, "Investigation of reactive cerium-based oxides for H2 production by thermochemical two-step water-splitting," *Journal of Materials Science,* vol. 45, pp. 4163-4173, 2010.

[188] B. Xu, Y. Bhawe and M. E. Davis, "Low-temperature, manganese oxide-based, thermochemical water splitting cycle," *Proceedings of the National Academy of Sciences,* vol. 109, no. 24, pp. 9260-9264, 2012.

[189] C. N. R. Rao and S. Dey, "Solar thermochemical splitting of water to generate hydrogen," *Proceedings of the National Academy of Sciences,* vol. 114, no. 51, pp. 13385-13393, 2017.

[190] R. B. Diver, J. E. Miller, M. D. Allendorf, N. P. Siegel and R. E. Hogan, "Solar Thermochemical Water-Splitting Ferrite-Cycle Heat Engines," *Journal of Solar Energy Engineering,* vol. 130, pp. 1-8, 2008.

[191] T. Kodama, Y. Nakamuro and T. Mizuno, "A Two-Step Thermochemical Water Splitting by Iron-Oxide on Stabilized Zirconia," *Journal of Solar Energy Engineering,* vol. 128, pp. 3-7, 2006.

[192] N. Nakamura, H. Miyaoka, T. Ichikawa and Y. Kojima, "Hydrogen production via thermochemical water-splitting by lithium redox reaction," *Journal of Alloys and Compounds,* vol. 580, pp. S410-S413, 2013.

[193] V. Chakrapani, J. Thangala and M. K. Sunkara, "WO3 and W2N nanowire arrays for photoelectrochemical hydrogen production," *International Journal of Hydrogen Energy,* vol. 34, pp. 9050-9059, 2009.

[194] I. S. Cho, Z. Chen, A. J. Forman, D. R. Kim, P. M. Rao, T. F. Jaramillo and X. Zheng, "Branched TiO2 Nanorods for Photoelectrochemical Hydrogen Production," *Nano Letters,* vol. 11, pp. 4978-4984, 2011.

[195] X. Shi, I. Y. Choi, K. Zhang, J. Kwon, D. Y. Kim, J. K. Lee, S. H. Oh, J. K. Kim and J. H. Park, "Efficient photoelectrochemical hydrogen production from bismuth vanadate-decorated tungsten trioxide helix nanostructures," *Nature Communications,* pp. 1-8, 2014.

[196] V. Chakrapani, J. Thangala and M. K. Sunkara, "WO3 and W2N nanowire arrays for photoelectrochemical hydrogen production," *International Journal of Hydrogen Energy,* vol. 34, pp. 9050-9059, 2009.

[197] J. A. Glasscock, P. R. F. Barnes, I. C. Plumb and N. Savvides, "Enhancement of Photoelectrochemical Hydrogen Production from Hematite Thin Films by the Introduction of Ti and Si," *The Journal of Physical Chemistry C,* vol. 111, pp. 16477-16488, 2007.

[198] R. E. Rocheleau, E. L. Miller and A. Misra, "High-Efficiency Photoelectrochemical Hydrogen Production Using Multijunction Amorphous Silicon Photoelectrodes," *Energy & Fuels,* vol. 12, pp. 3-10, 1998.

[199] Z. Chi, Y. Zheng, J. Ma and S. Chen, "Oleaginous yeast Cryptococcus curvatus culture with dark fermentation hydrogen production effluent as feedstock for microbial lipid production," *International Journal of Hydrogen Energy,* vol. 36, pp. 9542-9550, 2011.

[200] S. Pattra, S. Sangyoka, M. Boonmee and A. Reungsang, "Bio-hydrogen production from the fermentation of sugarcane bagasse hydrolysate by Clostridium butyricum," *International Journal of Hydrogen Energy,* vol. 33, pp. 5256-5265, 2008.

[201] X. M. Guo, E. Trably, E. Latrille, H. Carrère and J.-P. Steyer, "Hydrogen production from agricultural waste by dark fermentation: A review," *International Journal of Hydrogen Energy*, vol. 35, pp. 10660-10673, 2010.

[202] Coordinating Research Council, Inc., "Handbook of Aviation Fuel Properties," Society of Automotive Engineers, Inc., Warrendale, Pennsylvania 15096, 1983.

[203] C. Palm, P. Cremer, R. Peters and D. Stolten, "Small-scale testing of a precious metal catalyst in the autothermal reforming of various hydrocarbon feeds," *Journal of Power Sources,* vol. 106, pp. 231-237, 2002.

[204] V. A. Sethuraman and J. W. Weidner, "Analysis of Sulfur Poisoning on a PEM Fuel Cell Electrode," *Electrochimica Acta,* vol. 55, no. 20, pp. 5683-5694, 2010.

[205] I. Babich and J. Moulijn, "Science and technology of novel processes for deep desulfurization of oil refinery streams: a review," *Fuel,* vol. 82, pp. 607-631, 2003.

[206] X. Xu, S. Zhang, P. Li and Y. Shen, "Equilibrium and kinetics of Jet-A fuel desulfurization by selective adsorption at room temperatures," *Fuel,* vol. 111, pp. 172-179, 2013.

[207] X. Xu, S. Zhang, P. Li and Y. Shen, "Desulfurization of Jet-A fuel in a fixed-bed reactor at room temperature and ambient pressure using a novel selective adsorbent," *Fuel*, vol. 117, pp. 499-508, 2014.

[208] X. Xu, S. Zhang, P. Li and Y. Shen, "Adsorptive desulfurization of liquid Jet-A fuel at ambient conditions with an improved adsorbent for on-board fuel treatment for SOFC applications," *Fuel Processing Technology,* vol. 124, pp. 140-146, 2014.

[209] X. Xu, "Desulfurization and Autothermal Reforming of Jet-A Fuel to Produce Syngas for Onboard Solid Oxide Fuel Cell Applications," The University of Arizona, Tucson, AZ 85721, 2014.

[210] L. Villegas, N. Guilhaume and C. Mirodatos, "Autothermal syngas production from model gasoline over Ni, Rh and Ni–Rh/Al_2O_3 monolithic catalysts," *International Journal of Hydrogen Energy,* vol. 39, no. 11, pp. 5772-5780, 2014.

[211] A. Qi, S. Wang, G. Fu and D. Wu, "Autothermal reforming of n-octane on Ru-based catalysts," *Applied Catalysis A: General,* vol. 293, pp. 71-82, 2005.

[212] M. Nilsson, P. Jozsa and L. J. Pettersson, "Evaluation of Pd-based catalysts and the influence of operating conditions for autothermal reforming of dimethyl ether," *Applied Catalysis B: Environmental,* vol. 76, no. 1-2, pp. 42-50, 2007.

[213] X. Zhong, W. Xie, N. Wang, Y. Duan, R. Shang and L. Huang, "Dolomite-Derived Ni-Based Catalysts with Fe Modification for Hydrogen Production via Auto-Thermal Reforming of Acetic Acid," *Catalysts,* vol. 6, no. 6, p. 85, 2016.

[214] I. Kang, J. Bae and G. Bae, "Performance comparison of autothermal reforming for liquid hydrocarbons, gasoline and diesel for fuel cell applications," *Journal of Power Sources,* vol. 163, no. 1, pp. 538-546, 2006.

[215] B. D. Gould, X. Chen and J. W. Schwank, "Dodecane reforming over nickel-based monolith catalysts," *Journal of Catalysis*, vol. 250, no. 2, pp. 209-221, 2007.

[216] V. Palma, A. Ricca and P. Ciambelli, "Monolith and foam catalysts performances in ATR of liquid and gaseous fuels," *Chemical Engineering Journal*, Vols. 207-208, pp. 577-586, 2012.

[217] V. S. Guggilla, J. Akyurtlu, A. Akyurtlu and I. Blankson, "Steam Reforming of n-Dodecane over Ru−Ni-Based Catalysts," *Industrial & Engineering Chemistry Research,* vol. 49, no. 17, pp. 8164-8173, 2010.

[218] S. Cimino and L. Lisi, "Impact of Sulfur Poisoning on the Catalytic Partial Oxidation of Methane on Rhodium-Based Catalysts," *Industrial & Engineering Chemistry Research,* vol. 51, no. 22, pp. 7459-7466, 2012.

[219] C. Palm, P. Cremer, R. Peters and D. Stolten, "Small-scale testing of a precious metal catalyst in the autothermal reforming of various hydrocarbon feeds," *Journal of Power Sources,* vol. 106, no. 1-2, pp. 231-237, 2002.

[220] Y. Wang and R. T. Yang, "Desulfurization of Liquid Fuels by Adsorption on Carbon-Based Sorbents and Ultrasound-Assisted Sorbent Regeneration," *Langmuir,* vol. 23, pp. 3825-3831, 2007.

[221] Y. Qin, Z. Mo, W. Yu, S. Dong, L. Duan, X. Gao and L. Song, "Adsorption behaviors of thiophene, benzene, and cyclohexene on FAUzeolites: Comparison of CeY obtained by liquid-, and solid-stateion exchange," *Applied Surface Science,* vol. 292, pp. 5-15, 2014.

[222] J. J. Strohm, J. Zheng and C. Song, "Low-temperature steam reforming of jet fuel in the absence and presence of sulfur over Rh and Rh–Ni catalysts for fuel cells," *Journal of Catalysis,* vol. 238, no. 2, pp. 309-320, 2006.

[223] Q. Xue, L. Gao and Y. Lu, "Sulfur-tolerant Pt/Gd_2O_3–CeO_2–Al_2O_3 catalyst for high efficiency H_2 production from autothermal reforming of retail gasoline," *Catalysis Today,* vol. 146, no. 1-2, pp. 103-109, 2009.

[224] T. Zhu, D. Walsh, J. DesJardins, S. Roychoudhury, F. H. Holcomb and C. A. Feickert, "Microlith Supported Sulfur Tolerant Catalyst for Autothermal Reforming of E85 Fuel," *Journal of Fuel Cell Science and Technology,* vol. 7, no. 5, pp. 1-8, 2010.

[225] J. Pasel, R. C. Samsun, R. Peters, B. Thiele and D. Stolten, "Long-term stability at fuel processing of diesel and kerosene," *International Journal of Hydrogen Energy,* vol. 39, no. 31, pp. 18027-18036, 2014.

[226] J. Pasel, J. Meißner, Z. Porš, R. C. Samsun, A. Tschauder and R. Peters, "Autothermal reforming of commercial Jet A-1 on a 5kWe scale," *International Journal of Hydrogen Energy,* vol. 32, no. 18, pp. 4847-4858, 2007.

[227] F. Barrai and M. J. Castaldi, "Experimental Investigation of a JP8 Fuel Processor: Autothermal Reformer and CO-Cleanup Train," *Industrial & Engineering Chemistry Research,* vol. 49, no. 4, pp. 1577-1587, 2010.

[228] R. Scenna, T. G. DuBois and S. Nieh, "Autothermal reforming of synthetic JP-8 derived from a coal syngas stream," *Fuel,* vol. 108, pp. 731-739, 2013.

[229] A. Qi, S. Wang, G. Fu, C. Ni and D. Wu, "La–Ce–Ni–O monolithic perovskite catalysts potential for gasoline autothermal reforming system," *Applied Catalysis A: General,* vol. 281, pp. 233-246, 2005.

[230] Y. Joen, C. Lee, J. Rhee, G. Lee, J.-h. Myung, M. Park, J.-I. Park, H. Einaga and Y.-G. Shul, "Autothermal reforming of heavy-hydrocarbon fuels by morphology controlled perovskite catalysts using carbon templates," *Fuel,* vol. 187, pp. 446-456, 2017.

[231] X. Xu, S. Zhang and P. Li, "Autothermal reforming of n-dodecane and desulfurized Jet-A fuel for producing hydrogen-rich syngas," *International Journal of Hydrogen Energy,* vol. 39, pp. 19593-19602, 2014.

[232] Y. Choi and H. G. Stenger, "Water gas shift reaction kinetics and reactor modeling for fuel cell grade hydrogen," *Journal of Power Sources,* vol. 124, pp. 432-439, 2003.

[233] S. Ahmed and M. Krumpelt, "Hydrogen from hydrocarbon fuels for fuel cells," *International Journal of Hydrogen Energy,* vol. 26, no. 4, pp. 291-301, 2001.

[234] S. Yoon, S. Lee and J. Bae, "Development of a self-sustaining kWe-class integrated diesel fuel processing system for solid oxide fuel cells," *International Journal of Hydrogen Energy*, vol. 36, no. 16, pp. 10302-10310, 2011.

[235] S. Roychoudhury, M. Castaldi, M. Lyubovsky, R. LaPierre and S. Ahmed, "Microlith catalytic reactors for reforming iso-octane-based fuels into hydrogen," *Journal of Power Sources,* vol. 152, pp. 75-86, 2005.

[236] M. Zahedi nezhad, S. Rowshanzamir and M. H. Eikani, "Autothermal reforming of methane to synthesis gas: Modeling and simulation," *International Journal of Hydrogen Energy*, vol. 34, no. 3, pp. 1292-1300, 2009.

[237] C. Rhodes, B. P. Williams, F. King and G. J. Hutchings, "Promotion of Fe_3O_4/Cr_2O_3 high temperature water gas shift catalyst," *Catalysis Communications,* vol. 3, no. 8, pp. 381-384, 2002.

[238] T.-S. Wang, "Thermophysics Characterization of Kerosene Combustion.," *Journal of Thermophysics and Heat Transfer,* vol. 15, pp. 140-147, 2001.

[239] T. A. Davidson, "A Simple and Accurate Method for Calculating Viscosity of Gaseous Mixtures," The Interior Bureau of Mines, Pittsburgh, PA, 1993.

[240] H. Alkandry, I. Boyd and A. Martin, "Comparison of Models for Mixture Transport Properties for Numerical Simulations of Ablative Heat-Shields," in *51st AIAA Aerospace Sciences Meeting including the New Horizons Forum and Aerospace Exposition*, Grapevine (Dallas/Ft. Worth Region), Texas, 2013.

[241] J. Nakamura, . J. M. Campbell and C. T. Campbell, "Kinetics and mechanism of the water-gas shift reaction catalysed by the clean and Cs-promoted Cu(110) surface: a comparison with Cu(111)," *Journal of the Chemical Society, Faraday Transactions,* vol. 86, no. 15, pp. 2725-2734 , 1990.

[242] S. Ahmed, R. Ahluwalia, S. H. D. Lee and S. Lottes, "A gasoline fuel processor designed to study quick-start performance," *Journal of Power Sources,* vol. 154, pp. 214-222, 2006.

[243] C. Severin, S. Pischinger and J. Ogrzewalla, "Compact gasoline fuel processor for passenger vehicle APU," *Journal of Power Sources,* vol. 145, pp. 675-682, 2005.

[244] S. Pischinger, C. Schönfelder and J. Ogrzewalla, "Analysis of dynamic requirements for fuel cell systems for vehicle applications," *Journal of Power Sources,* vol. 154, pp. 420-427, 2006.

[245] M. Krumpelt, T. R. Krause, J. D. Carter, J. P. Kopasz and S. Ahmed, "Fuel processing for fuel cell systems in transportation and portable power applications," *Catalysis Today,* vol. 77, no. 1-2, pp. 3-16, 2002.

[246] B. J. Bowers, J. L. Zhao, M. Ruffo, R. Khan, D. Dattatraya, N. Dushman, J.-C. Beziat and F. Boudjemaa, "Onboard fuel processor for PEM fuel cell vehicles," *International Journal of Hydrogen Energy,* vol. 32, no. 10-11, pp. 1437-1442, 2007.

[247] B. J. Bowers, J. L. Zhao, D. Dattatraya, M. Ruffo and F. Boudjemaa, "Performance of an Onboard Fuel Processor for PEM Fuel Cell Vehicles," *SAE 2005 World Congress & Exhibition,* 2005.

[248] B. Bowers, J. Zhao, D. Dattatraya and P. Quet, "Multi-Fuel PEM Fuel Cell Power Plant for Vehicles," *SAE World Congress & Exhibition,* 2009.

[249] S. Yoon, S. Lee and J. Bae, "Development of a self-sustaining kWe-class integrated diesel fuel processing system for solid oxide fuel cells," *International Journal of Hydrogen Energy,* vol. 36, no. 16, pp. 10302-10310, 2011.

[250] J. Pasel, R. C. Samsun, A. Tschauder, R. Peters and D. Stolten, "A novel reactor type for autothermal reforming of diesel fuel and kerosene," *Applied Energy,* vol. 150, pp. 176-184, 2015.

[251] D. S. Newsome, "The Water-Gas Shift Reaction," *Catalysis Reviews* , vol. 21, no. 2, pp. 275-318, 1980.

[252] M. Zhu and I. E. Wachs, "Iron-Based Catalysts for the High-Temperature Water–Gas Shift (HT-WGS) Reaction: A Review," *ACS Catalysis,* vol. 6, no. 2, pp. 722-732, 2016.

[253] J. Nakamura, J. M. Campbell and C. T. Campbell , "Kinetics and mechanism of the water-gas shift reaction catalysed by the clean and Cs-promoted Cu(110) surface: a

comparison with Cu(111)," *Journal of the Chemical Society, Faraday Transactions,* vol. 86, no. 15, pp. 2725-2734 , 1990.

[254] C. Lang, X. Sécordel, A. Kiennemann and C. Courson, "Water gas shift catalysts for hydrogen production from biomass steam gasification," *Fuel Processing Technology,* vol. 156, pp. 246-252, 2017.

[255] Q. Fu, H. Saltsburg and M. F. Stephanopoulos, "Active Nonmetallic Au and Pt Species on Ceria-Based Water-Gas Shift Catalysts," *Science,* vol. 301, no. 5635, pp. 935-938, 2003.

[256] D. Miao, G. Cavusoglu, H. Lichtenberg, J. Yu, H. Xu, J. D. Grunwaldt and A. Goldbach, "Water-gas shift reaction over platinum/strontium apatite catalysts," *Applied Catalysis B: Environmental,* vol. 202, pp. 587-596, 2017.

[257] B. Smith, M. Loganathan and M. S. Shantha, "A Review of the Water Gas Shift Reaction Kinetics," *International Journal of Chemical Reactor Engineering,* vol. 8, no. 1, 2010.

[258] S. S. Hla, D. Park, G. J. Duffy, J. H. Edwards, D. G. Roberts, A. Ilyushechkin, L. D. Morpeth and T. Nguyen, "Kinetics of high-temperature water-gas shift reaction over two iron-based commercial catalysts using simulated coal-derived syngases," *Chemical Engineering Journal,* vol. 146, pp. 148-154, 2009.

[259] C. P. P. Singh and D. N. Saraf, "Simulation of High-Temperature Water-Gas Shift Reactors," *Industrial & Engineering Chemistry Process Design and Development,* vol. 16, no. 3, pp. 313-319, 1977.

[260] W. F. Podolski and Y. G. Kim, "Modeling the Water-Gas Shift Reaction," *Industrial & Engineering Chemistry Process Design and Development,* vol. 13, no. 4, pp. 415-421, 1974.

Appendix

Appendix A – Thermodynamics of Autothermal Reforming Reaction (MATLAB)

```
clear all, clc
format short, format compact

% Calculate heat of reaction as a function of oxygen to
fuel ratio (x value) at different temperatures based on the
autothermal reforming reaction:
% C11.6H22.3+x(O2+3.76N2)+(23.2-2x)H2O=11.6CO2+(34.35-
2x)H2+3.76xN2
% Delta_H=(34.35-2*x)*h_H2+11.6*h_CO2-h_dodecane-x*h_O2-
(23.2-2*x)*h_H2O
% x=(Delta_H-34.35*h_H2-
11.6*h_CO2+h_dodecane+23.2*h_H2O)/(2*h_H2O-2*h_H2-h_O2)
% Cp=A + B*t + C*t^2 + D*t^3 + E/(t^2)
% Delta_h=A*t + B*t^2/2 + C*t^3/3 + D*t^4/4 - E/t + F - H
% s=A*ln(t) + B*t + C*t^2/2 + D*t^3/3 + E/(2*t^2) + G
% Cp: J/(mol*K)
% Delta_h: kJ/mol
% s: J/(mol*K)
% T: K, t=T/1000

% H2
% 298-1000 K
A1_H2=33.066178;B1_H2=-11.363417;C1_H2=11.432816;D1_H2=-
2.772874;
E1_H2=-0.158558;F1_H2=-9.980797;G1_H2=172.707974;H1_H2=0;
% 1000-2500 K
A2_H2=18.563083;B2_H2=12.257357;C2_H2=-
2.859786;D2_H2=0.268238;
E2_H2=1.977990;F2_H2=-1.147438;G2_H2=156.288133;H2_H2=0;

% O2
% 298-700 K
A1_O2=31.32234;B1_O2=-20.23531;C1_O2=57.86644;D1_O2=-
36.50624;
E1_O2=-0.007374;F1_O2=-8.903471;G1_O2=246.7945;H1_O2=0;
% 700-2000 K
```

```
A2_O2=30.03235;B2_O2=8.772972;C2_O2=-
3.988133;D2_O2=0.788313;
E2_O2=-0.741599;F2_O2=-11.32468;G2_O2=236.1663;H2_O2=0;

% CO2
% h_CO2=Delta_h_CO2 + hf_CO2
hf_CO2=-393.5224;  % kJ/mol
% 298-1200 K
A1_CO2=24.99735;B1_CO2=55.18696;C1_CO2=-
33.69137;D1_CO2=7.948387;
E1_CO2=-0.136638;F1_CO2=-403.6075;G1_CO2=228.2431;H1_CO2=-
393.5224;

% H2O
% h_H2O=Delta_h_H2O + hf_H2O
hf_H2O_L=-285.8304;  % kJ/mol
hf_H2O_G=-241.8264;  % kJ/mol
% 298-500 K, LIQUID
A1_H2O=-203.6060;B1_H2O=1523.290;C1_H2O=-
3196.413;D1_H2O=2474.455;
E1_H2O=3.855326;F1_H2O=-256.5478;G1_H2O=-488.7163;H1_H2O=-
285.8304;
% 500-1700 K, GASEOUS
A2_H2O=30.09200;B2_H2O=6.832514;C2_H2O=6.793435;D2_H2O=-
2.534480;
E2_H2O=0.082139;F2_H2O=-250.8810;G2_H2O=223.3967;H2_H2O=-
241.8264;

% dodecane
% h_dodecane=Delta_h_dodecane + hf_dodecane
hf_dodecane_L=-352.1;  % kJ/mol
hf_dodecane_G=-290.9;  % kJ/mol
% 293-473 K, LIQUID
% 1) 293-373 K
Cp_dodecane_L1=(2.192+2.460)/2*170/1000;  % kJ/(mol*K)
% 2) 293-473 K
Cp_dodecane_L2=(2.192+2.894)/2*170/1000;  % kJ/(mol*K)
% 473-5000 K, GASEOUS
% h_dodecane=R*T*(A+B*T/2+C*T^2/3+D*T^3/4+E*T^4/5+F/T)
% 1) 473-1000 K
A1_dodecane=0.39508691e1;B1_dodecane=0.10207987;C1_dodecane
=0.13124466e-4;
D1_dodecane=-0.76649284e-7;E1_dodecane=0.34503763e-10;
F1_dodecane=-0.52093574e5;G1_dodecane=0.21980951e2;
% 2) 1000-5000 K
A2_dodecane=0.36440206e2;B2_dodecane=0.54614801e-1;
C2_dodecane=-0.16091151e-4;D2_dodecane=0.21478497e-8;
```

```
E2_dodecane=-0.1013118e-12;F2_dodecane=-
0.63890109e5;G2_dodecane=-0.15798973e3;

for T=[298 373 473 573 673 773 873 973 1073 1173]
    fprintf('The reaction temperature is %i K. \n',T)
    t=T/1000;
    % CO2
    Delta_h_CO2=A1_CO2*t + B1_CO2*t^2/2 + C1_CO2*t^3/3 +
D1_CO2*t^4/4 - E1_CO2/t + F1_CO2 - H1_CO2;
    h_CO2=Delta_h_CO2 + hf_CO2;
    s_CO2=A1_CO2*log(t) + B1_CO2*t + C1_CO2*t^2/2 +
D1_CO2*t^3/3 - E1_CO2/(2*t^2) + G1_CO2;
    % H2
    if T<=1000
        h_H2=A1_H2*t + B1_H2*t^2/2 + C1_H2*t^3/3 +
D1_H2*t^4/4 - E1_H2/t + F1_H2 - H1_H2;
        s_H2=A1_H2*log(t) + B1_H2*t + C1_H2*t^2/2 +
D1_H2*t^3/3 - E1_H2/(2*t^2) + G1_H2;
    else
        h_H2=A2_H2*t + B2_H2*t^2/2 + C2_H2*t^3/3 +
D2_H2*t^4/4 - E2_H2/t + F2_H2 - H2_H2;
        s_H2=A2_H2*log(t) + B2_H2*t + C2_H2*t^2/2 +
D2_H2*t^3/3 - E2_H2/(2*t^2) + G2_H2;
    end
    % O2
    if T<=700
        h_O2=A1_O2*t + B1_O2*t^2/2 + C1_O2*t^3/3 +
D1_O2*t^4/4 - E1_O2/t + F1_O2 - H1_O2;
        s_O2=A1_O2*log(t) + B1_O2*t + C1_O2*t^2/2 +
D1_O2*t^3/3 - E1_O2/(2*t^2) + G1_O2;
    else
        h_O2=A2_O2*t + B2_O2*t^2/2 + C2_O2*t^3/3 +
D2_O2*t^4/4 - E2_O2/t + F2_O2 - H2_O2;
        s_O2=A2_O2*log(t) + B2_O2*t + C2_O2*t^2/2 +
D2_O2*t^3/3 - E2_O2/(2*t^2) + G2_O2;
    end
    % H2O & dodecane
    if T<=373
        Delta_h_H2O=A1_H2O*t + B1_H2O*t^2/2 + C1_H2O*t^3/3
+ D1_H2O*t^4/4 - E1_H2O/t + F1_H2O - H1_H2O;
        h_H2O=Delta_h_H2O + hf_H2O_L;
        s_H2O=A1_H2O*log(t) + B1_H2O*t + C1_H2O*t^2/2 +
D1_H2O*t^3/3 - E1_H2O/(2*t^2) + G1_H2O;
        Delta_h_dodecane=Cp_dodecane_L1*(T-298);
        h_dodecane=Delta_h_dodecane + hf_dodecane_L;
        if T==298
            s_dodecane=490.66;
```

```
        else
            s_dodecane=573.4580;
        end
     elseif T>373 & T<=473
        Delta_h_H2O=A2_H2O*t + B2_H2O*t^2/2 + C2_H2O*t^3/3
+ D2_H2O*t^4/4 - E2_H2O/t + F2_H2O - H2_H2O;
        h_H2O=Delta_h_H2O + hf_H2O_G;
        s_H2O=A2_H2O*log(t) + B2_H2O*t + C2_H2O*t^2/2 +
D2_H2O*t^3/3 - E2_H2O/(2*t^2) + G2_H2O;
        Delta_h_dodecane=Cp_dodecane_L2*(T-298);
        h_dodecane=Delta_h_dodecane + hf_dodecane_L;
        s_dodecane=677.9350;
    elseif T>473 & T<=1000
        Delta_h_H2O=A2_H2O*t + B2_H2O*t^2/2 + C2_H2O*t^3/3
+ D2_H2O*t^4/4 - E2_H2O/t + F2_H2O - H2_H2O;
        h_H2O=Delta_h_H2O + hf_H2O_G;
        s_H2O=A2_H2O*log(t) + B2_H2O*t + C2_H2O*t^2/2 +
D2_H2O*t^3/3 - E2_H2O/(2*t^2) + G2_H2O;

h_dodecane=8.314/1000*T*(A1_dodecane+B1_dodecane*T/2+C1_dod
ecane*T^2/3+D1_dodecane*T^3/4+E1_dodecane*T^4/5+F1_dodecane
/T);

s_dodecane=8.314*(A1_dodecane*log(T)+B1_dodecane*T+C1_dodec
ane*T^2/2+D1_dodecane*T^3/3+E1_dodecane*T^4/4+G1_dodecane);
    else
        Delta_h_H2O=A2_H2O*t + B2_H2O*t^2/2 + C2_H2O*t^3/3
+ D2_H2O*t^4/4 - E2_H2O/t + F2_H2O - H2_H2O;
        h_H2O=Delta_h_H2O + hf_H2O_G;
        s_H2O=A2_H2O*log(t) + B2_H2O*t + C2_H2O*t^2/2 +
D2_H2O*t^3/3 - E2_H2O/(2*t^2) + G2_H2O;

h_dodecane=8.314/1000*T*(A2_dodecane+B2_dodecane*T/2+C2_dod
ecane*T^2/3+D2_dodecane*T^3/4+E2_dodecane*T^4/5+F2_dodecane
/T);

s_dodecane=8.314*(A2_dodecane*log(T)+B2_dodecane*T+C2_dodec
ane*T^2/2+D2_dodecane*T^3/3+E2_dodecane*T^4/4+G2_dodecane);
    end
    x1=0
    Delta_H1=(34.35-2*x1)*h_H2+11.6*h_CO2-h_dodecane-
x1*h_O2-(23.2-2*x1)*h_H2O
    Delta_S1=((34.35-2*x1)*s_H2+11.6*s_CO2-s_dodecane-
x1*s_O2-(23.2-2*x1)*s_H2O)/1000
    Delta_G1=Delta_H1-T*Delta_S1
    Delta_H2=0
```

```
    x2=(Delta_H2-34.35*h_H2-
11.6*h_CO2+h_dodecane+23.2*h_H2O)/(2*h_H2O-2*h_H2-h_O2)
    x3=6
    Delta_H3=(34.35-2*x3)*h_H2+11.6*h_CO2-h_dodecane-
x3*h_O2-(23.2-2*x3)*h_H2O
    Delta_S3=((34.35-2*x3)*s_H2+11.6*s_CO2-s_dodecane-
x3*s_O2-(23.2-2*x3)*s_H2O)/1000
    Delta_G3=Delta_H3-T*Delta_S3
    fprintf('\n')
    plot([x1,x2,x3],[Delta_H1,Delta_H2,Delta_H3])
    hold on
end
```

Appendix B – Excess Heat and Reaction Temperature Computation (MATLAB)

```
clear all, clc
format short, format compact

% Two processes were considered in this calculation based
on autothermal reforming itself and the heat exchanging
after reforming - the preheating process and the cooling
process. The heat balance equation was described simply as
Q_process = Q_preheating - Q_cooling, where Q_preheating
included preheat the temperature of the three reactants -
dodecane, air and water from 25oC to each feed temperature,
Q_cooling included cool the temperature of all the products
- H2, CO, CO2, H2O, N2 from each reformate temperature to
350oC which is the estimated feed temperature for WGS
reaction.

T_feed=[969.2 918.6 859.2 786.9 761.9];
T_reformate=[1116.6 1006 932.5 890.2 866.2];
C_reformate=[15.97 15.99 14.55 14.08 14.08];
X_reformate_H2=[0.292 0.229 0.192 0.13 0.154];
X_reformate_CO=[0.091 0.093 0.089 0.093 0.085];
X_reformate_CO2=[0.142 0.12 0.113 0.096 0.103];
X_reformate_N2=[0.439 0.509 0.579 0.676 0.643];
conversion=[0.8866 0.8471 0.7277 0.6106 0.5810];
for k=1:length(T_feed)
   t_feed=T_feed(k)/1000;
   t_reformate=T_reformate(k)/1000;
   % Q_preheating Calculation
   n_dodecane=3*0.81/161.5;  % mol/min
   n_H2O=7.9*1/18;  % mol/min
   n_O2=10.14*1.1839*0.21/29;  % mol/min
   n_N2=10.14*1.1839*0.79/29;  % mol/min
   % Delta_h_dodecane calculation
   hf_dodecane_L=-352.1;  % kJ/mol
   hf_dodecane_G=-290.9;  % kJ/mol
   % 293-473 K, LIQUID
   % 1) 293-373 K
   Cp_dodecane_L1=(2.192+2.460)/2*170/1000;  % kJ/(mol*K)
   % 2) 373-473 K
   Cp_dodecane_L2=(2.460+2.894)/2*170/1000;  % kJ/(mol*K)
   % 473-5000 K, GASEOUS
   % h_dodecane=R*T*(A+B*T/2+C*T^2/3+D*T^3/4+E*T^4/5+F/T)
   % 1) 473-1000 K
```

```
A1_dodecane=0.39508691e1;B1_dodecane=0.10207987;C1_dodecane
=0.13124466e-4;
   D1_dodecane=-0.76649284e-7;E1_dodecane=0.34503763e-10;
   F1_dodecane=-0.52093574e5;
   % 2) 1000-5000 K
   A2_dodecane=0.36440206e2;B2_dodecane=0.54614801e-1;
   C2_dodecane=-0.16091151e-4;D2_dodecane=0.21478497e-8;
   E2_dodecane=-0.1013118e-12;F2_dodecane=-0.63890109e5;
   if T_feed(k)<=1000

h_dodecane=8.314/1000*T_feed(k)*(A1_dodecane+B1_dodecane*T_
feed(k)/2+C1_dodecane*T_feed(k)^2/3+D1_dodecane*T_feed(k)^3
/4+E1_dodecane*T_feed(k)^4/5+F1_dodecane/T_feed(k));
       Delta_h_dodecane=h_dodecane-hf_dodecane_L;
   else

h_dodecane=8.314/1000*T_feed(k)*(A2_dodecane+B2_dodecane*T_
feed(k)/2+C2_dodecane*T_feed(k)^2/3+D2_dodecane*T_feed(k)^3
/4+E2_dodecane*T_feed(k)^4/5+F2_dodecane/T_feed(k));
       Delta_h_dodecane=h_dodecane-hf_dodecane_L;
   end
   % Delta_h_H2O calculation
   hf_H2O_L=-285.8304;  % kJ/mol
   hf_H2O_G=-241.8264;  % kJ/mol
   % 298-500 K, LIQUID
   A1_H2O=-203.6060;B1_H2O=1523.290;C1_H2O=-
3196.413;D1_H2O=2474.455;
   E1_H2O=3.855326;F1_H2O=-256.5478;G1_H2O=-
488.7163;H1_H2O=-285.8304;
   % 500-1700 K, GASEOUS
   A2_H2O=30.09200;B2_H2O=6.832514;C2_H2O=6.793435;D2_H2O=-
2.534480;
   E2_H2O=0.082139;F2_H2O=-
250.8810;G2_H2O=223.3967;H2_H2O=-241.8264;
   Delta_h_H2O_G=A2_H2O*t_feed + B2_H2O*t_feed^2/2 +
C2_H2O*t_feed^3/3 + D2_H2O*t_feed^4/4 - E2_H2O/t_feed +
F2_H2O - H2_H2O;
   h_H2O=Delta_h_H2O_G + hf_H2O_G;
   Delta_h_H2O=h_H2O-hf_H2O_L;
   % Delta_h_O2 calculation
   % 298-700 K
   A1_O2=31.32234;B1_O2=-20.23531;C1_O2=57.86644;D1_O2=-
36.50624;
   E1_O2=-0.007374;F1_O2=-8.903471;G1_O2=246.7945;H1_O2=0;
   % 700-2000 K
```

```
   A2_O2=30.03235;B2_O2=8.772972;C2_O2=-
3.988133;D2_O2=0.788313;
   E2_O2=-0.741599;F2_O2=-11.32468;G2_O2=236.1663;H2_O2=0;
   if T_feed(k)<=700
       Delta_h_O2=A1_O2*t_feed + B1_O2*t_feed^2/2 +
C1_O2*t_feed^3/3 + D1_O2*t_feed^4/4 - E1_O2/t_feed + F1_O2
- H1_O2;
   else
       Delta_h_O2=A2_O2*t_feed + B2_O2*t_feed^2/2 +
C2_O2*t_feed^3/3 + D2_O2*t_feed^4/4 - E2_O2/t_feed + F2_O2
- H2_O2;
   end
   % Delta_h_N2 calculation
   % 100-500 K
   A1_N2=28.98641;B1_N2=1.853978;C1_N2=-
9.647459;D1_N2=16.63537;
   E1_N2=0.000117;F1_N2=-8.671914;G1_N2=226.4168;H1_N2=0;
   % 500-2000 K
   A2_N2=19.50583;B2_N2=19.88705;C2_N2=-
8.598535;D2_N2=1.369784;
   E2_N2=0.527601;F2_N2=-4.935202;G2_N2=212.3900;H2_N2=0;
   Delta_h_N2=A2_N2*t_feed + B2_N2*t_feed^2/2 +
C2_N2*t_feed^3/3 + D2_N2*t_feed^4/4 - E2_N2/t_feed + F2_N2
- H2_N2;

Q_preheating=n_dodecane*Delta_h_dodecane+n_H2O*Delta_h_H2O+
n_O2*Delta_h_O2+n_N2*Delta_h_N2  % kJ/min

   % Q_cooling Calculation
   % First the mole flow rate of all the products needs to
be determined
   % based on both of the measured value and the reaction
equation (for
   % H2O).
   n_reformate_H2=C_reformate(k)/25*X_reformate_H2(k);  %
mol/min
   n_reformate_N2=C_reformate(k)/25*X_reformate_N2(k);  %
mol/min
   n_reformate_CO=C_reformate(k)/25*X_reformate_CO(k);  %
mol/min
   n_reformate_CO2=C_reformate(k)/25*X_reformate_CO2(k);  %
mol/min
   n_reformate_H2O=conversion(k)*n_dodecane*22.3/2+n_H2O-
n_reformate_H2;  %mol/min

   % Delta_h_reformate_H2 calculation
   % 298-1000 K
```

```
   A1_H2=33.066178;B1_H2=-11.363417;C1_H2=11.432816;D1_H2=-
2.772874;
   E1_H2=-0.158558;F1_H2=-
9.980797;G1_H2=172.707974;H1_H2=0;
   % 1000-2500 K
   A2_H2=18.563083;B2_H2=12.257357;C2_H2=-
2.859786;D2_H2=0.268238;
   E2_H2=1.977990;F2_H2=-1.147438;G2_H2=156.288133;H2_H2=0;
   Delta_h_reformate_H2_623=A1_H2*0.623 + B1_H2*0.623^2/2 +
C1_H2*0.623^3/3 + D1_H2*0.623^4/4 - E1_H2/0.623 + F1_H2 -
H1_H2;
   if T_reformate(k)<=1000
       Delta_h_reformate_H2_T5=A1_H2*t_reformate +
B1_H2*t_reformate^2/2 + C1_H2*t_reformate^3/3 +
D1_H2*t_reformate^4/4 - E1_H2/t_reformate + F1_H2 - H1_H2;
   else
       Delta_h_reformate_H2_T5=A2_H2*t_reformate +
B2_H2*t_reformate^2/2 + C2_H2*t_reformate^3/3 +
D2_H2*t_reformate^4/4 - E2_H2/t_reformate + F2_H2 - H2_H2;
   end
   Delta_h_reformate_H2=Delta_h_reformate_H2_T5-
Delta_h_reformate_H2_623;

   % Delta_h_reformate_CO calculation
   % 298-1300 K
   A1_CO=25.56759;B1_CO=6.096130;C1_CO=4.054656;D1_CO=-
2.671301;
   E1_CO=0.131021;F1_CO=-118.0089;G1_CO=227.3665;H1_CO=-
110.5271;
   % 1300-6000 K
   A2_CO=35.15070;B2_CO=1.300095;C2_CO=-
0.205921;D2_CO=0.013550;
   E2_CO=-3.282780;F2_CO=-127.8375;G2_CO=231.7120;H2_CO=-
110.5271;
   Delta_h_reformate_CO_623=A1_CO*0.623 + B1_CO*0.623^2/2 +
C1_CO*0.623^3/3 + D1_CO*0.623^4/4 - E1_CO/0.623 + F1_CO -
H1_CO;
   if T_reformate(k)<=1300
       Delta_h_reformate_CO_T5=A1_CO*t_reformate +
B1_CO*t_reformate^2/2 + C1_CO*t_reformate^3/3 +
D1_CO*t_reformate^4/4 - E1_CO/t_reformate + F1_CO - H1_CO;
   else
       Delta_h_reformate_CO_T5=A2_CO*t_reformate +
B2_CO*t_reformate^2/2 + C2_CO*t_reformate^3/3 +
D2_CO*t_reformate^4/4 - E2_CO/t_reformate + F2_CO - H2_CO;
   end
```

```
   Delta_h_reformate_CO=Delta_h_reformate_CO_T5-
Delta_h_reformate_CO_623;

   % Delta_h_reformate_CO2 calculation
   % 298-1200 K
   A1_CO2=24.99735;B1_CO2=55.18696;C1_CO2=-
33.69137;D1_CO2=7.948387;
   E1_CO2=-0.136638;F1_CO2=-
403.6075;G1_CO2=228.2431;H1_CO2=-393.5224;
   % 1200-6000 K
   A2_CO2=58.16639;B2_CO2=2.720074;C2_CO2=-
0.492289;D2_CO2=0.038844;
   E2_CO2=-6.447293;F2_CO2=-
425.9186;G2_CO2=263.6125;H2_CO2=-393.5224;
   Delta_h_reformate_CO2_623=A1_CO2*0.623 +
B1_CO2*0.623^2/2 + C1_CO2*0.623^3/3 + D1_CO2*0.623^4/4 -
E1_CO2/0.623 + F1_CO2 - H1_CO2;
   if T_reformate(k)<=1200
       Delta_h_reformate_CO2_T5=A1_CO2*t_reformate +
B1_CO2*t_reformate^2/2 + C1_CO2*t_reformate^3/3 +
D1_CO2*t_reformate^4/4 - E1_CO2/t_reformate + F1_CO2 -
H1_CO2;
   else
       Delta_h_reformate_CO2_T5=A2_CO2*t_reformate +
B2_CO2*t_reformate^2/2 + C2_CO2*t_reformate^3/3 +
D2_CO2*t_reformate^4/4 - E2_CO2/t_reformate + F2_CO2 -
H2_CO2;
   end
   Delta_h_reformate_CO2=Delta_h_reformate_CO2_T5-
Delta_h_reformate_CO2_623;

   % Delta_h_reformate_N2 calculation
   Delta_h_reformate_N2_623=A2_N2*0.623 + B2_N2*0.623^2/2 +
C2_N2*0.623^3/3 + D2_N2*0.623^4/4 - E2_N2/0.623 + F2_N2 -
H2_N2;
   if T_reformate(k)<=500
       Delta_h_reformate_N2_T5=A1_N2*t_reformate +
B1_N2*t_reformate^2/2 + C1_N2*t_reformate^3/3 +
D1_N2*t_reformate^4/4 - E1_N2/t_reformate + F1_N2 - H1_N2;
   else
       Delta_h_reformate_N2_T5=A2_N2*t_reformate +
B2_N2*t_reformate^2/2 + C2_N2*t_reformate^3/3 +
D2_N2*t_reformate^4/4 - E2_N2/t_reformate + F2_N2 - H2_N2;
   end
   Delta_h_reformate_N2=Delta_h_reformate_N2_T5-
Delta_h_reformate_N2_623;
```

```
   % Delta_h_reformate_H2O calculation
   Delta_h_reformate_H2O_623=A2_H2O*0.623 +
B2_H2O*0.623^2/2 + C2_H2O*0.623^3/3 + D2_H2O*0.623^4/4 -
E2_H2O/0.623 + F2_H2O - H2_H2O;
   Delta_h_reformate_H2O_T5=A2_H2O*t_reformate +
B2_H2O*t_reformate^2/2 + C2_H2O*t_reformate^3/3 +
D2_H2O*t_reformate^4/4 - E2_H2O/t_reformate + F2_H2O -
H2_H2O;
   Delta_h_reformate_H2O=Delta_h_reformate_H2O_T5-
Delta_h_reformate_H2O_623;

   % unconverted Delta_h_reformate_dodecane calculation
   n_reformate_dodecane=(1-conversion(k))*n_dodecane;

h_reformate_dodecane_623=8.314/1000*623*(A1_dodecane+B1_dod
ecane*623/2+C1_dodecane*623^2/3+D1_dodecane*623^3/4+E1_dode
cane*623^4/5+F1_dodecane/623);
   if T_reformate(k)<=1000

h_reformate_dodecane_T5=8.314/1000*T_reformate(k)*(A1_dodec
ane+B1_dodecane*T_reformate(k)/2+C1_dodecane*T_reformate(k)
^2/3+D1_dodecane*T_reformate(k)^3/4+E1_dodecane*T_reformate
(k)^4/5+F1_dodecane/T_reformate(k));
   else

h_reformate_dodecane_T5=8.314/1000*T_reformate(k)*(A2_dodec
ane+B2_dodecane*T_reformate(k)/2+C2_dodecane*T_reformate(k)
^2/3+D2_dodecane*T_reformate(k)^3/4+E2_dodecane*T_reformate
(k)^4/5+F2_dodecane/T_reformate(k));
   end
   Delta_h_reformate_dodecane_T5=h_reformate_dodecane_T5-
hf_dodecane_L;
   Delta_h_reformate_dodecane=h_reformate_dodecane_T5-
h_reformate_dodecane_623;

Q_cooling=n_reformate_H2*Delta_h_reformate_H2+n_reformate_C
O*Delta_h_reformate_CO+n_reformate_CO2*Delta_h_reformate_CO
2+n_reformate_N2*Delta_h_reformate_N2+n_reformate_H2O*Delta
_h_reformate_H2O+n_reformate_dodecane*Delta_h_reformate_dod
ecane  % kJ/min
   Q_process = Q_preheating - Q_cooling
end
```

Appendix C – Heat Exchanging Area Computation (MATLAB)

```
clear all, clc
format short, format compact

%%%%%%%%%%%%%%%%%% PART ONE. ENERGY BALANCE CALCULATION
%%%%%%%%%%%%%%%%%%
% The entire reforming energy transfer process is comprised
of the preheating energy Q_preheating used to preheat all
the reactancts, (the fuel n-dodecane to 140oC, the air to
175oC, and the steam to 250oC), the heating energy
Q_heating used to heat all the reactants to around 550oC,
the reforming process is assumed to be adiabatic and the
termperature of the reformate can be determined. The last
one Q_exchange which occurs inside the recuperator bring
the reformate temperature from T_reforming to 350oC.
Q_process = Q_preheating + Q_heating - Q_exchange

% Q_preheating Calculation
% For the previous experiment, the selected optimal
operating conditions were: S/C (steam to carbon ratio) =
1.5, O2/C = 0.45. Based on the two parameters and assuming
O2 will be used up after the reforming reaction, and N2/O2
= 3.76 in air. The overall autothermal reforming reaction
is going to be C12H26 + 18H2O + 5.4O2 + 20.3N2 = xCO + yCO2
+ zH2 + (31-z)H2O + 20.3N2. Here we assume methanation
reaction does not exist, therefore there is no CH4 in the
reformate. Then the stoichiometric coefficients of the
previous reaction should be determined before the energy
calculation. From the experiment result we know the
reformate composition is 38.7% H2, 15.4% CO, 9.2% CO2 and
0.4% CH4 (drop off). The mole ratio of H2 and CO is about
2.5 in this case. Then we can find the x, y, z in the
previous reaction equation.

syms x y z
[x, y, z] = vpasolve(x + y == 12, z / x == 2.5, x + 2 * y +
31 - z == 18 + 10.8, x, y, z)
% The reforming reaction equation becomes C12H26 + 18H2O +
5.4O2 + 20.3N2 = 7.5CO + 4.5CO2 + 18.7H2 + 12.3H2O +
20.3N2. Then the WGS reaction occurs in the WGS reactor can
be illustrated in the following way, 7.5CO + 4.5CO2 +
18.7H2 + 12.3H2O + 20.3N2 = 20.3N2 + 12CO2 + 26.2H2 +
4.8H2O. Thus the overall reaction is C12H26 + 18H2O +
5.4O2 + 20.3N2 = 20.3N2 + 12CO2 + 26.2H2 + 4.8H2O. The
```

entire calculation process is therefore based on one mole of hydrogen generated in the overall reaction.

```
n_H2_WGS = 1;                    % mol/min
n_C12H26 = n_H2_WGS / 26.2;      % mol/min
n_H2O = n_H2_WGS / 26.2 * 18;    % mol/min
n_O2 = n_H2_WGS / 26.2 * 5.4;    % mol/min
n_N2 = n_H2_WGS / 26.2 * 20.3;   % mol/min
n_H2_ATR = n_H2_WGS / 26.2 * 18.7;    % mol/min
n_CO_ATR = n_H2_WGS / 26.2 * 7.5;     % mol/min
n_CO2_ATR = n_H2_WGS / 26.2 * 4.5;    % mol/min
n_H2O_ATR = n_H2_WGS / 26.2 * 12.3;   % mol/min
n_CO2_WGS = n_H2_WGS / 26.2 * 12;     % mol/min
n_H2O_WGS = n_H2_WGS / 26.2 * 4.8;    % mol/min
M_C12H26 = 170.33;      % g/mol
M_H2O = 18;             % g/mol
M_O2 = 32;              % g/mol
M_N2 = 28;              % g/mol
M_CO2 = 44;             % g/mol
M_H2 = 2;               % g/mol
M_CO = 28;              % g/mol
T0 = 298;               % K
% Cp_C12H26 = 2.273845 - 4.559779e-3 * T + 1.843537e-5 * T
^ 2 -
% 1.306521e-8 * T ^ 3 in an interval of temperatures 273 to
433 K, kJ/(kg
% K).
% Cp_O2 = 31.32234 - 20.23531 * t + 57.86644 * t ^ 2 -
36.50624 * t ^ 3
% - 0.007374 / (t ^ 2) in an interval of temperatures 100
to 700 K, J/(mol
% K) t = T / 1000.
% Cp_N2 = 28.98641 + 1.853978 * t - 9.647459 * t ^ 2 +
16.63537 * t ^ 3 +
% 0.000117 / (t ^ 2) in an interval of temperatures 100 to
500 K, J/(mol K)
T1_C12H26 = 413;        % K
T1_H2O = 523;           % K
T1_O2 = 448;            % K
T1_N2 = 448;            % K
hf_H2O_298 = 104.29;    % kJ/kg
hg_H2O_523 = 2800.9;    % kJ/kg
t0 = 298 / 1000;
t1_O2 = 448 / 1000;
t1_N2 = 448 /1000;
Q_preheating = n_C12H26 * M_C12H26 * (2.273845 * (T1_C12H26
- T0) - 4.559779e-3 / 2 * (T1_C12H26 ^ 2 - T0 ^ 2) +
```

```
1.843537e-5 / 3 * (T1_C12H26 ^ 3 - T0 ^ 3) - 1.306521e-8 /
4 * (T1_C12H26 ^ 4 - T0 ^ 4)) + n_H2O * M_H2O * (hg_H2O_523
- hf_H2O_298) + n_O2 * 1000 * (31.32234 * (t1_O2 - t0)-
20.23531 / 2 * (t1_O2 ^ 2 - t0 ^ 2) + 57.86644 / 3 * (t1_O2
^ 3 - t0 ^ 3) - 36.50624 / 4 * (t1_O2 ^ 4 - t0 ^ 4) -
0.007374 * (-1) * (1 / t1_O2 - 1 / t0)) + n_N2 * 1000 *
(28.98641 * (t1_N2 - t0) + 1.853978 / 2 * (t1_N2 ^ 2 - t0 ^
2) - 9.647459 / 3 * (t1_N2 ^ 3 - t0 ^ 3) + 16.63537 / 4 *
(t1_N2 ^ 4 - t0 ^ 4) + 0.000117 * (-1) * (1 / t1_N2 - 1 /
t0))
% J/min

% Q_heating Calculation
% The previous runs of the reforming test proves that the
optimal operating
% temperature is 700oC for the furnace temperature. Then
the actual heating
% temperature for the reactants inside the furnace is
assumed at 527oC. The
% process becomes evaporating C12H26 and raise the
temperature of C12H26,
% water and O2, N2 to 527oC,
h_O2_448 = 4485;        % kJ/kmol
h_O2_800 = 15835;       % kJ/kmol
h_N2_448 = 4377;        % kJ/kmol
h_N2_800 = 15046;       % kJ/kmol
h_H2O_523 = 7741.04 - 241814;    % kJ/kmol
h_H2O_800 = 18002 - 241814;      % kJ/kmol
hf_C12H26_413 = -290720 + 287.1 * M_C12H26;   % kJ/kmol
hg_C12H26_800 = -146103;                  % kJ/kmol
Q_heating = n_C12H26 * (hg_C12H26_800 - hf_C12H26_413) +
n_H2O * (h_H2O_800 - h_H2O_523) + n_O2 * (h_O2_800 -
h_O2_448) + n_N2 * (h_N2_800 - h_N2_448)
% J/min

% Reforming Process Calculation
% As mentioned before, this process is adiabatic which
transfers the energy
% of reactants to reformate, i.e. CO, CO2, H2O, H2, N2.
Then the
% temperature of the reformate can be calculated based on
the energy
% balance.
H_reforming_r_800 = n_C12H26 * hg_C12H26_800 + n_H2O *
h_H2O_800 + n_O2 * h_O2_800 + n_N2 * h_N2_800;  % J/min
H_reforming_p_T_reforming = H_reforming_r_800;      % J/min
```

```
% Cp_CO = 25.56759 + 6.096130 * t + 4.054656 * t ^ 2 -
2.671301 * t ^ 3
% + 0.131021 / (t ^ 2) in an interval of temperatures 298
to 1300 K, J/(mol
% K).
% Cp_CO2 = 24.99735 + 55.18696 * t - 33.69137* t ^ 2 +
7.948387 * t ^ 3 -
% 0.136638 / (t ^ 2) in an interval of temperatures 298 to
1200 K, J/(mol
% K).
% Cp_H2O_g = 30.09200 + 6.832514 * t + 6.793435 * t ^ 2 -
2.534480 * t ^ 3
% + 0.082139 / (t ^ 2) in an interval of temperatures 500
to 1700 K, J/(mol
% K).
% Cp_H2 = 33.066178 - 11.363417 * t + 11.432816 * t ^ 2 -
2.772874 * t ^ 3
% - 0.158558 / (t ^ 2) in an interval of temperature 298 to
1000 K, J/(mol
% K).
% Cp_H2 = 18.563083 + 12.257357 * t - 2.859786 * t ^ 2 +
0.268238 * t ^ 3 +
% 1.977990 / (t ^ 2) in an interval of temperature 1000 to
2500 K, J/(mol K
% ).
% Cp_N2 = 19.50583 + 19.88705 * t - 8.598535 * t ^ 2 +
1.369784 * t ^ 3 +
% 0.527601 / (t ^ 2) in an interval of temperature 500 to
2000 K, J/(mol
% K).
syms t_reforming
t_reforming = vpasolve(H_reforming_p_T_reforming ==
n_CO_ATR * (-110530 + 1000 * (25.56759 * (t_reforming -
0.298) + 6.096130 / 2 * (t_reforming^2 - 0.298^2) +
4.054656 / 3 * (t_reforming^3 - 0.298^3) - 2.671301 / 4 *
(t_reforming^4 - 0.298^4) - 0.131021 * (1/t_reforming -
1/0.298))) + n_CO2_ATR * (-393510 + 1000 * (24.99735 *
(t_reforming - 0.298) + 55.18696 / 2 * (t_reforming^2 -
0.298^2) - 33.69137 / 3 * (t_reforming^3 - 0.298^3) +
7.948387 / 4 * (t_reforming^4 - 0.298^4) + 0.136638 *
(1/t_reforming - 1/0.298))) + n_H2O_ATR * (-241814 + 1000 *
(30.09200 * (t_reforming - 0.298) + 6.832514 / 2 *
(t_reforming^2 - 0.298^2) + 6.793435 / 3 * (t_reforming^3 -
0.298^3) - 2.534480 / 4 * (t_reforming^4 - 0.298^4) -
0.082139 *(1/t_reforming - 1/0.298))) + n_H2_ATR * 1000 *
(18.563083 * (t_reforming - 0.298) + 12.257357 / 2 *
(t_reforming^2 - 0.298^2) - 2.859786 / 3 * (t_reforming^3 -
```

```
0.298^3) + 0.268238 / 4 * (t_reforming^4 - 0.298^4) -
1.977990 * (1/t_reforming - 1/0.298)) + n_N2 * 1000 *
(19.50583 * (t_reforming - 0.298) + 19.88705 / 2 *
(t_reforming^2 - 0.298^2) - 8.598535 / 3 * (t_reforming^3 -
0.298^3) + 1.369784 / 4 * (t_reforming^4 - 0.298^4) -
0.527601 * (1/t_reforming - 1/0.298)), t_reforming, [0
Inf]);
T_reforming = t_reforming * 1000    % K

% Q_exchange Calculation
% Based on the assumption that the following WGS reaction
occurs at 350oC,
% and considering heat loss during the reforming process,
the heat
% recuperator brings the termperature of the reformate from
1123 K
% to 350oC.
h_CO_1123 = 25815.85 - 110530;         % kJ/kmol
h_CO_623 = 9648 - 110530;              % kJ/kmol
h_CO2_1123 = 40169.47 - 393510;        % kJ/kmol
h_CO2_623 = 14009 - 393510;            % kJ/kmol
h_H2_1123 = 24426.94;                  % kJ/kmol
h_H2_623 = 9486;                       % kJ/kmol
h_H2O_1123 = 31183.45 - 241814;        % kJ/kmol
h_H2O_623 = 11338 - 241814;            % kJ/kmol
h_N2_1123 = 25530.27;                  % kJ/kmol
h_N2_623 = 9590;                       % kJ/kmol
Q_exchange1 = n_CO_ATR * (h_CO_1123 - h_CO_623) + n_CO2_ATR
* (h_CO2_1123 - h_CO2_623) + n_H2_ATR * (h_H2_1123 -
h_H2_623) + n_H2O_ATR * (h_H2O_1123 - h_H2O_623) + n_N2 *
(h_N2_1123 - h_N2_623)
% J/min
Q_process = Q_preheating + Q_heating - Q_exchange1    %
J/min
% As long as the heat exchange between reformer and WGS
reactor is not
% enough to supply the whole reaction process, the
secondary recuperator
% will be needed to balance the energy consumption which
locates at the
% outlet of WGS reactor bringing the temperature from T_WSG
to 200oC.
% T_WSG can be found through the previous method.
H_WGS_r_623 = n_CO_ATR * h_CO_623 + n_CO2_ATR * h_CO2_623 +
n_H2_ATR * h_H2_623 +  n_H2O_ATR * h_H2O_623 + n_N2 *
h_N2_623;  % J/min
H_WGS_p_T_WGS = H_WGS_r_623;      % J/min
```

```
syms t_WGS
t_WGS = vpasolve(H_WGS_p_T_WGS == n_CO2_WGS * (-393510 +
1000 * (24.99735 * (t_WGS - 0.298) + 55.18696 / 2 *
(t_WGS^2 - 0.298^2) - 33.69137 / 3 * (t_WGS^3 - 0.298^3) +
7.948387 / 4 * (t_WGS^4 - 0.298^4) + 0.136638 * (1/t_WGS -
1/0.298))) + n_H2O_WGS * (-241814 + 1000 * (30.09200 *
(t_WGS - 0.298) + 6.832514 / 2 * (t_WGS^2 - 0.298^2) +
6.793435 / 3 * (t_WGS^3 - 0.298^3) - 2.534480 / 4 *
(t_WGS^4 - 0.298^4) - 0.082139 *(1/t_WGS - 1/0.298))) +
n_H2_WGS * 1000 * (33.066178 * (t_WGS - 0.298) - 11.363417
/ 2 * (t_WGS^2 - 0.298^2) + 11.432816 / 3 * (t_WGS^3 -
0.298^3) - 2.772874 / 4 * (t_WGS^4 - 0.298^4) + 0.158558 *
(1/t_WGS - 1/0.298)) + n_N2 * 1000 * (19.50583 * (t_WGS -
0.298) + 19.88705 / 2 * (t_WGS^2 - 0.298^2) - 8.598535 / 3
* (t_WGS^3 - 0.298^3) + 1.369784 / 4 * (t_WGS^4 - 0.298^4)
- 0.527601 * (1/t_WGS - 1/0.298)), t_WGS, [0 Inf]);
T_WGS = t_WGS * 1000                % K
h_CO2_756 = 20566 - 393510;         % kJ/kmol
h_CO2_473 = 7111 - 393510;          % kJ/kmol
h_H2_756 = 13570;                   % kJ/kmol
h_H2_473 = 5094;                    % kJ/kmol
h_H2O_756 = 16312 - 241814;         % kJ/kmol
h_H2O_473 = 5977 - 241814;          % kJ/kmol
h_N2_756 = 13669;                   % kJ/kmol
h_N2_473 = 5114;                    % kJ/kmol
Q_exchange2 = n_CO2_WGS * (h_CO2_756 - h_CO2_473) +
n_H2_WGS * (h_H2_756 - h_H2_473) + n_H2O_WGS * (h_H2O_756 -
h_H2O_473) + n_N2 * (h_N2_756 - h_N2_473)
% J/min
Q_process = Q_preheating + Q_heating - (Q_exchange1 +
Q_exchange2)   % J/min

%%
%%%%%%%%%%%%%%%%%% PART TWO. RECUPERATOR DESIGN
%%%%%%%%%%%%%%%%%%
% The secondary recuperator needs to be designed ahead of
the first
% recuperator in virtue of the tubing configuration. In
order to complete
% the design process the thermal and kinetic parameters of
the exiting gas
% mixture need to be determined first, such as density,
viscosity, thermal
% conductivity, heat capacity and average velocity, etc.

% Secondary recuperator design
```

```
% The overall heat transfer coefficient U_WGS consists of
three parts,
% heat convective coefficient of the effluent in the
reactor against the
% exterior wall of the heat exchange tubing het_WGS, heat
conductive
% coefficient of the tubing wall k_tubing, and the heat
convective
% coefficient of the reactant (i.e. fuel, water, air) in
the passages
% against the interior wall of the tubing hrt_WGS. U_WGS =
1 / (1 / het_WGS
% + d_wall / k_tubing + 1 / hrt_WGS), where d_wall is the
thickness of the
% heat exchange tubing wall.
% For calculation of het_WGS, het_WGS = Nusselt_WGS * k_WGS
/
% d_tubing_exterior, where Nusselt_WGS is the nusselt
number of tubing and
% effluent flow, k_WGS is the thermal conductivity of the
effluent,
% d_tubing_exterior is the exterior diameter of the tubing.
% In order to find Nusselt_WGS, appropriate correlation of
heat transfer
% process for flow across tube bundles needs to be found.
Then first of
% all, we need to know the Reynolds number
Reynolds_tubing_WGS and Prandtl
% number Prandtl_WGS. Reynolds_tubing_WGS = rho_WGS * u_WGS
*
% d_tubing_exterior / mu_WGS = m_WGS / Area_reactor *
d_tubing_exterior /
% mu_WGS, Prandtl_WGS = Cp_WGS * mu_WGS / k_WGS, where
m_WGS is the mass
% flow rate of effluent mixture, Area_reactor is the cross-
section area of
% the reactor, d_tubing_exterior is the exterior diameter
of tubing
% passages, mu_WGS, Cp_WGS and k_WGS are the viscosity,
heat capacity and
% thermal conductivity of the mixture, respectively.
% For WGS reaction, the composition of effluent is 20.3N2 +
12CO2 + 26.2H2
% + 4.8H2O and the temperature T_WGS = 756 K.
m_WGS = n_N2 * M_N2 + n_CO2_WGS * M_CO2 + n_H2_WGS * M_H2 +
n_H2O_WGS + M_H2O;      % g/min
d_reactor = 0.0427228;          % m 1-1/2 pipe ID 1.682"
```

```
Area_reactor = pi * (d_reactor / 2) ^ 2;    % m^2
d_tubing_exterior = 0.003175;    % m 1/8" tubing
X_N2_WGS = n_N2 / (n_N2 + n_CO2_WGS + n_H2_WGS + n_H2O_WGS)
X_CO2_WGS = n_CO2_WGS / (n_N2 + n_CO2_WGS + n_H2_WGS +
n_H2O_WGS)
X_H2_WGS = n_H2_WGS / (n_N2 + n_CO2_WGS + n_H2_WGS +
n_H2O_WGS)
X_H2O_WGS = n_H2O_WGS / (n_N2 + n_CO2_WGS + n_H2_WGS +
n_H2O_WGS)
% According to Davidson, the gas mixture dynamic viscosity
can be
% calculated by mu_WGS = 1 / f_WGS, where mu_WGS is the
dynamic viscocity
% of the effluent at the outlet of WGS reactor, f_WGS is
the fluidity of
% the gas mixture. f_WGS = sigma_ij (Y_i_WGS * Y_j_WGS *
Ee_ij ^ A / ((
% mu_i_WGS * mu_j_WGS) ^ (1 / 2))), where Y_i_WGS is the
momentum fraction
% of the ith component, Y_i_WGS = X_i_WGS * M_i ^ (1 / 2) /
(sigma (
% X_i_WGS * M_i ^ (1 / 2))), Ee_ij is the mean efficiency
with which body i
% transfers its momentum to body j, Ee_ij = 2 * (m_i_WGS *
m_j_WGS) ^ (1 /
% 2) / (m_i_WGS + m_j_WGS), where m_i_WGS is the mass flow
rate of the ith
% component in the gas mixture, A is the exponent of
momentum transfer
% efficiency Y_WGS, which is assumed to be the same for all
pairs. Based on
% the results Davidson got from the tests, A = 1 / 3.
Y_N2_WGS = X_N2_WGS * M_N2 ^ (1 / 2) / (X_N2_WGS * M_N2 ^
(1 / 2) + X_CO2_WGS * M_CO2 ^ (1 / 2) + X_H2_WGS * M_H2 ^
(1 / 2) + X_H2O_WGS * M_H2O ^ (1 / 2));
Y_CO2_WGS = X_CO2_WGS * M_CO2 ^ (1 / 2) / (X_N2_WGS * M_N2
^ (1 / 2) + X_CO2_WGS * M_CO2 ^ (1 / 2) + X_H2_WGS * M_H2 ^
(1 / 2) + X_H2O_WGS * M_H2O ^ (1 / 2));
Y_H2_WGS = X_H2_WGS * M_H2 ^ (1 / 2) / (X_N2_WGS * M_N2 ^
(1 / 2) + X_CO2_WGS * M_CO2 ^ (1 / 2) + X_H2_WGS * M_H2 ^
(1 / 2) + X_H2O_WGS * M_H2O ^ (1 / 2));
Y_H2O_WGS = X_H2O_WGS * M_H2O ^ (1 / 2) / (X_N2_WGS * M_N2
^ (1 / 2) + X_CO2_WGS * M_CO2 ^ (1 / 2) + X_H2_WGS * M_H2 ^
(1 / 2) + X_H2O_WGS * M_H2O ^ (1 / 2));
mu_N2_WGS_756 = 3.456e-5;            % kg/m-s
mu_CO2_WGS_756 = 3.362e-5;           % kg/m-s
mu_H2_WGS_756 = 1.678e-5;            % kg/m-s
```

```
mu_H2O_WGS_756 = 2.7863e-5;          % kg/m-s
A = 1 / 3;
m_N2_WGS = n_N2 * M_N2;           % g/min
m_CO2_WGS = n_CO2_WGS * M_CO2;    % g/min
m_H2_WGS = n_H2_WGS * M_H2;       % g/min
m_H2O_WGS = n_H2O_WGS * M_H2O;    % g/min
Ee_N2CO2 = 2 * (m_N2_WGS * m_CO2_WGS) ^ (1 / 2) / (m_N2_WGS
+ m_CO2_WGS);
Ee_N2H2 = 2 * (m_N2_WGS * m_H2_WGS) ^ (1 / 2) / (m_N2_WGS +
m_H2_WGS);
Ee_N2H2O = 2 * (m_N2_WGS * m_H2O_WGS) ^ (1 / 2) / (m_N2_WGS
+ m_H2O_WGS);
Ee_CO2H2 = 2 * (m_CO2_WGS * m_H2_WGS) ^ (1 / 2) /
(m_CO2_WGS + m_H2_WGS);
Ee_CO2H2O = 2 * (m_CO2_WGS * m_H2O_WGS) ^ (1 / 2) /
(m_CO2_WGS + m_H2O_WGS);
Ee_H2H2O = 2 * (m_H2_WGS * m_H2O_WGS) ^ (1 / 2) / (m_H2_WGS
+ m_H2O_WGS);
f_WGS_756 = Y_N2_WGS ^ 2 / mu_N2_WGS_756 + Y_CO2_WGS ^ 2 /
mu_CO2_WGS_756 + Y_H2_WGS ^ 2 / mu_H2_WGS_756 + Y_H2O_WGS ^
2 / mu_H2O_WGS_756 + 2 * Y_N2_WGS * Y_CO2_WGS * Ee_N2CO2 ^
A / ((mu_N2_WGS_756 * mu_CO2_WGS_756) ^ (1 / 2)) + 2 *
Y_N2_WGS * Y_H2_WGS * Ee_N2H2 ^ A / ((mu_N2_WGS_756 *
mu_H2_WGS_756) ^ (1 / 2)) + 2 * Y_N2_WGS * Y_H2O_WGS *
Ee_N2H2O ^ A / ((mu_N2_WGS_756 * mu_H2O_WGS_756) ^ (1 / 2))
+ 2 * Y_CO2_WGS * Y_H2_WGS * Ee_CO2H2 ^ A /
((mu_CO2_WGS_756 * mu_H2_WGS_756) ^ (1 / 2)) + 2 *
Y_CO2_WGS * Y_H2O_WGS * Ee_CO2H2O ^ A / ((mu_CO2_WGS_756 *
mu_H2O_WGS_756) ^ (1 / 2)) + 2 * Y_H2_WGS * Y_H2O_WGS *
Ee_H2H2O ^ A / ((mu_H2_WGS_756 * mu_H2O_WGS_756) ^ (1 /
2));
% m-s/kg
mu_WGS_756 = 1 / f_WGS_756;              % kg/m-s
Reynolds_d_tubing_WGS_756 = m_WGS / 1000 / 60 /
Area_reactor * d_tubing_exterior / mu_WGS_756
Cp_N2_WGS_756 = 19.50583 + 19.88705 * t_WGS - 8.598535 *
t_WGS ^ 2 + 1.369784 * t_WGS ^ 3 + 0.527601 / t_WGS ^ 2;
% J/mol-K
Cp_CO2_WGS_756 = 24.99735 + 55.18696 * t_WGS - 33.69137*
t_WGS ^ 2 + 7.948387 * t_WGS ^ 3 -  0.136638 / t_WGS ^ 2;
% J/mol-K
Cp_H2_WGS_756 = 33.066178 - 11.363417 * t_WGS + 11.432816 *
t_WGS ^ 2 - 2.772874 * t_WGS ^ 3 - 0.158558 / t_WGS ^ 2;  %
J/mol-K
Cp_H2O_WGS_756 = 30.09200 + 6.832514 * t_WGS + 6.793435 *
t_WGS ^ 2 - 2.534480 * t_WGS ^ 3 + 0.082139 / t_WGS ^ 2;
% J/mol-K
```

```
M_WGS = X_N2_WGS * M_N2 + X_CO2_WGS * M_CO2 + X_H2_WGS *
M_H2 + X_H2O_WGS * M_H2O;             % g/mol
Cp_WGS_756 = (X_N2_WGS * Cp_N2_WGS_756 + X_CO2_WGS *
Cp_CO2_WGS_756 + X_H2_WGS * Cp_H2_WGS_756 + X_H2O_WGS *
Cp_H2O_WGS_756) / (M_WGS / 1000);  % J/kg-K
% The Chapman-Enskog model can be used to predict the
thermal conductivity
% of gas mixtures. k_WGS = sigma_i (X_i_WGS * k_i_WGS /
(sigma_j (X_j_WGS
% * phi_ij_WGS))), where phi_ij_WGS can be calculated by
phi_ij_WGS = (1 +
% (mu_i_WGS / mu_j_WGS) ^ 0.5 * (M_j / M_i) ^ 0.25) ^ 2 /
(8 ^ 0.5 * (1 +
% M_i / M_j) ^ 0.5).
phi_N2CO2_WGS_756 = (1 + (mu_N2_WGS_756 / mu_CO2_WGS_756) ^
0.5 * (M_CO2 / M_N2) ^ 0.25) ^ 2 / (8 ^ 0.5 * (1 +  M_N2 /
M_CO2) ^ 0.5);
phi_N2H2_WGS_756 = (1 + (mu_N2_WGS_756 / mu_H2_WGS_756) ^
0.5 * (M_H2 / M_N2) ^ 0.25) ^ 2 / (8 ^ 0.5 * (1 +  M_N2 /
M_H2) ^ 0.5);
phi_N2H2O_WGS_756 = (1 + (mu_N2_WGS_756 / mu_H2O_WGS_756) ^
0.5 * (M_H2O / M_N2) ^ 0.25) ^ 2 / (8 ^ 0.5 * (1 +  M_N2 /
M_H2O) ^ 0.5);
phi_CO2N2_WGS_756 = (1 + (mu_CO2_WGS_756 / mu_N2_WGS_756) ^
0.5 * (M_N2 / M_CO2) ^ 0.25) ^ 2 / (8 ^ 0.5 * (1 +  M_CO2 /
M_N2) ^ 0.5);
phi_CO2H2_WGS_756 = (1 + (mu_CO2_WGS_756 / mu_H2_WGS_756) ^
0.5 * (M_H2 / M_CO2) ^ 0.25) ^ 2 / (8 ^ 0.5 * (1 +  M_CO2 /
M_H2) ^ 0.5);
phi_CO2H2O_WGS_756 = (1 + (mu_CO2_WGS_756 / mu_H2O_WGS_756)
^ 0.5 * (M_H2O / M_CO2) ^ 0.25) ^ 2 / (8 ^ 0.5 * (1 +
M_CO2 / M_H2O) ^ 0.5);
phi_H2N2_WGS_756 = (1 + (mu_H2_WGS_756 / mu_N2_WGS_756) ^
0.5 * (M_N2 / M_H2) ^ 0.25) ^ 2 / (8 ^ 0.5 * (1 +  M_H2 /
M_N2) ^ 0.5);
phi_H2CO2_WGS_756 = (1 + (mu_H2_WGS_756 / mu_CO2_WGS_756) ^
0.5 * (M_CO2 / M_H2) ^ 0.25) ^ 2 / (8 ^ 0.5 * (1 +  M_H2 /
M_CO2) ^ 0.5);
phi_H2H2O_WGS_756 = (1 + (mu_H2_WGS_756 / mu_H2O_WGS_756) ^
0.5 * (M_H2O / M_H2) ^ 0.25) ^ 2 / (8 ^ 0.5 * (1 +  M_H2 /
M_H2O) ^ 0.5);
phi_H2ON2_WGS_756 = (1 + (mu_H2O_WGS_756 / mu_N2_WGS_756) ^
0.5 * (M_N2 / M_H2O) ^ 0.25) ^ 2 / (8 ^ 0.5 * (1 +  M_H2O /
M_N2) ^ 0.5);
phi_H2OCO2_WGS_756 = (1 + (mu_H2O_WGS_756 / mu_CO2_WGS_756)
^ 0.5 * (M_CO2 / M_H2O) ^ 0.25) ^ 2 / (8 ^ 0.5 * (1 +
M_H2O / M_CO2) ^ 0.5);
```

```
phi_H2OH2_WGS_756 = (1 + (mu_H2O_WGS_756 / mu_H2_WGS_756) ^
0.5 * (M_H2 / M_H2O) ^ 0.25) ^ 2 / (8 ^ 0.5 * (1 +  M_H2O /
M_H2) ^ 0.5);
k_N2_WGS_756 = 53.250e-3;             % W/m-K
k_CO2_WGS_756 = 53.488e-3;            % W/m-K
k_H2_WGS_756 = 0.40359;               % W/m-K
k_H2O_WGS_756 = 64.830e-3;            % W/m-K
k_WGS_756 = X_N2_WGS * k_N2_WGS_756 / (X_N2_WGS + X_CO2_WGS
* phi_N2CO2_WGS_756 + X_H2_WGS * phi_N2H2_WGS_756 +
X_H2O_WGS * phi_N2H2O_WGS_756) + X_CO2_WGS * k_CO2_WGS_756
/ (X_N2_WGS * phi_CO2N2_WGS_756 + X_CO2_WGS + X_H2_WGS *
phi_CO2H2_WGS_756 + X_H2O_WGS * phi_CO2H2O_WGS_756) +
X_H2_WGS * k_H2_WGS_756 / (X_N2_WGS * phi_H2N2_WGS_756 +
X_CO2_WGS * phi_H2CO2_WGS_756 + X_H2_WGS + X_H2O_WGS *
phi_H2H2O_WGS_756) + X_H2O_WGS * k_H2O_WGS_756 / (X_N2_WGS
* phi_H2ON2_WGS_756 + X_CO2_WGS * phi_H2OCO2_WGS_756 +
X_H2_WGS * phi_H2OH2_WGS_756 + X_H2O_WGS);
% W/m-K
Prandtl_WGS_756 = Cp_WGS_756 * mu_WGS_756 / k_WGS_756
% Under this Reynolds number and Prandtl number the
correlation is
% presented by Zukauskas in the following way: Nusselt_WGS
= Prandtl_WGS ^
% 0.36 * fn_Reynolds_tubing_WGS, where
fn_Reynolds_tubing_WGS = 0.8 *
% Reynolds_tubing_WGS ^ 0.4.
fn_Reynolds_d_tubing_WGS_756 = 0.8 *
Reynolds_d_tubing_WGS_756 ^ 0.4;
Nusselt_WGS_756 = Prandtl_WGS_756 ^ 0.36 *
fn_Reynolds_d_tubing_WGS_756
het_WGS_756 = Nusselt_WGS_756 * k_WGS_756 /
d_tubing_exterior         % W/m^2-K
d_wall = 0.000508;                % m
k_tubing = 19;                    % W/m-K
% Before calculation of hrt_WGS of fuel, water, air against
the tubing
% interior wall, first of all the final temperature of
these three species
% after heat exchanging inside the secondary recuperator
need to be
% determined. Note that the maximum temperature they can
achieve in this
% recuperator is 473 K as the final temperature of the
effluent mixture is
% assigned at 473 K. Then we can assume the T_air_WGS = 473
K and
```

```
% T_C12H26_WGS = 433 K. Then the temperature of H2O can be
found based on
% the heat balance.
m_C12H26 = n_C12H26 * M_C12H26;      % g/min
m_H2O = n_H2O * M_H2O;               % g/min
m_air = n_O2 * M_O2 + n_N2 * M_N2;   % g/min
T_air_WGS = 473;                % K
T_C12H26_WGS = 433;             % K
h_air_473 = 601.66;             % kJ/kg
h_air_298 = 424.29;             % kJ/kg
hf_H2O_298 = 104.29;            % kJ/kg
hf_C12H26_433 = -160.60;        % kJ/kg
hf_C12H26_298 = -492.84;        % kJ/kg
Q_H2O_WGS = Q_exchange2 - m_air * (h_air_473 - h_air_298) -
m_C12H26 * (hf_C12H26_433 - hf_C12H26_298)
% J/min
hfg_H2O_T_WGS = Q_H2O_WGS / m_H2O + hf_H2O_298;       %
kJ/kg
T_H2O_WGS = 406.67;             % K with quality = 0.38608
% Then based on the temperatures hrt_WGS of C12H26 and air
can be found as
% the same as calculation of het_WGS, the Reynolds number,
Prandtl number
% as well as Nusselt number need to be determined for the
two species.
% Reynolds_tubing_i_WGS = 4 * m_i /
Perimeter_tubing_interior / mu_i_WGS,
% Prandtl_i_WGS = Cp_i_WGS * mu_i_WGS / k_i_WGS.
d_tubing_interior = 0.002159;        % m, OD 1/8"  ID
0.085"
Perimeter_tubing_interior = pi * d_tubing_interior;    % m
% C12H26, air and water should be considered separatetly as
the temperature
% of the bulk flow inside the reactor is different.
% For C12H26
mu_C12H26_WGS = 0.8e-3;              % kg/m-s
Reynolds_C12H26_WGS = 4 * m_C12H26 / 1000 / 60 /
Perimeter_tubing_interior / mu_C12H26_WGS
Cp_C12H26_WGS = 420.00;         % J/mol-K
k_C12H26_WGS = 0.140;           % W/m-K
Prandtl_C12H26_WGS = Cp_C12H26_WGS / M_C12H26 * 1000 *
mu_C12H26_WGS / k_C12H26_WGS
% Based on the Reynods number and Prandtl number derived
above, the C12H26
% heat transfer model can be treated as the constant wall
temperature heat
% transfer with Nusselt_C12H26_WGS = 3.66.
```

```
Nusselt_C12H26_WGS = 3.66;
hrt_C12H26_WGS = Nusselt_C12H26_WGS * k_C12H26_WGS /
d_tubing_interior   % W/m^2-K
% The overall heat transfer coefficient of C12H26 is then
determined as
% follows
U_C12H26_WGS = 1 / (1 / het_WGS_756 + d_wall / k_tubing + 1
/ hrt_C12H26_WGS)     % W/m^2-K
% After the heat transfer coefficient is calculated, the
heat exchanging
% area can be found based on the couter flow heat exchanger
design process.
Q_C12H26_WGS = m_C12H26 * (hf_C12H26_433 - hf_C12H26_298);
% J/min
% Find the logarithmic mean temperature difference (LMTD).
Delta_Ta_C12H26_WGS = T_WGS - T_C12H26_WGS;           % K
% Decide the temperature of effluents after the heat
exchanging with
% C12H26.
syms t_WGS_C12H26
t_WGS_C12H26 = vpasolve(Q_exchange2 - Q_C12H26_WGS ==
n_CO2_WGS * 1000 * (24.99735 * (t_WGS_C12H26 - 0.473) +
55.18696 / 2 * (t_WGS_C12H26^2 - 0.473^2) - 33.69137 / 3 *
(t_WGS_C12H26^3 - 0.473^3) + 7.948387 / 4 * (t_WGS_C12H26^4
- 0.473^4) + 0.136638 * (1/t_WGS_C12H26 - 1/0.473)) +
n_H2O_WGS * 1000 * (30.09200 * (t_WGS_C12H26 - 0.473) +
6.832514 / 2 * (t_WGS_C12H26^2 - 0.473^2) + 6.793435 / 3 *
(t_WGS_C12H26^3 - 0.473^3) - 2.534480 / 4 * (t_WGS_C12H26^4
- 0.473^4) - 0.082139 *(1/t_WGS_C12H26 - 1/0.473)) +
n_H2_WGS * 1000 * (33.066178 * (t_WGS_C12H26 - 0.473) -
11.363417 / 2 * (t_WGS_C12H26^2 - 0.473^2) + 11.432816 / 3
* (t_WGS_C12H26^3 - 0.473^3) - 2.772874 / 4 *
(t_WGS_C12H26^4 - 0.473^4) + 0.158558 * (1/t_WGS_C12H26 -
1/0.473)) + n_N2 * 1000 * (19.50583 * (t_WGS_C12H26 -
0.473) + 19.88705 / 2 * (t_WGS_C12H26^2 - 0.473^2) -
8.598535 / 3 * (t_WGS_C12H26^3 - 0.473^3) + 1.369784 / 4 *
(t_WGS_C12H26^4 - 0.473^4) - 0.527601 * (1/t_WGS_C12H26 -
1/0.473)), t_WGS_C12H26, [0 Inf]);
T_WGS_C12H26 = t_WGS_C12H26 * 1000                % K
Delta_Tb_C12H26_WGS = T_WGS_C12H26 - 298;         % K
LMTD_C12H26_WGS = (Delta_Ta_C12H26_WGS -
Delta_Tb_C12H26_WGS) / log(Delta_Ta_C12H26_WGS /
Delta_Tb_C12H26_WGS);    % K
% Use Q = U * P * L * LMTD to determine L for C12H26.
Perimeter_tubing_exterior = 3.14159 * d_tubing_exterior;
% m
```

```
Length_C12H26_WGS = Q_C12H26_WGS / 60 / LMTD_C12H26_WGS /
U_C12H26_WGS / Perimeter_tubing_exterior     % m

% Determine heat transfer process for air in the secondary
recuperator.
mu_N2_WGS_732 = 0.000033830;            % kg/m-s
mu_CO2_WGS_732 = 0.000032795;           % kg/m-s
mu_H2_WGS_732 = 0.000016412;            % kg/m-s
mu_H2O_WGS_732 = 0.000026879;           % kg/m-s
f_WGS_732 = Y_N2_WGS ^ 2 / mu_N2_WGS_732 + Y_CO2_WGS ^ 2 /
mu_CO2_WGS_732 + Y_H2_WGS ^ 2 / mu_H2_WGS_732 + Y_H2O_WGS ^
2 / mu_H2O_WGS_732 + 2 * Y_N2_WGS * Y_CO2_WGS * Ee_N2CO2 ^
A / ((mu_N2_WGS_732 * mu_CO2_WGS_732) ^ (1 / 2)) + 2 *
Y_N2_WGS * Y_H2_WGS * Ee_N2H2 ^ A / ((mu_N2_WGS_732 *
mu_H2_WGS_732) ^ (1 / 2)) + 2 * Y_N2_WGS * Y_H2O_WGS *
Ee_N2H2O ^ A / ((mu_N2_WGS_732 * mu_H2O_WGS_732) ^ (1 / 2))
+ 2 * Y_CO2_WGS * Y_H2_WGS * Ee_CO2H2 ^ A /
((mu_CO2_WGS_732 * mu_H2_WGS_732) ^ (1 / 2)) + 2 *
Y_CO2_WGS * Y_H2O_WGS * Ee_CO2H2O ^ A / ((mu_CO2_WGS_732 *
mu_H2O_WGS_732) ^ (1 / 2)) + 2 * Y_H2_WGS * Y_H2O_WGS *
Ee_H2H2O ^ A / ((mu_H2_WGS_732 * mu_H2O_WGS_732) ^ (1 /
2));
% m-s/kg
mu_WGS_732 = 1 / f_WGS_732;              % kg/m-s
Reynolds_tubing_WGS_732 = m_WGS / 1000 / 60 / Area_reactor
* d_tubing_exterior / mu_WGS_732
Cp_N2_WGS_732 = 19.50583 + 19.88705 * t_WGS_C12H26 -
8.598535 * t_WGS_C12H26 ^ 2 + 1.369784 * t_WGS_C12H26 ^ 3 +
0.527601 / t_WGS_C12H26 ^ 2;     % J/mol-K
Cp_CO2_WGS_732 = 24.99735 + 55.18696 * t_WGS_C12H26 -
33.69137* t_WGS_C12H26 ^ 2 + 7.948387 * t_WGS_C12H26 ^ 3 -
0.136638 / t_WGS_C12H26 ^ 2;    % J/mol-K
Cp_H2_WGS_732 = 33.066178 - 11.363417 * t_WGS_C12H26 +
11.432816 * t_WGS_C12H26 ^ 2 - 2.772874 * t_WGS_C12H26 ^ 3
- 0.158558 / t_WGS_C12H26 ^ 2;  % J/mol-K
Cp_H2O_WGS_732 = 30.09200 + 6.832514 * t_WGS_C12H26 +
6.793435 * t_WGS_C12H26 ^ 2 - 2.534480 * t_WGS_C12H26 ^ 3 +
0.082139 / t_WGS_C12H26 ^ 2;    % J/mol-K
Cp_WGS_732 = (X_N2_WGS * Cp_N2_WGS_732 + X_CO2_WGS *
Cp_CO2_WGS_732 + X_H2_WGS * Cp_H2_WGS_732 + X_H2O_WGS *
Cp_H2O_WGS_732) / (M_WGS / 1000);    % J/kg-K
phi_N2CO2_WGS_732 = (1 + (mu_N2_WGS_732 / mu_CO2_WGS_732) ^
0.5 * (M_CO2 / M_N2) ^ 0.25) ^ 2 / (8 ^ 0.5 * (1 +  M_N2 /
M_CO2) ^ 0.5);
phi_N2H2_WGS_732 = (1 + (mu_N2_WGS_732 / mu_H2_WGS_732) ^
0.5 * (M_H2 / M_N2) ^ 0.25) ^ 2 / (8 ^ 0.5 * (1 +  M_N2 /
M_H2) ^ 0.5);
```

```
phi_N2H2O_WGS_732 = (1 + (mu_N2_WGS_732 / mu_H2O_WGS_732) ^
0.5 * (M_H2O / M_N2) ^ 0.25) ^ 2 / (8 ^ 0.5 * (1 +  M_N2 /
M_H2O) ^ 0.5);
phi_CO2N2_WGS_732 = (1 + (mu_CO2_WGS_732 / mu_N2_WGS_732) ^
0.5 * (M_N2 / M_CO2) ^ 0.25) ^ 2 / (8 ^ 0.5 * (1 +  M_CO2 /
M_N2) ^ 0.5);
phi_CO2H2_WGS_732 = (1 + (mu_CO2_WGS_732 / mu_H2_WGS_732) ^
0.5 * (M_H2 / M_CO2) ^ 0.25) ^ 2 / (8 ^ 0.5 * (1 +  M_CO2 /
M_H2) ^ 0.5);
phi_CO2H2O_WGS_732 = (1 + (mu_CO2_WGS_732 / mu_H2O_WGS_732)
^ 0.5 * (M_H2O / M_CO2) ^ 0.25) ^ 2 / (8 ^ 0.5 * (1 +
M_CO2 / M_H2O) ^ 0.5);
phi_H2N2_WGS_732 = (1 + (mu_H2_WGS_732 / mu_N2_WGS_732) ^
0.5 * (M_N2 / M_H2) ^ 0.25) ^ 2 / (8 ^ 0.5 * (1 +  M_H2 /
M_N2) ^ 0.5);
phi_H2CO2_WGS_732 = (1 + (mu_H2_WGS_732 / mu_CO2_WGS_732) ^
0.5 * (M_CO2 / M_H2) ^ 0.25) ^ 2 / (8 ^ 0.5 * (1 +  M_H2 /
M_CO2) ^ 0.5);
phi_H2H2O_WGS_732 = (1 + (mu_H2_WGS_732 / mu_H2O_WGS_732) ^
0.5 * (M_H2O / M_H2) ^ 0.25) ^ 2 / (8 ^ 0.5 * (1 +  M_H2 /
M_H2O) ^ 0.5);
phi_H2ON2_WGS_732 = (1 + (mu_H2O_WGS_732 / mu_N2_WGS_732) ^
0.5 * (M_N2 / M_H2O) ^ 0.25) ^ 2 / (8 ^ 0.5 * (1 +  M_H2O /
M_N2) ^ 0.5);
phi_H2OCO2_WGS_732 = (1 + (mu_H2O_WGS_732 / mu_CO2_WGS_732)
^ 0.5 * (M_CO2 / M_H2O) ^ 0.25) ^ 2 / (8 ^ 0.5 * (1 +
M_H2O / M_CO2) ^ 0.5);
phi_H2OH2_WGS_732 = (1 + (mu_H2O_WGS_732 / mu_H2_WGS_732) ^
0.5 * (M_H2 / M_H2O) ^ 0.25) ^ 2 / (8 ^ 0.5 * (1 +  M_H2O /
M_H2) ^ 0.5);
k_N2_WGS_732 = 51.998e-3;             % W/m-K
k_CO2_WGS_732 = 51.704e-3;            % W/m-K
k_H2_WGS_732 = 0.39188;               % W/m-K
k_H2O_WGS_732 = 61.858e-3;            % W/m-K
k_WGS_732 = X_N2_WGS * k_N2_WGS_732 / (X_N2_WGS + X_CO2_WGS
* phi_N2CO2_WGS_732 + X_H2_WGS * phi_N2H2_WGS_732 +
X_H2O_WGS * phi_N2H2O_WGS_732) + X_CO2_WGS * k_CO2_WGS_732
/ (X_N2_WGS * phi_CO2N2_WGS_732 + X_CO2_WGS + X_H2_WGS *
phi_CO2H2_WGS_732 + X_H2O_WGS * phi_CO2H2O_WGS_732) +
X_H2_WGS * k_H2_WGS_732 / (X_N2_WGS * phi_H2N2_WGS_732 +
X_CO2_WGS * phi_H2CO2_WGS_732 + X_H2_WGS + X_H2O_WGS *
phi_H2H2O_WGS_732) + X_H2O_WGS * k_H2O_WGS_732 / (X_N2_WGS
* phi_H2ON2_WGS_732 + X_CO2_WGS * phi_H2OCO2_WGS_732 +
X_H2_WGS * phi_H2OH2_WGS_732 + X_H2O_WGS); % W/m-K
Prandtl_WGS_732 = Cp_WGS_732 * mu_WGS_732 / k_WGS_732
fn_Reynolds_tubing_WGS_732 = 0.8 * Reynolds_tubing_WGS_732
^ 0.4;
```

```
Nusselt_WGS_732 = Prandtl_WGS_732 ^ 0.36 *
fn_Reynolds_tubing_WGS_732
het_WGS_732 = Nusselt_WGS_732 * k_WGS_732 /
d_tubing_exterior         % W/m^2-K
% For air
mu_air_WGS = 2.2e-5;                  % kg/m-s
Reynolds_air_WGS = 4 * m_air / 1000 / 60 /
Perimeter_tubing_interior / mu_air_WGS
Cp_air_WGS = 1.009;              % J/g-K
k_air_WGS = 0.0314;              % W/m-K
Prandtl_air_WGS = Cp_air_WGS * 1000 * mu_air_WGS /
k_air_WGS
% The air heat tranfer process can be described by
Gnielinski's correlation
% for forced convection in turbulent pipe flow,
Nusselt_air_WGS =
% (f_air_WGS / 8) * (Reynolds_air_WGS - 1000) *
Prandtl_air_WGS / (1 + 12.7
% * (f_air_WGS / 8) ^ 0.5 * (Prandtl_air_WGS ^ (2 / 3) -
1)), where
% f_air_WGS is the Darcy friction factor, f_air_WGS = (0.79
*
% log(Reynolds_air_WGS) - 1.64) ^ (-2) by Petukhov's
formula.
f_air_WGS = (0.79 * log(Reynolds_air_WGS) - 1.64) ^ (-2);
Nusselt_air_WGS = (f_air_WGS / 8) * (Reynolds_air_WGS -
1000) * Prandtl_air_WGS / (1 + 12.7 * (f_air_WGS / 8) ^ 0.5
* (Prandtl_air_WGS ^ (2 / 3) - 1))
hrt_air_WGS = Nusselt_air_WGS * k_air_WGS /
d_tubing_interior            % W/m^2-K
% The overall heat transfer coefficients of the two species
are then
% determined as follows
U_air_WGS = 1 / (1 / het_WGS_732 + d_wall / k_tubing + 1 /
hrt_air_WGS)           % W/m^2-K
% Find the heat exchanged by air.
Q_air_WGS = m_air * (h_air_473 - h_air_298);
% J/min
% Find the logarithmic mean temperature difference (LMTD).
Delta_Ta_air_WGS = T_WGS_C12H26 - T_air_WGS;
% K
% Decide the temperature of effluents after the heat
exchanging with air.
syms t_WGS_air
t_WGS_air = vpasolve(Q_H2O_WGS == n_CO2_WGS * 1000 *
(24.99735 * (t_WGS_air - 0.473) + 55.18696 / 2 *
(t_WGS_air^2 - 0.473^2) - 33.69137 / 3 * (t_WGS_air^3 -
```

```
0.473^3) + 7.948387 / 4 * (t_WGS_air^4 - 0.473^4) +
0.136638 * (1/t_WGS_air - 1/0.473)) + n_H2O_WGS * 1000 *
(30.09200 * (t_WGS_air - 0.473) + 6.832514 / 2 *
(t_WGS_air^2 - 0.473^2) + 6.793435 / 3 * (t_WGS_air^3 -
0.473^3) - 2.534480 / 4 * (t_WGS_air^4 - 0.473^4) -
0.082139 *(1/t_WGS_air - 1/0.473)) + n_H2_WGS * 1000 *
(33.066178 * (t_WGS_air - 0.473) - 11.363417 / 2 *
(t_WGS_air^2 - 0.473^2) + 11.432816 / 3 * (t_WGS_air^3 -
0.473^3) - 2.772874 / 4 * (t_WGS_air^4 - 0.473^4) +
0.158558 * (1/t_WGS_air - 1/0.473)) + n_N2 * 1000 *
(19.50583 * (t_WGS_air - 0.473) + 19.88705 / 2 *
(t_WGS_air^2 - 0.473^2) - 8.598535 / 3 * (t_WGS_air^3 -
0.473^3) + 1.369784 / 4 * (t_WGS_air^4 - 0.473^4) -
0.527601 * (1/t_WGS_air - 1/0.473)), t_WGS_air, [0 Inf]);
T_WGS_air = t_WGS_air * 1000                % K
Delta_Tb_air_WGS = T_WGS_air - 298;         % K
LMTD_air_WGS = (Delta_Ta_air_WGS - Delta_Tb_air_WGS) /
log(Delta_Ta_air_WGS / Delta_Tb_air_WGS);    % K
Length_air_WGS = Q_air_WGS / 60 / LMTD_air_WGS / U_air_WGS
/ Perimeter_tubing_exterior     % m

% Determine heat transfer process for H2O in the secondary
recuperator.
mu_N2_WGS_672 = 0.000031943;            % kg/m-s
mu_CO2_WGS_672 = 0.000030675;           % kg/m-s
mu_H2_WGS_672 = 0.000015485;            % kg/m-s
mu_H2O_WGS_672 = 0.000024406;           % kg/m-s
f_WGS_672 = Y_N2_WGS ^ 2 / mu_N2_WGS_672 + Y_CO2_WGS ^ 2 /
mu_CO2_WGS_672 + Y_H2_WGS ^ 2 / mu_H2_WGS_672 + Y_H2O_WGS ^
2 / mu_H2O_WGS_672 + 2 * Y_N2_WGS * Y_CO2_WGS * Ee_N2CO2 ^
A / ((mu_N2_WGS_672 * mu_CO2_WGS_672) ^ (1 / 2)) + 2 *
Y_N2_WGS * Y_H2_WGS * Ee_N2H2 ^ A / ((mu_N2_WGS_672 *
mu_H2_WGS_672) ^ (1 / 2)) + 2 * Y_N2_WGS * Y_H2O_WGS *
Ee_N2H2O ^ A / ((mu_N2_WGS_672 * mu_H2O_WGS_672) ^ (1 / 2))
+ 2 * Y_CO2_WGS * Y_H2_WGS * Ee_CO2H2 ^ A /
((mu_CO2_WGS_672 * mu_H2_WGS_672) ^ (1 / 2)) + 2 *
Y_CO2_WGS * Y_H2O_WGS * Ee_CO2H2O ^ A / ((mu_CO2_WGS_672 *
mu_H2O_WGS_672) ^ (1 / 2)) + 2 * Y_H2_WGS * Y_H2O_WGS *
Ee_H2H2O ^ A / ((mu_H2_WGS_672 * mu_H2O_WGS_672) ^ (1 /
2));
% m-s/kg
mu_WGS_672 = 1 / f_WGS_672;              % kg/m-s
Reynolds_tubing_WGS_672 = m_WGS / 1000 / 60 / Area_reactor
* d_tubing_exterior / mu_WGS_672
Cp_N2_WGS_672 = 19.50583 + 19.88705 * t_WGS_air - 8.598535
* t_WGS_air ^ 2 + 1.369784 * t_WGS_air ^ 3 + 0.527601 /
t_WGS_air ^ 2;     % J/mol-K
```

```
Cp_CO2_WGS_672 = 24.99735 + 55.18696 * t_WGS_air -
33.69137* t_WGS_air ^ 2 + 7.948387 * t_WGS_air ^ 3 -
0.136638 / t_WGS_air ^ 2;    % J/mol-K
Cp_H2_WGS_672 = 33.066178 - 11.363417 * t_WGS_air +
11.432816 * t_WGS_air ^ 2 - 2.772874 * t_WGS_air ^ 3 -
0.158558 / t_WGS_air ^ 2;  % J/mol-K
Cp_H2O_WGS_672 = 30.09200 + 6.832514 * t_WGS_air + 6.793435
* t_WGS_air ^ 2 - 2.534480 * t_WGS_air ^ 3 + 0.082139 /
t_WGS_air ^ 2;    % J/mol-K
Cp_WGS_672 = (X_N2_WGS * Cp_N2_WGS_672 + X_CO2_WGS *
Cp_CO2_WGS_672 + X_H2_WGS * Cp_H2_WGS_672 + X_H2O_WGS *
Cp_H2O_WGS_672) / (M_WGS / 1000);    % J/kg-K
phi_N2CO2_WGS_672 = (1 + (mu_N2_WGS_672 / mu_CO2_WGS_672) ^
0.5 * (M_CO2 / M_N2) ^ 0.25) ^ 2 / (8 ^ 0.5 * (1 +  M_N2 /
M_CO2) ^ 0.5);
phi_N2H2_WGS_672 = (1 + (mu_N2_WGS_672 / mu_H2_WGS_672) ^
0.5 * (M_H2 / M_N2) ^ 0.25) ^ 2 / (8 ^ 0.5 * (1 +  M_N2 /
M_H2) ^ 0.5);
phi_N2H2O_WGS_672 = (1 + (mu_N2_WGS_672 / mu_H2O_WGS_672) ^
0.5 * (M_H2O / M_N2) ^ 0.25) ^ 2 / (8 ^ 0.5 * (1 +  M_N2 /
M_H2O) ^ 0.5);
phi_CO2N2_WGS_672 = (1 + (mu_CO2_WGS_672 / mu_N2_WGS_672) ^
0.5 * (M_N2 / M_CO2) ^ 0.25) ^ 2 / (8 ^ 0.5 * (1 +  M_CO2 /
M_N2) ^ 0.5);
phi_CO2H2_WGS_672 = (1 + (mu_CO2_WGS_672 / mu_H2_WGS_672) ^
0.5 * (M_H2 / M_CO2) ^ 0.25) ^ 2 / (8 ^ 0.5 * (1 +  M_CO2 /
M_H2) ^ 0.5);
phi_CO2H2O_WGS_672 = (1 + (mu_CO2_WGS_672 / mu_H2O_WGS_672)
^ 0.5 * (M_H2O / M_CO2) ^ 0.25) ^ 2 / (8 ^ 0.5 * (1 +
M_CO2 / M_H2O) ^ 0.5);
phi_H2N2_WGS_672 = (1 + (mu_H2_WGS_672 / mu_N2_WGS_672) ^
0.5 * (M_N2 / M_H2) ^ 0.25) ^ 2 / (8 ^ 0.5 * (1 +  M_H2 /
M_N2) ^ 0.5);
phi_H2CO2_WGS_672 = (1 + (mu_H2_WGS_672 / mu_CO2_WGS_672) ^
0.5 * (M_CO2 / M_H2) ^ 0.25) ^ 2 / (8 ^ 0.5 * (1 +  M_H2 /
M_CO2) ^ 0.5);
phi_H2H2O_WGS_672 = (1 + (mu_H2_WGS_672 / mu_H2O_WGS_672) ^
0.5 * (M_H2O / M_H2) ^ 0.25) ^ 2 / (8 ^ 0.5 * (1 +  M_H2 /
M_H2O) ^ 0.5);
phi_H2ON2_WGS_672 = (1 + (mu_H2O_WGS_672 / mu_N2_WGS_672) ^
0.5 * (M_N2 / M_H2O) ^ 0.25) ^ 2 / (8 ^ 0.5 * (1 +  M_H2O /
M_N2) ^ 0.5);
phi_H2OCO2_WGS_672 = (1 + (mu_H2O_WGS_672 / mu_CO2_WGS_672)
^ 0.5 * (M_CO2 / M_H2O) ^ 0.25) ^ 2 / (8 ^ 0.5 * (1 +
M_H2O / M_CO2) ^ 0.5);
```

```
phi_H2OH2_WGS_672 = (1 + (mu_H2O_WGS_672 / mu_H2_WGS_672) ^
0.5 * (M_H2 / M_H2O) ^ 0.25) ^ 2 / (8 ^ 0.5 * (1 +  M_H2O /
M_H2) ^ 0.5);
k_N2_WGS_672 = 48.804e-3;             % W/m-K
k_CO2_WGS_672 = 47.161e-3;            % W/m-K
k_H2_WGS_672 = 0.36274;               % W/m-K
k_H2O_WGS_672 = 54.625e-3;            % W/m-K
k_WGS_672 = X_N2_WGS * k_N2_WGS_672 / (X_N2_WGS + X_CO2_WGS
* phi_N2CO2_WGS_672 + X_H2_WGS * phi_N2H2_WGS_672 +
X_H2O_WGS * phi_N2H2O_WGS_672) + X_CO2_WGS * k_CO2_WGS_672
/ (X_N2_WGS * phi_CO2N2_WGS_672 + X_CO2_WGS + X_H2_WGS *
phi_CO2H2_WGS_672 + X_H2O_WGS * phi_CO2H2O_WGS_672) +
X_H2_WGS * k_H2_WGS_672 / (X_N2_WGS * phi_H2N2_WGS_672 +
X_CO2_WGS * phi_H2CO2_WGS_672 + X_H2_WGS + X_H2O_WGS *
phi_H2H2O_WGS_672) + X_H2O_WGS * k_H2O_WGS_672 / (X_N2_WGS
* phi_H2ON2_WGS_672 + X_CO2_WGS * phi_H2OCO2_WGS_672 +
X_H2_WGS * phi_H2OH2_WGS_672 + X_H2O_WGS); % W/m-K
Prandtl_WGS_672 = Cp_WGS_672 * mu_WGS_672 / k_WGS_672
fn_Reynolds_tubing_WGS_672 = 0.8 * Reynolds_tubing_WGS_672
^ 0.4;
Nusselt_WGS_672 = Prandtl_WGS_672 ^ 0.36 *
fn_Reynolds_tubing_WGS_672
het_WGS_672 = Nusselt_WGS_672 * k_WGS_672 /
d_tubing_exterior          % W/m^2-K
% For H2O heat transfer, a forced convection boiling
process in tubes need
% to be carried out in order to predict the
Nusselt_H2O_WGS. Here we apply
% Chen's method which is complex but fairly accurate. The
first step is to
% calculate the Martinelli parameter Xtt_H2O_WGS = ((1 -
x_H2O_WGS) /
% x_H2O_WGS) ^ 0.9 * (rhog_H2O_WGS / rhof_H2O_WGS) ^ 0.5 *
(muf_H2O_WGS /
% mug_H2O_WGS) ^ 0.1, where x_H2O_WGS is the quality of
water.
x_H2O_WGS = 0.38608;
rhog_H2O_WGS = 1.6507;          % kg/m^3
rhof_H2O_WGS = 931.82;          % kg/m^3
muf_H2O_WGS = 0.00020692;       % kg/m-s
mug_H2O_WGS = 0.000013394;      % kg/m-s
Xtt_H2O_WGS = ((1 - x_H2O_WGS) / x_H2O_WGS) ^ 0.9 *
(rhog_H2O_WGS / rhof_H2O_WGS) ^ 0.5 * (muf_H2O_WGS /
mug_H2O_WGS) ^ 0.1;
% Then from a empirical figure, the ratio of the two-phase
Reynolds number,
```

```
% ReynoldsTP_H2O_WGS to the conventional liquid-phase
Reynolds number,
% Reynoldsf_H2O_WGS - F_H2O_WGS is obtained.
F_H2O_WGS = 11.6;
% Calculate the superficial mas flux, G_H2O_WGS through the
tubing.
G_H2O_WGS = m_H2O / 60 / 1000 / (pi * (d_tubing_interior /
2) ^ 2);     % kg/m^2-s
% Calculate the ReynoldsTP_H2O_WGS.
ReynoldsTP_H2O_WGS = F_H2O_WGS ^ 1.25 * G_H2O_WGS * (1 -
x_H2O_WGS) * d_tubing_interior / muf_H2O_WGS
% Calculate the single-phase heat transfer coefficient,
hrtc_H2O_WGS from
% the Dittus-Boelter equation.
k_H2O_r_WGS = 0.4;              % W/m-K
Cp_H2O_r_WGS = 3.1813e3;        % J/kg-K
Prandtl_H2O_WGS = Cp_H2O_r_WGS * 1000 * muf_H2O_WGS /
k_H2O_r_WGS
hrtc_H2O_WGS = 0.0246 * k_H2O_r_WGS / d_tubing_interior *
Prandtl_H2O_WGS ^ 0.4 * ReynoldsTP_H2O_WGS ^ 0.8;
% Obtain the empirical factor S_H2O_WGS value from figure
at the known
% value of ReynoldsTP_H2O_WGS.
S_H2O_WGS = 0.64;
% Calculate a nucleate boiling heat transfer coefficient
hrtNB_H2O_WGS.
sigma_H2O_WGS = 52.204e-3;      % N/m, surface tension
hfg_H2O_WGS = 2163.5e3;         % J/kg
Delta_T_H2O_WGS = 5;            % K
Delta_p_H2O_WGS = 236400;       % N/m^2
hrtNB_H2O_WGS = 0.00122 * k_H2O_r_WGS ^ 0.79 * Cp_H2O_r_WGS
^ 0.45 * rhof_H2O_WGS ^ 0.49 / sigma_H2O_WGS^ 0.5 /
muf_H2O_WGS ^ 0.29 / hfg_H2O_WGS ^ 0.24 / rhog_H2O_WGS ^
0.24 * Delta_T_H2O_WGS ^ 0.24 * Delta_p_H2O_WGS ^ 0.75;  %
W/m^2-K
hrt_H2O_WGS = S_H2O_WGS * hrtNB_H2O_WGS + hrtc_H2O_WGS
% W/m^2-K
U_H2O_WGS = 1 / (1 / het_WGS_672 + d_wall / k_tubing + 1 /
hrt_H2O_WGS)        % W/m^2-K
% After all the heat transfer coefficients are calculated,
the heat
% exchanging area can be found based on the couter flow
heat exchanger
% design process.
Delta_Ta_H2O_WGS = T_WGS_air - T_H2O_WGS;             % K
T_WGS_H2O = 473;                                      % K
Delta_Tb_H2O_WGS = T_WGS_H2O - 298;                   % K
```

```
LMTD_H2O_WGS = (Delta_Ta_H2O_WGS - Delta_Tb_H2O_WGS) /
log(Delta_Ta_H2O_WGS / Delta_Tb_H2O_WGS);    % K
Length_H2O_WGS = Q_H2O_WGS / 60 / LMTD_H2O_WGS / U_H2O_WGS
/ Perimeter_tubing_exterior     % m

% First recuperator design
% Similar to the secondary recuperator, the overall heat
transfer
% coefficient U_ATR consists of three parts, heat
convective coefficient of
% the effluent in the reactor against the exterior wall of
the heat
% exchange tubing het_ATR, heat conductive coefficient of
the tubing wall
% k_tubing, and the heat convective coefficient of the
reactant (i.e. fuel,
% water, air) in the passages against the interior wall of
the tubing
% hrt_ATR. U_ATR = 1 / (1 / het_ATR + d_wall / k_tubing + 1
/ hrt_ATR).
% For calculation of het_ATR, het_ATR = Nusselt_ATR * k_ATR
/
% d_tubing_exterior, where Nusselt_ATR is the nusselt
number of tubing and
% effluent flow, k_ATR is the thermal conductivity of the
effluent.
% In order to find Nusselt_ATR, appropriate correlation of
heat transfer
% process for flow across tube bundles needs to be found.
Then first of
% all, we need to know the Reynolds number
Reynolds_tubing_ATR and Prandtl
% number Prandtl_ATR. Reynolds_tubing_ATR = rho_ATR * u_ATR
*
% d_tubing_exterior / mu_ATR = m_ATR / Area_reactor *
d_tubing_exterior /
% mu_ATR, Prandtl_ATR = Cp_ATR * mu_ATR / k_ATR, where
m_ATR is the mass
% flow rate of effluent mixture, mu_ATR, Cp_ATR and k_ATR
are the
% viscosity, heat capacity and thermal conductivity of the
mixture,
% respectively.
% For ATR reaction, the composition of effluent is 7.5CO +
4.5CO2 + 18.7H2
% + 12.3H2O + 20.3N2 and the temperature T_ATR = 1123 K,
% T_reforming_out = T_ATR_H2O = 623 K.
```

```
T_ATR = 1123;                % K
t_ATR = T_ATR / 1000;
T_ATR_H2O = 623;             % K
m_ATR = n_N2 * M_N2 + n_CO_ATR * M_CO + n_CO2_ATR * M_CO2 +
n_H2_ATR * M_H2 + n_H2O_ATR + M_H2O;      % g/min
X_N2_ATR = n_N2 / (n_N2 + n_CO2_ATR + n_H2_ATR + n_H2O_ATR
+ n_CO_ATR)
X_CO2_ATR = n_CO2_ATR / (n_N2 + n_CO2_ATR + n_H2_ATR +
n_H2O_ATR + n_CO_ATR)
X_H2_ATR = n_H2_ATR / (n_N2 + n_CO2_ATR + n_H2_ATR +
n_H2O_ATR + n_CO_ATR)
X_H2O_ATR = n_H2O_ATR / (n_N2 + n_CO2_ATR + n_H2_ATR +
n_H2O_ATR)
X_CO_ATR = n_CO_ATR / (n_N2 + n_CO2_ATR + n_H2_ATR +
n_H2O_ATR + n_CO_ATR)
Y_N2_ATR = X_N2_ATR * M_N2 ^ (1 / 2) / (X_N2_ATR * M_N2 ^
(1 / 2) + X_CO2_ATR * M_CO2 ^ (1 / 2) + X_H2_ATR * M_H2 ^
(1 / 2) + X_H2O_ATR * M_H2O ^ (1 / 2) + X_CO_ATR * M_CO ^
(1 / 2));
Y_CO2_ATR = X_CO2_ATR * M_CO2 ^ (1 / 2) / (X_N2_ATR * M_N2
^ (1 / 2) + X_CO2_ATR * M_CO2 ^ (1 / 2) + X_H2_ATR * M_H2 ^
(1 / 2) + X_H2O_ATR * M_H2O ^ (1 / 2) + X_CO_ATR * M_CO ^
(1 / 2));
Y_H2_ATR = X_H2_ATR * M_H2 ^ (1 / 2) / (X_N2_ATR * M_N2 ^
(1 / 2) + X_CO2_ATR * M_CO2 ^ (1 / 2) + X_H2_ATR * M_H2 ^
(1 / 2) + X_H2O_ATR * M_H2O ^ (1 / 2) + X_CO_ATR * M_CO ^
(1 / 2));
Y_H2O_ATR = X_H2O_ATR * M_H2O ^ (1 / 2) / (X_N2_ATR * M_N2
^ (1 / 2) + X_CO2_ATR * M_CO2 ^ (1 / 2) + X_H2_ATR * M_H2 ^
(1 / 2) + X_H2O_ATR * M_H2O ^ (1 / 2) + X_CO_ATR * M_CO ^
(1 / 2));
Y_CO_ATR = X_CO_ATR * M_CO ^ (1 / 2) / (X_N2_ATR * M_N2 ^
(1 / 2) + X_CO2_ATR * M_CO2 ^ (1 / 2) + X_H2_ATR * M_H2 ^
(1 / 2) + X_H2O_ATR * M_H2O ^ (1 / 2) + X_CO_ATR * M_CO ^
(1 / 2));
mu_N2_ATR_1123 = 0.000044797;            % kg/m-s
mu_CO2_ATR_1123 = 4.4712e-5;          % kg/m-s
mu_H2_ATR_1123 = 2.004e-5;            % kg/m-s
mu_H2O_ATR_1123 = 4.2322e-5;          % kg/m-s
mu_CO_ATR_1123 = 4.3318e-5;           % kg/m-s
m_N2_ATR = n_N2 * M_N2;           % g/min
m_CO2_ATR = n_CO2_ATR * M_CO2;    % g/min
m_H2_ATR = n_H2_ATR * M_H2;       % g/min
m_H2O_ATR = n_H2O_ATR * M_H2O;    % g/min
m_CO_ATR = n_CO_ATR * M_CO;       % g/min
Ee_N2CO2 = 2 * (m_N2_ATR * m_CO2_ATR) ^ (1 / 2) / (m_N2_ATR
+ m_CO2_ATR);
```

```
Ee_N2H2 = 2 * (m_N2_ATR * m_H2_ATR) ^ (1 / 2) / (m_N2_ATR +
m_H2_ATR);
Ee_N2H2O = 2 * (m_N2_ATR * m_H2O_ATR) ^ (1 / 2) / (m_N2_ATR
+ m_H2O_ATR);
Ee_N2CO = 2 * (m_N2_ATR * m_CO_ATR) ^ (1 / 2) / (m_N2_ATR +
m_CO_ATR);
Ee_CO2H2 = 2 * (m_CO2_ATR * m_H2_ATR) ^ (1 / 2) /
(m_CO2_ATR + m_H2_ATR);
Ee_CO2H2O = 2 * (m_CO2_ATR * m_H2O_ATR) ^ (1 / 2) /
(m_CO2_ATR + m_H2O_ATR);
Ee_CO2CO = 2 * (m_CO2_ATR * m_CO_ATR) ^ (1 / 2) /
(m_CO2_ATR + m_CO_ATR);
Ee_H2H2O = 2 * (m_H2_ATR * m_H2O_ATR) ^ (1 / 2) / (m_H2_ATR
+ m_H2O_ATR);
Ee_H2CO = 2 * (m_H2_ATR * m_CO_ATR) ^ (1 / 2) / (m_H2_ATR +
m_CO_ATR);
Ee_H2OCO = 2 * (m_H2O_ATR * m_CO_ATR) ^ (1 / 2) /
(m_H2O_ATR + m_CO_ATR);
f_ATR_1123 = Y_N2_ATR ^ 2 / mu_N2_ATR_1123 + Y_CO2_ATR ^ 2
/ mu_CO2_ATR_1123 + Y_H2_ATR ^ 2 / mu_H2_ATR_1123 +
Y_H2O_ATR ^ 2 / mu_H2O_ATR_1123 + Y_CO_ATR ^ 2 /
mu_CO_ATR_1123 + 2 * Y_N2_ATR * Y_CO2_ATR * Ee_N2CO2 ^ A /
((mu_N2_ATR_1123 * mu_CO2_ATR_1123) ^ (1 / 2)) + 2 *
Y_N2_ATR * Y_H2_ATR * Ee_N2H2 ^ A / ((mu_N2_ATR_1123 *
mu_H2_ATR_1123) ^ (1 / 2)) + 2 * Y_N2_ATR * Y_H2O_ATR *
Ee_N2H2O ^ A / ((mu_N2_ATR_1123 * mu_H2O_ATR_1123) ^ (1 /
2)) + 2 * Y_N2_ATR * Y_CO_ATR * Ee_N2CO ^ A /
((mu_N2_ATR_1123 * mu_CO_ATR_1123) ^ (1 / 2)) + 2 *
Y_CO2_ATR * Y_H2_ATR * Ee_CO2H2 ^ A / ((mu_CO2_ATR_1123 *
mu_H2_ATR_1123) ^ (1 / 2)) + 2 * Y_CO2_ATR * Y_H2O_ATR *
Ee_CO2H2O ^ A / ((mu_CO2_ATR_1123 * mu_H2O_ATR_1123) ^ (1 /
2)) + 2 * Y_CO2_ATR * Y_CO_ATR * Ee_CO2CO ^ A /
((mu_CO2_ATR_1123 * mu_CO_ATR_1123) ^ (1 / 2)) + 2 *
Y_H2_ATR * Y_H2O_ATR * Ee_H2H2O ^ A / ((mu_H2_ATR_1123 *
mu_H2O_ATR_1123) ^ (1 / 2)) + 2 * Y_H2_ATR * Y_CO_ATR *
Ee_H2CO ^ A / ((mu_H2_ATR_1123 * mu_CO_ATR_1123) ^ (1 / 2))
+ 2 * Y_H2O_ATR * Y_CO_ATR * Ee_H2OCO ^ A /
((mu_H2O_ATR_1123 * mu_CO_ATR_1123) ^ (1 / 2));
% m-s/kg
mu_ATR_1123 = 1 / f_ATR_1123;               % kg/m-s
Reynolds_tubing_ATR_1123 = m_ATR / 1000 / 60 / Area_reactor
* d_tubing_exterior / mu_ATR_1123
Cp_N2_ATR_1123 = 19.50583 + 19.88705 * t_ATR - 8.598535 *
t_ATR ^ 2 + 1.369784 * t_ATR ^ 3 + 0.527601 / t_ATR ^ 2;
% J/mol-K
```

```
Cp_CO2_ATR_1123 = 24.99735 + 55.18696 * t_ATR - 33.69137*
t_ATR ^ 2 + 7.948387 * t_ATR ^ 3 -  0.136638 / t_ATR ^ 2;
% J/mol-K
Cp_H2_ATR_1123 = 33.066178 - 11.363417 * t_ATR + 11.432816
* t_ATR ^ 2 - 2.772874 * t_ATR ^ 3 - 0.158558 / t_ATR ^ 2;
% J/mol-K
Cp_H2O_ATR_1123 = 30.09200 + 6.832514 * t_ATR + 6.793435 *
t_ATR ^ 2 - 2.534480 * t_ATR ^ 3 + 0.082139 / t_ATR ^ 2;
% J/mol-K
Cp_CO_ATR_1123 = 25.56759 + 6.096130 * t_ATR + 4.054656 *
t_ATR ^ 2 - 2.671301 * t_ATR ^ 3 + 0.131021 / (t_ATR ^ 2);
% J/mol-K
M_ATR = X_N2_ATR * M_N2 + X_CO2_ATR * M_CO2 + X_H2_ATR *
M_H2 + X_H2O_ATR * M_H2O + X_CO_ATR * M_CO;              %
g/mol
Cp_ATR_1123 = (X_N2_ATR * Cp_N2_ATR_1123 + X_CO2_ATR *
Cp_CO2_ATR_1123 + X_H2_ATR * Cp_H2_ATR_1123 + X_H2O_ATR *
Cp_H2O_ATR_1123 + X_CO_ATR * Cp_CO_ATR_1123) / (M_ATR /
1000);  % J/kg-K
phi_N2CO2_ATR_1123 = (1 + (mu_N2_ATR_1123 /
mu_CO2_ATR_1123) ^ 0.5 * (M_CO2 / M_N2) ^ 0.25) ^ 2 / (8 ^
0.5 * (1 +  M_N2 / M_CO2) ^ 0.5);
phi_N2H2_ATR_1123 = (1 + (mu_N2_ATR_1123 / mu_H2_ATR_1123)
^ 0.5 * (M_H2 / M_N2) ^ 0.25) ^ 2 / (8 ^ 0.5 * (1 +  M_N2 /
M_H2) ^ 0.5);
phi_N2H2O_ATR_1123 = (1 + (mu_N2_ATR_1123 /
mu_H2O_ATR_1123) ^ 0.5 * (M_H2O / M_N2) ^ 0.25) ^ 2 / (8 ^
0.5 * (1 +  M_N2 / M_H2O) ^ 0.5);
phi_N2CO_ATR_1123 = (1 + (mu_N2_ATR_1123 / mu_CO_ATR_1123)
^ 0.5 * (M_CO / M_N2) ^ 0.25) ^ 2 / (8 ^ 0.5 * (1 +  M_N2 /
M_CO) ^ 0.5);
phi_CO2N2_ATR_1123 = (1 + (mu_CO2_ATR_1123 /
mu_N2_ATR_1123) ^ 0.5 * (M_N2 / M_CO2) ^ 0.25) ^ 2 / (8 ^
0.5 * (1 +  M_CO2 / M_N2) ^ 0.5);
phi_CO2H2_ATR_1123 = (1 + (mu_CO2_ATR_1123 /
mu_H2_ATR_1123) ^ 0.5 * (M_H2 / M_CO2) ^ 0.25) ^ 2 / (8 ^
0.5 * (1 +  M_CO2 / M_H2) ^ 0.5);
phi_CO2H2O_ATR_1123 = (1 + (mu_CO2_ATR_1123 /
mu_H2O_ATR_1123) ^ 0.5 * (M_H2O / M_CO2) ^ 0.25) ^ 2 / (8 ^
0.5 * (1 +  M_CO2 / M_H2O) ^ 0.5);
phi_CO2CO_ATR_1123 = (1 + (mu_CO2_ATR_1123 /
mu_CO_ATR_1123) ^ 0.5 * (M_CO / M_CO2) ^ 0.25) ^ 2 / (8 ^
0.5 * (1 +  M_CO2 / M_CO) ^ 0.5);
phi_H2N2_ATR_1123 = (1 + (mu_H2_ATR_1123 / mu_N2_ATR_1123)
^ 0.5 * (M_N2 / M_H2) ^ 0.25) ^ 2 / (8 ^ 0.5 * (1 +  M_H2 /
M_N2) ^ 0.5);
```

```
phi_H2CO2_ATR_1123 = (1 + (mu_H2_ATR_1123 /
mu_CO2_ATR_1123) ^ 0.5 * (M_CO2 / M_H2) ^ 0.25) ^ 2 / (8 ^
0.5 * (1 +  M_H2 / M_CO2) ^ 0.5);
phi_H2H2O_ATR_1123 = (1 + (mu_H2_ATR_1123 /
mu_H2O_ATR_1123) ^ 0.5 * (M_H2O / M_H2) ^ 0.25) ^ 2 / (8 ^
0.5 * (1 +  M_H2 / M_H2O) ^ 0.5);
phi_H2CO_ATR_1123 = (1 + (mu_H2_ATR_1123 / mu_CO_ATR_1123)
^ 0.5 * (M_CO / M_H2) ^ 0.25) ^ 2 / (8 ^ 0.5 * (1 +  M_H2 /
M_CO) ^ 0.5);
phi_H2ON2_ATR_1123 = (1 + (mu_H2O_ATR_1123 /
mu_N2_ATR_1123) ^ 0.5 * (M_N2 / M_H2O) ^ 0.25) ^ 2 / (8 ^
0.5 * (1 +  M_H2O / M_N2) ^ 0.5);
phi_H2OCO2_ATR_1123 = (1 + (mu_H2O_ATR_1123 /
mu_CO2_ATR_1123) ^ 0.5 * (M_CO2 / M_H2O) ^ 0.25) ^ 2 / (8 ^
0.5 * (1 +  M_H2O / M_CO2) ^ 0.5);
phi_H2OH2_ATR_1123 = (1 + (mu_H2O_ATR_1123 /
mu_H2_ATR_1123) ^ 0.5 * (M_H2 / M_H2O) ^ 0.25) ^ 2 / (8 ^
0.5 * (1 +  M_H2O / M_H2) ^ 0.5);
phi_H2OCO_ATR_1123 = (1 + (mu_H2O_ATR_1123 /
mu_CO_ATR_1123) ^ 0.5 * (M_CO / M_H2O) ^ 0.25) ^ 2 / (8 ^
0.5 * (1 +  M_H2O / M_CO) ^ 0.5);
phi_CON2_ATR_1123 = (1 + (mu_CO_ATR_1123 / mu_N2_ATR_1123)
^ 0.5 * (M_N2 / M_CO) ^ 0.25) ^ 2 / (8 ^ 0.5 * (1 +  M_CO /
M_N2) ^ 0.5);
phi_COH2_ATR_1123 = (1 + (mu_CO_ATR_1123 / mu_H2_ATR_1123)
^ 0.5 * (M_H2 / M_CO) ^ 0.25) ^ 2 / (8 ^ 0.5 * (1 +  M_CO /
M_H2) ^ 0.5);
phi_COH2O_ATR_1123 = (1 + (mu_CO_ATR_1123 /
mu_H2O_ATR_1123) ^ 0.5 * (M_H2O / M_CO) ^ 0.25) ^ 2 / (8 ^
0.5 * (1 +  M_CO / M_H2O) ^ 0.5);
phi_COCO2_ATR_1123 = (1 + (mu_CO_ATR_1123 /
mu_CO2_ATR_1123) ^ 0.5 * (M_CO2 / M_CO) ^ 0.25) ^ 2 / (8 ^
0.5 * (1 +  M_CO / M_CO2) ^ 0.5);
k_N2_ATR_1123 = 71.142e-3;            % W/m-K
k_CO2_ATR_1123 = 78.489e-3;           % W/m-K
k_H2_ATR_1123 = 524.80e-3;            % W/m-K
k_H2O_ATR_1123 = 114.40e-3;           % W/m-K
k_CO_ATR_1123 = 76.61e-3;             % W/m-K
k_ATR_1123 = X_N2_ATR * k_N2_ATR_1123 / (X_N2_ATR +
X_CO2_ATR * phi_N2CO2_ATR_1123 + X_H2_ATR *
phi_N2H2_ATR_1123 + X_H2O_ATR * phi_N2H2O_ATR_1123 +
X_CO_ATR * phi_N2CO_ATR_1123) + X_CO2_ATR * k_CO2_ATR_1123
/ (X_N2_ATR * phi_CO2N2_ATR_1123 + X_CO2_ATR + X_H2_ATR *
phi_CO2H2_ATR_1123 + X_H2O_ATR * phi_CO2H2O_ATR_1123 +
X_CO_ATR * phi_CO2CO_ATR_1123) + X_H2_ATR * k_H2_ATR_1123 /
(X_N2_ATR * phi_H2N2_ATR_1123 + X_CO2_ATR *
phi_H2CO2_ATR_1123 + X_H2_ATR + X_H2O_ATR *
```

```
phi_H2H2O_ATR_1123 + X_CO_ATR * phi_H2CO_ATR_1123) +
X_H2O_ATR * k_H2O_ATR_1123 / (X_N2_ATR * phi_H2ON2_ATR_1123
+ X_CO2_ATR * phi_H2OCO2_ATR_1123 + X_H2_ATR *
phi_H2OH2_ATR_1123 + X_H2O_ATR + X_CO_ATR *
phi_H2OCO_ATR_1123) + X_CO_ATR * k_CO_ATR_1123 / (X_N2_ATR
* phi_CON2_ATR_1123 + X_CO2_ATR * phi_COCO2_ATR_1123 +
X_H2_ATR * phi_COH2_ATR_1123 + X_H2O_ATR *
phi_COH2O_ATR_1123 + X_CO_ATR);
% W/m-K
Prandtl_ATR_1123 = Cp_ATR_1123 * mu_ATR_1123 / k_ATR_1123
% Under this Reynolds number and Prandtl number the
correlation is
% presented by Zukauskas in the following way: Nusselt_ATR
= Prandtl_ATR ^
% 0.36 * fn_Reynolds_tubing_ATR, where
fn_Reynolds_tubing_ATR = 0.8 *
% Reynolds_tubing_ATR ^ 0.4.
fn_Reynolds_tubing_ATR_1123 = 0.8 *
Reynolds_tubing_ATR_1123 ^ 0.4;
Nusselt_ATR_1123 = Prandtl_ATR_1123 ^ 0.36 *
fn_Reynolds_tubing_ATR_1123
het_ATR_1123 = Nusselt_ATR_1123 * k_ATR_1123 /
d_tubing_exterior         % W/m^2-K
% As the temperature in this area is quite high, we can
assume that all the
% three reactants are under gaseous state during the most
of the passages.
% Then based on the temperature the Reynolds number,
Prandtl number
% as well as Nusselt number need to be determined for all
the three
% species.
% Reynolds_tubing_i_ATR = 4 * m_i /
Perimeter_tubing_interior / mu_i_ATR,
% Prandtl_i_ATR = Cp_i_ATR * mu_i_ATR / k_i_ATR.
% As high temperature will cause C12H26 becoming carbon,
T_C12H26 should
% not be higher than 160oC. We assume C12H26 injects
directly into the ATR
% reactor from the secondary recuperator. Therefore the
necessary heat
% supply for increasing the T_C12H26 from 160oC to 600oC
needs to shift to
% water and air. Here water is assumed to carry out the
energy first.
hf_C12H26_433_ATR = -290720 + (2.273845 * (433 - T0) -
4.559779e-3 / 2 * (433 ^ 2 - T0 ^ 2) + 1.843537e-5 / 3 *
```

```
(433 ^ 3 - T0 ^ 3) - 1.306521e-8 / 4 * (433 ^ 4 - T0 ^ 4))
* M_C12H26;   % kJ/kmol
hg_H2O_800 = 3546.3;      % kJ/kg
syms hg_H2Or_T_ATR
hg_H2Or_T_ATR = vpasolve(n_C12H26 * (hg_C12H26_800 -
hf_C12H26_433_ATR) + m_H2O * (hg_H2O_800 - hfg_H2O_T_WGS)
== m_H2O * (hg_H2Or_T_ATR - hfg_H2O_T_WGS), hg_H2Or_T_ATR)
% kJ/kg
% Find T_H2Or_ATR based on the hg_H2Or_T_ATR.
T_H2Or_ATR = 924.49;      % K
% Calculate water heat exchange coefficient.
mu_H2O_ATR = 0.000024097;       % kg/m-s
Reynolds_H2O_ATR = 4 * m_H2O / 1000 / 60 /
Perimeter_tubing_interior / mu_H2O_ATR
Cp_H2O_ATR = 2.1187;            % J/g-K
k_H2O_ATR = 57.153e-3;          % W/m-K
Prandtl_H2O_ATR = Cp_H2O_ATR * 1000 * mu_H2O_ATR /
k_H2O_ATR
% Based on the Reynods number and Prandtl number derived
above, the heat
% tranfer process of water can be described as the average
value of the h
% calculated by the same method as the calculation for
boiling inside the
% tubing and the h calculated by Gnielinski's correlation.
% By Chen's method.
hrt_H2O_ATR_C = 1.2240e+05;    % W/m^2-K
% By Gnielinski's correlation.
f_H2O_ATR = (0.79 * log(Reynolds_H2O_ATR) - 1.64) ^ (-2);
Nusselt_H2O_ATR_G = (f_H2O_ATR / 8) * (Reynolds_H2O_ATR -
1000) * Prandtl_H2O_ATR / (1 + 12.7 * (f_H2O_ATR / 8) ^ 0.5
* (Prandtl_H2O_ATR ^ (2 / 3) - 1));
hrt_H2O_ATR_G = Nusselt_H2O_ATR_G * k_H2O_ATR /
d_tubing_interior;        % W/m^2-K
hrt_H2O_ATR = (hrt_H2O_ATR_C + hrt_H2O_ATR_G) / 2
% W/m^2-K
U_H2O_ATR = 1 / (1 / het_ATR_1123 + d_wall / k_tubing + 1 /
hrt_H2O_ATR)      % W/m^2-K
% Find the exchanging energy.
Q_H2O_ATR = m_H2O * (hg_H2Or_T_ATR - hfg_H2O_T_WGS);
% J/min
% Find the temperature of the effluents after the heat
exchange process
% with water tubing.
syms t_ATR_H2O
t_ATR_H2O = vpasolve(Q_exchange1 - Q_H2O_ATR == n_CO_ATR *
1000 * (25.56759 * (t_ATR_H2O - 0.623) + 6.096130 / 2 *
```

```
(t_ATR_H2O^2 - 0.623^2) + 4.054656 / 3 * (t_ATR_H2O^3 -
0.623^3) - 2.671301 / 4 * (t_ATR_H2O^4 - 0.623^4) -
0.131021 * (1/t_ATR_H2O - 1/0.623)) + n_CO2_ATR * 1000 *
(24.99735 * (t_ATR_H2O - 0.623) + 55.18696 / 2 *
(t_ATR_H2O^2 - 0.623^2) - 33.69137 / 3 * (t_ATR_H2O^3 -
0.623^3) + 7.948387 / 4 * (t_ATR_H2O^4 - 0.623^4) +
0.136638 * (1/t_ATR_H2O - 1/0.623)) + n_H2O_ATR * 1000 *
(30.09200 * (t_ATR_H2O - 0.623) + 6.832514 / 2 *
(t_ATR_H2O^2 - 0.623^2) + 6.793435 / 3 * (t_ATR_H2O^3 -
0.623^3) - 2.534480 / 4 * (t_ATR_H2O^4 - 0.623^4) -
0.082139 *(1/t_ATR_H2O - 1/0.623)) + n_H2_ATR * 1000 *
(18.563083 * (t_ATR_H2O - 0.623) + 12.257357 / 2 *
(t_ATR_H2O^2 - 0.623^2) - 2.859786 / 3 * (t_ATR_H2O^3 -
0.623^3) + 0.268238 / 4 * (t_ATR_H2O^4 - 0.623^4) -
1.977990 * (1/t_ATR_H2O - 1/0.623)) + n_N2 * 1000 *
(19.50583 * (t_ATR_H2O - 0.623) + 19.88705 / 2 *
(t_ATR_H2O^2 - 0.623^2) - 8.598535 / 3 * (t_ATR_H2O^3 -
0.623^3) + 1.369784 / 4 * (t_ATR_H2O^4 - 0.623^4) -
0.527601 * (1/t_ATR_H2O - 1/0.623)), t_ATR_H2O, [0 Inf]);
T_ATR_H2O = t_ATR_H2O * 1000    % K
% Find the logarithmic mean temperature difference (LMTD).
Delta_Ta_H2O_ATR = T_ATR - T_H2Or_ATR;          % K
Delta_Tb_H2O_ATR = T_ATR_H2O - T_H2O_WGS;       % K
LMTD_H2O_ATR = (Delta_Ta_H2O_ATR - Delta_Tb_H2O_ATR) /
log(Delta_Ta_H2O_ATR / Delta_Tb_H2O_ATR);    % K
% Use Q = U * P * L * LMTD to determine L for each species.
Length_H2O_ATR = Q_H2O_ATR / 60 / LMTD_H2O_ATR / U_H2O_ATR
/ Perimeter_tubing_exterior       % m

% Calculate het_ATR at 766.3 K.
mu_N2_ATR_766 = 0.000034877;         % kg/m-s
mu_CO2_ATR_766 = 0.000033956;       % kg/m-s
mu_H2_ATR_766 = 0.000016927;        % kg/m-s
mu_H2O_ATR_766 = 0.000028272;       % kg/m-s
mu_CO_ATR_766 = 4.3318e-5;          % kg/m-s
f_ATR_766 = Y_N2_ATR ^ 2 / mu_N2_ATR_766 + Y_CO2_ATR ^ 2 /
mu_CO2_ATR_766 + Y_H2_ATR ^ 2 / mu_H2_ATR_766 + Y_H2O_ATR ^
2 / mu_H2O_ATR_766 + Y_CO_ATR ^ 2 / mu_CO_ATR_766 + 2 *
Y_N2_ATR * Y_CO2_ATR * Ee_N2CO2 ^ A / ((mu_N2_ATR_766 *
mu_CO2_ATR_766) ^ (1 / 2)) + 2 * Y_N2_ATR * Y_H2_ATR *
Ee_N2H2 ^ A / ((mu_N2_ATR_766 * mu_H2_ATR_766) ^ (1 / 2)) +
2 * Y_N2_ATR * Y_H2O_ATR * Ee_N2H2O ^ A / ((mu_N2_ATR_766 *
mu_H2O_ATR_766) ^ (1 / 2)) + 2 * Y_N2_ATR * Y_CO_ATR *
Ee_N2CO ^ A / ((mu_N2_ATR_766 * mu_CO_ATR_766) ^ (1 / 2)) +
2 * Y_CO2_ATR * Y_H2_ATR * Ee_CO2H2 ^ A / ((mu_CO2_ATR_766
* mu_H2_ATR_766) ^ (1 / 2)) + 2 * Y_CO2_ATR * Y_H2O_ATR *
Ee_CO2H2O ^ A / ((mu_CO2_ATR_766 * mu_H2O_ATR_766) ^ (1 /
```

```
2)) + 2 * Y_CO2_ATR * Y_CO_ATR * Ee_CO2CO ^ A /
((mu_CO2_ATR_766 * mu_CO_ATR_766) ^ (1 / 2)) + 2 * Y_H2_ATR
* Y_H2O_ATR * Ee_H2H2O ^ A / ((mu_H2_ATR_766 *
mu_H2O_ATR_766) ^ (1 / 2)) + 2 * Y_H2_ATR * Y_CO_ATR *
Ee_H2CO ^ A / ((mu_H2_ATR_766 * mu_CO_ATR_766) ^ (1 / 2)) +
2 * Y_H2O_ATR * Y_CO_ATR * Ee_H2OCO ^ A / ((mu_H2O_ATR_766
* mu_CO_ATR_766) ^ (1 / 2));
% m-s/kg
mu_ATR_766 = 1 / f_ATR_766;              % kg/m-s
Reynolds_tubing_ATR_766 = m_ATR / 1000 / 60 / Area_reactor
* d_tubing_exterior / mu_ATR_766
Cp_N2_ATR_766 = 19.50583 + 19.88705 * t_ATR_H2O - 8.598535
* t_ATR_H2O ^ 2 + 1.369784 * t_ATR_H2O ^ 3 + 0.527601 /
t_ATR_H2O ^ 2;     % J/mol-K
Cp_CO2_ATR_766 = 24.99735 + 55.18696 * t_ATR_H2O -
33.69137* t_ATR_H2O ^ 2 + 7.948387 * t_ATR_H2O ^ 3 -
0.136638 / t_ATR_H2O ^ 2;    % J/mol-K
Cp_H2_ATR_766 = 33.066178 - 11.363417 * t_ATR_H2O +
11.432816 * t_ATR_H2O ^ 2 - 2.772874 * t_ATR_H2O ^ 3 -
0.158558 / t_ATR_H2O ^ 2;  % J/mol-K
Cp_H2O_ATR_766 = 30.09200 + 6.832514 * t_ATR_H2O + 6.793435
* t_ATR_H2O ^ 2 - 2.534480 * t_ATR_H2O ^ 3 + 0.082139 /
t_ATR_H2O ^ 2;    % J/mol-K
Cp_CO_ATR_766 = 25.56759 + 6.096130 * t_ATR_H2O + 4.054656
* t_ATR_H2O ^ 2 - 2.671301 * t_ATR_H2O ^ 3 + 0.131021 /
(t_ATR_H2O ^ 2);   % J/mol-K
Cp_ATR_766 = (X_N2_ATR * Cp_N2_ATR_766 + X_CO2_ATR *
Cp_CO2_ATR_766 + X_H2_ATR * Cp_H2_ATR_766 + X_H2O_ATR *
Cp_H2O_ATR_766 + X_CO_ATR * Cp_CO_ATR_766) / (M_ATR /
1000);  % J/kg-K
phi_N2CO2_ATR_766 = (1 + (mu_N2_ATR_766 / mu_CO2_ATR_766) ^
0.5 * (M_CO2 / M_N2) ^ 0.25) ^ 2 / (8 ^ 0.5 * (1 +  M_N2 /
M_CO2) ^ 0.5);
phi_N2H2_ATR_766 = (1 + (mu_N2_ATR_766 / mu_H2_ATR_766) ^
0.5 * (M_H2 / M_N2) ^ 0.25) ^ 2 / (8 ^ 0.5 * (1 +  M_N2 /
M_H2) ^ 0.5);
phi_N2H2O_ATR_766 = (1 + (mu_N2_ATR_766 / mu_H2O_ATR_766) ^
0.5 * (M_H2O / M_N2) ^ 0.25) ^ 2 / (8 ^ 0.5 * (1 +  M_N2 /
M_H2O) ^ 0.5);
phi_N2CO_ATR_766 = (1 + (mu_N2_ATR_766 / mu_CO_ATR_766) ^
0.5 * (M_CO / M_N2) ^ 0.25) ^ 2 / (8 ^ 0.5 * (1 +  M_N2 /
M_CO) ^ 0.5);
phi_CO2N2_ATR_766 = (1 + (mu_CO2_ATR_766 / mu_N2_ATR_766) ^
0.5 * (M_N2 / M_CO2) ^ 0.25) ^ 2 / (8 ^ 0.5 * (1 +  M_CO2 /
M_N2) ^ 0.5);
```

```
phi_CO2H2_ATR_766 = (1 + (mu_CO2_ATR_766 / mu_H2_ATR_766) ^
0.5 * (M_H2 / M_CO2) ^ 0.25) ^ 2 / (8 ^ 0.5 * (1 +  M_CO2 /
M_H2) ^ 0.5);
phi_CO2H2O_ATR_766 = (1 + (mu_CO2_ATR_766 / mu_H2O_ATR_766)
^ 0.5 * (M_H2O / M_CO2) ^ 0.25) ^ 2 / (8 ^ 0.5 * (1 +
M_CO2 / M_H2O) ^ 0.5);
phi_CO2CO_ATR_766 = (1 + (mu_CO2_ATR_766 / mu_CO_ATR_766) ^
0.5 * (M_CO / M_CO2) ^ 0.25) ^ 2 / (8 ^ 0.5 * (1 +  M_CO2 /
M_CO) ^ 0.5);
phi_H2N2_ATR_766 = (1 + (mu_H2_ATR_766 / mu_N2_ATR_766) ^
0.5 * (M_N2 / M_H2) ^ 0.25) ^ 2 / (8 ^ 0.5 * (1 +  M_H2 /
M_N2) ^ 0.5);
phi_H2CO2_ATR_766 = (1 + (mu_H2_ATR_766 / mu_CO2_ATR_766) ^
0.5 * (M_CO2 / M_H2) ^ 0.25) ^ 2 / (8 ^ 0.5 * (1 +  M_H2 /
M_CO2) ^ 0.5);
phi_H2H2O_ATR_766 = (1 + (mu_H2_ATR_766 / mu_H2O_ATR_766) ^
0.5 * (M_H2O / M_H2) ^ 0.25) ^ 2 / (8 ^ 0.5 * (1 +  M_H2 /
M_H2O) ^ 0.5);
phi_H2CO_ATR_766 = (1 + (mu_H2_ATR_766 / mu_CO_ATR_766) ^
0.5 * (M_CO / M_H2) ^ 0.25) ^ 2 / (8 ^ 0.5 * (1 +  M_H2 /
M_CO) ^ 0.5);
phi_H2ON2_ATR_766 = (1 + (mu_H2O_ATR_766 / mu_N2_ATR_766) ^
0.5 * (M_N2 / M_H2O) ^ 0.25) ^ 2 / (8 ^ 0.5 * (1 +  M_H2O /
M_N2) ^ 0.5);
phi_H2OCO2_ATR_766 = (1 + (mu_H2O_ATR_766 / mu_CO2_ATR_766)
^ 0.5 * (M_CO2 / M_H2O) ^ 0.25) ^ 2 / (8 ^ 0.5 * (1 +
M_H2O / M_CO2) ^ 0.5);
phi_H2OH2_ATR_766 = (1 + (mu_H2O_ATR_766 / mu_H2_ATR_766) ^
0.5 * (M_H2 / M_H2O) ^ 0.25) ^ 2 / (8 ^ 0.5 * (1 +  M_H2O /
M_H2) ^ 0.5);
phi_H2OCO_ATR_766 = (1 + (mu_H2O_ATR_766 / mu_CO_ATR_766) ^
0.5 * (M_CO / M_H2O) ^ 0.25) ^ 2 / (8 ^ 0.5 * (1 +  M_H2O /
M_CO) ^ 0.5);
phi_CON2_ATR_766 = (1 + (mu_CO_ATR_766 / mu_N2_ATR_766) ^
0.5 * (M_N2 / M_CO) ^ 0.25) ^ 2 / (8 ^ 0.5 * (1 +  M_CO /
M_N2) ^ 0.5);
phi_COH2_ATR_766 = (1 + (mu_CO_ATR_766 / mu_H2_ATR_766) ^
0.5 * (M_H2 / M_CO) ^ 0.25) ^ 2 / (8 ^ 0.5 * (1 +  M_CO /
M_H2) ^ 0.5);
phi_COH2O_ATR_766 = (1 + (mu_CO_ATR_766 / mu_H2O_ATR_766) ^
0.5 * (M_H2O / M_CO) ^ 0.25) ^ 2 / (8 ^ 0.5 * (1 +  M_CO /
M_H2O) ^ 0.5);
phi_COCO2_ATR_766 = (1 + (mu_CO_ATR_766 / mu_CO2_ATR_766) ^
0.5 * (M_CO2 / M_CO) ^ 0.25) ^ 2 / (8 ^ 0.5 * (1 +  M_CO /
M_CO2) ^ 0.5);
k_N2_ATR_766 = 53.784e-3;             % W/m-K
k_CO2_ATR_766 = 54.226e-3;            % W/m-K
```

```
k_H2_ATR_766 = 408.49e-3;             % W/m-K
k_H2O_ATR_766 = 66.080e-3;            % W/m-K
k_CO_ATR_766 = 76.61e-3;              % W/m-K
k_ATR_766 = X_N2_ATR * k_N2_ATR_766 / (X_N2_ATR + X_CO2_ATR
* phi_N2CO2_ATR_766 + X_H2_ATR * phi_N2H2_ATR_766 +
X_H2O_ATR * phi_N2H2O_ATR_766 + X_CO_ATR *
phi_N2CO_ATR_766) + X_CO2_ATR * k_CO2_ATR_766 / (X_N2_ATR *
phi_CO2N2_ATR_766 + X_CO2_ATR + X_H2_ATR *
phi_CO2H2_ATR_766 + X_H2O_ATR * phi_CO2H2O_ATR_766 +
X_CO_ATR * phi_CO2CO_ATR_766) + X_H2_ATR * k_H2_ATR_766 /
(X_N2_ATR * phi_H2N2_ATR_766 + X_CO2_ATR *
phi_H2CO2_ATR_766 + X_H2_ATR + X_H2O_ATR *
phi_H2H2O_ATR_766 + X_CO_ATR * phi_H2CO_ATR_766) +
X_H2O_ATR * k_H2O_ATR_766 / (X_N2_ATR * phi_H2ON2_ATR_766 +
X_CO2_ATR * phi_H2OCO2_ATR_766 + X_H2_ATR *
phi_H2OH2_ATR_766 + X_H2O_ATR + X_CO_ATR *
phi_H2OCO_ATR_766) + X_CO_ATR * k_CO_ATR_766 / (X_N2_ATR *
phi_CON2_ATR_766 + X_CO2_ATR * phi_COCO2_ATR_766 + X_H2_ATR
* phi_COH2_ATR_766 + X_H2O_ATR * phi_COH2O_ATR_766 +
X_CO_ATR);
% W/m-K
Prandtl_ATR_766 = Cp_ATR_766 * mu_ATR_766 / k_ATR_766
fn_Reynolds_tubing_ATR_766 = 0.8 * Reynolds_tubing_ATR_766
^ 0.4;
Nusselt_ATR_766 = Prandtl_ATR_766 ^ 0.36 *
fn_Reynolds_tubing_ATR_766
het_ATR_766 = Nusselt_ATR_766 * k_ATR_766 /
d_tubing_exterior          % W/m^2-K
% Calculate T_ATR_air
h_O2_473 = 5247.4;         % J/mol
h_N2_473 = 5113.85;        % J/mol
Q_air_ATR = n_O2 * (h_O2_800 - h_O2_473) + n_N2 * (h_N2_800
- h_N2_473);         % J/min
syms t_ATR_air
t_ATR_air = vpasolve(Q_exchange1 - Q_H2O_ATR - Q_air_ATR ==
n_CO_ATR * 1000 * (25.56759 * (t_ATR_air - 0.623) +
6.096130 / 2 * (t_ATR_air^2 - 0.623^2) + 4.054656 / 3 *
(t_ATR_air^3 - 0.623^3) - 2.671301 / 4 * (t_ATR_air^4 -
0.623^4) - 0.131021 * (1/t_ATR_air - 1/0.623)) + n_CO2_ATR
* 1000 * (24.99735 * (t_ATR_air - 0.623) + 55.18696 / 2 *
(t_ATR_air^2 - 0.623^2) - 33.69137 / 3 * (t_ATR_air^3 -
0.623^3) + 7.948387 / 4 * (t_ATR_air^4 - 0.623^4) +
0.136638 * (1/t_ATR_air - 1/0.623)) + n_H2O_ATR * 1000 *
(30.09200 * (t_ATR_air - 0.623) + 6.832514 / 2 *
(t_ATR_air^2 - 0.623^2) + 6.793435 / 3 * (t_ATR_air^3 -
0.623^3) - 2.534480 / 4 * (t_ATR_air^4 - 0.623^4) -
0.082139 *(1/t_ATR_air - 1/0.623)) + n_H2_ATR * 1000 *
```

```
(18.563083 * (t_ATR_air - 0.623) + 12.257357 / 2 *
(t_ATR_air^2 - 0.623^2) - 2.859786 / 3 * (t_ATR_air^3 -
0.623^3) + 0.268238 / 4 * (t_ATR_air^4 - 0.623^4) -
1.977990 * (1/t_ATR_air - 1/0.623)) + n_N2 * 1000 *
(19.50583 * (t_ATR_air - 0.623) + 19.88705 / 2 *
(t_ATR_air^2 - 0.623^2) - 8.598535 / 3 * (t_ATR_air^3 -
0.623^3) + 1.369784 / 4 * (t_ATR_air^4 - 0.623^4) -
0.527601 * (1/t_ATR_air - 1/0.623)), t_ATR_air, [0 Inf]);
T_ATR_air = t_ATR_air * 1000    % K
% Calculate hrt_air_ATR.
mu_air_ATR = 3.737e-5;          % kg/m-s
Reynolds_air_ATR = 4 * m_air / 1000 / 60 /
Perimeter_tubing_interior / mu_air_ATR
Cp_air_ATR = 1.0512;            % J/g-K
k_air_ATR = 46.011e-3;          % W/m-K
Prandtl_air_ATR = Cp_air_ATR * 1000 * mu_air_ATR /
k_air_ATR
% Based on the Reynods number and Prandtl number derived
above, the heat
% tranfer process of air can be described by Gnielinski's
correlation for
% forced convection in turbulent pipe flow, Nusselt_i_ATR =
(f_i_ATR / 8) *
% (Reynolds_i_ATR - 1000) * Prandtl_i_ATR / (1 + 12.7 *
(f_i_ATR / 8) ^ 0.5
% * (Prandtl_i_ATR ^ (2 / 3) - 1)), where f_i_ATR is the
Darcy friction
% factor, f_i_ATR = (0.79 * log(Reynolds_i_ATR) - 1.64) ^
(-2) by
% Petukhov's formula.
f_air_ATR = (0.79 * log(Reynolds_air_ATR) - 1.64) ^ (-2);
Nusselt_air_ATR = (f_air_ATR / 8) * (Reynolds_air_ATR -
1000) * Prandtl_air_ATR / (1 + 12.7 * (f_air_ATR / 8) ^ 0.5
* (Prandtl_air_ATR ^ (2 / 3) - 1));
hrt_air_ATR = Nusselt_air_ATR * k_air_ATR /
d_tubing_interior               % W/m^2-K
U_air_ATR = 1 / (1 / het_ATR_766 + d_wall / k_tubing + 1 /
hrt_air_ATR)   % W/m^2-K
% Find the logarithmic mean temperature difference (LMTD).
Delta_Ta_air_ATR = T_ATR - 800;                 % K
Delta_Tb_air_ATR = T_ATR_air - T_air_WGS;       % K
LMTD_air_ATR = (Delta_Ta_air_ATR - Delta_Tb_air_ATR) /
log(Delta_Ta_air_ATR / Delta_Tb_air_ATR);      % K
% Use Q = U * P * L * LMTD to determine L for each species.
Length_air_ATR = Q_air_ATR / 60 / LMTD_air_ATR / U_air_ATR
/ Perimeter_tubing_exterior     % m
```

Appendix D – Tubular Furnace Temperature Calibration

Set T (C)	Actual T (C)		
	Cat Front	Cat Mid	Cat Back
Room T	22.5	22.5	22.5
50	43.6	43.2	42
100	76.6	77.3	74.2
150	115	116.8	111.9
200	164.5	166.6	160.4
250	212.9	214.4	206.6
300	263.7	263.9	254.3
350	317.7	315.6	304.3
400	370.2	366.3	353.2
450	424.9	418.8	404.4
500	478.4	470.9	455.4
550	531.3	523.3	507
600	583.1	575.1	558.3
650	633.9	626.3	609.6
700	684.7	677.5	661.1
750	735.3	728.6	712.4